University of Brighton

Numerical Modeling of Bubble Dynamics and Heat Transfer on Flow Boiling within Microchannels

A thesis submitted for the degree of
Doctor of Philosophy of University of Brighton by

Konstantinos Vontas

September 26, 2022

— 1 Corinthians 16:13

Be on your guard; stand firm in the faith; be courageous; be strong.

Acknowledgement

First and foremost I would like to thank my Mother, Father, Marianna and Eleni, who always loved and supported me. A special acknowledgement should be made to my Mother for her patience and love along the completion of this degree.

I would like to thank my supervisor Dr. Anastasios Georgoulas for his immense support throughout this PhD project. I feel profoundly grateful to him for what he has taught me and for all the opportunities that he offered to me.

I am thankful also to my co-supervisor, Prof. Marco Marengo for his guidance and support in my research. Special thanks to the external supervisor of this PhD thesis, Dr. Carlo DeFalco from Politecnico di Milano for giving me the opportunity to work with his research group.

I express my sincere thanks to the European Space Agency where I had the change to visit and contribute with my work to the ESA MAP project ENCOM4.

I also want like to thank the postdoctoral fellow of University of Brighton Dr. Andredaki as well as the visiting research students from Italy, Marco Paravani and Francesco Latella for the collaboration that we had and their contributions to the present thesis. A special thanks goes also to the postgraduate student Mattia Bonnini in Politecnico di Milano for our collaboration.

My warmest and heartfelt thanks to all my friends: Kostas, Erik, Dimitris and of course to Georgia.

Last but not least, I would like to thank the European Union's Horizon 2020 research and innovation programme for funding the present PhD project. Also I would like to acknowledge the computational support from the HPC cluster of the school of Architecture, Technology and Engineering in University of Brighton.

Abstract

The ongoing trend of modern electronic devices towards the device miniaturization in combination with the increase in power dissipation per unit area has made necessary the development of new, more effective cooling methods that will be able to dissipate high heat fluxes on the order of MW m^{-2}, meeting the demand of such high-performance electronics. Flow boiling within conventional tubes finds application in various engineering fields, and is regarded as one of the most efficient cooling solutions. However, wherever the space is limited, such as in the cooling of electronics chips, conventional tubes cannot be used due to their big size. Therefore, alternative cooling methods have been studied in the past years. The proposed method should offer efficient cooling and at the same time allow room for more advancement in the years to come while maintaining proper functioning. Flow boiling heat transfer within microchannel heat sinks has been already recognised as one of the most efficient thermal management solutions for such high-power density electronic components. The main advantage of the micro/minichannels is that they have relatively large surface area to volume ratios which enable higher heat transfer rates than conventional tubes or conventional channels. Ever since this cooling method was introduced, flow boiling in microchannels has drawn worldwide attention. In more detail, a high number of investigations have been performed to understand the physical mechanisms and influential parameters, aiming to further enhance the heat transfer and flow conditions but also provide answers to fundamental issues concerning flow boiling within microchannels. However, as of now, most of these fundamental open aspects remain unanswered. Numerical simulations can play a significant role in solving some of these fundamental issues and provide useful information that may be difficult to extract from the experimental data. In order to be able to predict such complex phenomena, the development of accurate numerical models and sub-models is required. However, as important characteristics of flow boiling in such micro-scale channels have not been yet clarified, the applicability of the existing methods and correlations used today developed for conventional tubes, in minichannels and microchannels is still under discussion. In this project, various fundamental issues of flow boiling heat transfer are examined numerically (e.g. the effect of surface wettability, aspect ratio, etc. on the first transient stages of flow development), aiming to answer important open aspects in the current state-of-the-art. Additionally, a numerical method which is suitable for more global multiphase Computational Fluid Dynamic methodologies for boiling heat transfer such as the Eulerian-Eulerian two-fluid modelling, will be examined.

Particularly, the present PhD thesis is divided into two main parts. In the first part, various controlling parameters of flow boiling within microchannels, that are previously reported in the literature as "unexplored open aspects", are studied qualitatively and quantitatively and their effect in the confined two-phase flow and heat transfer characteristics is identified and quantified. These parameters include: the surface wettability, the aspect ratio, the solid surface thermophysical properties and the hydraulic diameter of the microchannels. Each of these properties have been isolated, by performing parametric analysis and altering only the examined property. This parametric analysis also constitutes one of the main novelties of the present thesis.

In order to conduct this study, high-fidelity simulations were performed, utilising an enhanced customised Volume Of Fluid (VOF)-based solver that has been previously developed within the general framework of the OpenFOAM CFD toolbox. Particularly, the utilised solver enhancements involve an appropriate treatment for spurious velocities dampening (a well-known defect of VOF methods in general), an improved dynamic contact angle treatment, as well as the implementation of a phase-change model in the fluid domain. It is important to note that the utilised solver is also accounting for Conjugate Heat Transfer (CHT) with the solid domain, an important factor that is often not taken into account in flow boiling heat transfer studies.

The results indicate that surface wettability plays a significant role in the flow boiling regime and the associated dominant heat transfer mechanism, with hydrophilic surfaces achieving higher heat transfer rates compared to the hydrophobic surfaces, due to better performance of liquid film evaporation compared to contact line evaporation mechanism. Different channel aspect ratios also result in different flow boiling regimes and therefore in different heat transfer characteristics. It is also evident that as the hydraulic diameter of the microchannels becomes smaller, the difference of the time-averaged heat transfer coefficient of the two-phase flow stage of the simulations with the single-phase stage value progressively increases. Finally, the variation of the solid surface thermophysical properties substantially affects the resulting flow boiling regimes as well as the heat transfer characteristics and enhancement. A modified empirical correlation based on an existing correlation available in the literature is also proposed. This new correlation takes into consideration, for the first time in the literature, the thermal diffusivity of the solid material of the microchannel. It is shown that the improved correlation can better predict the direct numerical simulation VOF results in comparison to the original correlation that does not consider the solid material properties. It should be mentioned that one of the main novelties of the present thesis lies in the fact that the effect of the investigated controlling parameters is quantified on the resulting transient two-phase flow and heat transfer characteristics, focusing on the first transient stages, from the bubble nucleation and growth up to the two-phase flow development.

In the second part of the present PhD thesis, the capabilities of the Eulerian-Eulerian two-fluid model of OpenFOAM are examined initially against experiments of flow boiling within conventional tubes and subsequently against experimental data of flow boiling within microchannels. The purpose of conducting simulations using this numerical model is because it can successfully study complex phenomena such as flow boiling within conventional tubes, at lower computational cost compared to the VOF method and it is therefore applicable to device scale simulations. The results showed that the Eulerian-Eulerian two-fluid model of OpenFOAM is able to adequately predict the radial profiles of the vapour fraction and the liquid temperature, as well as the axial profiles of the heat transfer coefficient and wall temperature of a conventional tube, calibrating in each case the constitutive correlations through tuning of various empirical coefficients, by performing sensitivity analysis. However when the optimised/calibrated numerical simulation set-up was applied to numerically reproduce experiments of flow boiling within microchannels it has been found that the model is not able to predict the heat transfer coefficient trends for all of the examined cases successfully, especially for the case of low to moderate mass fluxes. This is attributed to the different underlying

physical phenomena of flow boiling within microchannels compared to conventional tubes, and by the fact that the included sub-models use empirical correlations based on experiments conducted in conventional tubes.

Finally, as it is evident from the overall results of the present thesis, in the future it is necessary to utilise a combination of high fidelity VOF-based numerical simulation results and high-resolution spatiotemporally resolved experimental measurements to develop new closure relationships to be implemented in the Eulerian-Eulerian two-fluid simulation framework to render it capable to accurately predict flow boiling within microchannels.

Latin Letters

$\dot{h}$	Energy source term	$[J/m^3]$
$\dot{V}$	Volumetric flow rate	$[m^3/s]$
$\dot{m}$	Mass flow	$[kg/s]$
h_{lv}	Latent heat of vaporization	$[m^2/s^2]$
q''	Heat transfer coefficient	$[kW/m^2]$
$\overline{R}$	Time-averaged thermal resistance	$[Km^2/W]$
$\vec{f}_g$	Momentum source term due to gravity	$[N/m^3]$
$\vec{f}_{st}$	Momentum source term due to surface tension	$[N/m^3]$
$\vec{n}$	Normal vector	$[-]$
$\vec{S}$	Surface area vector	$[m^2]$
C_D	Drag coefficient	$[-]$
c_p	Constant pressure specific heat	$[m^2/s^2K]$
D	Diameter	$[m]$
G	Mass flux	$[kg/m^2s]$
g	Gravitational accelaration	$[WmK]$
H	Enthalpy	$[J]$
h	Heat transfer coefficient	$[W/m^2s]$
j	Evaporating mass flux	$[kg/m^2K]$
L	Length	$[m]$
M	Molecular weight	$[kg/mol]$
p	Pressure	$[Pa]$
Q	Heat transfer rate	$[W]$
R	Thermal resistance	$[Km^2/W]$
r	Radius	$[m]$
R_{gas}	Gas constant	$[J/kgK]$

T	Temperature	[K]
t	Time	[s]
U	Velocity	[m/s]
V	Volume	[m^3]
W	Width	[m]

Greek Letters

α	1. Volume fraction 2. Thermal diffusivity	[W/mK]
β	Channels' aspect ratio	[−]
$\Delta\overline{\mathrm{h}}$	Percentage difference of time-averaged local heat transfer coefficient	[%]
ΔT	Temperature difference	[K]
δ	Thickness of the thermal/velocity boundary layer	[m]
$\Delta\rho$	Density difference	[kgm^3]
$\Delta\tau$	Time step	[s]
κ	Interface curvature	[1/m]
λ, κ	Thermal conductivity	[W/mK]
μ	Dynamic viscosity	[Pas]
ν	Kinematic viscosity	[m^2/s]
ρ	Density	[kg/m^3]
σ	Surface tension	[N/m]
θ	Contact angle	[°]

Abbreviations

AR	Aspect Ratio
CA	Contact Angle
CFD	Computational Fluid Dynamics
CHT	Conjugate Heat Transfer
DNS	Direct Numerical Simulations
E − E	Eulerian-Eulerian

FVM Finite-Volume-Method

HPC High-Performance Computing

IATE Interfacial Area Transport Equation

LS Level-Set

ONB Onset of Nucleate Boiling

PISO Pressure Implicit with Splitting of Operators

SS Stainless steel

VOF Volume-of-Fluid

Subscripts

0 Static reference

α Advancing

c Convection

$cline$ Contact line

cr Critical

eq Equilibrium

$evap, e$ Evaporation

f Fluid

gas Gas phase

$glob$ Global value

h Hydraulic

int Interface/interfacial

l Liquid

lv, if Liquid-vapour interface

$new - cor$ New correlation developed in the present study

$old - cor$ Old correlation developed by Li and Wu [1]

q Quenching

r Receding

ref Reference value

sat Saturation

$sp, s-p$ Single-phase stage of the simulation

sp Single-phase stage of the simulation

TD Turbulent dispersion

TI Turbulent impact

$tp, t-p$ Two-phase stage of the simulation

v Vapour

w Wall

WE Wake Entrainment

wt Waiting time

x Local value

Dimensionless Numbers

Ca Cappilary number $\left(\frac{\mu u_{\text{cline}}}{\sigma}\right)$

B_i Biot number $\left(Bi = \frac{h\delta}{\lambda}\right)$

B_l Boiling number $\left(Bl = \frac{q}{Gh_{lv}}\right)$

L^* Dimensionless length $\left(L^* = \frac{L(x)}{L_0}\right)$

Nu Nusselt number $\left(Nu = \frac{hD_h}{\lambda}\right)$

Pr Prandtl number $\left(\text{Pr} = \frac{c_p\mu}{\lambda}\right)$

Re Reynolds number $\left(Re = \frac{GD}{\mu}, Re = \frac{\rho UD}{\mu}\right)$

We Weber number $\left(We = \frac{\rho U^2 D}{\sigma}\right)$

Contents

List of Figures

List of Tables

1 Introduction

In this chapter, a brief introduction to the motivation for conducting the present PhD thesis as well as the main goals of this work together with a brief outline of the thesis, are presented.

1.1 A brief introduction to flow boiling in microchannels

The global tendency towards miniaturization driven by the micro-electronics industry is pushing systems and packaging towards unprecedented values of thermal load, with a parallel dramatic reduction of the surface area of the devices. The continuously increasing performance of these electronics results in the need for dissipation of continuously increasing high heat fluxes which can seriously damage or even destroy the devices. Investigations have reported that the average heat flux in computer chips is predicted to reach 2-4.5 $\mathrm{MW\,m^{-2}}$ by 2026 [2], while the next generation of computer chips is expected to produce localized heat fluxes over 10 $\mathrm{MW\,m^{-2}}$ [3, 4]. The highest values of heat flux at the chip level can be found in Insulated Gate Bipolar Transistors (IGBTs), where heat fluxes can reach values as high as 6.5-50 $\mathrm{MW\,m^{-2}}$ [5]. At the same time conventional cooling methods that are used today, such as air cooling through fans or pumped liquid cooling, cannot cope with such high cooling demands. This has led to important thermal management challenges for emerging electronic devices. To overcome this issue, new technologies of multiphase thermal systems for Smart Thermal Management (STM) have been developed [6–10]. Among numerous STM technologies, two-phase microchannel cooling technology is predicted to be a promising solution [11]. The concept of microchannel (high surface area to volume ratio) as a cooling mechanism was firstly introduced by Tuckerman and Pease [12]. Subsequently, a big amount of both experimental and numerical studies of flow boiling in microchannels have been performed, in order to better understand the underpinned phenomena and improve the heat transfer performance.

A two-phase flow (flow-boiling) cooling method is more effective compared to a single-phase flow due to the involvement of the latent heat of evaporation/condensation. This has made further investigations of phase-change cooling a necessity for better understanding the phenomena and facilitating higher heat transfer [13]. An additional advantage of phase change phenomena is that cooling can be achieved at a uniform temperature, in this way the possibility of hot-spot formation on the surface of electronic devices that can even cause a failure is eliminated.

On the other hand, flow instability is the major challenge that hampers the implementation of two-phase microchannel heat sinks in some practical applications [1] (a problem that is encountered in multiple parallel microchannels). Making difficult the prediction of flow both experimentally and numerically. However, it has been found that the heat transfer coefficient (HTC) can rise when notches in the sidewalls of microchannels are created, as well as quasi-steady flow boiling conditions can be achieved by using inlet flow restrictions [14].

As mentioned above, for optimising the existing STM systems and their components, the development of new numerical simulation techniques is required. The existing models, that are available in the literature for flow boiling in microchannels, rely on

empirical correlations from experiments based on conventional channels, where the heat transfer characteristics are different compared to microchannels [2]. Furthermore, they also consider only specific liquids (mostly water), while in the industry is very common that different liquids with other properties than water are used as well [15]. The main aim of the present PhD Thesis is to utilise an existing, enhanced Volume-Of-Fluid-based (VOF-based) direct numerical simulation approach for fundamental research on boiling heat transfer, providing valuable information on the underlying physics and heat transfer characteristics on flow boiling within microchannels. The scope is two-fold, i.e. to utilise the enhanced VOF method in order to give answers to important unresolved aspects of flow boiling within microchannels (e.g. the examination of various parameters such as surface wettability, channels' aspect ratio, solid surface thermophysical properties and channels' hydraulic diameter) and to create a database that can be used to explore the weaknesses and limitations of existing closure relationships and sub-models in more global multiphase Computational Fluid Dynamic (CFD) methodologies for boiling heat transfer such as the Eulerian-Eulerian two-fluid modelling approach. Therefore, the capabilities of the Eulerian-Eulerian two-fluid method are also tested, after performing a sensitivity analysis, against experiments of flow boiling within conventional tubes and microchannels, utilising literature-assailable experimental data. The overall results from the application of the VOF as well as the Eulerian-Eulerian multiphase approaches contribute significantly to the current state of the art by identifying and quantifying important unresolved aspects of flow boiling within micro-channels and by illustrating the necessity for significant future modification of the Eulerian-Eulerian two-fluid methodology for the successful prediction of the main fluid flow and heat transfer characteristics.

1.2 Thesis Outline

Chapter 1 presents the motivation and aim of this Ph.D. thesis.

Chapter 2 provides some fundamental background on heat transfer and boiling characteristics. This chapter also presents a review of the state-of-the-art on both experimental and numerical works on flow boiling characteristics within microchannels.

Chapter 3 describes the formulation of the enhanced VOF-based solver, utilised in the present thesis. Additionally, the governing equations of the Eulerian-Eulerian two-fluid model for boiling heat transfer that is utilised in the present thesis are presented along with the necessary closure models. All the sub-models utilised for the simulations of the present thesis are also presented.

Chapter 4 reports the results from the application of the VOF-based numerical simulation framework. In this chapter, various fundamental unresolved research aspects and issues of flow boiling within microchannels are investigated (i.e. the effect of solid surface wettability, channel aspect ratio, channel hydraulic diameter and solid surface thermophysical properties). For each of the investigated aspects, an extended literature review, as well as qualitative and quantitative results together with detailed conclusions, are reported.

Chapter 5 shows the numerical simulations conducted utilising the

Eulerian-Eulerian two-fluid method. In this, chapter a sensitivity analysis is performed in order to initially validate/tune the method against experiments of flow boiling within conventional channels. Subsequently, the accuracy of the optimum/validated model set-up from the conventional channel simulations is checked against experiments of flow boiling within microchannels, indicating the necessity of replacing the existing correlations with correlations based on data from investigations of microchannels. Potential reasons for the discrepancy of the predictions for the case of microchannels are discussed in relation to the VOF results database of Chapter 4.

Chapter 6 summarizes the conclusions based on the results presented in the previous chapters. Finally, recommendations for future work are discussed as well.

2 State of the art review

2.1 Introduction

Phase-change heat transfer is a broad field that finds applications in many of the engineering disciplines [16–20]. Boiling and condensation are two of the most important phase-change processes as they are generally associated with high heat transfer rates [21–24]. In this section, fundamentals of pool and flow boiling heat transfer will be presented, in order to give a fundamental overview to the present work. More detailed representation of the boiling theory can be found in [25–28].

2.2 Boiling phenomena

At a solid-liquid interface, boiling occurs when the temperature of the solid surface, where the liquid is in contact with, is higher than the saturation temperature T_{sat} of the liquid at any specific pressure. Important parameters in boiling are the latent heat of vapourisation h_{fg}, the surface tension σ at the liquid-vapour interface and the density difference between the two phases [29]. This difference induces a buoyancy force, which is proportional to $g(\rho_l - \rho_\nu)$, where g is the gravitational acceleration, ρ_l and ρ_ν are the saturated density of the liquid and vapour phase, respectively.

Thanks to the combined latent heat and buoyancy-driven flow effects, boiling and condensation heat transfer coefficients and rates are much higher than those characteristics of convection heat transfer without phase-change (e.g. single-phase) [29]. Particularly, latent heat is the heat required for an object to change phase and buoyancy-driven flow effects is a result of density difference due to a temperature gradient. The rate of heat transfer by convection is expressed by Newton's law of cooling :

$$q = hA(T_w - T_{bulk}) \tag{1}$$

where, h is the heat transfer coefficient in $\mathrm{W\,m^{-2}\,K^{-1}}$, A is the surface area involved in the heat transfer (area of the microchannel) in $\mathrm{m^2}$, while T_w and T_{bulk} are the temperatures of the solid wall and the bulk liquid respectively in K. In cases where saturated liquid flows into the channel from the inlet, the bulk temperature (T_{bulk}) is equal to the saturation temperature T_{sat} at the specific pressure of the considered flow.

From equation 1 it can be seen that the available options for improving the heat transfer are by either increasing the heat transfer coefficient h, the surface area A or the temperature difference of the wall $T_w - T_{sat}$. Increasing the area A means higher cost, more weight and bigger size of the heat sink, which is against the miniaturization design of the nowadays devices that, as mentioned previously, has led to smaller devices and therefore smaller areas. Increasing the heated wall temperature T_w can negatively affect the efficiency of the heat exchanger or even damage the device. Hence, increasing the heat transfer coefficient h is considered the most efficient and safe way for enhancing the heat transfer of heat sinks.

From equation 1, and for the case of saturated liquid flowing into a microchannel, the local heat transfer coefficient at any specific location along a heated wall can be easily obtained as follows:

$$h_{(x)} = \frac{q}{A(T_{w(x)} - T_{sat})} \tag{2}$$

where x represents the position along the central longitudinal axis of the conjugate heat transfer boundary.

2.2.1 Pool boiling

Pool boiling is defined as a stationary flow while bubbles grow and rise due to buoyancy effects. Saturated pool boiling term is employed when the temperature of the liquid reaches its boiling point, while the term subcooling refers to a liquid existing at a temperature below its normal boiling point. Nukiyama [30] was the first who identified experimentally and published different regimes that can be encountered in pool boiling of saturated water at 1 atm. Particularly, in his work, shown in Fig. 1, it is stated that boiling takes different forms which are functions of the wall superheat ΔT_e, which is termed as the temperature difference between the wall temperature T_w and the fluids saturation temperature T_{sat}. Pool boiling (of water) consists of four primary regimes:

- **Natural convection boiling** *(where $\Delta T_e < 5\,^{\circ}C$)*: Up to point A, heat is removed by natural convection in the pool and then by evaporation at the free surface. As the excess temperature is increased, bubble inception will eventually occur, but below point A, referred to as the onset of nucleate boiling ONB, fluid motion is determined principally by free convection effects. Finally, at point A or the ONB the first bubbles will appear.

- **Nucleate boiling** *(where, $5\,^{\circ}C < \Delta T_e < 30\,^{\circ}C$)*: In this regime most of the heat exchange is through direct transfer from the surface to liquid in motion at the surface, and not through the vapour bubbles rising from the surface. In the region $A - B$ bubbles are formed but collapse and dissipate into the liquid rapidly (subcooled boiling region). In the region $B - C$, the vapour escapes as columns, which subsequently merge into slugs of vapour (saturated boiling region). Point P of Fig. 1 shows a change in the behavior of the boiling curve. Before point P, the boiling curve can be approximated as a straight line on a log–log plot. The heat flux, after this point increases more slowly as ΔT_e is increased, with the maximum heat transfer coefficient h to be achieved when the heated surface is covered by bubbles. The point where the maximum h occurs is known as the Critical Heat Flux (CHF) (point C).

- **Transition boiling** *(where, $30\,^{\circ}C < \Delta T_e < 200\,^{\circ}C$)*: After the CHF point is reached, the transition boiling regime occurs. Now the heated surface is covered by a vapour layer, which acts as a thermal insulator. At any point on the surface, conditions can oscillate between nucleate and film boiling, with the fraction of the total surface covered by the vapour film increasing with the increase of the ΔT_e. As a result, due to the significantly lower thermal conductivity of the vapour phase in comparison to the liquid phase, a fast drop in the overall heat transfer occurs at this boiling regime.

- **Film boiling** *(where,* $200\,^{\circ}C < \Delta T_e$*)*: At point D of the boiling curve, referred as Leidenfrost point, a stable film boiling in the heated surface has been developed. This is also the point with the lowest heat flux when the vapour completely covers the heating surface $q''_{s,D} = q''_{min}$. Heat transfer from the surface to the liquid occurs by conduction and radiation through the vapour layer, with the radiation to be more significant as the ΔT_e increases. At this stage, the heat flux also increases with the increase of the ΔT_e. At such wall superheat, bubbles bounce off or prowl above the heating surface without any form of wetting taking place.

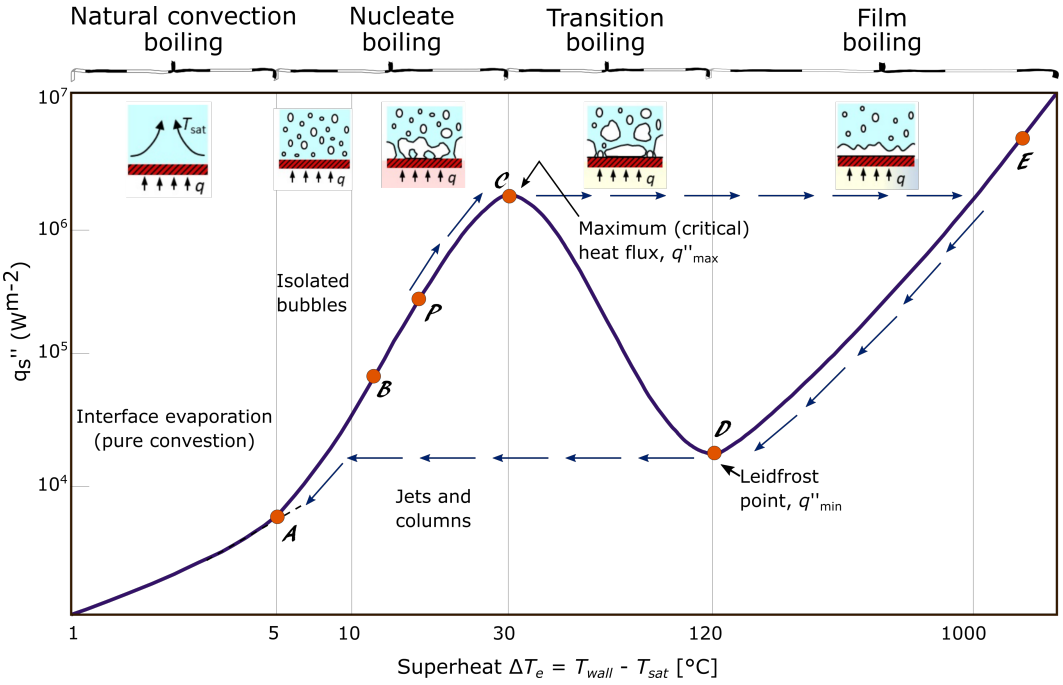

Figure 1: Boiling curve of water at atmospheric pressure [30].

More details regarding Nukiyama's work and the resulting boiling regimes observed can be found here [29].

For the prediction of the heat transfer in the nucleate boiling regime, there are not any theoretical relations available. Instead, experimental-based correlations are used. Some of the most commonly used correlations for the prediction of pool boiling in different regimes are shown in Table 1.

2.2.2 Flow boiling

Flow boiling combines pool boiling with flow convection and is classified into two categories: internal flow and external flow. External flow is similar to pool boiling with additional heat flux due to flow motion. However, in internal flow, vapour and liquid are forced to move together and there is no path for vapour to escape to free surface. Forced convection boiling is commonly referred to as two-phase flow and is characterized by rapid changes from liquid to vapour in the flow direction. The two-phase flow within a tube, minichannel or microchannel exhibits different flow boiling regimes, depending

Table 1: Proposed correlations for pool boiling available in literature

Reference	Model	Regime
Cooper [31]	$h = 1.7 \times 55 P_r^{(0.12-0.2 log C_{sf})}(-log P_r)^{-0.55} \bar{M}^{-0.5} \times q_{wall}^{0.67}$ $P_r = P_{sat}/P_{crt}, \bar{M} = 102.03 (for R134a)$	General
Ribatski & Jobardo [32]	$h = 100 \times P_r^{(0.45)}(-log P_r)^{-0.8} \bar{M}^{-0.5} \mathrm{Re}_a^{0.2} \times q_{wall}^{0.9-0.3 P_r^{(0.3)}}$	Nucleate boiling
Jung [33]	$Nu = \frac{hD}{\lambda_l T_{sat}} = 10(\frac{q_{wall}\phi}{A \lambda_l T_{sat}})^{c1}(1-T_r)^{-1.4} Pr_l^{-0.25}$ $\phi = 0.0146\sqrt{2\sigma/g(\rho_l - \rho_v)}, T_r = \frac{T_{sat}}{T_{crt}}$ $c_1 = 0.855(\frac{\rho_v}{\rho_l})^{0.309} Pr^{-0.437}$	Nucleate boiling
Rohsenow [34]	$q_{wall} = \mu_l h_{lv}[\frac{g(\rho_l - \rho_v)}{\sigma}]^{0.5}[\frac{Cp_v(T_{wall} - T_{sat}}{C_{sf} h_{lv} Pr_l^{1.0}}]^3$	Nucleate boiling
Stephan & Abdelsalam [35]	$Nu = \frac{hD}{\lambda_l} = 0.0546[(\frac{\rho_v}{\rho_l})^{0.5} \frac{q_{wall} d_w}{\lambda_l T_{sat}}]^{0.67}$ $\times [\frac{h_{lv} d_w}{a_L^2}]^{(0.248)}[\frac{\rho_l - \rho_v}{\rho_l}]^{-4.33}$	Nucleate boiling
Bromley [34]	$q_{wall} = 0.62[\frac{g\lambda_l^3 \rho_v(\rho_l - \rho_v)[h_{lv} + 0.4 Cp_v(T_{wall} - T_{sat})]}{\mu_v D(T_{wall} - T_{sat})}]^{0.25}$ $\times (T_{wall} - T_{sat})$	Film boiling

on several parameters [36–38], making the understanding of the phenomena even more difficult.

Internal flow regimes can be divided into bubbly, slug, annular, transition and mist flow [34]. The different stages in flow boiling in a heated tube, together with the corresponding heat transfer coefficient variation along the tube are shown in Fig. 2. In more detail, in the inlet of the channel, the liquid is under its saturation temperature and the heat transfer to the liquid is by forced convection process. Subsequently, as the temperature of the liquid increases, bubble nucleation near the wall is observed. However, because the bulk temperature of the liquid remains under the saturation temperature, the bubbles, after reaching their critical dimension, detach from the heated wall, and condense into the liquid, heating it, generating subcooled flow boiling. As the bulk temperature of the liquid continuously raises and finally reaches its saturation temperature, bubbles start to appear everywhere, detach, grow and rise from the heated surface resulting in a bubbly flow. As the liquid is heated further, the formed bubbles

begin to coalescence forming slugs of vapour. Later along the tube an annular flow can be seen and characterised by a liquid that is confined on the walls while the core of the tube is filled with vapour. This leads to very high heat transfer coefficients. The continuous heating of the wall has as a result the annular liquid layer to become thinner and thinner, with eventually dry patches (elongated vapour areas) at the inner surface of the channel appearing. The appearance of such dry patches is associated with a sharp decrease of the heat transfer coefficient, leading to transition flow which is observed until the inner surface is completely dry. During this stage, any liquid exists in the form of droplets suspended in the vapour core until it has vanished. This is referred to as mist-flow regime. At the end of the mist-flow regime, there is saturated vapour, which becomes superheated with any further application of heat. Table 2 shows various flow boiling correlation that have been developed, based on microchannel and minichannel experiments and are available in literature.

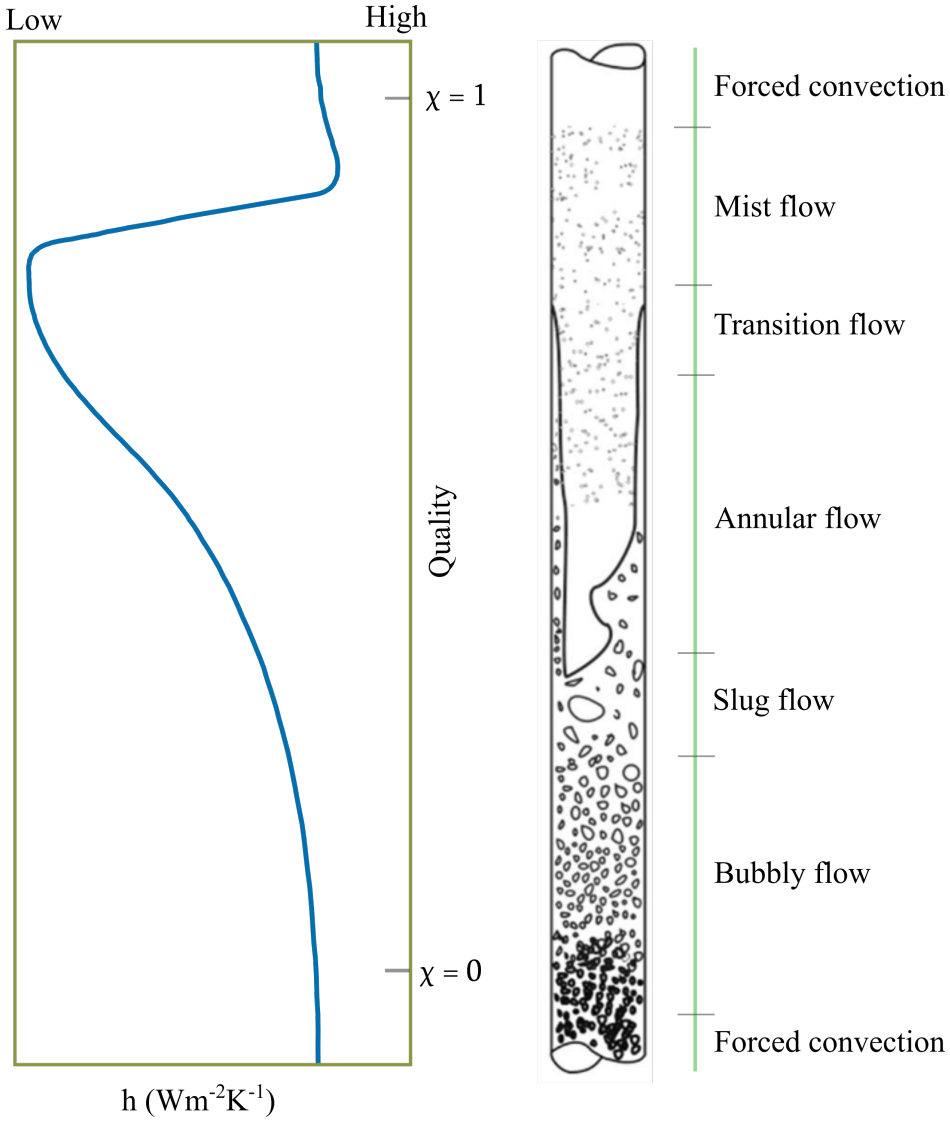

Figure 2: Boiling curve of water at atmospheric pressure (left) and flow boiling regimes within a tube under forced convection [29].

2.3 State of the art

2.3.1 Experimental and numerical investigations of flow boiling within micochannels

Over the past years numerous investigations, both experimental and numerical, were conducted in order to analyze and understand important parameters which can affect single-phase heat transfer as well as flow boiling within microchannels. Such parameters include the geometry of the channel [51–55], fluid and flow characteristics [56–59], the channel aspect ratio [60–62] and surface characteristics [63–65]. In this section, a brief review of the most relevant experimental studies will be given. In the next chapters a more detailed and comprehensive literature review examining each parameter separately will be presented.

In the bibliography various morphologies of microchannels have been investigated and proposed [66–70]. In more detail, Chung et al. [71] performed experiments of two-phase flow on square and circular microchannels under adiabatic conditions and found out that under the same experimental conditions, only slug flow was identified in both geometries. Sempértegui-Tapiaa and Ribatski [72], conducted experiments of convective boiling heat transfer of different heat flux values of refrigerant R134a for circular, square and triangular microchannels and it was found that for low heat fluxes, the heat transfer coefficient for the circular channel is higher, whereas for high heat fluxes, the heat transfer coefficient for the triangular channel is higher than for circular and square channels.

Flow regimes themselves can play a significant role in the overall heat transfer rates during flow boiling within microchannels. Geometry and dimensions of the channel (in addition to fluid parameters), can determine the flow regimes within the channel. Harirchian and Garimella [73] performed experiments of flow boiling of a dielectric fluid, Fluorinert FC-77 in a microchannel to investigate the effects of channel size and mass flux in flow regimes. In total, twelve different flow regime maps were plotted for the six channel dimensions considered using coordinates of mass flux versus vapour quality and of liquid superficial velocity versus vapour superficial velocity. Both types of flow regime maps depended on channel dimensions; hence, for each channel dimension, a separate flow regime map was required to capture the flow regime transitions accurately. The proposed flow maps are depicted in Fig. 3.

Different coolants are used as working fluids (e.g. water R134a, R113 etc.), in microchannel heat sinks. In their review, Tulius et al. [74] found out that the most commonly used fluids are air, water and refrigerants. Some of these fluids have limited heat transfer capabilities due to their transport properties. More specifically, air has been a preferred fluid used in microchannel heat sinks for the cooling of electronic components in the past. However, nowadays cooling methods of air have become insufficient for most cases due to the rapid increase of the dissipated heat fluxes which are above $1000\,\mathrm{kW\,m^{-2}}$ for most applications. On the other hand, liquids have a much higher convection heat transfer coefficient providing a better performance in cooling [75]. As mentioned before, one way to reduce convection resistance is by increasing heat transfer coefficient. A qualitative comparison of different heat transfer coefficients is presented in Fig. 4. As it can be observed the heat transfer coefficients that can be

Table 2: Proposed correlations available in literature for flow boiling within mini/microchannels.

Comments	Model	Ref
For mini/ microchannels D_h= 0.19 to 32mm G=13 to 8179kg/m^{2}s^{-1} P=0.4 to 64 bar water, refrigerants	$h_{tp} = max(h_{CBD}, h_{NBD})(1-\chi)^{0.8} h_{lo}$ $h_{NBD} = 0.6683 N_{Co}^{-0.2} + 1058 Bo^{0.7} F_{Fl})$ $h_{CBD} = 1.136 N_{Co}^{-0.9} + 667.2 Bo^{0.7} F_{Fl})$ $h_{lo} = \frac{Re_{lo} Pr_l (f/2)(k_l/D_h)}{1 + 12.7(Pr_l^{2/3} - 1(f/2)^{0.5}}, 10^4 \leq Re_{lo} \leq 5 \times 10^6$ $h_{lo} = \frac{(Re_{lo} - 1000) Pr_l (f/2)(k_l/D)}{1 + 12.7(Pr_l^{2/3} - 1(f/2)^{0.5}}, 3 \times 10^3 \leq Re_{lo} \leq 5 \times 10^4$ For $1600 < Re_{lo} < 3000$), h_{lo} is calculated by interpolation between $Re_{lo} = 1600$ and 3000 For $Re_{lo} < 1600$, h_{lo} is calculated from Nu = constant For $Re_{lo} < 100$, $h_{tp} = h_{NBD}(1-\chi)^{0.8} h_{lo}$	[39]
For minichannel D_h= 3.1 mm Based on 728 data points G=125 to 750kg/m^{2}s P=1.3 to 4.1 bar Bo = 2.3×10^{-4} to 76×10^{-4} coolant: R113	$h_{tp} = \frac{k_l}{D_h}(30 Re_{lo^{0.857}} Bo^{0.714})$	[40]
For mini/ microchannels Based on R141b and water flow in circular tube with diameter 1.39 to 3.69mm	$h_{tp} = (30 Re_{lo}^{0.857} Bo^{0.714} (1-\chi)^{0.143})$	[41]
For minichannel coolant: FC-84 D_h=0.75mm $0.00027 \leq$ Bo ≤ 0.00089 $0.03 \leq \chi \leq 0.55$	$h_{tp} = [1 + 6Bo^{1/16} - 5.3\chi^{0.65}(1 - 855Bo)]\frac{4.36 k_l}{D_h}$	[42]
For minichannel for flow boiling in small horizontal tube D_h= 2.98mm G=50 to 200kg/m^{2}s P=200kPa	$h = 6400000(Bo^2 We_l)^{0.27}(\rho_l/\rho_g)^{-0.2}$	[43]

Table 2: (continued) Proposed correlations available in literature for flow boiling within mini/microchannels.

Comments	Model	Ref
For minichannel D_h= 3.1 mm Based on 728 data points G=125 to 750kg/m^{2}s P=1.3 to 4.1 bar Bo = 2.3×10^{-4} to 76×10^{-4} coolant: R113	For $0 < \chi \leq 0.05, h_{tp} = 3.856X^{0.267}h_l$ $h_l = Nu_3 k/D_h$ $Nu_3 = 8.235(1 - 1.883\alpha + 3.767\alpha^2$ $-5.814\alpha^3 + 5.361\alpha^4 - 2\alpha^5)$ $X_{vv} = (\frac{\mu_l}{\mu_g})^{0.5}(\frac{1-\chi}{\chi})^{0.5}(\frac{\nu_l}{\nu_g})^{0.5}$ $X_{vt} = (\frac{f_l Re_g^{0.2}}{0.046})^{0.5}(\frac{1-\chi}{\chi})(\frac{\nu_l}{\nu_g})^{0.5}$ $Re_g = \frac{G\chi D_h}{\mu_l}$ For $0.05 < \chi \leq 0.55$, $h_{tp} = 436.48Bo^{0522}We_l^{0.351}X^{0.665}h_l$ For $0.55 < x \leq 1, h_{tp} = MAX(108.6X^{1.665}h_g, h_g)$ $h_g = Nu_g k/D_h$ $Nug = 0023Re_g^{0.8}Pr_g^{0.4}$(for turbulent gas flow)	[44]
For mini/ microchannels Based on 3700 data and 13 coolants D_h=0.2 to 3mm	$h_{tp} = 334Bl^{0.3}(BoRe_l^{0.36})^{0.4}\frac{k_l}{D_h}$	[45]
For mini/ microchannels based on 3700 data and 12 fluids. Out of these 12 , one is water and remaining fluids are wetting fluids only such as refrigerants, liquid N2 and FC-77 D_h= 0.16 to 2.92mm G=20 to 3000kg/m^{2}s q"=4 to 1150 kW/m^2 χ=0 to 1	$h_{tp} = Sh_{nb} + Eh_{conv}$ Modified cooper correlation suggested by Jones and Garimella [46] $h_{np} = 55P_r^{0.12}R_p^{(1-P_r)//5}(-log_{10}P_r)^{-0.55}M_w^{-0.5}q^{0.67}$ $h_{conv} = (1-\chi)h_{lo} + \chi h_{go}$ For turbulent flow h_{lo} and h_{go} are calculated from the Dittus–Boelter equation For laminar flow: $h_{lo/go} = \frac{k_{l/g}}{D_h}\left[3.66 + \frac{0.0668\frac{D_h}{l}Re_{lo/go}Pr_{l/g}}{1 + 0.04((D_h Re_{lo/go}\frac{Pr_{l/g}}{l})^{2/3}}\right]$ $S = (1-\chi)$ $E = 1 + 80(\chi^2 - \chi^6)exp(-0.6Co)$ $Co = (\|\ \sigma/g\Delta\rho\|)^{0.5}/D_h$	[47]

Table 2: (continued) Proposed correlations available in literature for flow boiling within mini/microchannels.

Comments	Model	Ref
For mini/ microchannel Based on 8561 data and R134a coolant D_h= 0.52 to 4.26mm G=100 to 500kg/m^{2}s q"=2.4 to 175.4kw/m^2 P=6 to 14bar	For $D_h = 0.52mm, \chi \leq 0.3$ $h_{tp} = 3320\frac{Bo^{0.63}We_l^{0.2}Re_l^{0.11}}{Co^{0.6}}\frac{k_l}{D_h}$ For $D_h = 0.52mm, \chi > 0.3$ $h_{tp} = 5324\left[\frac{Bo^{0.3}We_l^{0.25}}{No_{Co}^{0.6}}\right]\frac{k_l}{D_h}$	[48]
For mini/ microchannel Based on 5152 data points and R134a coolant D_h= 0.52 to 4.26mm G=100 to 700kg/m^{2}s q"=1.7 to 158kw/m^2 P=6 to 14bar	$h_{tp} = S_{new}hCooper + E_{new}h_l$ $h_{Cooper} = 55Pr^{0.12-0.434lnR_p}(-logPr)^{-0.55}M_w^{-0.5}q^{0.67}$ $h_l = 4.36\frac{k_l}{d_h}$ for $Re_l < 2000$ $h_l = 0.023Re_l^{0.8}Pr_l^{0.4}\frac{k_l}{d_h}Re_l > 3000$ $Re_l = \frac{(1-\chi)GD_h}{\mu_l}$ $E_{new} = \left(1 + \frac{2.812Co^{-0.408}}{X}\right)^{0.64}$ $S_{new} = \frac{1}{1 + 2.56 \times 10^{-6}(Re_l E_{new}^{1.25})^{1.17}}$ $X = \left(\frac{f_l}{f_g}\right)^{0.5}\left(\frac{\rho_g}{\rho_l}\frac{1-\chi}{\chi}\right)$	[48]
For mini/ microchannel Based on 2505 data and 11 coolants D_h= 0.21 to 6.05mm G=44 to 1500kg/m^{2}s q"=5 to 109kw/m^2	$h_{tp} = \left[\frac{6Re_{lo}^{1.05}Bo^{0.54}}{We_l^{0.191}(\rho_l/\rho_g)^{0.142}}]\frac{k_l}{D_h}\right]$	[49]

Table 2: (continued) Proposed correlations available in literature for flow boiling within mini/microchannels.

Comments	Model	Ref
For minichanel Based on 1157 data and NH_3 coolant D_h= 1.22 to 32mm G=10 to 600kg/m^{2}s q"=2.0 to 240.0kw/m^2 P=1.9 to 16bar	$h = 0.00061(S+F)Re_1 Pr_1^{0.4} Fa^{0.11\frac{k_l}{\mu_{lw}}} / \left(\frac{b\mu_{lf}}{\mu_{lw}}\right)$ $Fa = \frac{(\rho_l - \rho_g)\sigma}{G^2 d_h}$ $b = \begin{cases} -1.936 + 2.966\mu_{lf}/\mu_{lw} \\ -2.589 + 3.543\mu_{lf}/\mu_{lw} \end{cases}$ $S = \begin{cases} 81000Bo^{1.191} + 0.66 \\ 58000Bo^{1.15} + 2.6 \end{cases}$ $F = \left(\frac{x}{1-x}\right)\left(\frac{\rho_l}{\rho_g}\right)$	[50]

achieved with flow boiling are orders of magnitude higher than conventional single-phase convective flows.

In the literature there are several parameters related the enhancement of heat transfer in microchannels, that are still under investigation. This has hampered the transition of this innovative cooling methods from laboratory research to commercial applications. Karayiannis and Mahmoud [2] presented their experimental research on flow boiling in single tubes as well as rectangular parallel microchannels and discussed the following fundamental, unresolved issues: (1) the definition of a microchannel (e.g. what ranges of hydraulic diameter are considered as microchannels), (2) the resulting flow patterns and prevailing heat transfer mechanisms during flow boiling within micro-passages, (3) the occurring flow instabilities (encountered in multiple channels) and reversals and their effect on the heat transfer rates, (4) effect of channel solid surface characteristics and (5) the accurate prediction of the critical heat flux values.

Additionally, it should be mentioned that in numerical investigations an important issue for predicting heat transfer and flow boiling characteristics within microhannels is that the utilised sub-models are based on data based on conventional tubes experiments, something that is not representative for microchannels problems. Last but not least, pressure drop along the channels is also considered a fundamental design parameter for applications of flow boiling in microchannels and accurate predictive correlations must be developed. Many experimental and numerical investigation focused on this issue over the past years. Liang-ming Pan et al.[76] performed experiments of flow boiling in order to investigate the characteristics of pressure drop in parallel microchannels. They used various heat and mass flux ranges with constant hydraulic diameter and constant inlet temperature. The experimental results show that the pressure drop resulted in slight

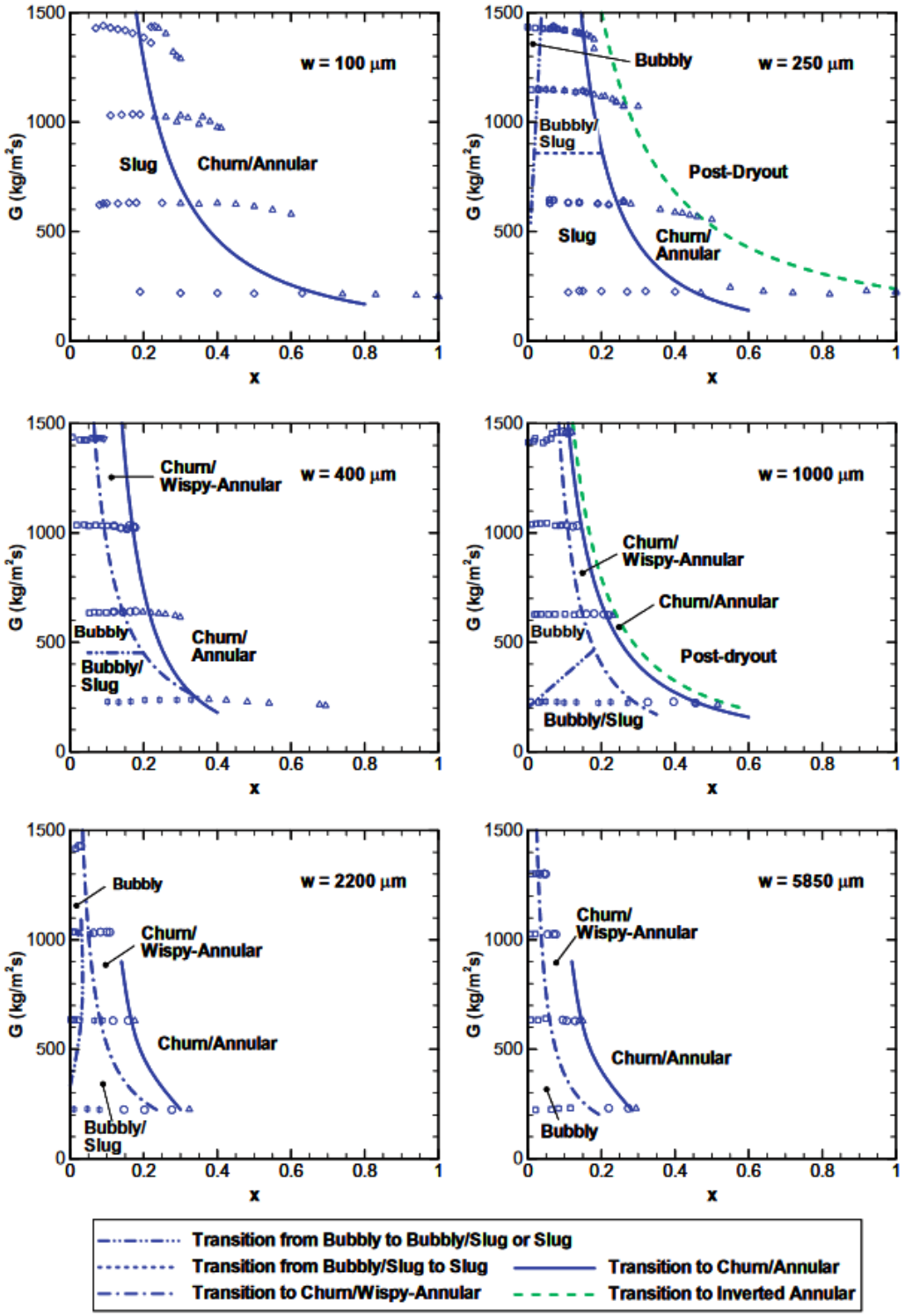

Figure 3: Flow regime maps on mass flux-vapour quality coordinates with transition lines for six microchannels width (w) as presented by [73].

decrease and subsequently rapid increase of heat flux under constant inlet temperature and mass flux. Finally it was concluded that mass flux, heat flux and inlet temperature

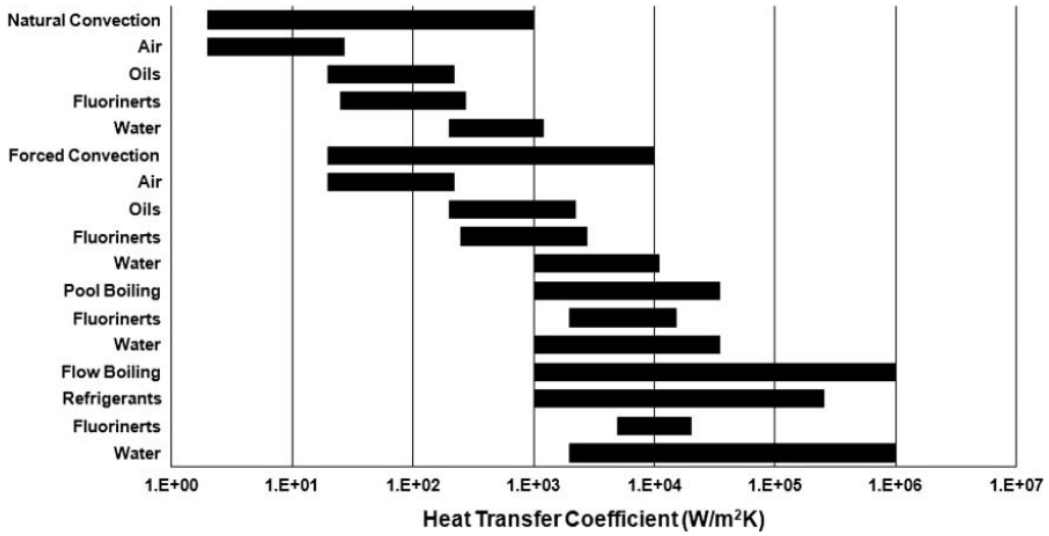

Figure 4: Thermal properties of different fluids in different modes of convective flows [74].

play a vital role for the variation of pressure drop. The experimental investigation from Sempértegui-Tapia and Ribatski [77] on two-phase frictional pressure drop in horizontal micro-scale circular, square and triangular channels, revealed that increasing the mass velocity results to an increment on frictional pressure gradient. Additionally, it was found that when saturation temperature is increased, the frictional pressure drop decreases. The highest pressure drop gradients were observed for the triangular channel followed by square and circular geometries. In another work, flow boiling experiments were conducted in copper stepped fin microchannels over a wide range of heat fluxes by Balasubramanian et al. [78], they concluded that two-phase pressure drop varies as a function of exit vapour quality and mass flux proportionally, because of the increase in friction and body drag effects. But also that heat transfer coefficient is minimum as the pressure drop fluctuation amplitudes are very low in a stepped fin microchannel. This shows that a stable boiling enhances heat transfer performance, this agrees with the conclusion of Lee and Pan [79].

2.4 Conclusions

From the above literature review on the major experimental and numerical investigations on two-phase flows within micro-passages, some worth mentioning conclusions can be drawn. These can be summarised as follows:

1. Microchannel heat exchangers have the potential of achieving very high heat transfer rates compared to conventional heat exchangers due to the very high surface area to volume ratio as well as due to the associated latent heat of phase-change. Therefore flow boiling in microchannels constitutes one of the most promising cooling methods for electronic devices.

2. Like with two-phase phenomena, researchers rely heavily on empirical correlations

to predict flow boiling phenomena in microchannels. However, since the correlations are valid for specific fluids and limited ranges of operating and flow parameters, there is great uncertainty when attempting to apply them to other fluids or beyond the validity range of the involved flow parameters.

3. Fundamental issues such as the geometry of the channel, pressure drop, surface characteristics (including wettability), flow regimes and flow instability (e.g. backflow) as well as prediction of critical heat flux, remain unanswered.

From the above conclusions it can be understood that even though cooling of devices with the method of flow boiling in microchannels has seen great improvements since the method was firstly introduced, fundamental unanswered questions (e.g. the one presented earlier by Karayannis and Mahmoud) hinder the proposed method to advance towards a higher Technology Readiness Level (TRL) in order to achieve a transition from the laboratory applications to real commercial applications.

3 Numerical methodology

In this chapter, the numerical methodology which are used to simulate flow boiling are presented and discussed. An important parameter when two-phase flow and boiling phenomena are simulated is the phase change sub-model. This can be subdivided into the calculation of the local rate of evaporation and the calculation of corresponding source terms for the conservation equations (e.g. heat and mass transfer at liquid-vapour interfaces) [26]. In the following section the phase-change sub-model and the mechanisms that required modeling are described in detail.

The heat transfer in fluids occurs through convection and is a result of diffusion and advection, whereas in solid heat transfer occurs through conduction (only diffusion). Conjugate heat transfer concerns the coupled analysis of heat transfer between fluids and solids. Numerically, in order to simulate conjugate heat transfer phenomena, the partial differential equations (PDEs) that are used to describe the different physics in solids and fluid are coupled, at the solid-fluid interface, where the continuity of the temperature and the heat flux must be satisfied.

Conjugate heat transfer finds applications in several engineering applications, where an accurate prediction of the heat transfer and the thermal loading is important, due to the relation of the thermal management of a device to its life cycle. Different examples of conjugate heat transfer applications are listed below:

- Heating, ventilation, and air-conditioning (HVAC)
- Cooling of electronic devices
- Heat exchangers
- Gas turbines
- Engine cooling

Due to its complexity in numerical modeling, conjugate heat transfer problems are often ignored in numerical works, however, they play a significant role for the accurate prediction of fluid flow and heat transfer characteristics.

3.1 Numerical methods for two-phase flows and boiling

Generally, for the numerical simulation of two-phase flows, there are three approaches that are mainly applied in inhouse, commercial and open-source CFD codes:

- **Complete or "Direct" Numerical Simulations (DNS):** utilizing a combination of interface tracking/capturing methods with appropriate phase-change models, constitutes a powerful and quite promising way for the numerical simulation of boiling heat transfer. The state of the art in this numerical modeling direction, clearly shows that most of the important sub-processes that take place in boiling heat transfer can be directly resolved by such models leading to the development of complete numerical models that could be applied to a wide

range of geometrical configurations, spatial and temporal scales as well as to a variety of flow conditions. The main drawback of this method is that since it relies on interface tracking/capturing techniques it requires a great number of computational cells to capture the complex interface dynamics that are usually associated with boiling heat transfer (e.g. bubble detachment from heated walls, bubble break-up and coalescence events). Therefore this kind of modeling approach due to the high computational cost is usually applied to study in detail local phenomena within parts of heat transfer devices, focusing on single or multiple bubble events [80].

- **Eulerian-Lagrangian approach**: a certain number of individual bubbles is tracked and its interaction with the continuous phase is modelled with single particle models (Lagrangian). The continuous phase is solved by phase-averaged equations integrated on an Eulerian mesh (fixed in space) covering the flow domain. The problem with this approach is that in dense flows the number of bubbles required for a reasonable accuracy is high, and thus the number of equations needed to be solved (every particle is "moved" by its own equation) and computational cost are correspondingly high [81].

- **Eulerian-Eulerian (E-E) approach**: the dispersed and continuous phases are solved by phase-averaged equations integrated on an Eulerian mesh, and all interactions between both phases are volume averaged within a control volume. The major advantage of this approach is that the number of equations only depends on the number of phases, and not on the number of particles, as in the Eulerian-Lagrangian approach. The total amount of cells required is also much less than DNS interface tracking/capturing methods. However, the main drawback of this approach is that it relies on empirical problem-specific closures for the interactions between the phases [25, 82].

  In the following sub-sections of the present thesis, only the DNS and the E-E methodologies will be further described since the numerical investigation is focused on these two methods.

3.2 Numerical methods of tracking and capturing the interfaces

Single-phase flows involves the derivation of field equations which describe the conservation of mass, momentum as well as energy equations which later are complemented by the appropriate fundamental correlations for thermodynamic state and energy transfer. On the other hand, in multi-phase flows equations derivation is more difficult due to the existence of the moving interfaces between the phases which have as a result in important variations and discontinuities of the fluid properties. In order to be able to solve numerically such complicated phenomena, the utilisation of the correct interface capturing and tracking methods, which can determine the shape and position of the interface at every time instant is needed [83].

The numerical methods for tracking and capturing the interfaces can be categorized into two main categories. The "interface tracking methods" and the "interface capturing methods". Each of these categories is used for specific occasions [84]. Initially, the

interface tracking methods can represent the interface between two immiscible fluids explicitly. This can be done either by adapting the Eulerian fluid mesh in a way to resemble the interface, usually known as the Moving-Mesh method [85], or introducing an immersed boundary representing the interface, i.e. Front-Tracking method [86]. The Moving-Mesh methods can accurately reproduce the jump condition due to the corresponding fluid properties jump across the interface and also impose the force acting along the interface since they include the surface tension parameter. Conversely, the Front-Tracking methods do not require altering the Eulerian fluid mesh, therefore this method is limited to topological changes in a multiphase-fluid, such as merging or breaking of bubbles, during coalescence or break-up events [87].

Interface capturing methods rely on an implicit interface representation, which means the explicit position and shape of the interface is not known [88]. There are many numerical models for interface capturing that are used today. Some of them are presented and analyzed by Mirjalili et al. [89].

The most well-known and broadly used interface capturing methods are the *Volume-Of-Fluid (VOF)* and the *Level-Set (LS)* methods, introduced by Hirt and Nichols [90] and Sethian [91], respectively. The VOF and LS methods are the most suitable methods for studying complex gas/liquid interface topologies, by modeling both fluid phases as a single mixture.

In VOF methods, the fluids on each side of the interface are marked by an indicator function. In more detail, the volume fraction α is tracked for this purpose. It takes values between zero and one in order to distinguish the two different phases while cells with a volume fraction value between zero and unity represent the interface region (Fig. 5). The volume fraction is advected based on the underlying flow field. The VOF method is accurate in the sense of volume preserving, and break-up or merging of droplets and/or bubbles can be captured, but very fine meshes are needed to diminish numerical artifacts. A usual drawback of some VOF methods that involve interface reconstruction is that the reconstruction process makes it difficult to keep the topology of the interface [92]. Another usual drawback of VOF methods is that the errors in the calculation of the interface curvature lead to the development of spurious velocities in the vicinity of the interface that for the case of boiling flows especially in small scales might lead to nonphysical results.

The Level-set (LS) method is another quite commonly used method today. This method uses a distance function from the interface. The implicit interface representation is given by the zero set of the scalar field ϕ. When $\phi = 0$ it means that this is where the interface lies (the surface has no height). Positive and negative values mark the two different phases, respectively. The LS method can provide accurate results when the interface is advected parallel to one of the coordinate axes. It has simple mathematical formulation and it is easy to solve. However, an important drawback of this method is that volume is not always preserved while advecting the interface [88].

For the initial stage of this thesis, the VOF method is adopted. Particularly, a previously developed and tested enhanced version of the VOF-based solver of OpenFOAM interFoam is utilised [93–99]. Subsequently, in the second part of the thesis, the Eulerian-Eulerian two-fluid method is used.

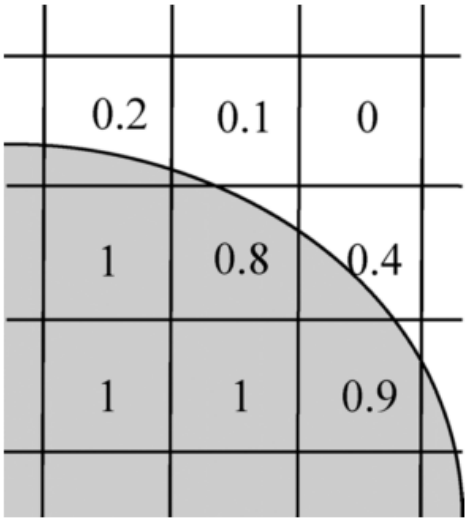

Figure 5: Schematic of VOF method on computational cells: a volume fraction value of 0 represents 100% phase A and a volume fraction value of 1 represents 100% phase B. The interface position is approximated by the 0.5 volume fraction contour

3.3 CFD toolbox

For both numerical simulation strategies that are followed in the present PhD thesis the opensource CFD toolbox of OpenFOAM is used. In more detail, a customised enhanced version of the original VOF-based solver in OpenFOAM (developed in version 2.2.1) is utilised for the interface capturing simulations while one of the existing original Eulerian-Eulerian solvers of OpenFOAM (from the original distribution of version 8.0).

The overall details and the theoretical background of these two different numerical simulation methodologies are given in detail in the following subsections.

3.4 The Volume-of-Fluid Method

As mentioned previously for the purposes of the present PhD project, and particularly during the first two objectives, an enhanced Volume Of Fluid (VOF) based numerical simulation framework that accounts for conjugate heat transfer between a solid region and a two-phase flow region with phase-change due to evaporation and/or condensation, is utilised in order to perform a wide series of parametric numerical simulations aiming to identify and quantify in detail the effect of fundamental flow controlling parameters on the resulting bubble growth and detachment characteristics for the case of isolated bubbles within micro-passages, and additionally on bubble coalescence and break-up events for the case of multiple bubbles within micro-passages. The utilised, enhanced, VOF-based numerical model, has been extensively validated in the past against existing analytical solutions and experimental data on adiabatic and diabatic bubble and droplet dynamics and it has also been applied for the investigation of adiabatic and diabatic two-phase flows within mini and microchannels [93–96, 100–102]. Some, of these validation results are shown in Fig. 6. As it can be observed, the proposed VOF-based numerical modeling framework, accurately predicts adiabatic and diabatic bubble and

droplet dynamics as well as conjugate heat transfer between solid and two-phase fluid domains. Therefore, since all underpinned mechanisms have been validated in the past (interfacial dynamics, phase-change, wettability, conjugate heat transfer) it can safely be used for the purposes of the present PhD project.

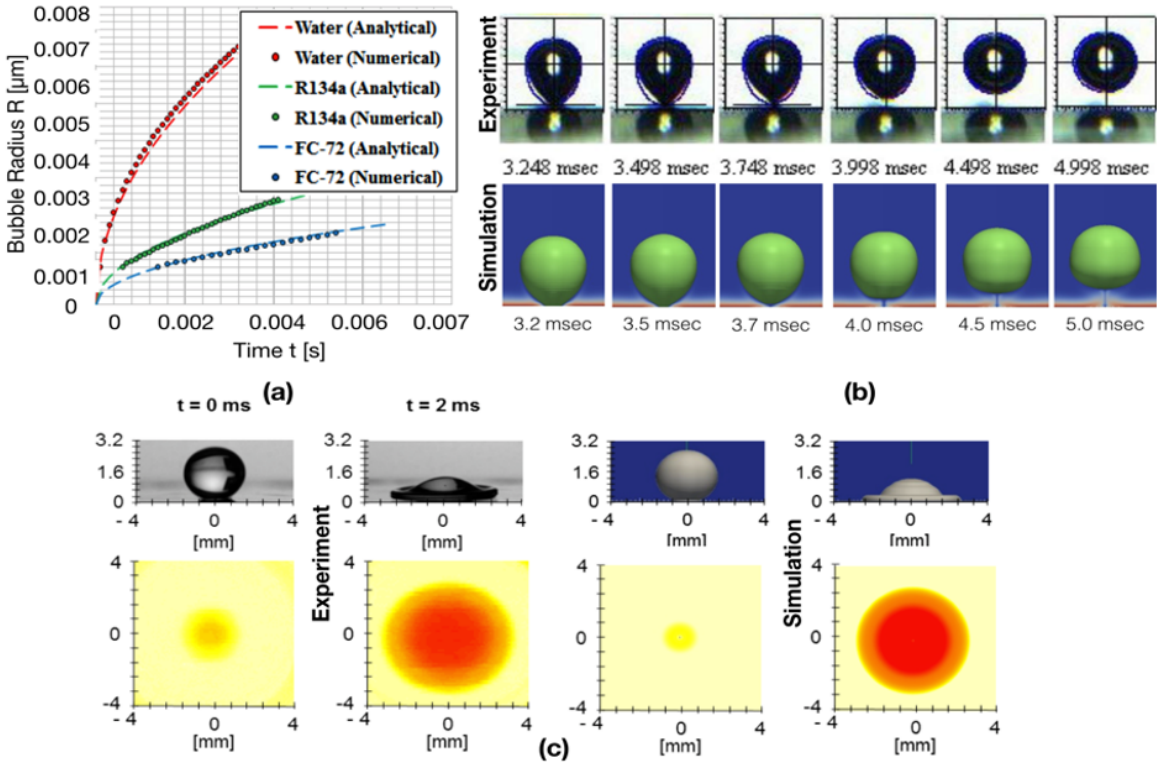

Figure 6: (a) Comparison between numerical simulation and analytical solution results for a bubble evaporating in a superheated domain [94], (b) numerical simulation results and experimental results in pool boiling [94], (c) conjugate heat transfer numerical simulation results and experimental measurements on droplet impact cooling [95].

3.4.1 Governing equations

In this section, the governing equations for mass, momentum, energy, and volume fraction are presented. It should be mentioned that liquid and vapour phases are both treated as incompressible, Newtonian fluids. The mass conservation equation is given as:

$$\frac{\partial \rho}{\partial t} + \nabla \cdot (\rho \vec{U}) = 0 \tag{3}$$

where $\vec{U}$ is the fluid velocity, ρ is the bulk density and t is the time. The source term on the right-hand side accounts for the phase change [103]. The conservation of momentum is given by the following equation:

$$\frac{\partial}{\partial t}(\rho \vec{U}) + \nabla \cdot (\rho \vec{U} \vec{U}) - \nabla \cdot \left\{ \mu \left[(\nabla \vec{U} + (\nabla \vec{U})^T \right] \right\} = -\nabla p + \vec{F_{st}} + \vec{F_g} \tag{4}$$

where p is the pressure and μ is the bulk dynamic viscosity. The momentum source terms on the right-hand side of the equation account for the effects of surface tension and gravity, respectively. The surface tension term is modelled according to the classical approach of Brackbill et al. [104]. The conservation of energy balance is given by the following equation:

$$\frac{\partial}{\partial t}(\rho \mathrm{c_p} T) + \nabla \cdot (\vec{U} \rho \mathrm{c_p} T) - \nabla \cdot (\lambda \nabla T) = \dot{h} \tag{5}$$

where c_p is the bulk heat capacity, T the temperature field, and λ is the bulk thermal conductivity. The source term on the right-hand side of the equation represents the contribution of the enthalpy of evaporation/condensation or else the cooling/heating associated with the latent heat of the phase-change. The volume fraction α is advected by the flow field by the following equation:

$$\frac{\partial a}{\partial t} + \nabla \cdot (\alpha \vec{U}) - \nabla \cdot (\alpha(1-\alpha)\vec{U_r} = \frac{\dot{\rho}}{\rho}\alpha \tag{6}$$

Interface sharpening is very important in simulating two-phase flows of two immiscible fluids. In OpenFOAM the sharpening of the interface is achieved artificially by introducing the extra compression term $\nabla \cdot (\alpha(1-\alpha)\vec{U_r})$ in Equation 6. U_r is an artificial compression velocity which is calculated from the following relationship:

$$\vec{U_r} = \min(C_\gamma \left|\vec{U}\right|, \max(\left|\vec{U}\right|)) \frac{\nabla \alpha}{|\nabla \alpha|} \tag{7}$$

where C_γ is a coefficient that controls the artificial compression of the interface diffusion, where its value can be set between 0 and 4.Further details can be found in the following work [105].

The divergence of the compression velocity $\vec{U_r}$, ensures the conservation of the volume fraction α, while the term $\alpha(1-\alpha)$ limits this artificial compression approach only in the vicinity of the interface, where $0 < \alpha < 1$ [106]. The level of compression depends on the value of C_γ ([106], [107]). For the simulations of the present investigation, initial, trial simulations indicated that a value of $\mathrm{C}_\gamma = 1$ should be used, in order to maintain a quite sharp interface without at the same time having nonphysical results. The source term on the right-hand side of the Equation 6 is needed because, due to the local mass source terms, the velocity field is not free of divergence.

It should be mentioned that the VOF method in OpenFOAM does not solve Equation 6 implicitly, but instead by applying a multidimensional universal limiter through an explicit solution algorithm (MULES), which preserves the boundedness of volume fraction. Together with the interface compression algorithm, this method ensures a sharp interface and bounds the volume fraction values between 0 and 1 [108]. Finally, the bulk fluid properties γ_b are computed as the averages over the liquid (γ_l) and vapour (γ_v) phases, weighted with the volume fraction α.

The bulk physical properties of the mixture are calculated as weighted averages of the corresponding properties of the liquid and gaseous phases:

$$\gamma_b = \alpha \gamma_l + (1-\alpha)\gamma_g \tag{8}$$

As it is mentioned previously, the VOF method usually suffers from non-physical spurious currents in the interface region. These spurious velocities are due to errors in the calculation of the normal vectors and the curvature of the interface that are used for the calculation of the interfacial forces. These errors emerge from the fact that in the VOF method the interface is implicitly represented by the volume fraction values that encounter sharp changes over a thin region [109]. The VOF-based solver that is used in the present investigation has been modified accordingly in order to account for an adequate level of spurious currents suppression. The proposed modification involves the calculation of the interface curvature κ using smoothed volume fraction values $\tilde{a}$ that are obtained from the initially calculated sharp volume fraction field α, smoothing it over a finite region in the vicinity of the interface:

$$\kappa = \nabla \cdot \left(\frac{\nabla \widetilde{\alpha}}{|\nabla \widetilde{\alpha}|} \right) \tag{9}$$

All other equations are using the initially calculated (non-smoothed) volume fraction values of α. The proposed smoothing is achieved by the application of a Laplacian filter which can be described by the following equation:

$$\tilde{a_P} = \frac{\Sigma \alpha_f S_f}{\Sigma S_f} \tag{10}$$

In Equation 10, the subscripts P and f denote the cell and face index respectively and α_f is the linearly interpolated value of α at the face center and S_f is the surface area of the cell face. The application of the proposed filter can be repeated more than one time in order to obtain an adequately smoothed field. For the applications of the present investigation, initial trial simulations indicated that the filter should applied no more than 2 times, in order to avoid the leveling out of high curvature regions. The proposed, enhancement to the originally distributed VOF solver has been tested and verified against literature available experimental results in isothermal bubble dynamics with an excellent degree of convergence. More details on the proposed validation as well as on the proposed improvement of the VOF method can be found in the paper by Georgoulas et al. [93].

The conservation of energy equation in the solid domains is defined as:

$$\rho \mathrm{c_{ps}} \frac{\partial}{\partial t}(T) = \nabla \cdot (\lambda_s \nabla T) \tag{11}$$

where the subscript "s" indicates that the properties are of the solid only. The coupling at the interface between the solid region and fluid region is achieved iteratively through the following conditions:

$$T_f = T_s \tag{12}$$

$$\lambda_f \frac{\partial T_f}{\partial n} = \lambda_s \frac{\partial T_s}{\partial n} \tag{13}$$

3.4.2 Phase change model

The utilized phase change model that was implemented in the improved OpenFOAM VOF solver that is used in the present investigation, will be described briefly in this section. In the case of evaporation, the evaporating mass flux at the liquid - vapour interface $\mathrm{j_{evap}}$ is calculated from the following equation:

$$\mathrm{j_{evap}} = \frac{T_{int} - T_{sat}}{R_{int}\mathrm{h_{lv}}} \tag{14}$$

where T_{int} is the temperature of the interface and is calculated from the simulations, T_{sat} is the saturation temperature, R_{int} is the interfacial heat resistance and $\mathrm{h_{lv}}$ is the latent heat of evaporation at the saturation temperature [110]. The amount of liquid that evaporates is calculated locally and the resulting source term field is artificially smeared over a few cells in order to avoid numerical instabilities. The evaporating mass is taken away on the liquid side of the interface and reappears on the vapour side, following the process originally suggested in the work of Hardt and Wondra [111].

The interfacial heat resistance is calculated by the following equation based in the considerations of Schrage [110]

$$\mathrm{R_{int}} = \frac{2-\gamma}{\gamma}\frac{\sqrt{2\pi R_{gas}}}{\mathrm{h_{lv}^2}}\frac{T_{sat}^{3/2}}{\rho v'} \tag{15}$$

It is clear that this last equation is in fact a fitting function, due to the uncertainty of the parameter γ, which is eventually may vary in the range $0< \gamma < 1$. For the cases that will be presented here, the constant γ that is also known as the evaporation/condensation coefficient is taken equal to unity from the literature (e.g. [26, 112, 113]), ([109, 114, 115]) (because these simulations concerned condensation phenomena). However, it should be noted that in different cases that are not presented in the present investigation, the value of the proposed coefficient needed to be significantly lower than unity. R_{gas} is the specific gas constant of the working fluid that is calculated from the universal gas constant and the molecular weight of the working fluid. According to previous investigations (e.g [26], [112], [113]), ([109], [114], [115]), despite the fact that Eqs. 14 and 15 are derived from considerations on length scales which are several orders smaller than the typical grid size used in the simulations, the proposed evaporation model leads to correct evaporation rates since it acts like a control loop. The more the temperature at the interface deviates from the saturation value, the more liquid evaporates and the more the temperature drops locally. This ensures that the temperature at the liquid–vapour interface always remains close to the saturation temperature [26]. The evaporating/condensing mass flux is calculated from Eq. 14 and must be incorporated into the conservation equations, by the definition of volumetric source terms. This is done by multiplying the evaporating mass flux at the liquid–vapour interface by the magnitude of the volume fraction gradient, as indicated in the following equation:

$$\dot{\rho}_0 = \mathrm{j_{evap}}|\nabla a| \tag{16}$$

This initial Sharp Source Term Field (SSTF) is integrated over the whole computational domain to calculate the "Net Mass Flow" through the entire liquid-vapour interface, using the following equation:

$$\dot{m}_{int} = \iiint \dot{\rho}_0 dV \tag{17}$$

This value is important for the global mass conservation, in order to ensure that the magnitudes of the mass sources in the liquid and vapour parts are equal and correspond to the net evaporation rate. The sharp source term field is then smeared over several cells, by solving the following diffusion equation for the smooth distribution of source terms

$$\rho_1 - \nabla \cdot \left[(D\Delta\tau)\nabla\rho_1 \right] = \dot{\rho}_0 \tag{18}$$

$\Delta\tau$ is an artificial time step and Neumann boundary conditions are imposed for the smooth source term field on all boundaries of the domain. Therefore, the integral values of the sharp and the smooth source fields remain the same, in spite of the smearing. The width of the smeared source term field is proportional to the square root of the product of the diffusion constant "D" and the artificial time step "$\Delta\tau$". It should be mentioned that the value of "D" must be adjusted to the mesh resolution such that the source term field is smeared over several cells. Then, the source terms in all cells that do not contain pure liquid or vapour ($\alpha <$ 1-α_{cut} and $\alpha > \alpha_{cut}$, where α_{cut} may be set to 0.001) are artificially set to zero. This cropping step ensures that source terms are shifted into the pure vapour and liquid cells only in the vicinity of the interface. The interface therefore is not subjected to any source terms and is only transported by the calculated velocity field. Therefore, the transport algorithm for the volume fraction field as well as the associated interface compression, can work efficiently without any interference with the source term field. The remaining source term field is scaled individually on the liquid and the vapour side through the application of appropriate scaling coefficients. This scaling step ensures that the mass is globally conserved and that the evaporating or condensing mass flow, corresponds globally to the net mass flow through the interface. The proposed scaling coefficients N_l and N_v are calculated by integrating the smooth source term field in each of the pure phases and comparing it to the net mass flow $\dot{m}_{int}$ (Equation 17), utilizing the following equations:

$$N_l = \dot{m}_{int} \left[\iiint (\alpha - 1 + a_{cut}) \dot{\rho}_1 dV \right]^{-1} \tag{19}$$

$$N_v = \dot{m}_{int} \left[\iiint (a_{cut} - a) \dot{\rho}_1 dV \right]^{-1} \tag{20}$$

Finally, the final source term distribution is calculated using the above scaling factors in the following equation:

$$\dot{\rho} = N_v(a_{cut} - a)\dot{\rho}_1 - N_l(a - 1 + a_{cut})\dot{\rho}_1 \tag{21}$$

An example of the aforementioned final source term distribution is depicted indicatively in Fig. 7 below.

The source term of $\dot{h}$ of Eq. 5 is obtained from Eq. 22:

$$\dot{h} = [N_v(1 - a)C_{pv} - N_l a C_{pl}]\dot{\rho}_1 T) - \dot{\rho} h_{lv} \tag{22}$$

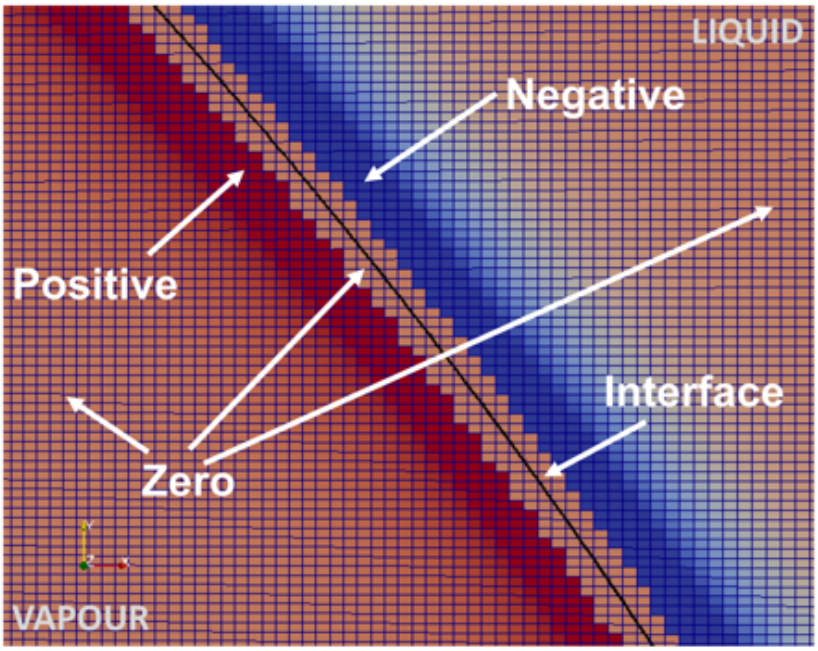

Figure 7: Distribution of the final source terms in the computational domain for the case of an evaporating bubble [94].

where C_{pv} and C_{pl} represent the heat capacity of the vapour and liquid phases respectively. The first part of the source term corresponds to a correction source term that removes artefacts that emerge due to the structure or the mass source term in the proposed methodology. The second part of the source term represents the contribution of the enthalpy of evaporation or else the cooling associated with the latent heat of the phase-change. Further details can be found in the work of Hardt and Wondra [111]. The proposed implementation of the phase-change model into the enhanced, customised VOF solver that is used in the present PhD thesis as well as its validation against existing analytical solutions and experimental measurements on boiling heat transfer can be found here [94].

3.4.3 Dynamic contact angle modeling

The utilised VOF-based solver includes also an implementation of the dynamic contact angle (DCA) model originally suggested by Kistler [116]. This implementation has been validated in the past against experiments available in the literature for droplet impact on flat surfaces[96] with different wettability, but also on droplet impact on porous surfaces[97] as well as against experiments of pool boiling in biphilic surfaces [98], with excellent degree of convergence between the experimental measurements and the numerical predictions.

In the proposed dynamic contact angle model, the dynamic contact angle θ_d is given as a function of the contact line velocity (u_{cline}), through the capillary number Ca and the inverse of Hoffman's function. The θ_d, can be calculated by the following equation:

$$\theta_{\mathrm{d}} = \mathrm{f_H}\left[\mathrm{Ca} + \mathrm{f_H^{-1}}\left(\theta_{\mathrm{eq}}\right)\right] \tag{23}$$

where H^{-1} is the inverse function of the Hoffman's empirical fundtion, which is given by:

$$f_H = \arccos\left\{1 - 2\tanh\left[5.16\left(\frac{x}{1+1.31x^{0.99}}\right)\right]^{0.706}\right\} \tag{24}$$

where x is defined as:

$$x = f_H\left[Ca + f_H^{-1}(\theta_{eq})\right] \tag{25}$$

The capillary number is defined as:

$$Ca = \frac{\mu u_{cline}}{\sigma} \tag{26}$$

The equilibrium angle θ_{eq} is replaced by either a limiting advancing or receding contact angle θ_α or θ_r , depending on the sign of the velocity vector at the contact line.

3.5 The Eulerian-Eulerian approach

The Eulerian multiphase flow approach is based on a two-fluid model. In this approach, governing equations for mass, momentum and energy are written for each phase, separately, weighted by the so-called Volume Fraction, which represents the ensemble-averaged probability of occurrence for each phase at a certain point in time and space [117]. Interaction/exchange terms between the phases appear as source/sink terms in the governing equations. These exchange terms normally consist of analytical or empirical correlations, expressing the interfacial forces, as well as heat and mass fluxes, as functions of the average flow parameters. However, most of these correlations are highly problem specific and therefore their applicability and validity range must be carefully considered [117]. Moreover, for the case of boiling flows, where heat is transferred into the fluid from a heated wall at rates that boiling happens and vapour is generated, additional source terms describing the physics of these processes at the heated wall have to be included. For this purpose, these global multi-phase CFD models are usually coupled with appropriate wall boiling sub-models, like the most widely used wall partitioning model of Kurul and Podowski [118]. Some representative and relatively recent numerical investigations in this branch are the works by Steiner et al. [119], Koncar and Krepper [120], Lopez-de-Bertodano et al. [121], Yun et al. [122], Krepper et al. [123]. However, such wall boiling sub-models require additional closure relationships that predict the bubble departure characteristics and the density of the active nucleation sites that incorporate a lot of model constants, the value of which, can be found only for specific flow conditions and working fluids [117]. In the works of Prabhudharwadkar et al. [124] and Cheung et al. [125], the performance of a wide combination range of the existing closure relationships is examined through comparison with a wide range of experimental data. In their works, it is stated that not one single combination of empirical correlations has shown the propensity of providing satisfactory predictions covering the entire range of the simulated conditions.

3.6 Numerical framework of the Eulerian-Eulerian solver

In the following paragraphs a detailed description of the Eulerian-Eulerian two-fluid numerical framework will be presented. More information about the averaging procedure can be found in the works conducted by Enwald et al. [126] and Crowe et al. [127].

3.6.1 Averaging procedure

For almost all practical purposes, the exact determination of the characteristics of the flow or the tracking of the interface are not of real interest. Much more interesting is the knowledge of the overall characteristics of the flow, so the application of a sort of averaging process on the derivation of the effective conservation equations for the *two fluid* model. The disadvantage of this procedure is that only macroscopic phenomena are computable, and conservation laws must be closed by *constitutive* equations, derived both from theoretical and empirical analysis. Taking this into account, the accuracy of numerical results depends strongly on the closure models for the conservation laws, that are being selected for predicting the flow. Generally, the averaging procedure can be done in three different ways:

- Time averaging :

$$\overline{\phi} = \lim_{T\to\infty} \frac{1}{T} \int_T \phi(\mathbf{x}, t) dt \tag{27}$$

- Space averaging:

$$\langle \phi \rangle_V = \frac{1}{V} \int_V \phi(\mathbf{x}, t) dV \tag{28}$$

- Ensemble averaging:

$$\langle \phi \rangle_E = \lim_{N\to\infty} \frac{1}{N} \sum_{n=1}^{N} \phi(\mathbf{x}, t) \tag{29}$$

where ϕ is a generic transported quantity. While the averaging process allows a computationally lighter solution, the lost information regarding local gradients must be reconstructed using semi-empirical closure relationships, (*constitutive* equations).

These averaging procedures itself cannot be considered adequate, due the fact that they lead to equations expressed in function of averaged products of instantaneous quantities. For overcoming this issue, it is necessary to derive equations where all quantities are averaged. In order to achieve that, the time Favre-averaging method [128] is usually adopted, because it leads to equations where oscillation in quantities like density and phase fraction are automatically filtered. A suitable solution for that is to think that a generic quantity can be expressed as the sum of a mean part and a fluctuating part:

$$\phi(t) = \overline{\phi(t)} + \phi'(t) \tag{30}$$

This decomposition allows separation between mean and fluctuating value of quantities. In multiphase flow generally two kind of averaged quantities are preferred, the phase-weighted average, defined by:

$$\overline{\langle \psi \rangle} = \frac{\overline{\langle \chi_k \psi \rangle}}{\overline{\langle \chi_k \rangle}} \tag{31}$$

where χ_k represent the *phase indicator function* of k_{th} phase (defined in section 3.7 at page 29) and the density-weighted average, defined by:

$$\overline{\langle\zeta\rangle} = \frac{\overline{\langle\rho_k\zeta\rangle}}{\overline{\langle\rho_k\rangle}} \tag{32}$$

In this manner, the instantaneous volume averaged variables can be written as:

$$\langle\psi\rangle = \overline{\langle\psi\rangle} + \psi' \tag{33}$$

for the phase-weighted average method, and by:

$$\langle\zeta\rangle = \overline{\langle\zeta\rangle} + \zeta' \tag{34}$$

for the density-weighted average method; the two terms ψ' and ζ' are the fluctuating components of quantities $\langle\psi\rangle$ and $\langle\zeta\rangle$, respectively. Multiplying equation (33) by $\langle\chi_k\rangle$, and averaging in time, is gives the following equation:

$$\overline{\langle\chi_k\psi\rangle} = \overline{\langle\chi_k\rangle\overline{\langle\psi\rangle}} + \overline{\langle\chi_k\rangle\psi'} = \overline{\langle\chi_k\rangle}\ \overline{\langle\psi\rangle} \tag{35}$$

The second term on the right-hand side of equation (35) is zero by definition. A similar, but formally equivalent result as (35) can be obtained for (34), multiplying it this time for $\langle\rho_k\rangle$.

3.7 Equation of motion for continuous phases

The equation of motion for each continuous phase are deducted by the fundamentals principles of conservation laws of physics, which are *mass conservation*, *momentum conservation* and *energy conservation*. Through introduction of a *phase indicator equation* to these mathematical equations and an averaging process that it is carried out over each phase, the equations governing the mass, momentum and energy conservation are subsequently derived in the *interpenetrating continua* framework.

3.7.1 Conservation of mass

Considering an elemental volume, fixed in space dV containing any k_{th} phase of the flow, it can be deducted that the rate of increase of mass within the elemental volume of fluid is equal to the net rate of mass that enters into the elemental volume of fluid; locally it can be expressed as:

$$\frac{\partial\alpha_k\rho_k}{\partial t} + \nabla\cdot(\alpha_k\rho_k\mathbf{U}_k) = \dot{m}_{kj} - \dot{m}_{jk} \tag{36}$$

where $\dot{m}_{kj}$ and $\dot{m}_{jk}$ is the mass transfer rate between the k^{th} and j^{th} phases and vice versa. Equation (36) represent the local instantaneous equation for the conservation of mass for the k_{th} phase. But before averaging it, it is important to define the so called *phase indicator function* $\chi_k(\mathbf{x},t)$, that has the role of distinguishing between the various phases that are present within the flow. By definition:

$$\chi_k(\mathbf{x},t) = \begin{cases} 1 & \text{when } \mathbf{x} \text{ is on phase } k_{th} \text{ at time } t \\ 0 & \text{otherwise} \end{cases} \tag{37}$$

3.7.2 Conservation of momentum

The momentum equation for phase κ is given by:

$$\frac{\partial \alpha_k \rho_k \mathbf{U}_k}{\partial t} + \nabla \cdot (\alpha_k \rho_k \mathbf{U}_k \mathbf{U}_k) = -\alpha_k \nabla p_k + \nabla \cdot [\alpha_k (\tau_k + \tau_k^{Re})] + \alpha_k \rho_k \mathbf{g} + \mathbf{M}_{ki} \quad (38)$$

where α_k, ρ_k, $\mathbf{U}_k$ are the volume fraction, density and the velocity vector for each phase k, respectively. The terms τ_k, τ_κ^{Re} are the viscous and Reynolds (turbulent) stresses, respectively. Additionally, $\mathbf{M}_{ki}$ is the averaged inter-phase momentum transfer term.

The Reynolds and viscous stress tensors are modeled using Boussinesq hypothesis which uses the Newtonian strain-stress relation. It is given by

$$\tau_k + \tau_k^{Re} = -(\mu_k + \mu_k^t)(\nabla \mathbf{U}_k + \nabla \mathbf{U}_k^T - \frac{2}{3} I \nabla \times \mathbf{U}_k) + \frac{2}{3} I k_k, \quad (39)$$

where I, μ_k, μ_k^t, k_k, are the identity tensor, physical dynamic viscosity, turbulent dynamic viscosity and turbulent kinetic energy of phase k, respectively.

3.7.3 Conservation of energy

To describe the conservation of energy in Eulerian multiphase applications, a separate enthalpy equation can be written for each phase:

$$\begin{aligned} \frac{\partial (\alpha_k \rho_k H_k)}{\partial t} + \nabla \cdot (\alpha_k \rho_k \mathbf{U}_k H_k) = \nabla \cdot (\alpha_k \lambda_k \nabla T_k) + \nabla \cdot (\alpha_k \frac{\mu_{T,k}}{Pr_{T,k}} \nabla H_k) \\ + \sum_{l=1}^{2} (\dot{m}_{jk} H_j - \dot{m}_{kj} H_k) + Q_{H,int} \end{aligned} \quad (40)$$

where H_j and H_k, is the enthalpy of the j^{th} and k^{th} phases λ_k is the thermal conductivity of phase k, $\dot{m}_{jk}$ and $\dot{m}_{kj}$ are the mass transfer rates between the k^{th} and j^{th} phases, $Pr_{T,k}$ is the turbulent Prandtl number, $Q_{H,int}$ is the heat flux exchanged by the interface between two phases, and the terms inside the summation represent the total enthalpy exchanged in case of phase change.

3.7.4 Turbulence modeling

For the continuous liquid phase, the turbulent fluctuations are modelled by a shear stress turbulence (SST) $\kappa - \omega$ model (*KOmegaSSTSato*) introduced by Sato et al. [129] and later by Menter et al. [130]. The SST model works by solving a turbulence/frequency-based model $\kappa - \omega$ near the wall and a $\kappa - \epsilon$ model in the bulk flow. The $\kappa - \epsilon$ turbulence model (*continuousGasKEpsilon*) is used for the dispersed gas phase. This particular turbulence model is used for gas-phase in a two-phase system as a stable numerical framework that supports phase-inversion. In more detail, in this turbulence model when the fraction of the gas phase approaches to zero, a contribution from the liquid phase is blended into the turbulence equations. This results to the model being reverted in a pure single-phase form.

3.8 Interfacial momentum transfer

From the momentum equation (eq. 38) it is clear that the interfacial momentum term cannot be ignored as plays an important role in determining the overall flow dynamics. Particulalrly, the interfacial momentum transfer is caused by the forces acting between two phases such as the forces acting on rising bubbles from the liquid which surrounds it, and are a function of primarily four established interfacial momentum transfer mechanisms. These include the drag force $\mathbf{M_{ki}^{D}}$, the lift force $\mathbf{M_{ki}^{L}}$, the wall lubrication force $\mathbf{M_{ki}^{WL}}$, the turbulent dispersion force $\mathbf{M_{ki}^{TD}}$ and the virtual mass force $\mathbf{M_{ki}^{VM}}$. Hence, the interfacial momentum exchange is the sum of these forces:

$$\mathbf{M_{ki}} = \mathbf{M_{ki}^{D}} + \mathbf{M_{ki}^{L}} + \mathbf{M_{ki}^{WL}} + \mathbf{M_{ki}^{TD}} \tag{41}$$

The virtual mass force becomes dominant when there are big density differences within the flow, however in the present study this term is neglected, as steady state of flow is concerned [131, 132].

3.8.1 Drag force model

3.8.2 Drag force

The drag force represents the force acting on the rising bubbles by the fluid and it depends on the bubble size and shape. The drag model describes how the drag affects the phases that impart onto one another. In the present work the Ishii-Zuber correlation [133] has been chosen and is expressed as:

$$\mathbf{M_{ki}^{D}} = -\frac{3}{4}\frac{C_D}{d_B}\rho_l \alpha_g |\mathbf{U_g} - \mathbf{U_l}|(\mathbf{U_g} - \mathbf{U_l}) \tag{42}$$

where, d_B is the bubble diameter, ρ_l is the density of the liquid phase, C_D is the drag coefficient and is modeled differently for various flow and bubble shape regimes and is given as

$$C_D = max(min(C_{D,ellipse}, C_{D,cap}), C_{D,sphere}) \tag{43}$$

where,

$$C_{D,sphere} = max\left(\frac{24}{Re_b}(1 + 0.15Re_b^{0.687}), 0.44\right) \tag{44a}$$

$$C_{D,ellipse} = \frac{2}{3}Eo_d^{(1/2)} \tag{44b}$$

$$C_{D,cap} = \frac{8}{3} \tag{44c}$$

the above equation is valid for bubble Reynolds number $Re_b > 1000$, where,

$$Re_b = \frac{\rho_l \, ||\mathbf{U}_g - \mathbf{U}_l|| \, d_B}{\mu_m} \tag{45}$$

with μ_m being the mixture viscosity. Eo_d is the dimensionless Eötvös number to consider bubble shapes in drag correlations and is defined as follows:

$$Eo_d = \frac{g(\rho_l - \rho_g)D_d^2}{\sigma} \tag{46}$$

where g is the gravitational force, σ is the surface tension, and D_d the maximum bubble horizontal dimension.

3.8.3 Lift force

For gas-liquid flows, non-drag forces have a huge influence on flow characteristics, especially in dispersed flows. The lift force plays an important role and has a large effect on the radial distribution of bubbles. According to Drew and Lahey [134], the lift force has a general formulation expressed as:

$$\mathbf{M}_{\mathbf{ki}}^{\mathbf{L}} = -C_L \alpha_d \rho_c (\mathbf{U}_g - \mathbf{U}_l) \times (\nabla \times \mathbf{U}_l) \tag{47}$$

where C_L express the lift force coefficient, α_d the dispersed phase fraction, ρ_c the continuous phase density, with $\mathbf{U}_g$ and $\mathbf{U}_l$ disperse and continuous phase velocities and the symbol "$\times$" represents the curl product.

Models have been developed based on empirical correlations for the calculation of the lift force coefficient C_L. In the present study the model of [135] is adopted. The principal characteristic of this model is that the sign of the lift force can change when the bubble becomes substantially non-spherical [136]. The model is defined on the basis of the Eötvös number as:

$$C_L = \begin{cases} min[0.288\tanh(0.121Re_b), f(Eo_d)] & \text{if } Eo_d < 4 \\ f(Eo_d) = 0.00105Eo_d^3 - 0.0159Eo_d^2 - 0.0204Eo_d + 0.474 & \text{if } 4 \leq Eo_d \leq 10 \\ -0.288 & \text{if } Eo_d > 10 \end{cases}$$

where the function $f(Eo_d)$ is defined as:

$$f\left(Eo_d\right) = 0.00105Eo_d^3 - 0.0159Eo_d^2 - 0.0204Eo_d + 0.474 \tag{48}$$

3.8.4 Wall lubrication force model

This force constitutes another lateral force due to surface tension, and prevents the bubbles from attaching onto the solid wall. In simulations, it leads in a low gas-phase fraction in proximity of the wall area. This force can be generally expressed, according to Antal et al. [137] model which is adopted also in the present model, as:

$$\begin{aligned} \mathbf{F}_{wl,d} = \frac{\alpha_d \rho_c \left[(\mathbf{U}_d - \mathbf{U}_c) - ((\mathbf{U}_d - \mathbf{U}_c) \cdot \mathbf{n}_w)\mathbf{n}_w\right]}{D_s} \\ \times \left(C_{w1} + C_{w2}\frac{D_s}{y_w}\right)\mathbf{n}_w \end{aligned} \tag{49}$$

where $\mathbf{n}_w$ represents the wall normal vector, D_S the Sauter diameter, y_w is the distance from the wall and $C_{w1} = -0.01, C_{w2} = 0.05$ are two constants, whose values were determined through experiments on a sphere and have been used also in the present PhD thesis.

3.8.5 Turbulent dispersion force model

The turbulent dispersion force accounts for the effect of the dispersion of bubbles in the turbulent liquid flow. In the present work the expression proposed by Lopez de Bertodano [138] has been used,

$$\mathbf{M_{ki}^{TD}} = C_{TD}\rho_b k e_b \nabla \alpha_g \tag{50}$$

where C_{TD} is a modifiable constant and has been set as default equal to 1.0, ke_b is the turbulent kinetic energy and $\nabla\alpha_g$ is the divergence gas volume fraction.

3.8.6 Inter-phase heat transfer

With regards to the heat transfer, an appropriate modeling is required in order to compute the heat exchanged between two phases. Newton's law of cooling that was presented in equation 1 is used in order to find the applied heat flux on the heated wall.

The liquid-gas interfacial heat transfer coefficient h_{if}, is expressed as

$$h_{if} = \frac{\lambda_l}{d_s} Nu \tag{51}$$

where λ_l is the liquid thermal conductivity and d_s is a length scale which is assumed equal to the bubble diameter. The Nu number is calculated from a formula proposed by Ranz-Marshall [139], expressed as:

$$Nu = 2 + 0.6 Re_b^{0.5} Pr^{0.33} \tag{52}$$

where Re_b is the bubble Reynolds number.

3.9 Boiling model (RPI wall boiling model)

In order the boiling process to occur, the heated wall temperature needs to exceed the saturation temperature of the working liquid. In numerical models, the bubble generation rate is determined by the wall heat flux partitioning model. In the past years, various mechanistic wall heat flux partitioning models have been proposed for the prediction of the boiling heat transfer [140], [118]. In the present model the so called Rensselaer Polytechnic Institute (RPI) model proposed by Kurul & Podowski [118] is utilised. The key novelty of this wall boiling model is that it divides the total wall heat flux into several components as shown in the following equation 53,

$$q_w = q_q + q_e + q_c \tag{53}$$

here, the term q_w is the total wall heat flux, q_q represents the so called quenching heat flux, q_e the evaporation heat flux and q_c the heat flux transferred to the liquid by turbulent convection.

The quenching heat flux q_q is the heat flux exchanged due to liquid filling the wall vicinity after bubble detachment, and can be expressed as:

$$q_q = C_{wt} \frac{2k_l}{\sqrt{\pi \lambda_l}} \sqrt{f} (T_w - T_l) \tag{54}$$

where C_{wt} is the bubble waiting time coefficient, k_l is the liquid conductivity, $\lambda_l = k_l/(\rho_l c_{p,l})$ is the liquid thermal diffusivity, f is the bubble detachment frequency and T_w is the wall temperature.

The evaporative heat flux q_e is computed as the latent heat carried away by the bubbles departing from the wall and is given by

$$q_e = (\frac{\pi}{6} D_w^3) N_w \rho_g h_{fg} f \tag{55}$$

where D_w is the bubble departure diameter (calculated from eq. 61), N_w is nucleation site density, h_{fg} is the latent heat of evaporation and f is the detachment frequency. The last term q_c concerns the single-phase convective heat flux and can be expressed as:

$$q_c = h_c(T_w - T_l)(1 - A_b) \tag{56}$$

where h_c is single phase convection heat transfer coefficient and A_b is the bubble influence area coefficient. The coefficient A_b can be computed as:

$$A_b = min\left(1, K\frac{N_w \pi D_w^2}{4}\right) \tag{57}$$

where the coefficient K according to Del Valle & Kenning [141] can be calculated from the following relationship,

$$K = 4.8e^{\left(-\frac{J_{\text{sub}}}{80}\right)} \tag{58}$$

where J_{sub} is the subcooled Jacob number.

3.9.1 Closure relations

As shown in the above wall heat flux equations, the accurate modeling of bubble nucleation quantities, including the bubble departure diameter, the bubble departure frequency, and the nucleation sites density, is required because they have a direct effect on the bubble generation and on the heat partitioning at the heated wall. Below the selected models of these parameters are presented.

3.9.2 Nucleation site density

For the calculation of the nucleation site density, which mostly depends on the material of the wall and the wall superheat, a modified correlation [142] originally proposed by Lemmert and Chawla [143] is used:

$$N_w = C_n N_{ref}\left(\frac{T_W - T_L}{\Delta T_{ref}}\right)^p \tag{59}$$

where C_n is an empirical constant. N_{ref} is the number of nucleation bubbles per unit area, T_W and T_L is the wall and liquid temperature and ΔT_{refN} is the reference temperature which in the present study varies between 10 to 30 K.

3.9.3 Bubble detachment frequency

The bubble departure frequency denotes the cycle of bubble generation and growth to the size of bubble departure diameter detaching from the wall at one given nucleation site. Due to the high importance of this parameter, several investigations have been performed on the bubble departure frequency. In this study the model proposed by Kocamustafaogullari and Ishii [144] is selected and is computed according to

$$f = \frac{C_f}{D_l}\left(\frac{\sigma\Delta\rho}{\rho_l^2}\right)^{0.25} \tag{60}$$

where C_f is an empirical constant and usually has value of 1.18 and D_dp is the bubble departure diameter.

3.9.4 Bubble departure diameter

Generally, the bubble departure diameter D_w is a function of contact angle, thermal properties of the working fluid and the mass flux. The most widely used correlation for the calculation of D_w in the RPI model is the Tolubinsky-Konstanchuk's [145] correlation and is given by

$$D_w = d_{ref} e^{\frac{-\Delta T_w}{\Delta T_{ref}}} \tag{61}$$

where, d_{ref} is a reference value of bubble diameter , ΔT_w is the wall super-heat, and $\Delta T_{ref} = 45\,\mathrm{K}$.

3.10 IATE model

It has been shown [117] that bubble coalescence and breakup can significantly affect the predicted results of two-phase flows within small tubes/channels. A widely used model that accounts for bubble coalescence and breakup is the interfacial area transport equation (IATE) method proposed by Wu et al. [146] and further developed by Ishii et al. [147]. The model is expressed as:

$$\frac{\partial a_i}{\partial t} + \nabla\cdot(a_i\vec{v}_i) = \frac{2}{3}\left(\frac{a_i}{\alpha}\right)\left(\frac{\partial\alpha}{\partial t} + \nabla\cdot\alpha\vec{v}_g\right) + \frac{1}{3\psi}\left(\frac{\alpha}{a_i}\right)^2 [R_{TI} - R_{RC} - R_{WE}] \tag{62}$$

where $\vec{v}_g$ is the velocity of the bubble, $\vec{v}_i$ is the interfacial velocity and a_i is the interfacial area concentration. The first term on the right hand side accounts for pressure effects on the expansion or contraction of the gas phase, whereas the last three parameters constitute important bubble interaction mechanisms. The expression of each of these mechanism is written below.

3.10.1 Bubble Breakup Due to Turbulent Impact

R_{TI} is the bubble breakup rate caused by turbulent impact and is defined as

$$R_{TI} = C_{TI}\left(\frac{nu_t}{D_b}\right)\exp\left(-\frac{We_{cr}}{We}\right)\sqrt{1-\frac{We_{cr}}{We}},\ \text{where } We > We_{cr} \tag{63}$$

where C_{TI} is an experimental coefficient, $u_t = \epsilon^{1/3} d_b^{1/3}$ is the mean bubble fluctuating velocity, $We = (\rho u_t^2 d_b)/\sigma$ is the Weber number, and We_{cr} is an experimentally determined critical value of the Weber number.

3.10.2 Bubble Coalescence Due to Random Collisions

The bubble coalescence rate R_{RC} is caused by random collision and is expressed as

$$R_{RC} = C_{RC}\left[\frac{n^2 u_t D_b^2}{\alpha_{\max}^{1/3}\left(\alpha_{\max}^{1/3}-\alpha^{1/3}\right)}\right]\left[1-\exp\left(-C\frac{\alpha_{\max}^{1/3}\alpha^{1/3}}{\alpha_{\max}^{1/3}-\alpha^{1/3}}\right)\right] \tag{64}$$

where, α_{max} is the maximum allowable void fraction and C_{RC} and C are two model constants.

3.10.3 Bubble Coalescence Due to Wake Entrainment

Finally, R_{WE} is the bubble coalescence rate caused by wake entrainment, is given by

$$R_{WE} = C_{WE} C_D^{V/3} n^2 D_b^2 u_r \tag{65}$$

where C_{WE} is an experimental coefficient, u_r is the bubble terminal velocity. For further details about the IATE model the reader is referred to [117, 146, 147].

4 Application of the enhanced VOF based numerical simulation framework

As it was concluded from the state-of-the-art review, various important parameters that may influence the fluid flow and heat transfer characteristics during flow boiling within microchannels remain unexplored. In this section, some of these parameters are investigated extensively by utilising an enhanced VOF-based solver of OpenFOAM. For every parameter, a detailed literature review on previous investigations that examined this parameter is conducted and the utilised numerical set-up for the present numerical simulations is presented. Subsequently, a qualitative and quantitative representation of the numerical predictions as well as a detailed analysis and discussion is conducted. Finally, the main conclusions withdrawn from each particular study are summarised at the end of each subsection.

4.1 Effect of surface wettability on the bubble growth and detachment characteristics during saturated flow boiling within micro-passages

4.1.1 Scope

Surface wettability is considered a critical parameter in micro-scale phenomena, especially in two-phase flows, where the surface tension force becomes dominant as the size decreases [148]. Therefore, many investigations under different experimental conditions have been focused on surface wettability effects of two-phase flow in microchannels [149–154]. Nevertheless, as Kandlikar [155] reported even if wettability effects are of great importance in flow boiling within microchannels, there is a limitation of available experimental reports having considered flow boiling micro-scale channels in the literature. According to Kandlikar & Grande [156] the main reason for this could be the difficulties in fabrication. Some older and more recent experimental investigations on wettability effects of flow boiling in microchannel are presented as follows [157] [158–162].

Flow boiling experiments that investigated the effects of wettability in multiple small channels were first studied by Rioboo et al. [157]. In this work, deionized Milli-Q water is used. Hydrophobic surfaces ($\theta_\alpha/\theta_\mathrm{r} = 107.3°/80.3°$) ($\theta_\alpha/\theta_\mathrm{r} = 94.8°/55.5°$) heated on the bottom side (with a total applied power of 500W) have been used, whereas the liquid mean velocities tested were 0.0309 and 0.0386 $\mathrm{m\,s^{-1}}$. The overall channel dimensions were (L, W, H: 18, 0.1 and 0.6 mm). It was found that the resulting phase-change is linked to the local density of nanobubbles which depends on the surface hydrophobicity.

Wang et al. [163] experimentally studied the wettability effects of a chemically-patterned surface and compared the results with homogeneous hydrophilic microchannel with a hydraulic diameter of 311.76 µm and heat flux values between 25.6 $\mathrm{kW\,m^{-2}}$ to 786.1 $\mathrm{kW\,m^{-2}}$. It was found that the HTC increased up to 22% for the patterned surface in comparison to the hydrophilic microchannel and when the mass flux increases, HTC is accordingly enhanced. An enhanced HTC and CHF of heterogenous surfaces is also reported by Kim et al. [164] who tested the flow boiling

performance of water on a hydrophilic (57°) rectangular channel with hydraulic diameter 7.5 mm coated with SiO_2 , having hydrophobic (120°) stripes with different widths and directions coated with Teflon. Particularly, it was observed that higher HTC and CHF were generated for narrow patterns, compared to the wide patterns. The influence of heterogeneous wetting surfaces was explored also numerically by Kim et al. [165] who tested a rectangular channel of a hydrophilic (30°) surface combined with hydrophobic (110°) patterns (crosswise, parallel and dotted). The working fluid was water, and the hydraulic diameter was 0.95 mm, while constant heat flux of 350 kW m^{-2} is applied, whereas the mass flux values ranged between 100-800 kg m^{-2} s^{-1}. Their model included a nucleation site density correlation. They found that nucleation site density was higher for the case of the dotted patterns at high mass fluxes resulting in better heat transfer performance. However, very wide or narrow hydrophobic areas result in reduced heat transfer performance. Since however, the present investigation is focused on homogeneous wettability surfaces the following paragraphs review works on microchannels with homogeneous wettability.

Phan et al. [158] conducted an experimental investigation of flow boiling of water in rectangular microchannels with the applied heat flux varied from 30 kW m^{-2} to 80 kW m^{-2}, and for different vapour qualities. In total three hydrophilic plus one hydrophobic surfaces with an equilibrium contact angle of 26°, 49°, 63° and 104° were used, respectively. From the experiments, it was shown that different flow patterns such as bubbly flow, slug flow, and semi-annular flow resulted in a significant variation on the overall heat transfer. Additionally, it was also observed that when the contact angle increases, the superheat needed for onset of nucleate boiling decreases. They concluded that a low superheat for onset of nucleate boiling, in combination with good control of bubbles emission frequency, is an important factor in improving the heat transfer performance of flow boiling within microchannels

Concerning the evaluation of the flow boiling hydraulic and thermal performance in microchannels Liu et al. [159] performed experiments on 3 different microchannels with dimensions of 105, 1000 and 30 000 µm^3, with different wettability characteristics. The three surfaces included a super-hydrophilic surface after growth of nanowire arrays with a contact angle of almost 0°, a plain silicon wafer hydrophilic surface machined through a plasma etching process with a contact angle of 36° and a hydrophobic surface coated by a thin film of low surface energy material with a contact angle of 103°. Different boiling flow patterns on surfaces with different wettabilities were found, leading to large differences in temperature oscillations and hence in the resulting HTC. In detail, for the super-hydrophilic case, a generation of a high number of nucleation sites was observed, possibly due to the high number of defects formed between the nano-spaced rings on the nanowire fabricated surface. For the hydrophilic case a cyclic flow process occurred mostly associated with the corresponding cyclic nucleation, growth and coalescence of bubbles. Finally, for the hydrophobic surface, a severe superheat of the liquid phase was encountered, leading to the fast growth of the nucleated bubbles after boiling incipience.

More recently, Li et al. [160] conducted an experimental study of saturated flow boiling of water in a bare silicon wafer hydrophilic surface which was later converted to super-hydrophilic after deposition of nanoscale silicon dioxide particles, with a deposition thickness of 100 nm, through the plasma enhanced chemical vapor deposition (PECVD)

process. The corresponding contact angles were measured to be 65° and less than 5°, respectively. The applied heat flux values ranged between 40 kW m^{-2} to 200 kW m^{-2} while the mass fluxes spanned from 120 kg m^{-2} s^{-1} to 360 kg m^{-2} s^{-1}. It was reported that in the annular flow regime the local HTC decreased until approaching a minimum value and later increased towards the exit along the flow direction. At low mass flux and high vapour quality, a delay of the partial dryout occurrence on the super-hydrophilic surface was observed. The averaged HTC of the hydrophilic surface decreased with increments of heat or mass flux, indicating that in the bared wall hydrophilic surface dryout patches and high wall temperature are more easily formed in comparison to the super-hydrophilic surface. Another study on subcooled boiling in microchannels using the same set-up as in [160], but with the possibility of varying the channel orientation, was conducted by Li et al. [161]. The applied heat fluxes were ranged from 40 to 250 kW m^{-2} and the mass fluxes from 200 to 500 kg m^{-2} s^{-1}. It was shown that due to the enhancement of convective heat transfer caused by bubble disturbance near the exit and the suppression of nucleate boiling caused by high subcooling close to the entrance, the HTC increased along the flow direction. An earlier occurrence of the Critical Heat Flux value (CHF) was observed for the cases of vertical downflows. It was also shown that at low mass flux, the super-hydrophilic surface delays CHF without an increased pressure drop penalty when it is in a vertical orientation either in an up-flow or downflow configuration. By changing the orientation to horizontal, the super-hydrophilic surface showed a higher heat transfer coefficient by 10% with a corresponding 37% increase in the pressure drop for the bottom-heated flow, while for the top-heated flow, the HTC decreased by 16% and the pressure drop increased by 15%, compared to the hydrophilic surface. It was concluded that the effect of surface wettability is more significant in the horizontal orientation.

Choi et al. [162] conducted experiments of flow boiling of water in rectangular hydrophilic and hydrophobic microchannels, in order to investigate the effect of wettability. It was reported that the HTC of the hydrophobic microchannel was higher than the hydrophilic microchannel, mostly due to the associated nucleation site density and the resulting flow instabilities. However, the pressure drop in the hydrophobic surface was higher than that of the hydrophilic case, due to the unstable motion of bubbles and the formation of liquid films.

Numerical investigations in wettability effects of flow boiling in microchannels are even more limited in the literature, mainly due to the complex physics involved with such micro-scale two-phase flows and also due to the fact that the available contact angle treatments in commercial as well as opensource CFD codes are failing to accurately capture the dynamic nature of the apparent contact angles during bubble growth. Gong & Cheng [166] developed a 2D model where the Lattice Boltzmann method was utilised. The effects of contact angle, inlet velocity, and heater size on the resulting flow patterns, under constant heat flux conditions, were studied. Their model could also provide information about nucleation time and temperature using an empirical correlation [167]. The results showed that the variation of the static contact angle does not influence the bubble departure size. Nevertheless, nucleation time and nucleation temperature appeared to decrease when the contact angle is increased. Examining the resulting Nusselt numbers, an increase was observed with the increase of the Re number or

with an increase in the superheat degree. Conversely, a corresponding decrease in the resulting Nusselt numbers with an increase in the imposed contact angle was found. Finally, along the centreline in the superheated liquid from the inlet to the outlet, the pressure was shown to drop almost linearly, except in the exit region of the flow where unphysically large pressure jumps and drops in liquid-vapour interface regions were observed, which were attributed to the equation of state for real gases adopted in the model.

Wettability and inertia effects on heat transfer during flow boiling in microchannels were numerically investigated by Kim & Lee [168]. A constant heat flux of $350\,\mathrm{kW\,m^{-2}}$ was applied at the bottom surface of the utilised rectangular channel with dimensions (L, W, H: 30, 0.2 and 0.5 mm), while the mass flux value varied between 20 to $500\,\mathrm{kg\,m^{-2}\,s^{-1}}$. A hydrophilic and a hydrophobic surface with contact angles of 30° and 110°, respectively, were utilised. The computational mesh consisted of 1.536 M cells with 12.5 µm cell size. In their numerical model, the fluid interface is tracked by the volume of fluid approach, while the same phase change model as proposed by Hardt and Wondra [111] was used. Their model included also a nucleation site density submodel utilising an empirical correlation. For the prediction of the contact angle, a dynamic contact angle model based on Tanner's Law was used. Their results were compared with experimental data available in the literature. From their results, it was observed that wettability did not influence the flow patterns when cases with the same mass flux were compared. By increasing the mass flux different flow patterns could be seen (annular flow at $20\,\mathrm{kg\,m^{-2}\,s^{-1}}$, churn flow at $50\,\mathrm{kg\,m^{-2}\,s^{-1}}$, slug flow at $100\,\mathrm{kg\,m^{-2}\,s^{-1}}$, confined bubble flow at $200\,\mathrm{kg\,m^{-2}\,s^{-1}}$ and bubbly flow for mass fluxes above $350\,\mathrm{kg\,m^{-2}\,s^{-1}}$). With regards to the temperature of the channel, at low mass flux, a higher temperature could be seen in the hydrophobic surface due to the presence of a thin liquid film which is covering the interface between the solid and the vapour and is working as a lubricant. Under low mass fluxes (20-100 $\mathrm{kg\,m^{-2}\,s^{-1}}$), the hydrophilic channel had higher CHF compared to the hydrophobic. This trend was reversed for high heat fluxes (200-500 $\mathrm{kg\,m^{-2}\,s^{-1}}$). Finally, the numerical model overestimated HTC by approximately 10% compared to the experimental results, concluding that the model can be adequately used for boiling simulations in microchannels.

A 3D conjugate heat transfer numerical study of flow boiling in diverging mini and microchannels with different inlet and outlet width (between 0.2 and 0.8 mm) has been carried out by Alugoju et al. [169], in order to investigate the bubble pattern and heat transfer characteristics of flow boiling. The simulations were performed by using the volume of fluid method of ANSYS-FLUENT©18.0, coupled with a phase change and a surface tension force model [104]. A uniform heat flux condition varying between 500 and $2000\,\mathrm{kW\,m^{-2}}$ is applied at the bottom surface of the channel, with the rest of the walls to be considered adiabatic, while the mass flux ranges between 240 and $710\,\mathrm{kg\,m^{-2}\,s^{-1}}$. A hydrophilic and a hydrophobic surface were utilised with contact angles of 65° and 140°, respectively, while water was used as the working fluid. Empirical correlations proposed by Bertsch et al. [47] which account for convective heat transfer and nucleate boiling terms were included in the model. They reported that different bubble patterns between the two surfaces were observed. Particularly, for the hydrophilic case, the bubble separation rate from the wall is less, thereby creating

localized hotspots, while for the hydrophobic surface the generated bubbles are detached from the wall surface and flow along with the fluid stream. Other observations included that when the hydraulic diameter is increased, smaller elongated bubbles are observed. In smaller channels and at low flow rate localized flow reversal could be seen. Finally, for some cases when the mass flux increases higher values of localized heat transfer could be seen in channels with lower hydraulic diameter, and as the diameter is increased, the values are reduced, due to the different nucleation time and bubble pattern.

As can be seen from all these works, there is a considerable influence of wettability on flow boiling characteristics within micro-passages. However, so far most of the experimental investigations related to surface characteristics and/or wettability effects are focusing on heat transfer enhancement, with the underpinned physical mechanisms, as for how heat transfer coefficient is enhanced, still not completely understood. Additionally, in the experimental investigations, in order to alter the surface wettability characteristics, different solid materials are used, or the channel surfaces are treated accordingly through the application of coatings [170] that alter the structure, properties and chemical composition of the surfaces. This might lead to the alteration of other factors, apart from the solid/liquid/vapour contact angle, that can additionally affect the flow boiling characteristics, such as the nucleation site density and the solid surface thermal response. Therefore, the exact effect of wettability cannot be isolated and directly identified and quantified, utilising experimental measurements. On the other hand, the numerical investigations available in literature can isolate the effect of wettability by altering only the contact angle, however in most cases, they use either a constant contact angle model or a dynamic contact angle model without adequate accuracy in the predictions. Additionally, the examined ranges of contact angles in the literature are not wide enough (e.g. only hydrophilic and only hydrophobic surfaces) to adequately capture the effects of hydrophilicity or hydrophobicity, taking also into account the effect of contact angle hysteresis. In this section, the first series of parametric numerical simulations of the present thesis regarding flow boiling within a single microchannel are conducted, to thoroughly investigate wettability effects on the two-phase flow and heat transfer characteristics. The main focus is to isolate, identify and quantify the effect of wettability at the initial stages of the bubble growth process within a few milliseconds from the bubble nucleation. Initially, single, isolated bubbles are considered. Subsequently, simulations of multiple nucleation sites and multiple nucleation events are also performed. All simulations are performed with the enhanced conjugate heat transfer VOF-based solver described in section 3. As it has also been mentioned in Chapter 3, in the utilised conjugate heat transfer VOF-based solver, the dynamic contact angle treatment of Kistler [116] has been implemented, as it performs better than the already implemented dynamic contact angle treatments in the original distribution of OpenFOAM (version 2.2.1). The proposed implementation has been tested in the past against droplet impact experiments on surfaces with different wettabilities as well as against droplet impact experiments on suspended metallic meshes by the present PhD candidate. More details on these works can be found here [96, 171]. Furthermore, a comparison with experiments on pool boiling in bi-philic surfaces has been also performed with an excellent degree of convergence in [98], by the supervisor and collaborators of the present PhD Candidate.

Application of numerical method

4.1.2 Computational geometry, mesh and boundary conditions

A single microchannel consisting of a fluid domain on top of a solid domain is considered for the present investigation (Figure 8). The computational mesh has been generated by discretising the computational domain in two parts. The solid domain mesh and the fluid domain mesh. A uniform, structured computational mesh, consisting of hexahedral elements is utilised. The physical dimensions of the fluid domain (length, height and width) are $L_f = 2.40\,\text{mm}$, $H_f = 0.30\,\text{mm}$, $W_f = 0.15\,\text{mm}$ and the solid domain dimensions are $L_s = 2.40\,\text{mm}$, $H_s = 0.09\,\text{mm}$, $W_s = 0.15\,\text{mm}$, respectively. The hydraulic diameter of the microchannel is $D_h = 0.2\,\text{mm}$ and the aspect ratio ($\beta = \text{W/H}$) is 0.5. The generated computational geometry, the mesh and the applied boundary conditions are illustrated in Figure 9. These dimensions have been selected in order to represent typical rectangular microchannel geometries from the literature [172, 173].

With respect to the boundary conditions, apart from the inlet and outlet in the fluid domain, the bottom side of the solid domain (where constant heat flux is applied) and the CHT boundary (interface between fluid and solid domains), all the rest surfaces are considered to be adiabatic walls. At the solid walls of the fluid domain, including the CHT boundary, a no-slip velocity boundary condition is used with a fixed flux pressure boundary condition for the pressure values. Additionally, a dynamic contact angle boundary condition is imposed for the volume fraction field by assigning the maximum advancing and minimum receding contact angle values from sessile drop measurements, that are then used for the calculation of the dynamic (apparent) contact angle values during the computations. For the sidewalls of the fluid and solid domains, a zero gradient boundary condition is used for the temperature field, representing an insulated microchannel. At the outlet, a fixed-value pressure boundary condition and a zero-gradient boundary condition for the volume fraction were used, while for the velocity values a special (combined) type of boundary condition is used that applies a zero-gradient when the fluid mixture exits the computational domain and a fixed value condition to the tangential velocity component, in cases that the fluid mixture enters the domain. Finally, a zero gradient boundary condition for the temperature field was also prescribed at the outlet boundary. For the inlet, a constant uniform velocity value was imposed as well as a fixed flux pressure condition. The volume fraction value was assigned as unity, as saturated liquid only enters from the inlet during the calculations. Hence, the temperature of the liquid at the inlet was also fixed at the saturation temperature. As mentioned earlier both the temperature values as well as the heat fluxes are coupled at the CHT interface (between the solid and fluid domains) for each calculation time step through an inner iteration process.

4.1.3 Numerical simulation set-up and process

As shown in Figs. 8 and 9 the considered configuration for the present parametric numerical investigation consists of a single microchannel with a constant uniform heat flux q'' applied at its bottom solid wall. Therefore, the generated 3D computational domain consists of a solid domain (representing the bottom solid wall of the channel) that is in contact with the fluid domain that corresponds to the considered micro-passage.

All the simulations are performed in two main stages. During the first stage, a specified heat flux is applied to the bottom surface of the solid domain and a single-phase liquid flow is considered initially with saturated liquid, flowing with a specified mass flow rate. This is run up to a point that a steady state condition is reached and both the hydrodynamic and thermal boundary layers have been developed, as shown in Fig. 10a.

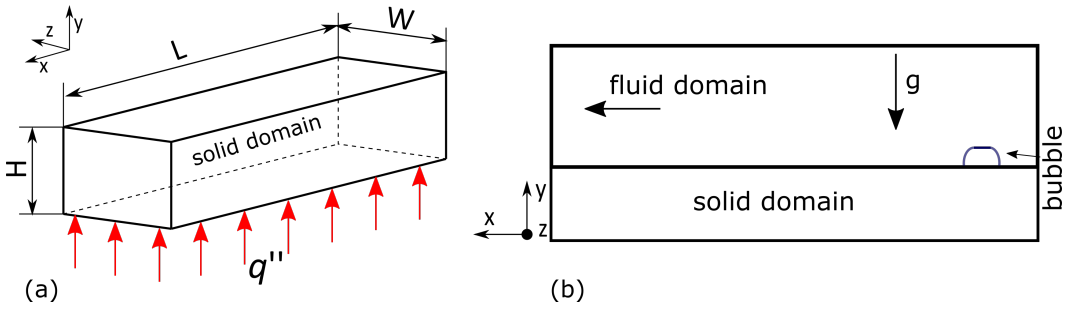

Figure 8: (a) 3D sketch of the heated solid domain. (b) Side view of solid wall and fluid domain. The position of the imposed bubble at t = 0 ms is shown as well.

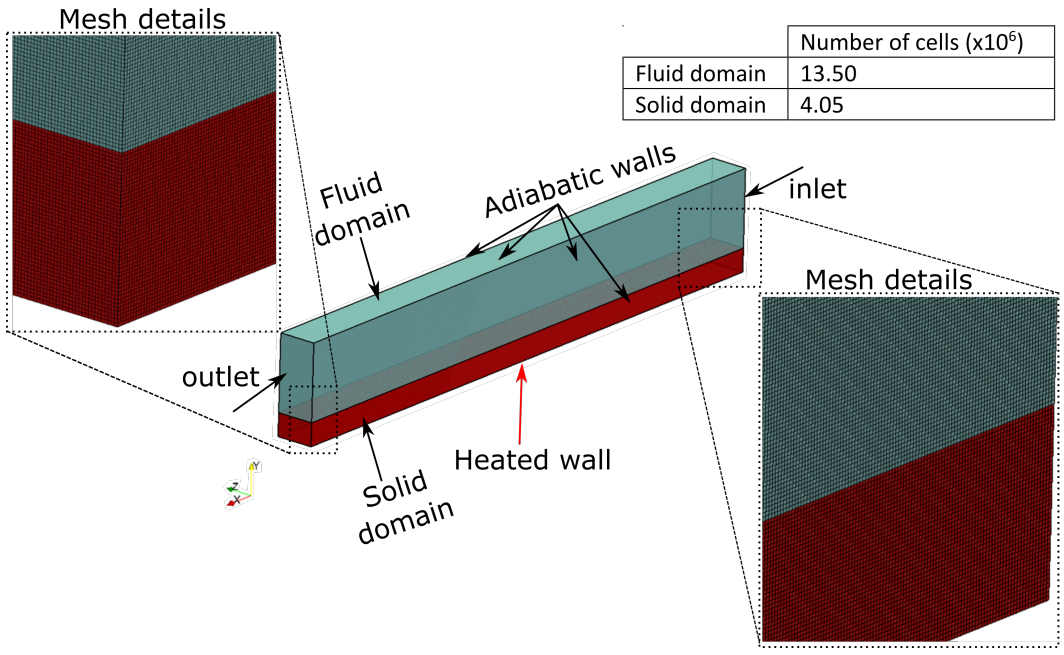

Figure 9: Computational domain, mesh and boundary conditions.

The velocity of the liquid U_l is constant and uniform through the inlet boundary and the flow is laminar. The first stage is conducted for all simulations presented in this study. At the second stage (Fig. 10b) a small vapour nucleus (bubble seed), represented as a half-sphere with a radius of 20 µm, is patched on the conjugate heat transfer boundary (interface between the fluid and solid domains) at a distance of 200 µm from the channel inlet, at saturation temperature. Since the initial bubble seed is patched within the previously developed thermal boundary layer, where the temperature is higher than the saturation temperature, boiling occurs at the meniscus

(solid/liquid/vapour triple line) as well as at the parts of the liquid/vapour interface that are in contact with temperatures higher than the saturation temperature.

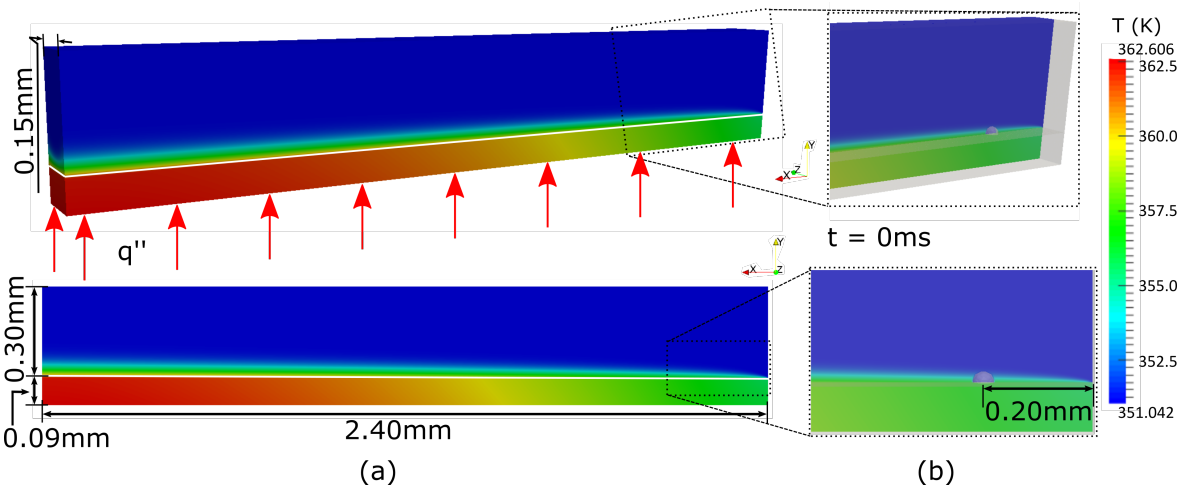

Figure 10: (a) Developed thermal boundary layer at the end of the first stage of simulations (single-phase), (b) patched bubble seed position at the beginning of the second phase of simulation (referred as initial time t = 0 ms) , for q″ = 20 kW m^{-2} and G = 150 kg m^{-2} s^{-1}.

It should be mentioned that for all of the simulations conducted for the present investigation, the liquid and vapour phase properties are taken as these of Ethanol liquid and vapour at the saturation equilibrium point for pressure of P_{sat}= 1 bar, which corresponds to a saturation temperature of T_{sat}=351.05 K (REFPROP NIST software [174]). As for the solid domain, stainless steel properties were used, for all cases. The exact values of the fluid and solid properties that were used in all simulations conducted for the purposes of the present study are summarised in Tables 3 and 4, respectively. The advancing and receding contact angles for the base case of the present parametric analysis were taken as these of Ethanol with a particular stainless-steel sample at an average roughness Ra = 0.4 µm, having values of θ_α = 19° and θ_r = 8°, respectively. In order to investigate the isolated effect of wettability in the bubble growth characteristics as well as its effect on the local heat transfer, in the rest of the runs, the values of θ_α and θ_r were varied, while all the rest fluid and solid properties and operating conditions were kept unaltered. The contact angle values that were selected for this purpose correspond to realistic contact angles for different combinations of Ethanol as well as other working fluids (e.g. R-113, Glycerol and Water) with other uncoated or coated Stainless Steel (SS) 316 samples of the same or different grades. For the exact fluid-solid combination contact angle values the reader is referred to [175]. To observe the effects of wettability at different heat fluxes, the overall analysis for all of the selected contact angle values was performed for three different values of applied heat flux (q″ = 20, 50, 100 kW m^{-2}) and three different values of mass flux (G = 74, 150 and 295 kg m^{-2} s^{-1}). These values, as well as the material of the solid domain, were selected due to the fact that they are often used in the literature on flow boiling experiments within micro-passages and have a broad range of industrial applications [2, 159]. At this point, it should be mentioned

Table 3: Ethanol properties at saturation temperature that were used in the simulations.

T_{sat} (K)	P_{sat} (kPa)	ρ_l ($\frac{\text{kg}}{\text{m}^3}$)	ρ_v ($\frac{\text{kg}}{\text{m}^3}$)	ν_l ($\frac{\text{m}^2}{\text{s}}$)	ν_v ($\frac{\text{m}^2}{\text{s}}$)	λ_f ($\frac{\text{W}}{\text{m K}}$)	λ_v ($\frac{\text{W}}{\text{m K}}$)	Cp_l ($\frac{\text{m}^2}{\text{s}^2 \text{K}}$)	Cp_v ($\frac{\text{m}^2}{\text{s}^2 \text{K}}$)	h_lv ($\frac{\text{kJ}}{\text{K}}$)	σ ($\frac{\text{N}}{\text{m}}$)
351.05	100	736.78	1.63	6.01×10^{-7}	6.37×10^{-6}	0.153	0.02	3182	1804	850.5	0.15

Table 4: Steel properties that were used for the simulations.

ρ_s (kg m^{-3})	c_v ($\text{m}^2 \text{K}^{-1} \text{s}^{-2}$)	κ_s ($\text{W m}^{-1} \text{K}^{-1}$)
7840	500	16.2

Table 5: Considered wettability characteristics all these cases are considered for $\text{q}'' = 20, 50, 100\,\text{kW m}^{-2}$ and $\text{G} = 74, 150, 295\,\text{kg m}^{-2}\,\text{s}^{-1}$.

Case	Surface	θ_α (°)	θ_r (°)	CAH (°)
I	Hydrophilic / Low hysteresis	19	8	11
II	Hydrophilic / High hysteresis	49	0	49
III	Hydrophilic / High hysteresis	72	40	32
IV	Hydrophobic / Low hysteresis	101	95	6
V	Hydrophobic / High hysteresis	120	80	40
VI	Hydrophobic Low hysteresis	120	115	5

that mass flux is a parameter that is often used in investigations of fluid flow within channels and is defined as

$$G = \frac{\dot{V}\rho_l}{nA_c} \tag{66}$$

where ρ_l is the liquid density, n is the number of the microchannels, Ac is the cross-sectional area, and $\dot{V}$ is the volumetric flow rate which is equal to,

$$\dot{V} = U_l A_C \tag{67}$$

In order to cover a wide range of contact angles (CAs), the selected values represent cases of hydrophilic and hydrophobic surfaces with both small and high Contact Angle Hysteresis (CAH = θ_α - θ_r). The overall details, regarding the wettability characteristics considered for each of the applied heat and mass flux values in the numerical simulations, are summarised in Table 5. As it can be seen, a combination of six different advancing and receding contact angles have been chosen, and considering all heat fluxes and mass fluxes tested, 54 in total, 3D, transient, numerical simulations were performed. A High-Performance Computing (HPC) cluster was utilized for these runs. Each run utilised 100 computational cores. The duration of the computation for each of the nine

single-phase simulations (one for each q″ value) was approximately 10 days, as seconds of real flow was required for a steady state condition to be reached. For the two-phase simulations, the duration of the computation was only a couple of days since just a few milliseconds of real flow were required for the generated vapour bubble to reach the outlet of the channel. In total, more than 1 million core-hours were utilised for the overall runs that are presented in the present investigation. A variable calculation time step was utilised for the two-phase runs with the Courant number kept constant at 0.5. Hence the calculation time step was varied automatically ranging approximately from 10^{-8} up to 10^{-6} s.

4.1.4 Mesh independence study

A mesh independence study was carried out, to select the optimum cell size in the utilised, uniform, structured, computational mesh for the parametric numerical simulations. Four different structured meshes, consisting of hexahedral cells, were constructed for this purpose, with a uniform cell size of 6 µm, 4 µm, 2 µm and 1 µm, respectively. The mesh independency study was performed for the case of $q'' = 50\,kW\,m^{-2}$, $G = 74\,kg\,m^{-2}\,s^{-1}$ for a hydrophilic surface with θ_a=19° and θ_r=8°. The material properties were these of Ethanol liquid and vapour at the saturation equilibrium point of Table 3 for the fluid domain, while the stainless steel properties of Table 4 were used for the solid domain.

The local time-averaged Nu number ($\overline{Nu}(x)$) over the non-dimensional length of the channel L^* ($L^* = L_{(x)}/L_{max}$) predictions for all four computational meshes are compared in Figure 11. The average relative errors of the 2 µm case in comparison with the 1 µm case is 0.285% and in comparison with the 4 µm and 6 µm cases, the average errors are 0.527% and 0.674%, respectively. The maximum local relative error

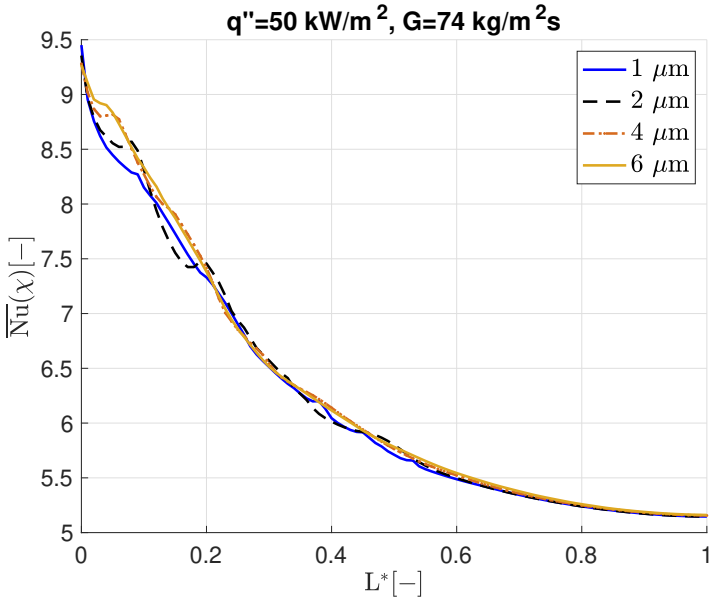

Figure 11: Mesh independency study results for $q'' = 50\,kW\,m^{-2}$ and $G = 74\,kg\,m^{-2}\,s^{-1}$. Hydrophilic surface ($\theta_a$=19°, θ_r=8°). Averaged Nusselt number over dimensionless length is tested.

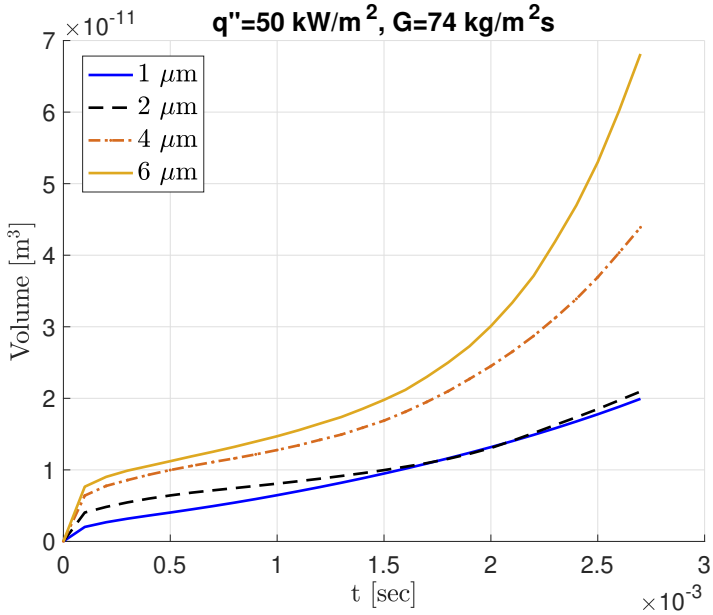

Figure 12: Mesh independency study results for $q'' = 50\,kW\,m^{-2}$ and $G = 74\,kg\,m^{-2}\,s^{-1}$. Hydrophilic surface ($\theta_a$=19°, θ_r=8°). Volume evolution of the bubble over dimensionless time is tested.

of the 2 µm case compared with the 1 µm, 4 µm and 6 µm cases is 1.626%, 2.721% and 3.362%, respectively. Additionally, another property of the simulation results has been plotted (Figure 12). Particularly the volume of the bubble over the dimensionless time is examined for the above-mentioned mesh sizes. For this comparison, the maximum local relative error of the 2 µm case compared with the 1 µm, 4 µm and 6 µm cases is 10.805%, 80.272%, 130.838%, respectively.

Since this particular result constitutes the main outcome aim of the present parametric numerical investigation the selected mesh size of 2 µm can be safely considered as the mesh independent solution. Furthermore, from previous investigations [93–95, 98, 99, 176], where the same solver was utilised, it has been shown that a 2 µm cell size is sufficient for capturing correct interface dynamics and evaporation rates. The selected mesh consists of a total number of 17.55M cells (4.05M cells in the solid and 13.50M cells in the fluid domain).

4.1.5 Additional validation of numerical simulation framework

In order to further validate the utilised solver on flow boiling within rectangular/square microchannels, a benchmark experimental work performed by Mukherjee et al. [177] has been chosen to be numerically reproduced. These experiments concern a single bubble growth within a microchannel and have been reproduced in the past by different researchers [178, 179]. Mukherjee et al. [177] assumed that the bottom and side walls have a constant temperature of 2.1 K above the saturation temperature and the top wall is adiabatic. Additionally, the inlet and the initial temperature are 2 K above the saturation temperature (superheated state). The same boundary conditions and initial conditions have been adopted also for the validation run of the present investigation.

The working fluid is water and the properties of water at 1 bar have been used, whereas the microchannel has equal width and height of 229 µm. It is important to note that these parameters concern only this additional validation part of the present study. Prior to patching of the single bubble nucleus, a single-phase simulation for obtaining fully developed initial thermal and hydrodynamic boundary layers is performed. In Figures 13 and 14 the predicted equivalent diameter over time for the generated vapour bubble with the present numerical solver is compared with the corresponding experimental as well as the numerical results of Mukherjee et al. [177]. As it can be seen the present solver, initially, overpredicts slightly the numerical and experimental results by Mukherjee et al. but this may be attributed to the fact that the initial bubble seed is placed within developed boundary layers, as correctly pointed out also by Zhang and Jia [179]. However, overall, it can be seen that the experimental results and the simulation results of the present numerical solver show good agreement within an acceptable average error value of less than 5%. This further ensures the accuracy of the present, customised numerical simulation solver for the purposes of the investigations presented in this chapter.

Effect of surface wettability - Numerical simulation results

4.1.6 Effect of wettability on micro-passages – Single nucleation site, single nucleation event

In this subsection, the numerical results of flow boiling of a single nucleation event at a single nucleation site within a rectangular microchannel will be presented. As previously shown in Table 5, numerical simulations of three different heat flux values have been performed, each of them separately investigated with three different mass flux values. In total six surfaces with different wettability characteristics (three hydrophilic

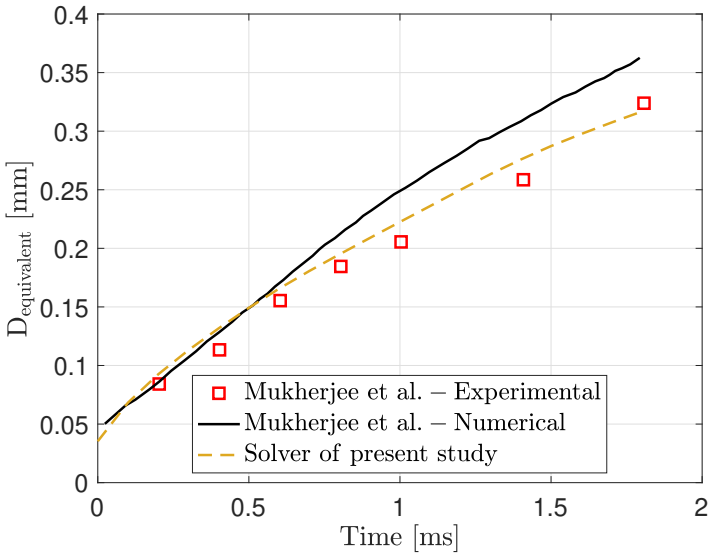

Figure 13: Comparison of the present numerical solver predictions against the experimental and numerical results reported by Mukherjee et al. [177].

and three hydrophobic surfaces) will be examined. At this point, it is important to mention that in the present numerical model the nucleation event is not a result of the simulation but an imposed condition. In more detail, as also mentioned earlier, a single liquid-phase simulation is initially performed to develop the hydrodynamic and thermal boundary layers. Then a small bubble nucleus is artificially placed at the heated wall a finite distance from the microchannel inlet, which initiated the boiling process at that particular position, with a bubble that grows and either slide along the channel walls from the previously developed liquid-cross flow (being in contact at certain points with the channel walls) or detaches from the wall and continues its growth as an evaporating vapour slug, due to liquid film evaporation.

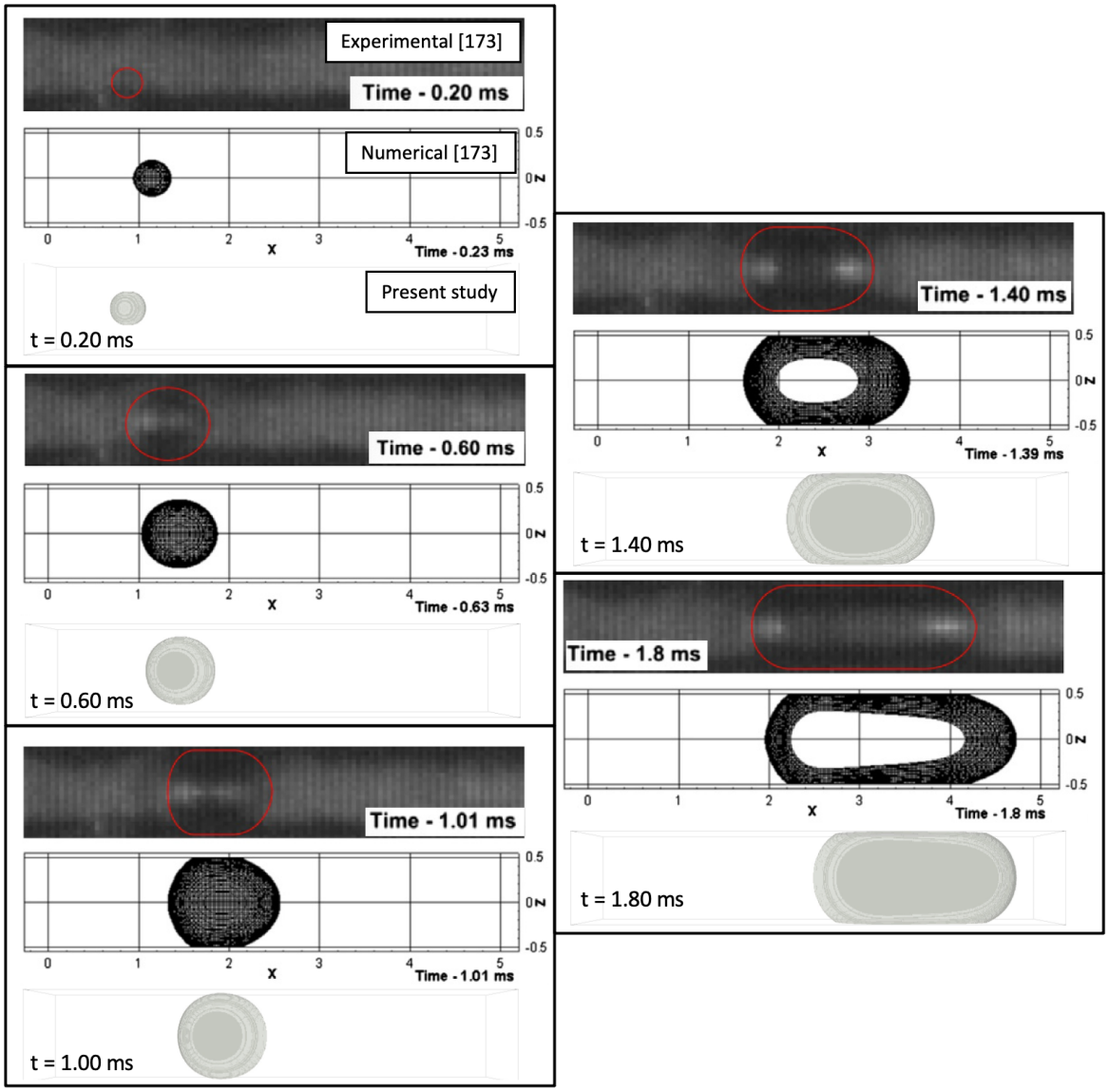

Figure 14: Qualitative comparison of the present numerical solver predictions against the experimental and numerical and experimental results reported by Mukherjee et al. [177].

Indicative qualitative/macroscopic results of the spatial and temporal evolution of the generated vapour bubbles, for three different cases, are shown in Figs.15 and 16. In the isometric view snapshots, the coloured contours in the clip section that extends from one side of the channel up to its middle plane, reveal the developed temperature fields in both the fluid and solid regions of the computational domain. In the top view snapshots, the coloured contours also show the instantaneous temperature distribution in the CHT boundary, i.e. the interface between the fluid and solid domains. The transparent grey surface constitutes the liquid/vapour interface which is represented by the 0.5 volume fraction iso-surface.

Both Figs. 15 and 16 correspond to cases with low heat and mass flux. Figure 15 compares hydrophilic cases and Fig. 16 hydrophobic cases. The spatial evolution of the liquid/vapour interface for three successive time instants is illustrated, in each case, through a 2D top view and a 3D isometric view. The first two time instants are common among the different wettability cases (0.4 ms and 4.2 ms), but the last time instant is chosen differently for each case, corresponding to the time that the leading edge of the bubble reaches the outlet of the channel. The macroscopic results of the remainder of the cases, for the rest of the tested mass fluxes and heat fluxes, due to space limitation, are only shown for the last time instant until the nose of the bubble touches the end of the microchannel, in Figs. 17, 18 and 19.

Focusing on Figs. 15 and 16, from a bubble dynamics point of view, a complete detachment of the bubble from the walls and the formation of a liquid film between the walls and the vapour bubble is observed for some of the cases, while, in some other cases, partial detachment or even no detachment with respect to the heated wall, as the bubble grows and slides towards the outlet, is observed. This can be attributed to the high cohesion and low adhesion forces that hydrophilic surfaces show and to high adhesion forces that the hydrophobic surfaces show. It should be mentioned that the imposed contact angles are applied for all walls of the channel and not only at the bottom heated wall.

In Figs. 15 and 16 the results for different wettability cases and for the low heat and mass fluxes ($q'' = 20\,kW\,m^{-2}$, $G = 74\,kg\,m^{-2}\,s^{-1}$) are shown. When comparing the three hydrophilic surfaces to each other (Figures 15a, 15b, 15c at time instants t=7.9 ms, t=9.8 ms and t=13.1 ms, respectively) it is observed that for the low advancing contact angle case (Figure 15a: θ_a=19°, θ_r=8°), a thin liquid film is formed between the bubble and the bottom heated wall as well as the top adiabatic wall of the considered microchannel in the frontal part of the bubble, while the remaining trailing part of the bubble is staying in direct contact with the bottom and top walls through a relatively large dry patch at the bottom wall and a smaller one at the top wall. It is also evident that the bubble is in contact with the side channel walls throughout almost its entire length. However, as the advancing contact angle is increasing the length of these dry patches decreases gradually (Fig. 15b: θ_a=49°, θ_r=0°) up to a point where no liquid film is present at all (15c: θ_a=70°, θ_r=40°).

As for the hydrophobic cases that are illustrated in Fig. 16, no presence of liquid film is observed as well. Therefore, it seems that there is a critical value of advancing contact angle (∼70°) after which there is no formation of liquid film occurring. Furthermore, it is evident that for the cases with small CAH (θ_a=101°, θ_r=95° and θ_a=120°, θ_r=115°),

the growing bubble remains in contact with the side and bottom wall of the channel throughout its entire path within the microchannel without touching the top wall. However, for the higher CAH case (θ_a=120°, θ_r=80°) the generated vapour bubble comes also in contact with the top wall of the channel at a certain stage. From all these macroscopic observations it can be concluded that, for relatively low heat and mass fluxes, the variation of the advancing and receding contact angles (i.e. the wettability characteristics) has a quite significant effect on the resulting bubble growth characteristics as well as in the size and the shape of the bubble, resulting also in different contact line dynamics (i.e. triple liquid/vapour/solid line evolution behaviour). For all cases, due to the associated latent heat of evaporation, as the bubble grows and slides along the solid wall, the temperature of the solid is decreasing. Depending on the imposed contact angle values the bubble grows either due to evaporation at the triple line or to a combination of triple line evaporation and liquid film evaporation, as a result of different adhesion and cohesion forces and according to Kim et al. [168] due to inertia and surface tension forces, which is also related to the delayed bubble growth of the hydrophobic surface (higher inertia). The combination of the two mechanisms is more evident for relatively small contact angle values (i.e. more hydrophilic cases, Figs. 15a and 15b). The contribution of the liquid film evaporation to the overall evaporation rate is reduced as the hydrophilicity is reduced and it seems to be a threshold ($\theta_a \sim 70°$), just after which the main evaporation mechanism is solely contact line evaporation (i.e. less hydrophilic and hydrophobic cases, Figs. 15c, 16a, 16b and 16c).

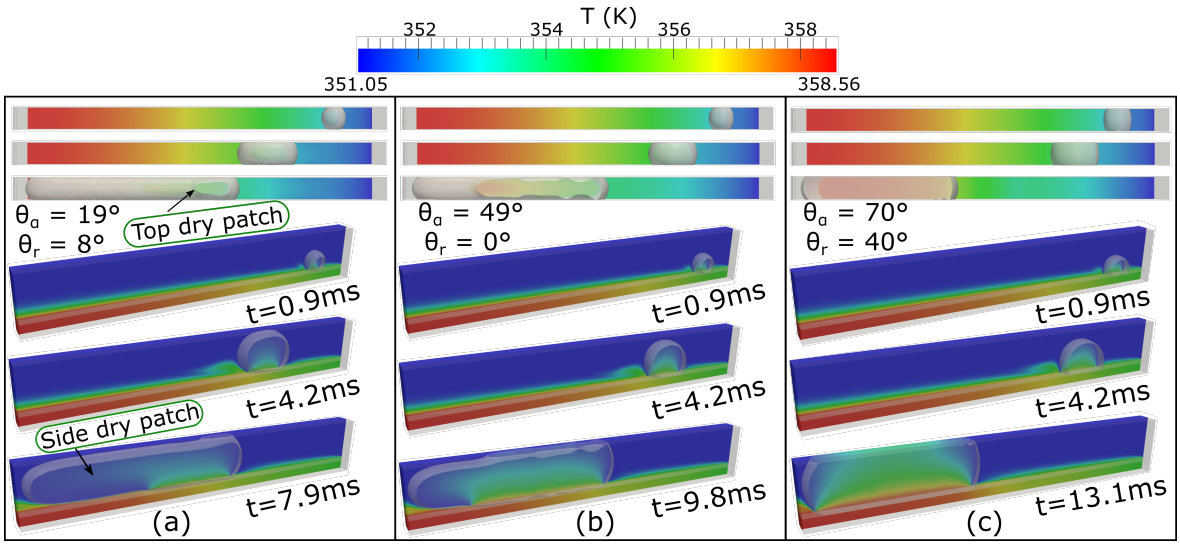

Figure 15: Flow visualisation results of hydrophilic cases, for $q'' = 20\,\mathrm{kW\,m^{-2}}$ and $G = 74\,\mathrm{kg\,m^{-2}\,s^{-1}}$, (a) $\theta_a/\theta_r = 19°/8°$, (b) $\theta_a/\theta_r = 49°/0°$, (c) $\theta_a/\theta_r = 70°/40°$. In each case a 2D top view and a 3D isometric view of the phenomenon for two common time instants (0.9 ms and 4.2 ms) and a last time instant that corresponds to the time that the leading edge of the bubble reaches the outlet of the microchannel are shown.

Figure 17 illustrates only the last time period before the generated vapour bubble reaches the outlet of the channel, for two higher values of mass flux cases ($G = 150\,\mathrm{kg\,m^{-2}\,s^{-1}}$ and $G = 295\,\mathrm{kg\,m^{-2}\,s^{-1}}$), but for the same applied heat flux

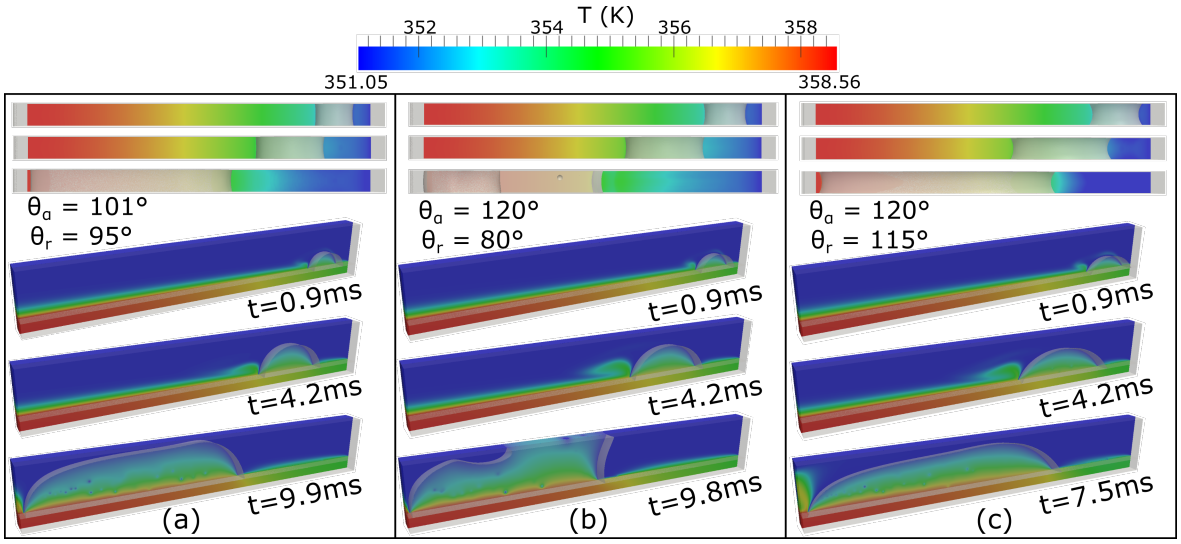

Figure 16: Flow visualisation results of hydrophobic cases, for $q'' = 20\,kW\,m^{-2}$ and $G = 74\,kg\,m^{-2}\,s^{-1}$, (a) $\theta_a/\theta_r = 101°/95°$, (b) $\theta_a/\theta_r = 120°/80°$, (c) $\theta_a/\theta_r = 120°/115°$. In each case a 2D top view and a 3D isometric view of the phenomenon for two common time instants (0.9 ms and 4.2 ms) and a last time instant that corresponds to the time that the leading edge of the bubble reaches the outlet of the microchannel are shown.

as in Figs. 15 and 16 ($q'' = 20\,kW\,m^{-2}$) for all of the considered wettabilities. As it can be seen, also for higher values of mass flux a similar trend is observed, with the development of liquid films for the low and medium hydrophilicity cases and direct contact of the vapour slug with the heated surface for the hydrophobic cases. It is also evident that as the mass flux increases and the heat flux remains constant, the contact areas of the generated vapour slugs with the heated wall are reducing in dimension. The overall volume of the vapour bubbles also seems to decrease with an increase of the mass flux. Finally, it is also evident that the increase of the mass flux tends to eliminate the previously observed trend of the generated vapour slug in the case of the high CAH hydrophobic surface to get in contact with the top wall of the channel (please see Figs. 17e and 17k).

Figure 18, summarises the corresponding flow visualisation results for the medium of the applied heat fluxes ($q'' = 50\,kW\,m^{-2}$), for all three of the considered mass flux values ($G = 74\,kg\,m^{-2}\,s^{-1}$, $G = 150\,kg\,m^{-2}\,s^{-1}$, $G = 295\,kg\,m^{-2}\,s^{-1}$). In the hydrophilic cases, the leading edge of the bubble has developed a characteristic bullet-shape nose, which has a more rounded (less pointy) profile for the medium and high mass flux values, resulting in a slightly thinner liquid film compared to the simulation with the low mass flux. Very similar predictions can be seen between the two hydrophobic cases with low (θ_a=101°, θ_r=95°) and medium (θ_a=120°, θ_r=80°) advancing contact angles. In more detail, for $G = 74\,kg\,m^{-2}\,s^{-1}$ and $G = 150\,kg\,m^{-2}\,s^{-1}$ almost a complete detachment of the bubble is observed with respect to the heated wall, except for a small part in the trailing side of the bubble which remains in contact with the heated surface. However, a complete detachment and development of liquid film between the entire bottom side of the bubble and the heated wall can be seen when the mass flux is $295\,kg\,m^{-2}\,s^{-1}$,

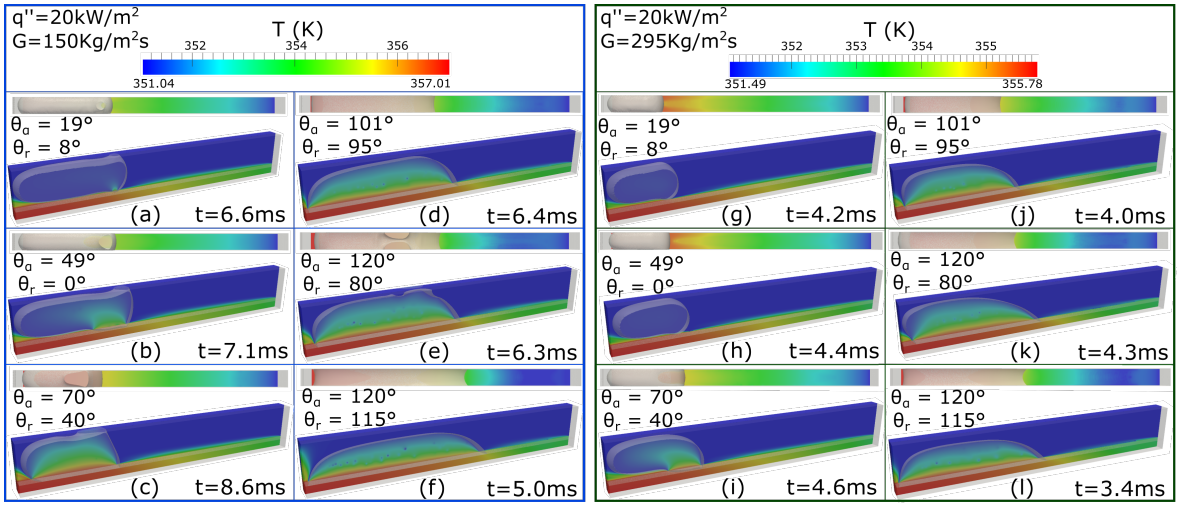

Figure 17: Macroscopic view of the numerical simulation results, showing only the last time instant before the bubble reaches the outlet of the microchannel for: $q'' = 20\,kW\,m^{-2}$ and $G = 150\,kg\,m^{-2}\,s^{-1}$ (left), and $q'' = 20\,kW\,m^{-2}$ and $G = 295\,kg\,m^{-2}\,s^{-1}$ (right).

meaning that the CAH difference between these two cases affects neither the bubble shape nor the bubble growth rate. Different behaviour is observed for the case with high hydrophilicity (θ_a=70°, θ_r=40°), where, for low mass flux, the bubble is entirely detached from the heated surface. However, for medium and high mass flux simulations, the high receding contact angle value, compared to the other two hydrophilic cases, has resulted in partial contact of the bubble with the heated wall. A contact area between the heated wall and the bubble is also observed, for the hydrophobic surface cases. Particularly, the cases with small CAH (θ_a=101°, θ_r=95° and θ_a=120°, θ_r=115°) maintain contact area with the heated wall throughout the entire bubble growth process, for all three mass flux cases. Conversely, when the mass flux is $295\,kg\,m^{-2}\,s^{-1}$ for the case with high CAH (θ_a=120°, θ_r=80°), about 70% of the bubble is still in contact with the heated wall, while the remainder 30% has similar a shape as the one described previously for the hydrophilic cases, with presence of a thin liquid film between the bubble and the top and the bottom wall of the microchannel.

Finally, the corresponding qualitative results for the high heat flux value ($q'' = 100\,kW\,m^{-2}$) are illustrated in Figure 19. For $G = 74\,kg\,m^{-2}\,s^{-1}$ a different flow pattern is observed, compared to the cases with lower heat flux that have been discussed earlier. Particularly, for all the examined surfaces churn flow is observed. This can be attributed to the high wall superheat, which has resulted in a prompt growth of the nucleation bubble and unstable/asymmetrical flow, for the first few time periods until the wall superheat is cooled down due to the heat transfer mechanisms. When the mass flux is increased to $G = 150\,kg\,m^{-2}\,s^{-1}$ and $G = 295\,kg\,m^{-2}\,s^{-1}$, a slug flow boiling regime is evident for both hydrophilic and hydrophobic cases. For the medium mass flux ($G = 150\,kg\,m^{-2}\,s^{-1}$), a total detachment of the developed vapour bubble from the heated surface is observed for the hydrophilic cases. However, for the hydrophobic cases, a contact areas with the heated wall are observed mainly towards the trailing

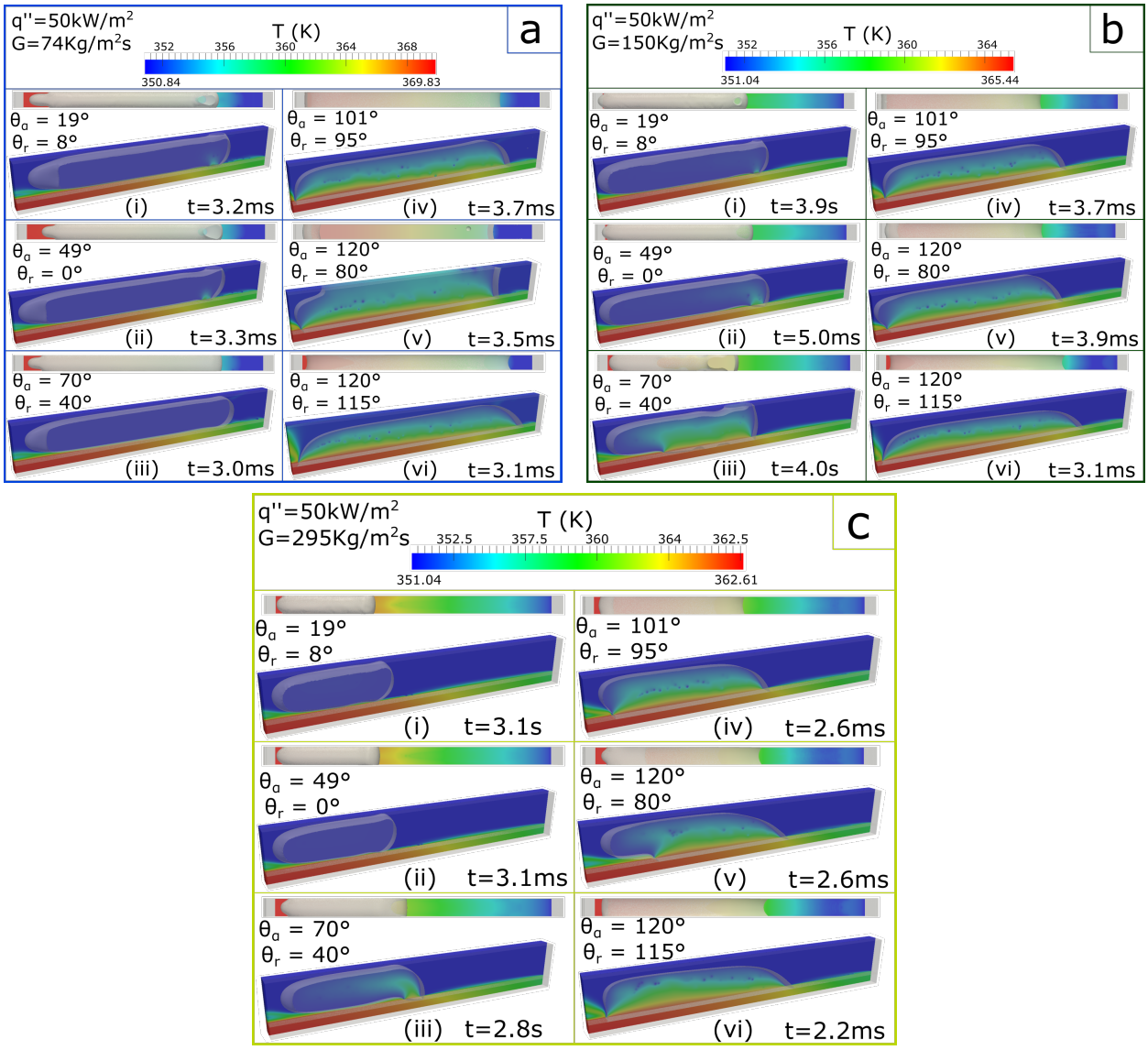

Figure 18: Macroscopic view of the numerical simulation results for $q'' = 50\,\mathrm{kW\,m^{-2}}$ at mass flux values 74, 150 and 295 $\mathrm{kg\,m^{-2}\,s^{-1}}$ from the top to the bottom box, respectively. In each box a 2D top view and a 3D isometric view for the last time period before the leading edge of the bubble touches the outlet of the microchannel for the six different wettability cases that are investigated, is shown.

part of the generated bubbles. For the high mass flux simulations ($G = 295\,\mathrm{kg\,m^{-2}\,s^{-1}}$), the hydrophilic cases with low receding contact angle have detached from the heated wall, while the trailing part of the hydrophilic case with high receding contact angle maintains contact with the heated surface.

From the overall flow visualisation results so far, the following conclusions can be drawn:

1. Slug flow boiling regime is observed in all cases, with the exception of the case with high heat flux and low mass flux, where a churn flow can be observed. In

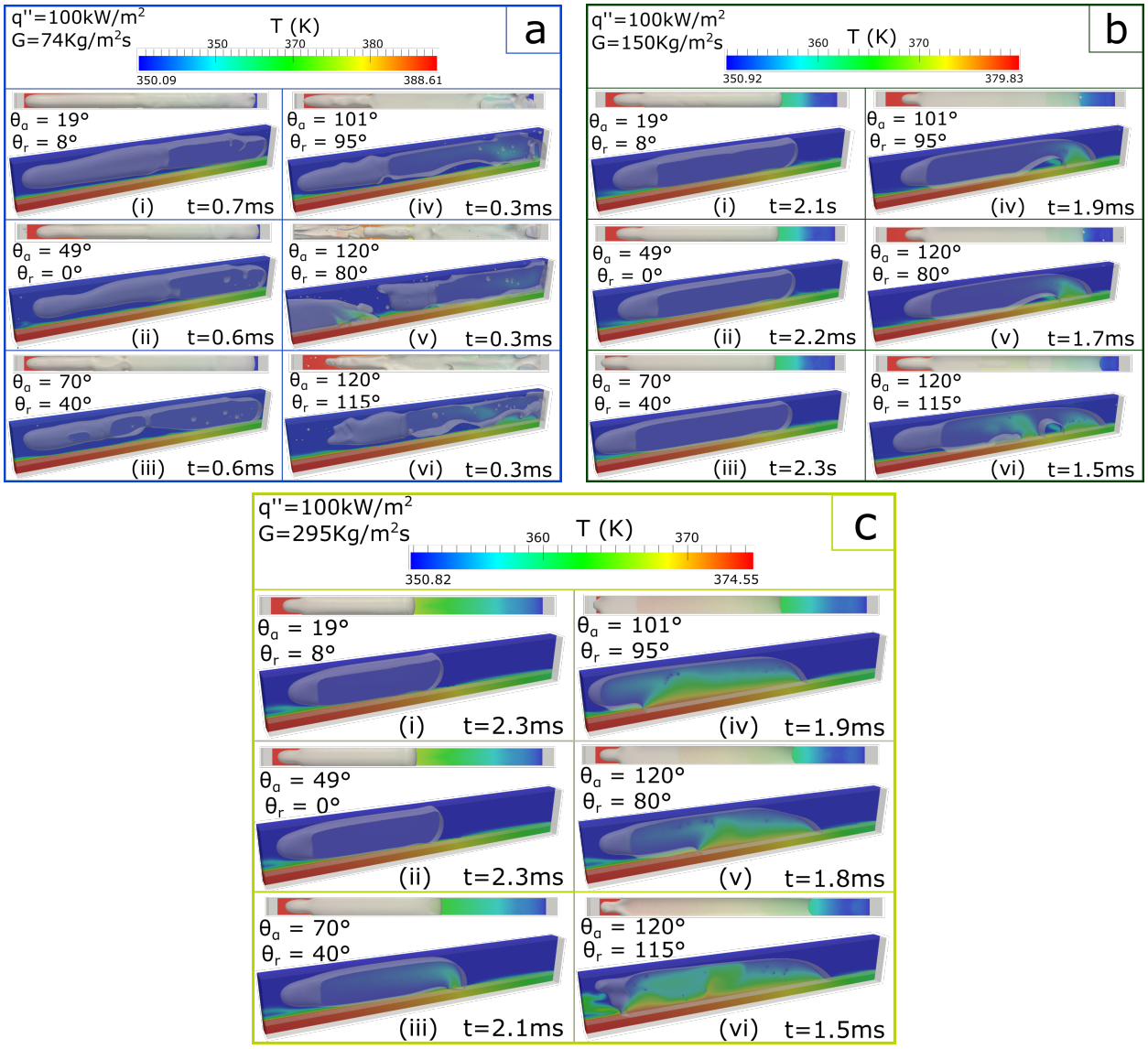

Figure 19: Macroscopic view of the numerical simulation results for $q'' = 100\,kW\,m^{-2}$ at mass flux values 74, 150 and 295 $kg\,m^{-2}\,s^{-1}$ from the top to the bottom box, respectively. In each box a 2D top view and a 3D isometric view for the last time period before the leading edge of the bubble touches the outlet of the microchannel for the six different wettability cases that are investigated, is shown.

both flow regimes, the bubbles grow within a few milliseconds and fill almost the entire cross-section of the microchannel.

2. Low heat flux or high mass flux (e.g. $q'' = 20\,kW\,m^{-2}$, $G = 295\,kg\,m^{-2}\,s^{-1}$) is associated with smaller bubble sizes (less vapour volume). Conversely, high heat flux or low mass flux (e.g. $q'' = 100\,kW\,m^{-2}$, $G = 74\,kg\,m^{-2}\,s^{-1}$) is associated with higher bubble sizes (higher vapour volume).

3. The contact line areas with the heated wall is relatively small for the hydrophilic

cases in comparison to the hydrophobic surfaces.

4. Apart from the heat and mass flux values, the wettability characteristics of the heated surface also determine the prevailing evaporation mechanism (liquid film versus contact line evaporation).

5. Liquid film evaporation is the main and sometimes the only heat transfer mechanism observed in hydrophilic surfaces, while in hydrophobic surfaces the dominant heat transfer mechanism is contact line evaporation.

6. For all three of the examined heat fluxes the maximum values of the wall superheat decrease with the increase of the mass flux for both hydrophilic and hydrophobic surfaces.

7. When the wall superheat becomes significantly large (for the examined cases there is a threshold of $>19\,^{\circ}\mathrm{C}$), for the hydrophilic cases, the radius of the curvature of the nose decreases, resulting in a sharper nose, and hence, a thicker liquid film.

8. The receding contact angle value plays a significant role in the trailing part of the generated bubbles. In many cases, this value prevents a complete detachment of the bubble from the heated wall for the hydrophilic surfaces (especially at high mass flux) and sometimes for hydrophobic surfaces as well (at high heat flux).

In order to better identify and quantify the effect of wettability on flow boiling performance, quantitative results for the simulations, described above, are presented and discussed in the following paragraphs. Figures 20, 21 and 22 report the dimensionless time-averaged local Nusselt numbers $\overline{Nu}(x)$, over the dimensionless length of the channel L^* , for all of the examined advancing and receding contact angle combinations together with the single-phase stage of the proposed numerical runs that is used as a reference, for each of the considered applied heat and mass fluxes, respectively. The percentage differences of the global Nusselt numbers (Nu_{glob}) for each advancing and receding contact angle combination with the corresponding Nu_{glob} of the single-phase stage of each numerical run, are summarised in Tables 6, 7 and 8, for applied heat flux values of $\mathrm{q}'' =$ 20, 50 and $100\,\mathrm{kW\,m^{-2}}$, respectively.

In order to evaluate the local Nusselt number, the local heat transfer coefficient $h_{(x)}$ needs to be calculated from expression 2.

The Nu number can be calculated from the following relationship:

$$Nu = \frac{h_{(\chi)} D_h}{\lambda_l} \tag{68}$$

where D_h is the hydraulic diameter of the channel and λ_l is the thermal conductivity of the liquid phase. The global averaged Nusselt number Nu_{glob} represents the area below the resulting in each case local time-averaged Nu ($\overline{Nu}(x)$), over dimensionless length L^* curve and is calculated as follows:

$$Nu_{glob} = \sum_{i=j}^{n} \frac{Nu_{j,n}}{L^*} \tag{69}$$

The Nu_{glob} has been calculated using a Matlab script. It is important to mention at this point that the single-phase stage of the numerical runs that is used as a reference for the local and/or global Nu numbers, might be much higher than the corresponding forced convection Nu numbers of a real single-phase liquid flow, due to the fact that in the numerical simulation the nucleation is not a result of the simulation but instead a bubble is patched artificially in a previously developed single-phase flow that has reached a steady state without any nucleate boiling initiation when the onset temperature is reached. Therefore, this "numerical" single-phase stage is used here as a reference in order to identify and quantify the enhancement in the heat transfer from each two-phase flow stage that corresponds to each combination of advancing and receding contact angles. A quantitative comparison of the $\overline{Nu}(x)$ versus L^*, for $q'' = 100\,kW\,m^{-2}$ is conducted in Fig. 20, for G = 74, 150, 295 $kg\,m^{-2}\,s^{-1}$. For low mass flux, hydrophobic surfaces (solid line) appear to have slightly higher $\overline{Nu}(x)$ values compared to the hydrophobic surfaces (dash-dotted line). However, for medium and high mass fluxes the $\overline{Nu}(x)$ values in hydrophilic surfaces gradually decrease while in the hydrophobic surfaces gradually increase with respect to the single-phase flow reference curve. The above observations are also reflected in Table 6, where the percentage difference of the Nu_{glob} between the single-phase reference and each two-phase flow result is depicted, for $q'' = 20\,kW\,m^{-2}$. It is evident that hydrophilic surfaces perform better at G = 74 $kg\,m^{-2}\,s^{-1}$. This might be due to the fact that for cases with low and medium hydrophilicity, both liquid film and contact line evaporation contribute to the overall heat transfer, while for the high hydrophilicity case heat transfer occurs only due to the contact line evaporation. For G = 150 $kg\,m^{-2}\,s^{-1}$, the differences between hydrophilic and hydrophobic cases can be considered as minor as the percentage difference with the single-phase flow reference is in all cases around 3%. Finally, hydrophilic surfaces and liquid film evaporation mechanism leads to inferior heat transfer performance, compared to the hydrophobic surface, at high mass flux G = 295 $kg\,m^{-2}\,s^{-1}$.

Table 6: Percentage difference between the global Nu number and the single-phase for $q'' = 20\,kW\,m^{-2}$.

θ_α (°)	θ_r (°)	G ($\frac{kg}{m^2 s}$)	Nu_{glob} (-)	%Diff.	G ($\frac{kg}{m^2 s}$)	Nu_{glob} (-)	%Diff.	G ($\frac{kg}{m^2 s}$)	Nu_{glob} (-)	%Diff.
Single phase			4.493	-		5.866	-		7.689	-
19	8		4.658	3.682		6.042	3.002		7.873	2.392
49	0	74	4.631	3.075	150	6.036	2.892	295	7.875	2.420
70	40		4.604	2.457		6.006	2.398		7.902	2.771
101	95		4.580	1.945		6.036	2.901		7.960	3.530
120	80		4.568	1.677		6.044	3.034		8.039	4.550
120	115		4.589	2.135		6.078	3.618		8.057	4.794

The time-averaged local Nu over the non-dimensional L^* (Nu_{glob}) of the considered hydrophilic and hydrophobic surfaces for the medium heat flux value $q'' = 50\,kW\,m^{-2}$ and all three investigated mass flux values is presented in Fig. 21. Similar behavior is observed for the simulations of $q'' = 50\,kW\,m^{-2}$. As it can be seen from Fig. 21

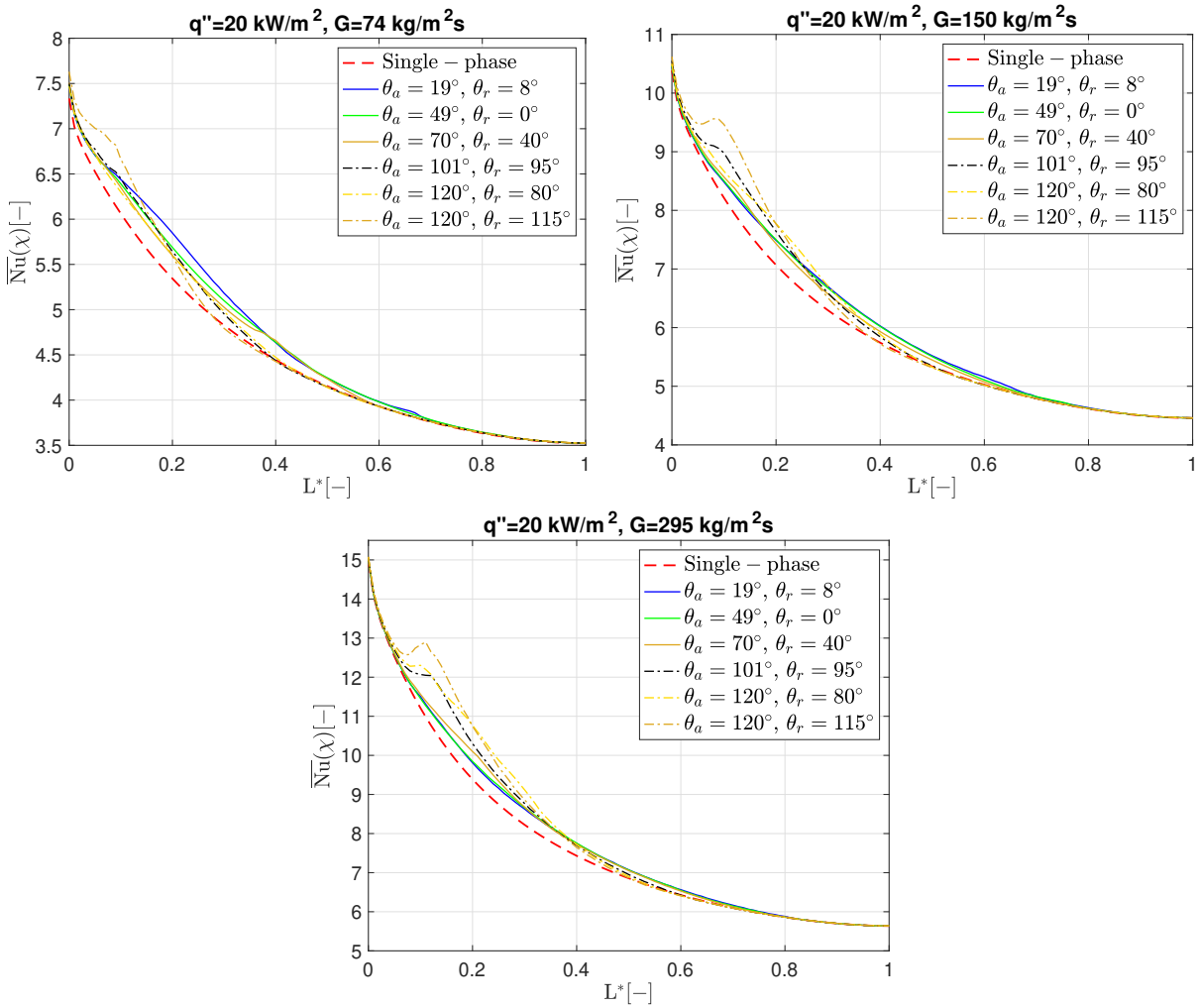

Figure 20: Time-averaged local Nu along the conjugate heat transfer interface versus dimensionless Length for q″ = 20 kW m^{-2} and G =74, 150 and 295 kg/m^2/s

and Table 7, for mass the fluxes of 74 and 150 kg m^{-2} s^{-1}, for the hydrophilic surfaces where the liquid film evaporation has been the dominant heat transfer mechanism (for low mass flux: θ_a/θ_r=19°/8°, θ_a/θ_r=49°/0°, θ_a/θ_r=70°/40°; and for medium mass flux: θ_a/θ_r=19°/8°, θ_a/θ_r=49°/0°), higher Nu_{glob} is observed. For mass flux 295 kg m^{-2} s^{-1}, hydrophobic surfaces with the underpinned contact line evaporation mainly contributing towards the overall heat transfer, perform slightly better than the hydrophilic cases. Among the three hydrophobic cases, the surface with the high CAH hysteresis shows the highest increase in the overall heat transfer in comparison to the single-phase flow reference. The reason for this is expected to be the comparatively higher radius of the curvature of the nose which in some cases has resulted in the presence of liquid film, and therefore, enhancement of heat transfer, due to a combination of liquid film and contact line evaporation.

Finally, the Nu_{glob} for the high heat flux value (q″ = 100 kW m^{-2}), for all of the investigated advancing and receding contact angle combinations as well as the percentage difference between the Nu_{glob} of the two-phase flows and with the corresponding

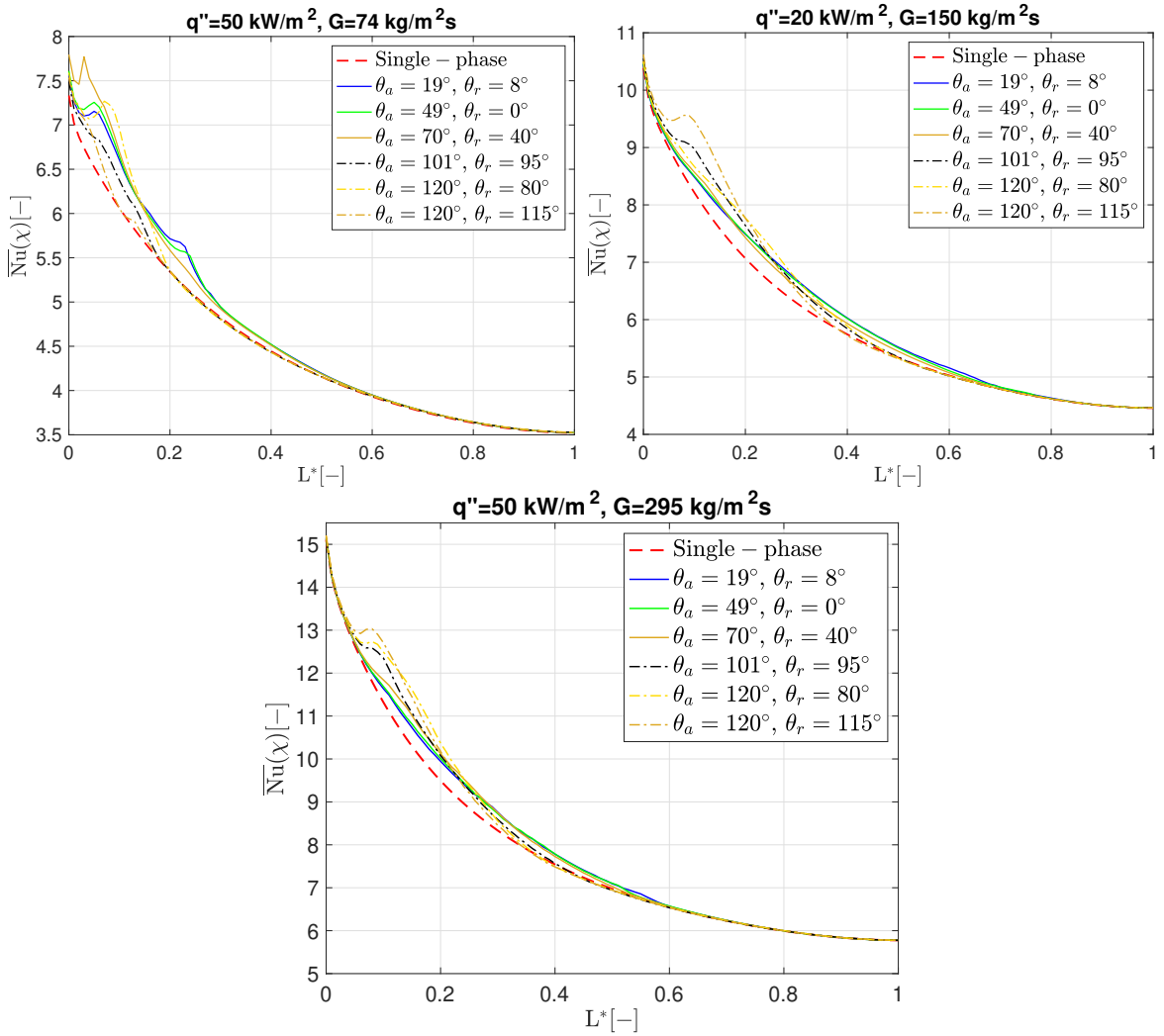

Figure 21: Time-averaged local Nu along the conjugate heat transfer interface versus dimensionless Length for $q'' = 50\,kW\,m^{-2}$ and G = 74, 150 and 295 $kg/m^2/s$

Table 7: Percentage difference between the global Nu number and the single-phase for $q'' = 50\,kW\,m^{-2}$.

θ_α (°)	θ_r (°)	G ($\frac{kg}{m^2 s}$)	Nu_{glob} (-)	%Diff.	G ($\frac{kg}{m^2 s}$)	Nu_{glob} (-)	%Diff.	G ($\frac{kg}{m^2 s}$)	Nu_{glob} (-)	%Diff.
Single phase			4.493	-		5.866	-		7.689	-
19	8	74	4.658	3.682	150	6.042	3.002	295	7.873	2.392
49	0		4.631	3.075		6.036	2.892		7.875	2.420
70	40		4.604	2.457		6.006	2.398		7.902	2.771
101	95		4.580	1.945		6.036	2.901		7.960	3.530
120	80		4.568	1.677		6.044	3.034		8.039	4.550
120	115		4.589	2.135		6.078	3.618		8.057	4.794

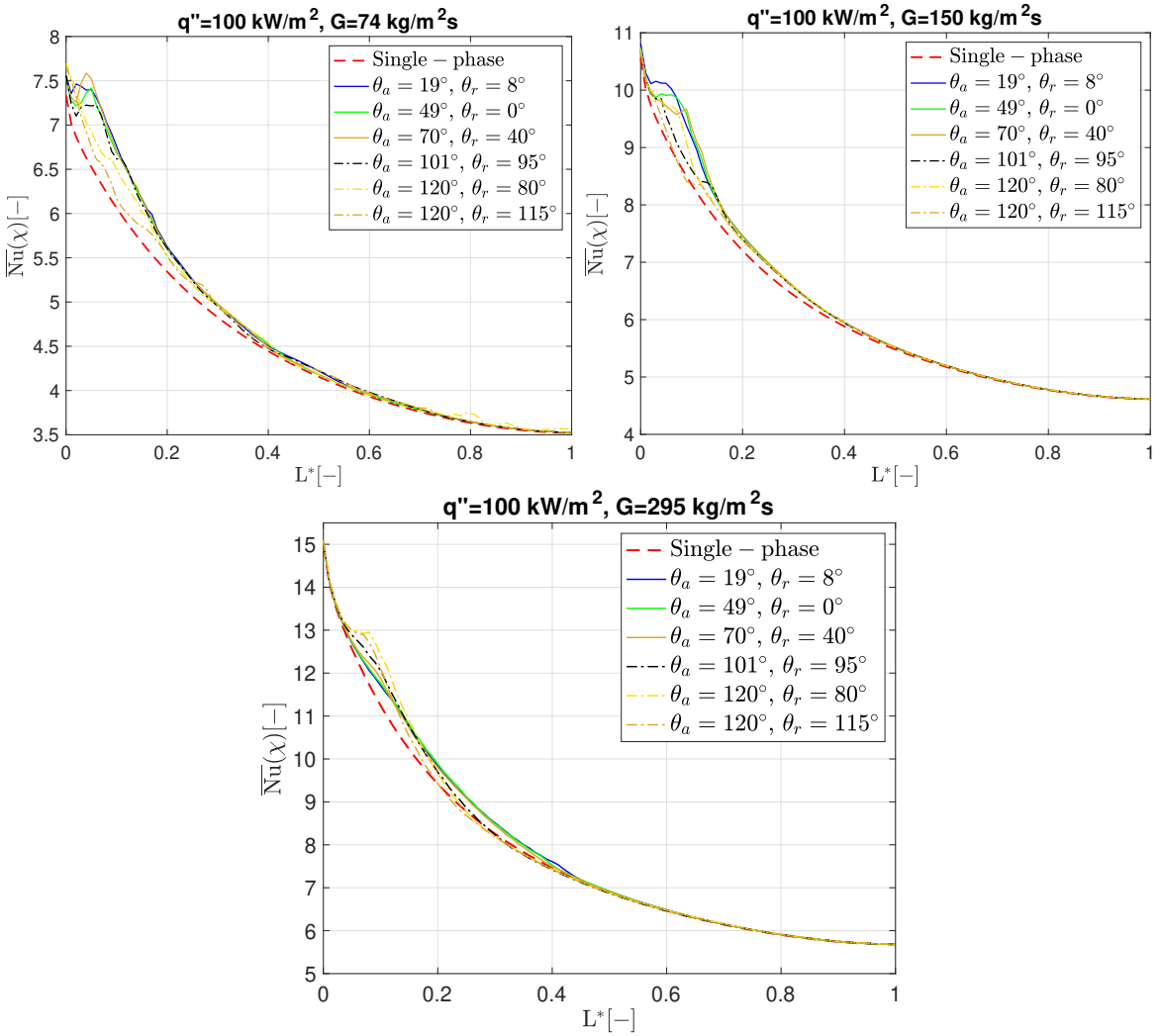

Figure 22: Time-averaged local Nu along the conjugate heat transfer interface versus dimensionless Length for $q'' = 100\,\mathrm{kW\,m^{-2}}$ and G = 74, 150 and 295 $\mathrm{kg/m^2/s}$

Table 8: Percentage difference between the global Nu number and the single-phase for $q'' = 100\,\mathrm{kW\,m^{-2}}$.

θ_α (°)	θ_r (°)	G ($\frac{kg}{m^2 s}$)	Nu_{glob} (-)	%Diff.	G ($\frac{kg}{m^2 s}$)	Nu_{glob} (-)	%Diff.	G ($\frac{kg}{m^2 s}$)	Nu_{glob} (-)	%Diff.
Single phase			4.493	-		5.866	-		7.689	-
19	8	74	4.659	3.683	150	6.173	2.684	295	7.858	1.700
49	0		4.643	3.333		6.169	2.610		7.861	1.742
70	40		4.655	3.613		6.166	2.559		7.848	1.582
101	95		4.635	3.158		6.110	1.625		7.820	1.211
120	80		4.615	2.711		6.127	1.924		7.852	1.628
120	115		4.581	1.955		6.077	1.093		7.798	0.925

single-phase flow references, are summarised in Figure 22 and Table 8, respectively. Overall, it can be seen that hydrophilic surfaces show slightly better performance for all mass fluxes compared to the hydrophobic. Additionally, it can be seen that the decrease of the mass flux results in a corresponding decrease in the percentage difference between the two-phase simulations and the corresponding single-phase flow reference. As mentioned earlier, churn flow was observed for the low mass flux simulations for all surfaces. It is important to note that by comparing Figs. 20, 21 and 22 we observe that for single-phase flow we do not have significant difference in heat transfer, however, this is not the case for two-phase flow. This may attributed to the fact that in two-phase flows when q″ is changing then the evaporation rates are also changing, as well as the two-phase flow patterns are changing and therefore different heat transfer rates are observed.

From all these quantitative comparisons and analyses of the numerical simulation predictions, the following conclusions can be made:

1. Overall, as expected for the same heat flux, the Nu_{glob} is increased linearly with the corresponding increase of the mass flux.

2. In all graphs at $L^* = 0$, the curve starts with the maximum local time-averaged Nu number in the inlet region of the considered microchannel. This can be attributed due to the sudden release of the patched bubble.

3. In many cases up to $L^* = 0.15$, a sudden increase of the time-averaged Nu is observed. This behavior is related to the nucleation of the bubble and the rapid bubble growth in this region.

4. For $q'' = 20\,\mathrm{kW\,m^{-2}}$ the Nu_{glob} curve of two-phase simulation cases and numerical single-phase diminish the difference and have almost same results after the $L^* = 0.7$. For higher mass fluxes the difference between the two-phase and single-phase is approximately at $L^* = 0.5$.

5. The time-averaged Nu varies with respect to the existent flow boiling regime and the corresponding heat transfer mechanism, which were found to be; a) film boiling evaporation and b) contact line evaporation.

6. For the same heat flux applied, the hydrophilic surfaces result in better heat transfer performance for low mass flux ($G = 74\,\mathrm{kg\,m^{-2}\,s^{-1}}$). Hydrophilic surfaces perform slightly better for the medium mass flux cases ($G = 150\,\mathrm{kg\,m^{-2}\,s^{-1}}$) as well, with the only exemption of the case with low heat flux ($q'' = 20\,\mathrm{kW\,m^{-2}}$), where the Nu_{glob} of hydrophobic cases is marginally higher, compared to the hydrophilic cases. For the highest mass flux value ($G = 295\,\mathrm{kg\,m^{-2}\,s^{-1}}$) and the lowest heat flux value ($q'' = 20\,\mathrm{kW\,m^{-2}}$), hydrophobic cases performed better. Conversely, for $G = 295\,\mathrm{kg\,m^{-2}\,s^{-1}}$, the cases which have as dominant heat transfer mechanism the contact line evaporation it is shown to perform slightly worse when the value of the heat flux increases (e.g. 50 and $100\,\mathrm{kW\,m^{-2}}$).

7. When it comes to the Nu_{glob} and percentage difference with respect to the reference single-phase stages of the simulations, the highest difference between the

hydrophilic and the hydrophobic surfaces is found to be between the two extreme contact angle cases (θ_a=19°, θ_r=8° versus θ_a=120°, θ_r=115°) for $q'' = 20\,kW\,m^{-2}$ and $G = 295\,kg\,m^{-2}\,s^{-1}$. Particularly, the hydrophobic surface had a percentage difference of 4.794% compared to 2.392% of the hydrophilic case (approx. 2.4% difference). The smaller percentage difference is found to be for $q'' = 50\,kW\,m^{-2}$ and $G = 295\,kg\,m^{-2}\,s^{-1}$ between θ_a=19°, θ_r=8° and θ_a=120°, θ_r=80°, with the hydrophilic case to have percentage difference of 2.011% and the hydrophobic surface 2.795% (approx. 0.8% difference).

Overall, it can be concluded that for the examined heat and mass flux ranges, the effect of wettability plays a significant role on the bubble growth dynamics that are directly linked to the developed flow regime causing a noticeable effect in the resulting heat transfer characteristics. However, considering a single nucleation site and a single nucleation event the effect of wettability on Nu_{glob} is evident but nor significant.

4.1.7 Effect of wettability on micro-passages – Single nucleation site, multiple recurring nucleation events

In a wide range of practical applications, considering a single nucleation site bubble nucleation constitutes a recurring event. Therefore, in order to create a more realistic case where the initiated nucleation event is recurring, an additional numerical study is performed using the same simulation set-up but with multiple recurring single nucleation events for the same overall flow time interval. In total two simulations are conducted, one for hydrophilic (θ_a=19°, θ_r=8°) and one for hydrophobic (θ_a=120°, θ_r=115°) surface. The applied heat and mass flux values are $50\,\mathrm{kW\,m^{-2}}$ and $295\,\mathrm{kg\,m^{-2}\,s^{-1}}$, respectively. These values are specifically selected because Nu_{glob} percentage difference between the hydrophilic and hydrophobic surfaces, as can be seen in Table 7, are minimal, showing in this way the effect of wettability on multiple recurring nucleation events for the worst-case scenario heat and mass flux values. In these simulations, after the initial patch of the bubble nucleus, a new bubble is patched at the same point after a certain time period. The time interval that each bubble is patched is chosen to be 1.2 ms. The first bubble is patched at 0ms, which corresponds to the time that the thermal boundary layer is fully developed (first single-phase stage of each simulation), up to 8.4 ms, where the last bubble seed is patched. The simulations were run up to 8.4 ms, completing seven nucleation cycles in total (one nucleation cycle = 1.2 ms). All the bubble seeds were patched at the same position (same as in the previous simulations shown, at 200 µm distance from the inlet of the microchannel). As it can be seen from Figure 23, the proposed time interval has been selected after plotting the surface temperature (for a single nucleation event, shown in the previous section) at the nucleation point over time and it is found that this is the common point between the two surfaces for the temperature to stabilise for the first time, after its initial drop due the contact line evaporation. As mentioned earlier, the proposed numerical model does not include any prediction of the onset temperature. Therefore, in the following simulations, it is considered that the temperature at the surface is enough for producing multiple recurring nucleation events of a single bubble with the given frequency.

Qualitative, flow visualisation results of the multiple recurring nucleation events are shown in Figure 24. In total, four different time periods using a 3D isometric view as well as a 2D top view of the investigated cases are depicted. The spatial and temporal evolution of the vapour bubble of the hydrophilic case is shown on the left side of the Fig. 27, while results for the same time period of the hydrophobic surface can be seen on the right side. In both cases, a similar flow regime that resembles a slug flow can be observed, however, the dominant heat transfer mechanism is different in each case. In more detail, for the hydrophilic case, the imposed bubble seed maintains a contact area with the heated wall, at the early stages of each nucleation cycle.

The average time needed for each bubble to completely detach from the heated wall is 1.5 ms, after its appearance in the microchannel. Subsequently, the bubble(s) detaches from the surface covering almost the entire cross-section of the channel, with the presence of a thin liquid film between the bubble and the channel walls. Some temporary dry patches with the side walls of the channel are evident at specific time periods. Therefore, in this case, the dominant heat transfer mechanism is liquid film evaporation while contact line evaporation contributes only at the initial stages of the

Table 9: Percentage difference between the global Nu number and the single-phase for $q'' = 50\,kW\,m^{-2}$ and $G = 295\,kg\,m^{-2}\,s^{-1}$ for a hydrophilic and a hydrophobic surface.

θ_a/θ_r	Bubble cycle	Bubble growth event duration (ms)	% Difference
19, 8	Single nucl. cycle	0-3.1	2.011
	1st nucleation cycle	0-1.2	0.745
	2nd nucleation cycle	0-2.4	1.947
	3rd nucleation cycle	0-3.6	3.584
	4th nucleation cycle	0-4.8	5.479
	5th nucleation cycle	0-6.0	7.239
	6th nucleation cycle	0-7.2	8.958
	7th Nucleation cycle	0-8.4	10.704
120, 115	Single nucl. event	0-2.2	2.526
	1st nucleation cycle	0-1.2	0.573
	2nd nucleation cycle	0-2.4	2.256
	3rd nucleation cycle	0-3.6	4.956
	4th nucleation cycle	0-4.8	7.673
	5th nucleation cycle	0-6.0	10.487
	6th nucleation cycle	0-7.2	13.370
	7th nucleation cycle	0-8.4	16.314

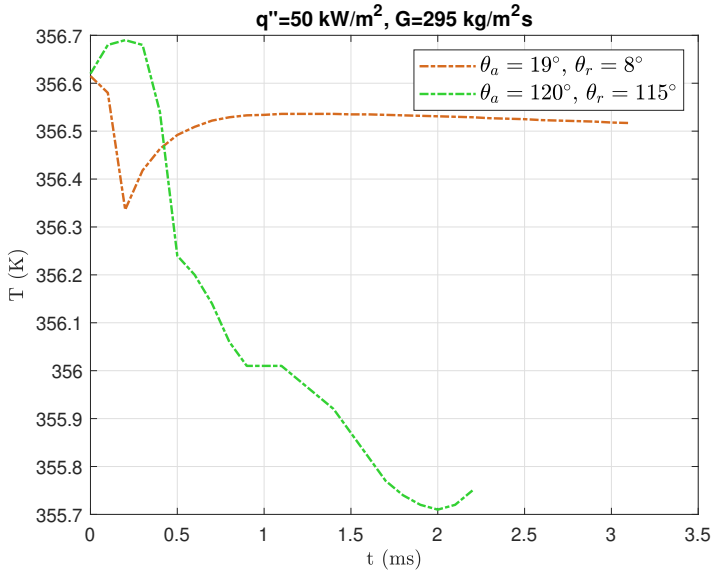

Figure 23: Temperature evolution of a hydrophobic and a hydrophilic case measured at the center of the initial position of the patched bubble (e.g. 200 µm from the entrance of the microchannel) over time.

bubble growth after nucleation. On the contrary, the dominant heat transfer mechanism for the hydrophobic surface is in fact the contact line evaporation, with the growing bubble(s) maintaining contact area with the heated wall throughout the entire transport process. Moreover, it is characteristic that in the hydrophilic case, the bubbles are in continuous contact with the side walls of the channel throughout the entire process. In both surfaces, someone can clearly see that the colour of the surface near the outlet of the channel has changed from red (for t = 1.2 ms) into orange for the hydrophilic surface and into green for the hydrophobic surface (for t = 8.4 ms), reducing significantly the superheat of the wall, compared to the single nucleation event simulations.

This is evident by seeing the quantitative results of the two simulations. In Figure 25 the Nu_{glob} of each recurring nucleation cycle is compared with the reference single-phase curve as well as with the simulation presented in the previous section with the bubble growth from a single nucleation event for the same heat flux, mass flux and wettability. In both sub-figures it can be seen that each cycle is increasing the Nu_{glob} gradually, enhancing significantly the overall heat transfer. The percentage differences between the Nu_{glob} of each nucleation recurring event and the single-phase simulation, can be seen in Table 9. Initially, it should be noted that the Nu_{glob} percentage difference of the hydrophilic surface (2.011%) was slightly lower than the hydrophobic surface (2.526%) for the single nucleation event simulations, and for every nucleation cycle, this difference is farther increased. In more detail, the percentage difference of the Nu_{glob} for the hydrophilic surface from 0 ms up to 8.4 ms is 10.704%, while for the hydrophobic surface it is 16.314%. This difference for such a small time frame and for the utilised mass flux, which was earlier shown that the wettability effect diminishes as the mass flux increases (for the $q'' = 50\,\mathrm{kW\,m^{-2}}$), can be considered as a significant enhancement of the heat transfer due to the different surface wettability.

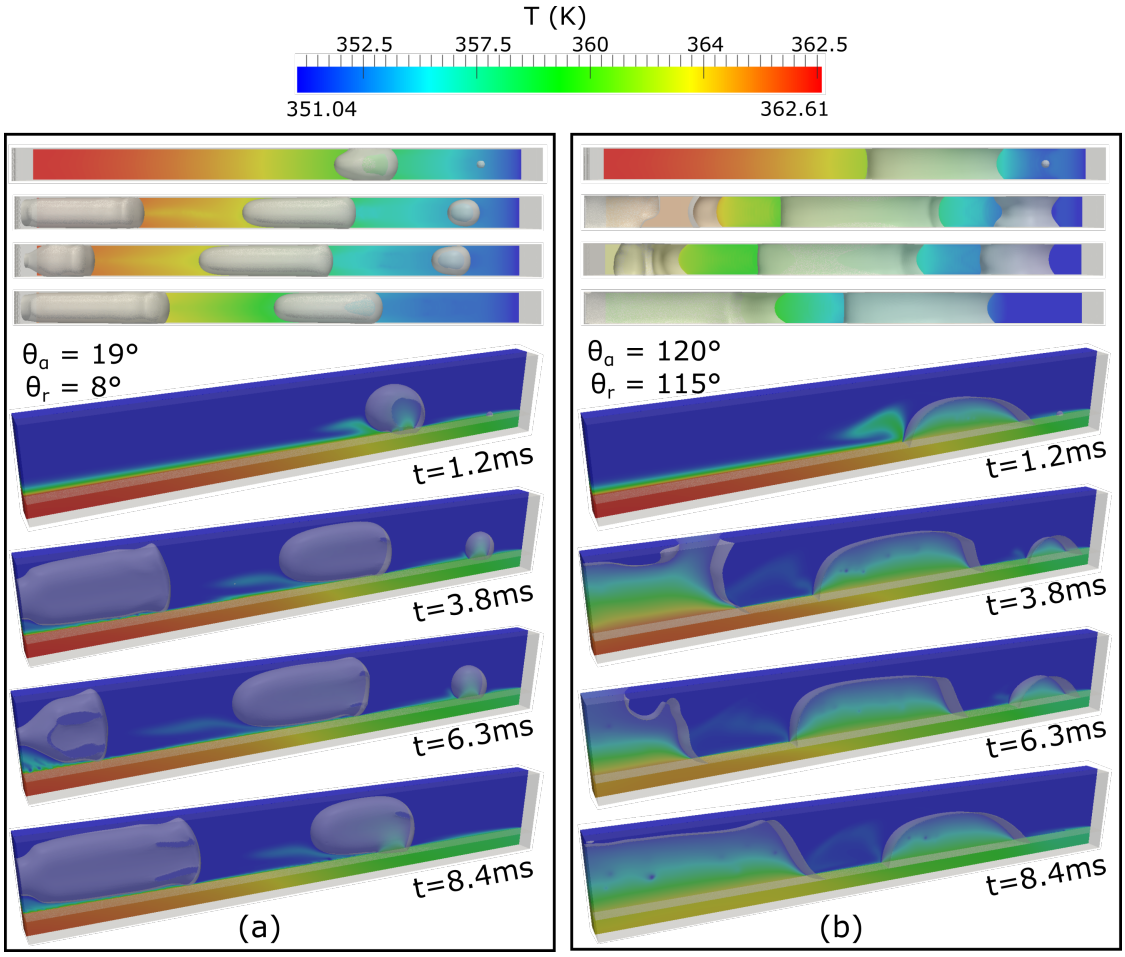

Figure 24: Simulation results of a single bubble growth and multiple nucleation events with time interval 1.2 ms. The heat and mass flux values are 50 kW m^{-2} and 295 kg m^{-2} s^{-1}. (a) Hydrophilic surface (θ_a/θ_r=19°/8°), (b) hydrophobic surface (θ_a/θ_r=120°/115°).

4.1.8 Effect of wettability on micro-passages – Multiple nucleation sites, multiple recurring nucleation events

In order to investigate an even more realistic case with respect to the previous investigations, numerical simulations of flow boiling in microchannels, with 29 recurring nucleation sites arbitrarily distributed on the heated wall, were also conducted. The simulations use the same parameters as the ones previously presented, where the heat and mass flux is 50 kW m^{-2} and 295 kg m^{-2} s^{-1}, respectively, and the bubble radius is 20 µm. The 29 nucleation sites are recurring every 1.2 ms, up to 8.4 ms (seven nucleation cycles in total). The position of the 29 nucleation sites remains the same for all recurring cycles. In Figure 26, the position of the 29 arbitrarily distributed bubble seeds is shown at 0 ms.

Figure 27 shows the evolution of the phenomenon through four successive time instants. Again, as in the previous figures, a 2D top view and a 3D isometric view of the phenomenon for the hydrophilic and the hydrophobic surface can be seen. Qualitatively,

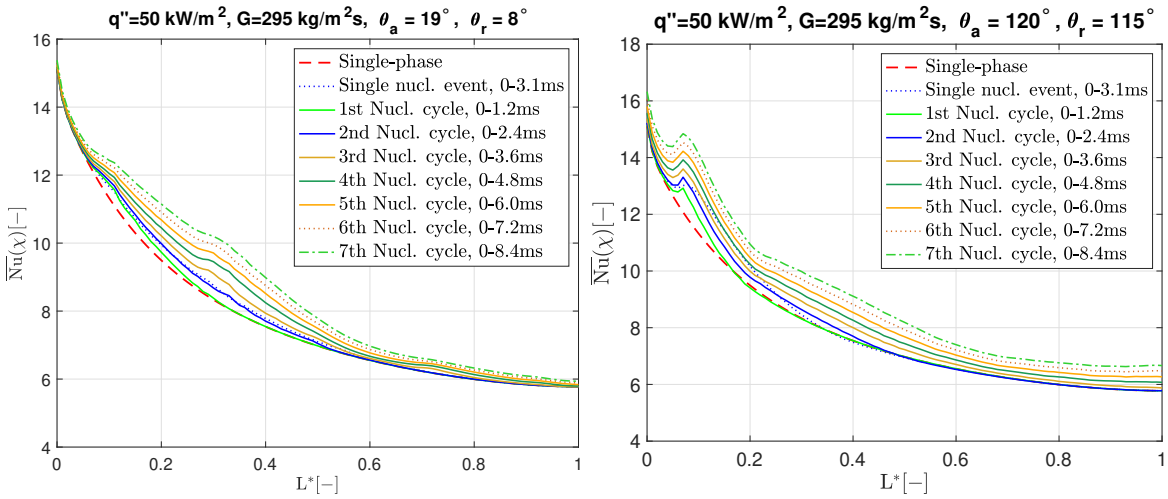

Figure 25: Results of a single nucleation site and multiple nucleation events for $q'' = 50\,\mathrm{kW\,m^{-2}}$ and $G = 295\,\mathrm{kg\,m^{-2}\,s^{-1}}$. Comparison of the seven nucleation cycles with time interval 1.2 ms with the single-phase reference simulation and the previous single nucleation event simulation. Left: Hydrophilic surface (θ_a/θ_r=19°/8°). Right: Hydrophobic surface (θ_a/θ_r=120°/115°).

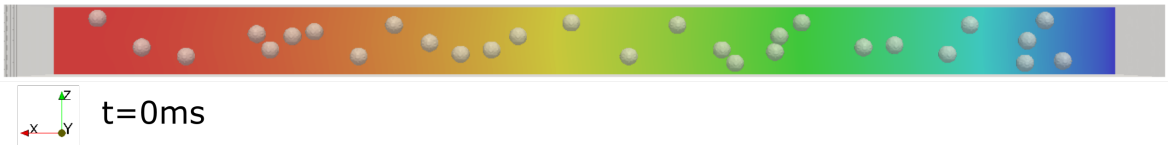

Figure 26: Top view of the position of the 29 arbitrarily distributed along the heated microchannel bubble seeds. In total, seven recurring nucleation events of 29 nucleation sites, at the same position, were conducted.

it is evident that the flow regime can be affected by the total number of nucleation sites. Particularly, for the hydrophilic case, the transition from churn to slug flow is observed. Churn flow can be seen at the beginning of each cycle and mostly at the second half of the length of the microchannel, where the wall superheat is higher. This phenomenon is more profound in the early stages of the simulation and diminishes as the wall superheat decreases. Liquid film evaporation is the dominant heat transfer mechanism in the hydrophilic surface case, with small contribution of contact line evaporation, mostly in the first half of the microchannel, until the full departure of the bubbles from the heated surface. Conversely, slug flow is only observed for the hydrophobic surface and contact line evaporation is the only heat transfer mechanism. By observing the colour of the heated wall at each time period for both surfaces, it is evident that the wall temperature of the hydrophilic surface due to the liquid film evaporation is considerably lower, resulting in a smaller wall superheat. Therefore, it seems that liquid film evaporation is a more effective mechanism from the overall heat transfer.

This can also be clearly seen from the time-averaged Nu number for each nucleation cycle over the non-dimensional length L^* for the hydrophilic and hydrophobic surfaces

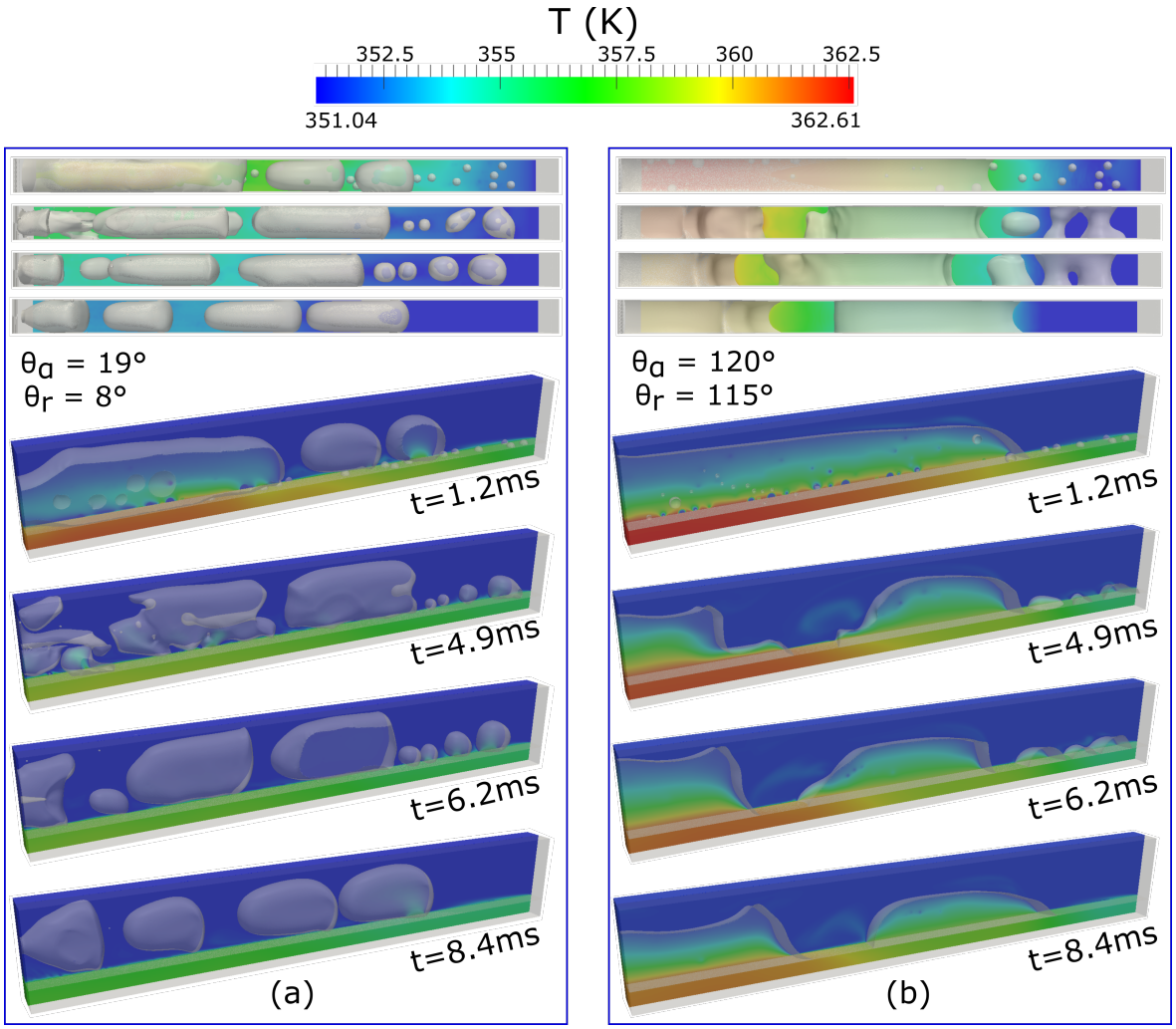

Figure 27: Top and 3D views of the numerical results for $q'' = 50\,\mathrm{kW\,m^{-2}}$ and $G = 295\,\mathrm{kg\,m^{-1}\,s^{-1}}$. (a) Single nucleation site and single nucleation event of bubble growth, for the last time period before the leading edge reaches the outlet of the channel, for a hydrophilic and hydrophobic surface. (b) Four different time periods for simulations of multiple nucleation sites (29 bubble seeds placed arbitrarily) and recurring nucleation cycles (1.2, 4.9, 6.2 and 8.4 ms).

shown in Figures 27a and 27b, respectively, as well as from Table 10, where the percentage difference between each nucleation cycle and the reference single-phase Nu_{glob} is shown.

As in the previous simulations of single nucleation bubble, the highest time-averaged Nu values are observed at the inlet of the channel. The hydrophobic surface performs better locally, particularly within the first 15% of the microchannel length. After that, a sharp decrease of the time-averaged Nu up to 30% of the microchannels' length is observed, with the reduction continuing at a more moderate rate, up to the end of the channel. Even though the maximum local time-averaged Nu in the first 15% of the microchannel is lower in the hydrophilic surfaces, for the remainder 85% the time-averaged Nu is significantly higher.

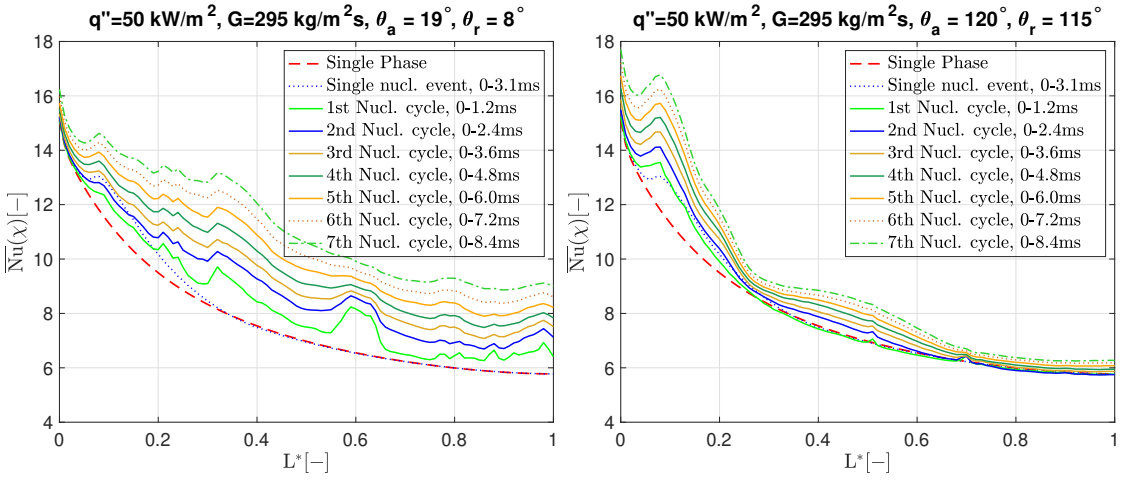

Figure 28: Results of 29 nucleation bubble sites and multiple nucleation events for $q'' = 50\,\mathrm{kW\,m^{-2}}$ and $G = 295\,\mathrm{kg\,m^{-2}\,s^{-1}}$. Comparison of the seven nucleation cycles with time interval 1.2 ms with the single-phase simulation and the single nucleation event simulation, up to the point where the nose of the bubble touches the outlet of the microchannel. Left: Hydrophilic surface ($\theta_a/\theta_r = 19°/8°$). Right: Hydrophobic surface ($\theta_a/\theta_r = 120°/115°$).

Quantitatively, in both cases, it can be seen that the multiple nucleation events and the numerous nucleation sites have significantly enhanced the heat transfer coefficient resulting in higher a Nu_{glob}. In the simulations of the single nucleation event and single nucleation site as well as in the case of a single nucleation site with multiple recurring nucleation events, it has been concluded that the hydrophobic surface performed slightly better compared to the equivalent hydrophilic case. However, in this set of simulations, the hydrophobic surface performs better locally (from $L^* = 0$ to 0.15), while the hydrophilic surface performs better overall, along the microchannel. The Nu_{glob} is increased in total by 43.9% compared to the single-phase. A very high Nu_{glob} enhancement of 17.8% compared to the single-phase can be seen also in the hydrophobic surface for all the nucleation cycles. The above results indicate the importance and the significance of the wettability on the global Nu number, and hence, on the time-averaged local Nu number.

Table 10: Percentage difference between the global Nu number and the single-phase for $q'' = 50\,kW\,m^{-2}$ and $G = 295\,kg\,m^{-2}\,s^{-1}$ for a hydrophilic and a hydrophobic surface.

θ_a/θ_r	Bubble cycle	Bubble growth event duration (ms)	% Difference
19, 8	Single nucl. cycle	0-3.1	2.011
	1st nucleation cycle	0-1.2	9.039
	2nd nucleation cycle	0-2.4	16.214
	3rd nucleation cycle	0-3.6	21.492
	4th nucleation cycle	0-4.8	26.762
	5th nucleation cycle	0-6.0	32.372
	6th nucleation cycle	0-7.2	38.156
	7th Nucleation cycle	0-8.4	43.896
120, 115	Single nucl. event	0-2.2	2.526
	1st nucleation cycle	0-1.2	1.916
	2nd nucleation cycle	0-2.4	4.758
	3rd nucleation cycle	0-3.6	7.507
	4th nucleation cycle	0-4.8	10.101
	5th nucleation cycle	0-6.0	12.718
	6th nucleation cycle	0-7.2	15.292
	7th nucleation cycle	0-8.4	17.854

4.1.9 Conclusions

CFD simulations have been performed for saturated flow boiling of Ethanol in a single rectangular channel having a hydraulic diameter of 0.2 mm and a channel length of 2.4mm in order to identify and quantify the effect of wettability characteristics on the resulting flow regimes as well as on the local and global heat transfer coefficients. The numerical experiments were conducted for six different surface wettabilities, with all the other parameters remaining the same. In total, three sets of simulations were performed:

A) Simulations considering a single nucleation site and a single nucleation event, for heat fluxes of 20, 50 and 100 $\mathrm{kW\,m^{-2}}$ and mass fluxes of 74, 150 and 295 $\mathrm{kg\,m^{-2}\,s^{-1}}$.

B) Simulations considering single nucleation sites and seven recurring nucleation events every 1.2 ms, for a heat flux 50 $\mathrm{kW\,m^{-2}}$ and a mass flux 295 $\mathrm{kg\,m^{-2}\,s^{-1}}$).

C) Multiple nucleation sites (29 bubble seeds arbitrarily distributed along the microchannel) and multiple (seven) nucleation recurring events every 1.2 ms, for a heat flux of 50 $\mathrm{kW\,m^{-2}}$ and a mass flux 295 $\mathrm{kg\,m^{-2}\,s^{-1}}$.

The following remarks summarize the conclusions of the present investigation:

A) Conclusions that are drawn from the simulations of a single nucleation site and a single nucleation event:

- Surface wettability plays a significant role in the flow regime and the associated dominant heat transfer mechanism, for all the above-described scenarios.
- The effect of surface wettability on Nu glob number for simulations with a single nucleation site and a single nucleation event is found to be minor.
- Liquid film evaporation is the dominant heat transfer mechanism for hydrophilic surfaces.
- On hydrophobic surfaces contact line evaporation is found to be the main heat transfer mechanism.
- By observing the local time-averaged Nusselt number over the non-dimensional length plot L^*, it can be seen that the hydrophobic surface performs better locally (e.g. from $L^* = 0$ to 0.15), while the hydrophilic surface performs better in overall along the microchannel.
- For a single nucleation event and a single nucleation site, hydrophilic surfaces performed better at low mass flux (74 $\mathrm{kg\,m^{-2}\,s^{-1}}$), for all three examined heat fluxes, but also for the cases of high heat flux (100 $\mathrm{kW\,m^{-2}}$). Hydrophobic surfaces performed better for the cases with heat flux 20 $\mathrm{kW\,m^{-2}}$ and mass flux 295 $\mathrm{kg\,m^{-2}\,s^{-1}}$, and slightly better for heat flux 20 $\mathrm{kW\,m^{-2}}$ and mass flux 150 $\mathrm{kg\,m^{-2}\,s^{-1}}$ as well as for 50 $\mathrm{kW\,m^{-2}}$ and 295 $\mathrm{kg\,m^{-2}\,s^{-1}}$. For the same set of simulations, when comparing the percentage difference between the global Nusselt number of the numerical single-phase and each of the examined contact angle simulations, the highest difference between the hydrophilic and the hydrophobic surfaces is found to be between the two extreme contact angle cases ($\theta_a = 19^\circ$, $\theta_r = 8^\circ$ versus $\theta_a = 120^\circ$, $\theta_r = 115^\circ$) for $\mathrm{q'' = 20\,kW\,m^{-2}}$ and $\mathrm{G = 295\,kg\,m^{-2}\,s^{-1}}$,

where the hydrophobic surface had percentage difference of 4.794% compared to 2.392% of the hydrophilic case (approx. 2.4% difference). The smaller percentage difference is found to be for $q'' = 50\,kW\,m^{-2}$ and $G = 295\,kg\,m^{-2}\,s^{-1}$ between $\theta_a = 19°$, $\theta_r = 8°$and $\theta_a = 120°$, $\theta_r = 840°$, with the hydrophilic case to have percentage difference of 2.011% and the hydrophobic surface 2.795% (approx. 0.8% difference).

- Among the hydrophilic surfaces, bubble departure from the heated surface is faster for the cases with low hydrophilicity (e.g. $\theta_a = 19°$, $\theta_r = 8°$ and $\theta_a = 49°$, $\theta_r = 40°$). For the case $\theta_a = 70°$, $\theta_r = 40°$ the high receding contact angle has led to either delayed bubble departure or no departure of the trailing part of the bubble, leading to two simultaneous heat transfer mechanisms (liquid film evaporation and contact line evaporation).

- By increasing the applied heat flux value and keeping the mass flux constant, a minor effect on the time-averaged Nu number is observed, however, when the mass flux is in- creased, the heat transfer coefficient is found to increase linearly.

- A slug flow regime is observed in all examined cases, except from the case with high heat flux and low mass flux ($100\,kW\,m^{-2}$ and $295\,kg\,m^{-2}\,s^{-1}$, respectively), where churn flow can be seen at the initial stages of the nucleation. In both flow regimes, the bubbles grow within few milliseconds and fill almost the entire cross-section of the microchannel.

B) Conclusions that are drawn from the simulations of a single nucleation site and multiple recurring nucleation events:

- The flow regime did not change, remaining slug flow for both surfaces.

- For the first two sets of simulations, where numerical experiments of a single nucleation site are conducted, contact line evaporation is found to be the most efficient cooling mechanism, resulting in a higher heat transfer rate.

- The global Nusselt number is seen to be increased significantly, by each nucleation cycle, achieving within 8.4 ms a 10.70% increase compared to the single-phase for the hydrophilic surface and 16.31% for the hydrophobic surface. Meaning that for the considered set of simulations as well as the heat and mass flux values, contact line evaporation, which is the dominant heat transfer mechanism for the hydrophobic surface, is more efficient.

C) Conclusions that are drawn from the simulations of multiple nucleation sites and multiple nucleation recurring events:

- For the last set of simulations, where 29 arbitrarily distributed bubble seeds are patched and are periodically recurred for seven nucleation cycles, it is found that surface wettability plays a significant role on global Nusselt number, and hence, on the heat transfer coefficient.

- Within 8.4 ms the global Nusselt number is increased by 43.9%, compared to the single-phase. The increase of the hydrophobic surface compared to the single-phase is 17.8%.

- For the hydrophobic case, a transition from churn flow to slug flow at the beginning of each nucleation cycle (e.g. within 0.2 ms) can be observed at the second half of the length of the microchannel, where the wall superheat is higher. For the hydrophobic surface, only slug flow is observed.

- Liquid film evaporation is the dominant heat transfer mechanism in the hydrophilic surface case, with small contribution of contact line evaporation, mostly in the first half of the microchannel until fully departure of the bubble from the heated surface occurs. On the other hand, contact line evaporation is the dominant heat transfer mechanism in the hydrophobic surface case.

- The wettability effects on this set of simulations are expected to be even more effective on cases with low and/or high heat and mass flux (e.g. $q'' = 20\,kW\,m^{-2}$ and $G = 295\,kg\,m^{-2}\,s^{-1}$), where the percentage difference for the first set of simulations was even higher, compared to heat and mass flux utilised in these cases.

- By the presence of multiple nucleation sites, liquid film evaporation has significantly enhanced the overall heat transfer coefficient, and for the proposed simulation parameters it can be considered a much more efficient heat transfer mechanism compared to contact line evaporation.

Summarising, in this study for the first time in the literature, the effect of surface wettability in the bubble dynamics and the associated heat transfer characteristics, for cases of flow boiling within microchannels, is isolated, identified and quantified, giving significant insight into the wettability dependent dominance of the various different heat transfer mechanisms (liquid film versus con- tact line evaporation) providing their quantified effect, on the local and global heat transfer characteristics

4.2 Effect of aspect ratio on flow boiling in microchannels

4.2.1 Scope

In flow boiling, the microchannel shape and cross-section dimensions are very important due to their relation with the liquid film thickness, two-phase flow pattern and heat transfer characteristics. As it has been stated by many researchers, the aspect ratio notably affects the flow boiling characteristics and has been reported as one of the still open fundamental research aspects and ambiguities. In detail, in the case of rectangular microchannels, the developed flow patterns, the heat transfer mechanisms and rates as well as the encountered pressure drops, can be affected by the aspect ratio of the channel cross-section, defined as the ratio of the channel width over the channel height ($\beta = W/H$). In this (sub)section, experimental and numerical works published related to the effects of the aspect ratio (AR) on flow boiling within microchannels are presented.

Markal et al. [180] studied the influence of aspect ratio on the saturated flow boiling characteristics, conducting experiments of parallel rectangular microchannels of deionized water, with constant hydraulic diameter of 100 µm for various ranges of mass (151-324 $\mathrm{kg\,m^{-2}\,s^{-1}}$) and heat (71–131 $\mathrm{kW\,m^{-2}}$) flux values. The examined aspect ratio defined as the depth to width ratio for the particular investigation, were 0.37, 0.82, 1.22, 2.71, 3.54 and 5.00. It is concluded that the heat transfer coefficient increases with an increase in the aspect ratio up to AR = 3.54, followed by a decrease for the highest aspect ratio case. AR = 1.22 appeared as a threshold value for the heat transfer coefficient. Additionally, it was reported that for all aspect ratio cases investigated, pressure drop increases with an increase in the heat flux due to the increased evaporation momentum force. It was observed that extended bubbles towards the inlet of the channel begin to apply more force and therefore flow resistance was increased. In a more recent work by Markal et al. [181], using the experimental data from their previous work [180], a new correlation including the aspect ratio effect was proposed to predict the heat transfer coefficient for saturated flow boiling in microchannels. The proposed correlation showed very good predictions with an overall Mean Absolute Error (MAE) of 16.9% and 86.4%, 96.2% and 99.5% of the predicted data falling within ±30, ±40 and ±50% error bands, respectively.

Soupremanien et al. [182] performed experiments of flow boiling in rectangular channels using Forane 365 HX as the working fluid. The experiments were conducted in two microchannels with AR_1=7 and AR_2= 2.3, while the hydraulic diameter was kept constant at 1.4 mm, for various heat flux values. It was reported that higher values of heat transfer coefficient could be seen in the case with larger aspect ratio and low heat flux but lower heat transfer coefficient at high heat fluxes, highlighting the importance of aspect ratio on flow boiling heat transfer.

In another study, Fu et al. [183] investigated the influence of various aspect ratio channels (0.83, 0.99, 1.65, 2.47, 4.23 and 6.06) with a constant hydraulic diameter 1.2 mm on flow boiling heat transfer using HFE-7100 as the working fluid. The results showed that the aspect ratio has a significant effect on the flow boiling heat transfer with the case of AR = 0.99 having the best heat transfer performance (both with respect to the CHF and the heat transfer coefficient). This was due to the existence of the liquid film around the channel corners of the square channel. The lower heat transfer coefficient reported in the channels with other aspect ratios was due to the possibility of partial dryout regions (non-wetted walls).

Singh et al. [184] focused on the impact of varying the aspect ratio of rectangular microchannels, on the overall pressure drop involving water boiling. Rectangular microchannels were fabricated with varying aspect ratios (β) but constant hydraulic diameter of 142 ± 2 µm and length of 20 mm. The invariant nature of the hydraulic diameter is confirmed through two independent means: physical measurements using a profilometer and by measuring the pressure drop in a single-phase fluid flow. These experimental results show that the pressure drop for two-phase flow in rectangular microchannels experiences minima at an aspect ratio of about 1.6. The minimum is possibly due to opposing trends of frictional and acceleration pressure drops, with respect to aspect ratio. In a certain heat flux and mass flux range, it was observed that the two-phase pressure drop was lower than the corresponding single-phase value. This

was also among the first studies to investigate the effect of aspect ratio in two-phase flow in microchannels.

In the work by Wang et al. [185], flow boiling heat transfer in high aspect ratio (β) micro-channels was experimentally investigated. Three high-aspect-ratio rectangular micro-channels were used, with the hydraulic diameters of which being 571 µm, 762 µm and 1454 µm. Mass fluxes of 11.2 $\mathrm{kg\,m^{-2}\,s^{-1}}$), 22.4 $\mathrm{kg\,m^{-2}\,s^{-1}}$) and 44.8 $\mathrm{kg\,m^{-2}\,s^{-1}}$) and a wide range of heat fluxes were applied. Visualisation results, thermography measurements and heat transfer characteristics of FC-72 and ethanol were obtained. Moreover, ten existing correlations for macro-, mini- and micro-channels were assessed. For ethanol, good predictions of three micro-channel correlations were achieved (MAE = 16.4–18.8%). However, all the correlations showed very high MAE for FC-72 (MAE = 80.7–641.3%). It was found that liquid properties and the unique high-aspect-ratio micro-channel geometry are crucial in developing a more accurate correlation. A modified correlation was therefore proposed for FC-72 and ethanol with an MAE of 23.6%. They concluded that the effects of channel aspect ratio and liquid properties need to be emphasised to develop more accurate correlations for flow boiling heat transfer in high-aspect-ratio micro-channels.

More recently, Al-Zaidi et al [186], investigated the effect of aspect ratio in flow boiling heat transfer within horizontal multi-microchannels using HFE-7100 as well. In total 3 different types of fabricated channels with aspect ratios of 0.5, 1.0 and 2.0 were studied. The results demonstrated that the heat transfer coefficient increases with heat flux, while there is an insignificant effect of mass flux. Additionally, the local heat transfer coefficient was found to increase with the increase of the aspect ratio. Furthermore it was concluded that bubble size in the higher aspect ratio case was smaller than that in the lower aspect ratio case. Furthermore, it was observed that the vapour slug length was longer for the smaller aspect ratio channels.

Candan et al. [187] conducted experiments of flow boiling of deionized water within a single minichannel with different aspect ratios (0.25, 0.50, 1.00, 2.00 and 4.00) with various heat (70–310 $\mathrm{kW\,m^{-2}}$) and mass (108-296 $\mathrm{kg\,m^{-2}\,s^{-1}}$) flux values, for studying their influence in heat transfer and pressure drop. It was reported that the AR has a significant effect on the local two-phase heat transfer coefficient, with the case of AR=1 demonstrating the best performance while the case of 0.25 showing the poorest one. The heat transfer coefficient was found to increase with the corresponding increase of the heat flux, mass flux, as well as with the local vapor quality. Regarding the pressure drop, the results showed a significant effect on the aspect ratio. Particularly, the lowest values of the pressure drop are obtained at the extreme values of the aspect ratio (0.25 and 4), with the total pressure drop increasing with the corresponding increase in the heat flux, mass flux and exit vapor quality. Finally, the obtained results were compared with similar experiments of microchannel heat sinks [180], showing that in minichannels the dominant heat transfer mechanism is nucleate boiling, and the flow patterns are quite different. Therefore, it was concluded that the underlying reason for the fundamental differences with the microchannel cases is the effect of confinement.

Lee and Mudawar [188, 189] examined experimentally the effects of micro-channel hydraulic diameter and aspect ratio ($1/\beta$ = H/W) on flow boiling heat transfer of HFE-7100 in four horizontal rectangular multi-microchannels made of oxygen-free

copper, with the hydraulic diameter ranging from 0.176 to 0.416 mm and aspect ratio (width to height) range of 0.25–0.41. They reported that the heat sink with a smaller hydraulic diameter exhibited better heat transfer performance compared to channels with large diameters. This was attributed to an increase in the wetted area and mass velocity for the small hydraulic diameter. Reviewing the work by Lee and Mudawar [188, 189] Ozdemir et al. [190] reported that the effect of diameter was studied while the channel aspect ratio was not fixed. Hence, the change in the wetted area could be due to a change in the aspect ratio rather than a change in diameter.

In their recent work, Ozdemir et al. [190] presented the experimental results of flow boiling of water in single rectangular microchannels. Three rectangular copper microchannels having the same hydraulic diameter (0.56 mm) and length (62 mm) but different aspect ratios (β = 0.5, 2.56, and 4.94) were investigated using de-ionized water as the working fluid. The experiments were conducted over the experimental range of mass flux 200–800 $\mathrm{kg\,m^{-2}\,s^{-1}}$), heat flux 4–1350 $\mathrm{kW\,m^{-2}}$) and inlet subcooling of $\sim$ 14 K. The results showed that the channel with smaller aspect ratio exhibited better heat transfer performance up to certain heat fluxes ($\sim$480–500 $\mathrm{kW\,m^{-2}}$), whilst the effect of channel aspect ratio became insignificant for higher heat fluxes. The flow boiling patterns were observed and the main flow regimes were bubbly, slug, churn, and annular flow. Flow reversal was also observed which caused a periodic flow in the two microchannels having smaller aspect ratio. A comparison of the experimental results with widely used macro and micro-scale heat transfer correlations is presented. The macro-scale correlations failed to predict the experimental data while some micro-scale correlations could predict the data reasonably well. Ozdemir et al. [190] reported, reviewing previous investigations, that the effect of aspect ratio is very complex. Markal et al. [180] concluded that the heat transfer coefficient increased with increasing heat flux in deep channels while it decreases with heat flux in shallow channels. On the contrary, Candan et al. [187] reported that the deep channels exhibited poor heat transfer performance due to the occurrence of dry-out, while Al-Zaidi et al. [186] reported that, for HFE-7100, the local heat transfer coefficient increases with increasing aspect ratio for all their tested conditions.

The effect of aspect ratio on flow boiling characteristics such as the heat transfer coefficient, pressure drop and flow patterns in copper multi-microchannel evaporators was experimentally studied by Al-Zaidi et al. [191]. The hydraulic diameter of each channel was 0.46 mm with ARs of 0.5, 1.0 and 2.0, while HFE-7100 was utilised as coolant. Constant heat flux with values ranging between 9.6 to 191.6 $\mathrm{kW\,m^{-2}}$ were applied while the mass flux was varied between 50 to 250 $\mathrm{kg\,m^{-2}\,s^{-1}}$. From the experimental visualisation flow patterns such as bubbly, slug, churn, and annular flow were observed. It was observed that when the AR increased the volume fraction decreased, possibly due to the confinement effect as well as the lower heat transfer from the side walls. Additionally, the nose of the vapour slugs become rounder when the AR was decreased. The heat transfer coefficient increased by about 14% when the channel AR was increased from 0.5 to 2, while the pressure drop decreased with the increase of the aspect ratio and increased when the heat flux was increased as well. The authors highlighted the fact that the AR can play a significant role on both the base heat flux and pressure drop and identified the AR as a parameter that needs to be taken into account when

designing such thermal management systems. However, the authors concluded that additional investigations with different ARs, operating conditions and working fluids need to be conducted in order to better understand the proposed effect.

Lee and Garimella [192] performed numerical simulations, based on the finite volume method, to predict steady, laminar heat transfer coefficients in hydrodynamically developed but thermally developing flow within rectangular microchannels of different aspect ratios ($1/\beta$ = H/W). Generalised correlations for both the local and average Nusselt numbers in the thermal entrance region were proposed. The proposed correlations allow accurate predictions of the thermal performance of microchannel heat sinks. The same authors investigated in another work experimentally flow boiling in arrays of parallel microchannels, using a silicon test piece with embedded discrete heat sources and integrated local temperature sensors [193]. The considered microchannels ranged in width from 102 µm to 997 µm, with the channel depth being nominally 400 µm in each case resulting in different aspect ratios ($1/\beta$ = H/W). Each test piece had a footprint of 1.27 cm by 1.27 cm with parallel microchannels diced into one surface. Twenty-five microsensors integrated into the microchannel heat sinks allowed for accurate local temperature measurements over the entire test piece. The experiments were conducted with deionized water which enters the channels in a purely liquid state. Results were presented in terms of temperatures and pressure drops as a function of imposed heat flux. The experimental results allowed a critical assessment of the applicability of existing models and correlations in predicting the heat transfer rates and pressure drops in microchannel arrays and led to the development of models for predicting the two-phase pressure drop and saturated boiling heat transfer coefficient.

In a more recent work [194], a numerical study, utilised ANSYS CFX 14.5, commercially available CFD code, has been carried out to investigate the heat transfer enhancement and fluid flow characteristics for various aspect ratios ($1/\beta$ = H/W) of single-phase rectangular micro channel heat sinks (MCHS). The channel size optimization has been carried out numerically to obtain effective heat removal from the MCHS. Average convective heat transfer coefficient, outlet temperature, friction and pressure drop, pumping power and thermal resistance (76) have been plotted against the Reynolds number. The Nusselt number has been plotted as a function of the Reynolds number for three heat sinks with different aspect ratios: 20, 30 and 46.66. From the numerical analysis, aspect ratio of 30 is the preferred choice and amount of the heat removal is at an optimum level. The proposed investigation also considers conjugate heat transfer, between solid and single-phase flow domains.

More recently Magnini and Matar [195] performed a systematic numerical analysis examining the effect of the channel shape on the bubble dynamics and heat transfer, under flow boiling conditions within microchannels, using their customised VOF method in OpenFOAM in order to capture the liquid-vapour interface dynamics. A benchmark flow model was utilised, where a single isolated Taylor bubble was seeded at the channel upstream and transported by a liquid flow across a diabatic section, which was heated by a constant and uniform heat flux. Flow conditions that apply well to the flow boiling of water or refrigerant fluids in sub-millimetre channels at low heat flux (10 kW m^{-2}) were investigated, with cross-section aspect ratios (β = W/H) ranging from 1 to 8, while the hydraulic diameter of the channel was fixed. It was shown that the heat

transfer performances for different channel shapes are closely related to the perimetral distribution of the liquid film surrounding the elongated vapour slugs that are generated due to liquid film evaporation. It was also illustrated that square channels ($\beta = 1$) exhibit the highest heat transfer coefficients at low flow rates, due to a very thin liquid film that forms at the centre of the wall, however, they are more at a risk of film dryout. High aspect ratio rectangular channels may be beneficial at larger flow rates, as they promote the formation of an extended liquid film that covers up to 80% of the cross-section perimeter. Finally, at larger aspect-ratios, the average heat transfer coefficient along the shorter wall becomes orders of magnitude smaller than the value detected along the longer wall, owing to a strong asymmetry in the liquid film perimetral distribution. The proposed work constitutes a two-phase flow investigation related to flow boiling within microchannels, however, it does not account for conjugate heat transfer between solid and two-phase flow domains.

As can be seen from the above review, despite its potential and its significant effect, there are only a few studies in the literature that examine the influence of aspect ratio in two-phase flows within microchannels, with the majority of them being experimental. Additionally, most of these studies investigate the effect of the aspect ratio on an already quasi-steady state two-phase flow conditions, whereas the first transient stages of the two-phase flow development from bubble nucleation up to two-phase flow development, still remain unexplored. Therefore, fundamental analysis of the role of the channel aspect ratio focusing both on the bubble dynamics and heat transfer characteristics at the early transient stages of the bubble growth within confined micro-passages, under saturated flow boiling conditions, is conducted and presented in the following paragraphs. This study has been recently published by Andredaki et al. [99, 196].

4.2.2 Numerical simulations set-up and process

For the performance of the numerical simulations, the same boundary conditions as described in section 4.1.3 are used. Furthermore, the working coolant remains ethanol and the microchannel is considered as stainless steel. Both properties can be found in Table 3 and Table 4. The advancing and receding contact angle values are 19° and 8°, respectively. Three different aspect ratios are considered ($\beta = 0.5$, 1.0, 2.5), and for all three different aspect ratios, a fixed channel hydraulic diameter of $D_h = 200\,\mu m$ was used. Three different values of applied heat flux ($q'' = 20$, 50, $100\,kW\,m^{-2}$) and mass flux (G = 73.7, 149.6, $249.7\,kW\,m^{-2}\,s^{-1}$ for $\beta = 0.5$, G = 98.2, 199.5, $392.9\,kW\,m^{-2}\,s^{-1}$ for β =1.0 and G = 171.7, 349.1, $687.6\,kW\,m^{-2}\,s^{-1}$ for $\beta = 2.5$) are also considered. Since the hydraulic diameter of the channels with the different aspect ratios as well as the applied heat fluxes in each sub-series of runs remain constant, while both the height and the width of the channels vary to achieve the different aspect ratios, the total power dissipated in each case is slightly different. Therefore, the low, medium and high mass fluxes, applied for each channel aspect ratio, were varied accordingly in order to maintain the same total power to mass flux ratios, i.e., maintaining a constant enthalpy.

In order to obtain a fully developed thermal and hydrodynamic boundary layer, single-phase simulations for each case were conducted for a few hundreds of ms (following the same strategy as described in 4.1.3). In total two series of simulations were performed

Table 11: Considered channel aspect ratios and corresponding dimensions of the solid and fluid domain.

	Solid domain				Fluid domain			
β	L_s (mm)	H_s (mm)	W_s (mm)	total number of cells	L_f (mm)	H_f (mm)	W_f (mm)	total number of cells
0.5	2.4	0.09	0.15	4.05M	2.4	0.30	0.25	13.50M
1.0	2.4	0.09	0.20	5.40M	2.4	0.20	0.20	12.00M
2.5	2.4	0.09	0.35	9.45M	2.4	0.14	0.35	14.70M

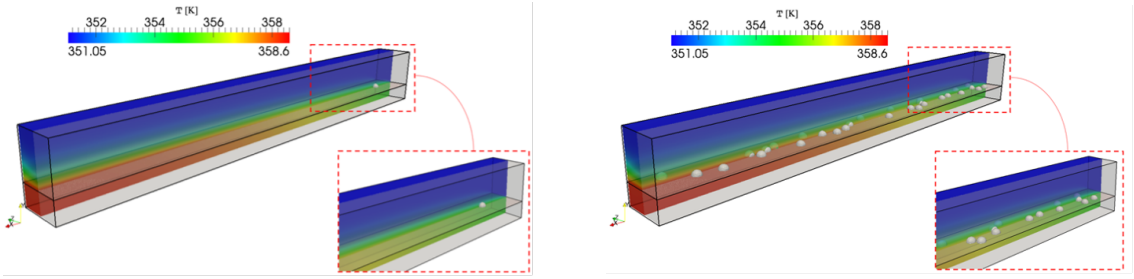

(a) **(b)**

Figure 29: Initial condition for the second (two-phase) stage of numerical simulations for Series 1 (a) and Series 2 (b) numerical simulations. In both cases the initial condition that is illustrated indicatively here, corresponds to a channel aspect ratio of β =1.0, an applied heat flux of q″=20 kW m^{-2} and a mass flux of G = 98.2 kg m^{-2} s^{-1}.

in this study. Initially, simulations of a single nucleation site (single bubble) with a radius of 20 µm placed in a distance of 200 µm from the inlet of the channel, are performed. After that, a second series, where 30 arbitrarily distributed bubble seeds, with a radius of 20 µm are placed simultaneously on the conjugate boundary, were conducted. In order to examine the early stages of bubble growth dynamics and heat transfer characteristics, only the first 10 ms from the bubble nucleation event are considered in each case. The computational domain for one of the cases (β = 0.5) is shown in Figure 9. The dimensions of each utilised microchannel are shown in Table 11. Figure 29 illustrates the position of the bubble(s) of the first (a) and second series (b) of simulations.

For the first series of numerical simulations, in order to observe the effects of channel aspect ratio at different heat fluxes, the overall analysis for all of the three considered channel aspect ratio values, was performed for three different values of applied heat flux, q″=20, 50 and 100 kW m^{-2} and three different liquid velocities at the inlet (indicated as low, medium and high). For the second series of numerical simulations, only the lowest heat flux and mass flux for each channel aspect ratio are considered. The overall details regarding the different channel aspect ratio cases considered for each of the main two series of numerical simulations are summarised in Table 12 and Table 13, respectively.

Table 12: Considered channel aspect ratios and corresponding mass flow rates for Series 1 of numerical simulations (these cases are considered for q″ = 20, 50 and 100 kW m^{-2}).

Series 1		W (mm)	H (mm)	D_h mm	β (-)	G (kg m^{-2} s^{-1})	U (m s^{-1})
I	a	0.15	0.3	0.2	0.5	73.7	0.1
	b					149.6	0.2
	c					294.7	0.4
II	a	0.2	0.2	0.2	1	98.2	0.13
	b					199.5	0.27
	c					392.9	0.53
III	a	0.35	0.14	0.2	2.5	171.9	0.23
	b					349.1	0.47
	c					687.6	0.93

Table 13: Considered channel aspect ratios and corresponding mass flow rates for Series 2 of numerical simulations (these cases are considered only for 20 kW m^{-2}).

Series 2	W (mm)	H (mm)	D_h (mm)	β (-)	G (kg m^{-2} s^{-1})	U (m s^{-1})
I	0.15	0.3	0.2	0.5	73.7	0.1
II	0.2	0.2	0.2	1	98.2	0.13
III	0.35	0.14	0.2	2.5	171.9	0.23

Finally, it should be mentioned that more than 1,700,000 core-hours were utilised for the final runs of both series of numerical simulations.

4.2.3 Single bubble seed numerical simulations

The spatial and temporal evolution of the generated vapour bubbles for Cases Ib, IIb and IIIb, of Table 12, for an applied heat flux value of q″ = 20 kW m^{-2} , is depicted, indicatively, in Figure 30. The grey semi-transparent surface represents the liquid/vapour interface, while the coloured contours in a clip section that extends from one side of the channel up to its middle plane, reveal the instantaneous temperature fields in both the fluid and solid regions of the computational domain. The equivalent bubble diameter, calculated as a sphere with the same volume, is indicated for each time instance.

It is evident that the variation of the channel aspect ratio has a quite significant effect on the resulting bubble growth dynamics. For $\beta = 0.5$, the bubble grows into a Taylor bubble maintaining minimal contact with the channel walls, with a liquid film formed between the bubble and the channel walls, apart from some small dry patches at the side walls. For $\beta = 2.5$, the bubble grows into an elongated vapour slug that maintains contact with the top and bottom walls of the channel, throughout most of its length. However, no dry patches at the side walls are observed in this case. Therefore, for $\beta = 0.5$, the bubble grows mainly due to liquid film evaporation, while for $\beta = 2.5$ the bubble grows due to vapour/liquid/solid contact line evaporation. In the case of $\beta = 1.0$, the generated bubble grows into an elongated vapour slug that maintains

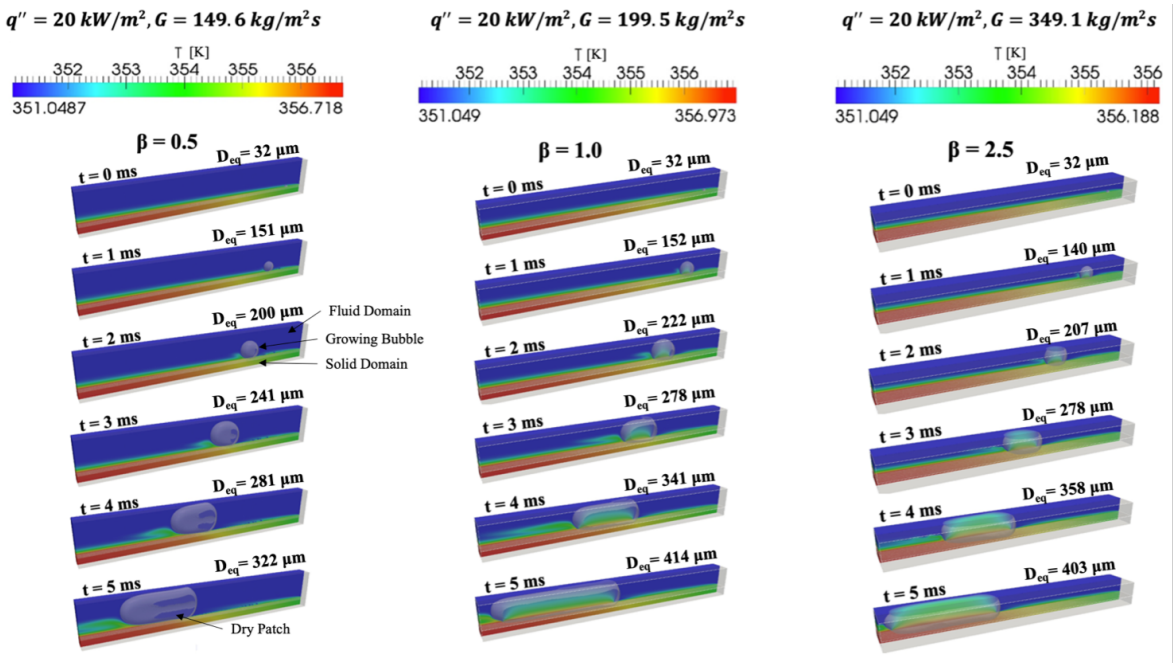

Figure 30: The spatial and temporal evolution of the generated vapour bubble ($q'' = 20\,kW\,m^{-2}$ and G = 149.6, 199.5 and 349.1 $kg\,m^{-2}\,s^{-1}$ for $\beta = 0.5$, 1.0 and 2.5, respectively).

continuous contact with the bottom heated boundary almost for its entire length, while some minimal contact with the top boundary is evident after t = 3 ms without however, this contact extending for the entire length as in the case of the bottom boundary of the fluid domain. Dry patches with the side walls of the microchannel are also evident that extend almost for the entire length of the bubble, after t = 3 ms. Therefore, also in this case, since there is no liquid film formed in the vicinity of the bottom heated wall, the dominant heat transfer mechanism is only the contact line evaporation. As expected, in all three cases, due to the associated latent heat of evaporation, as the bubble grows and moves towards the outlet, the temperature of the heated solid domain is decreasing since the solid domain cools down.

In Figures 31 and 32, the corresponding temporal and spatial bubble evolution is also shown, once more for the medium velocity (i.e., mass flux) cases, Cases Ib, IIb and IIIb, of Table 12, for applied heat flux values of $50\,kW\,m^{-2}$ and $100\,kW\,m^{-2}$, respectively.

It is evident that the previous observations still hold for the $\beta = 0.5$ cases, as the applied heat flux subsequently increases. Also, for the higher applied heat fluxes, the bubble grows into a Taylor bubble maintaining minimal contact with the channel walls, with a liquid film formed between the bubble and the channel walls, apart from some small dry patches at the side walls. It is, however, obvious that with the subsequent increase in the heat flux, the generated bubble reaches at a similar volume at much earlier flow times, which indicates a subsequent increase in the evaporation rates (t=5.0 ms for $q'' = 20\,kW\,m^{-2}$, t = 2.0 ms for $q'' = 50\,kW\,m^{-2}$ and t=0.9 ms for $q'' = 100\,kW\,m^{-2}$). For the cases of $\beta = 1.0$ and $\beta = 2.5$ and for $q'' = 100\,kW\,m^{-2}$, it is observed that the increase in the applied heat flux from $q'' = 20\,kW\,m^{-2}$ to $q'' = 50\,kW\,m^{-2}$ leads

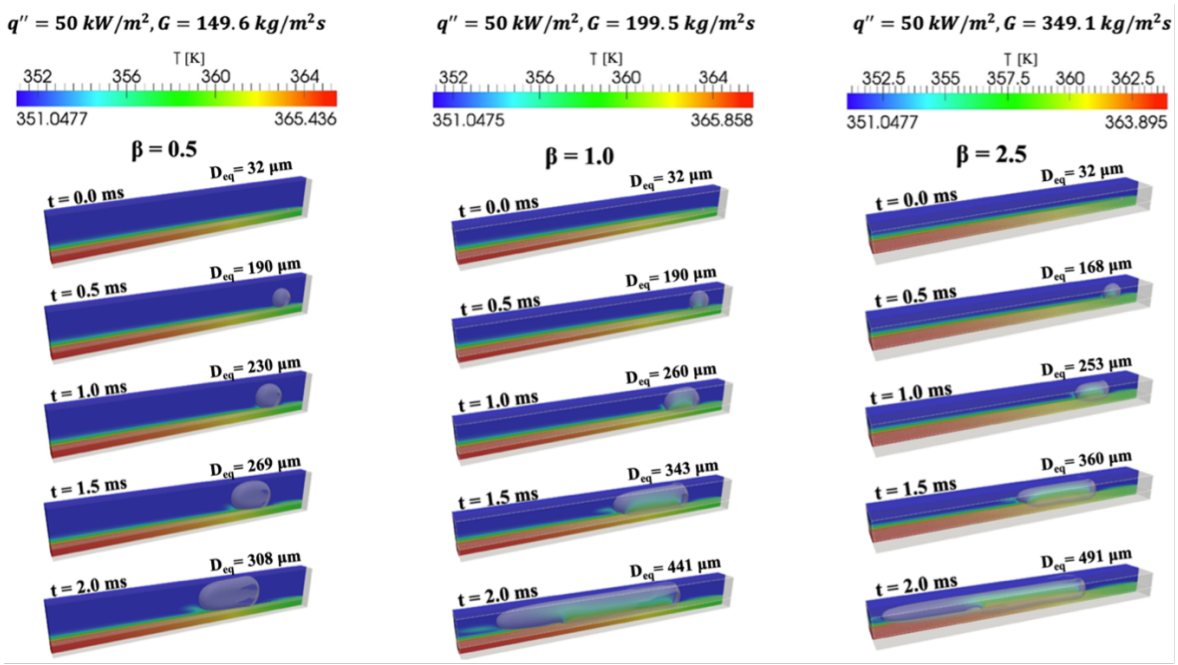

Figure 31: The spatial and temporal evolution of the generated vapour bubble ($q'' = 50\,kW\,m^{-2}$ and G = 149.6, 199.5 and $349.1\,kg\,m^{-2}\,s^{-1}$ for β = 0.5, 1.0 and 2.5, respectively).

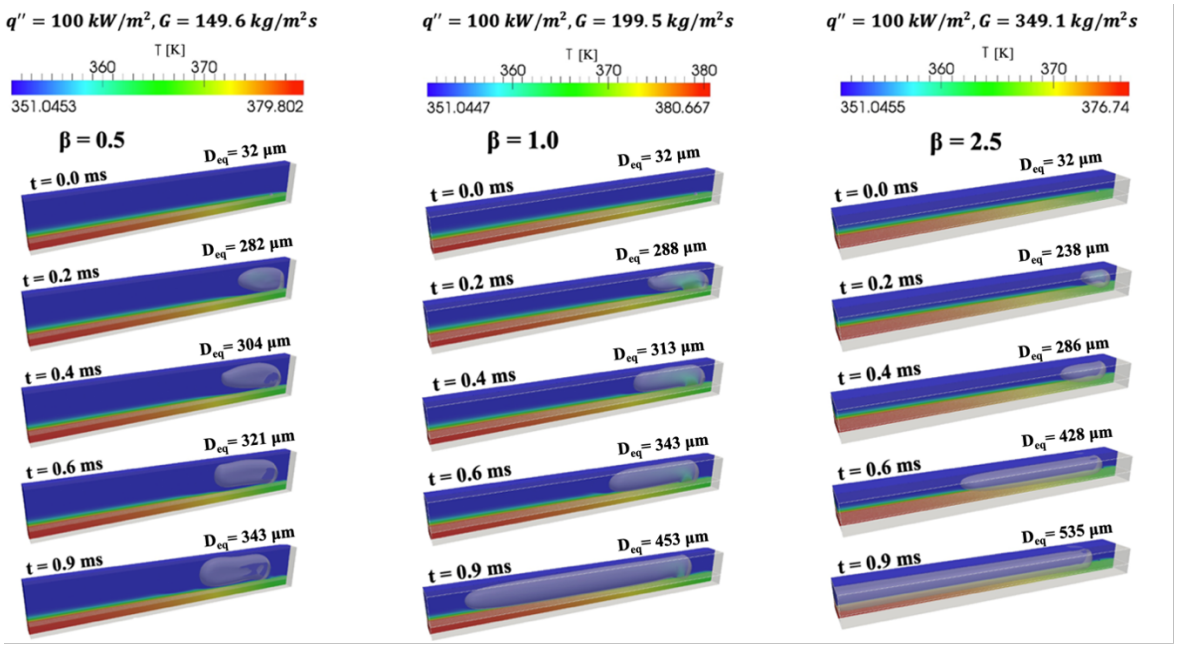

Figure 32: The spatial and temporal evolution of the generated vapour bubble ($q'' = 100\,kW\,m^{-2}$, G = 149.6, 199.5 and $349.1\,kg\,m^{-2}\,s^{-1}$ for β = 0.5, 1.0 and 2.5, respectively).

to the development of a liquid film at the later stages of the bubble development that extends from the leading edge of the elongated bubble up to a quite significant

portion upstream (t = 2.0 ms, β = 1.0, 2.5). This development of the liquid film for β = 1.0 and β = 2.5 is further enhanced with the further increase of the applied heat flux to $q'' = 100\,kW\,m^{-2}$. As it can be seen, the liquid film development for $q'' = 100\,kW\,m^{-2}$ starts much earlier (t = 0.2 ms) for both β = 1.0 and β = 2.5 than in the corresponding cases of $q'' = 50\,kW\,m^{-2}$ (t = 1.5 ms). Summarising, it is evident that also for higher values of applied heat flux, the variation of the channel aspect ratio has a quite significant effect on the resulting bubble growth dynamics. It is also evident that as the applied heat flux increases, the liquid film evaporation starts to become progressively more dominant for higher aspect ratio channels. The effect of the variation of the applied liquid mass flux at the channel inlet on the generated vapour slug dynamics is indicatively shown for the lowest of the considered applied heat fluxes ($q'' = 20\,kW\,m^{-2}$) and for all three considered aspect ratios, in Figures 33, 34 and 35.

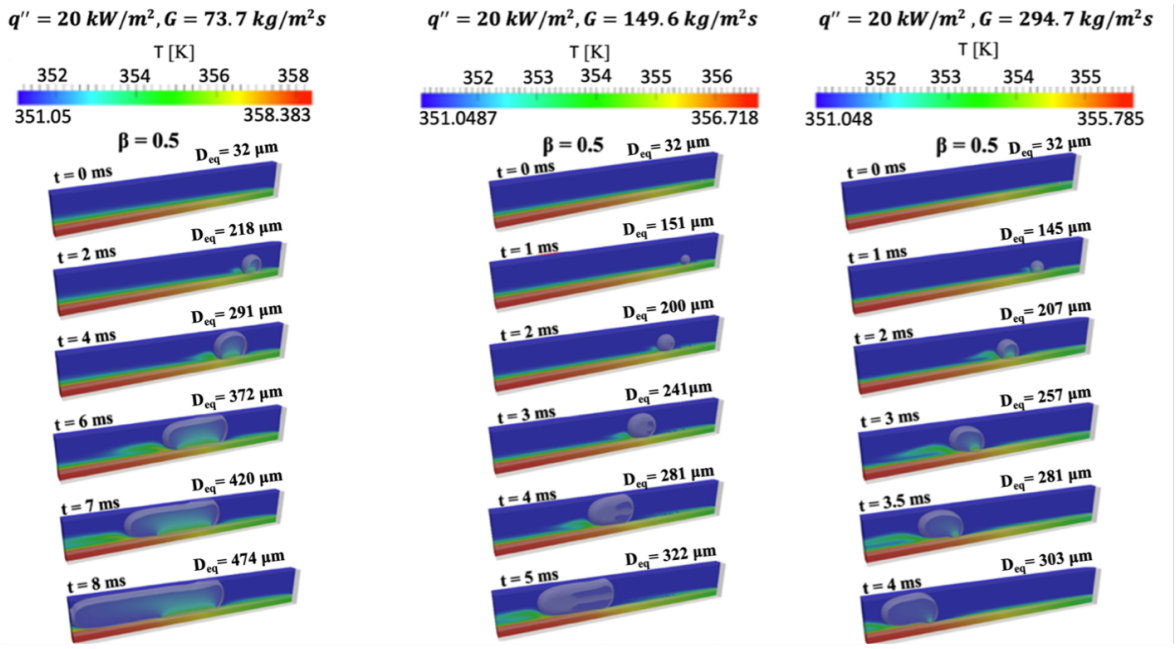

Figure 33: The spatial and temporal evolution of the generated vapour bubble ($q'' = 20\,kW\,m^{-2}$, β = 0.5 and G = 73.7, 149.6, 294.7 $kg\,m^{-2}\,s^{-1}$).

As can be observed, the area of the dry patches with the side walls that was already observed in the medium mass flux case is enhanced at lower and higher mass fluxes for β = 0.5. Moreover, for both lower and higher mass fluxes, a direct contact of the generated bubble with the bottom heated wall is observed. Therefore, it is obvious that for β = 0.5 and for low and high mass fluxes, contact line evaporation also occurs in combination with the liquid film evaporation that was dominant in the case of the medium mass flux. However, in all of the examined mass fluxes, liquid film evaporation appears to be the prevailing heat transfer mechanism for β = 0.5. Finally, in general, it is evident that the increase of the mass flux leads to a subsequent decrease in the vapour slug volume that reaches the outlet of the micro-channel. This is due to the higher traveling speed of the generated bubble and hence, the resulting less time that it experiences evaporation.

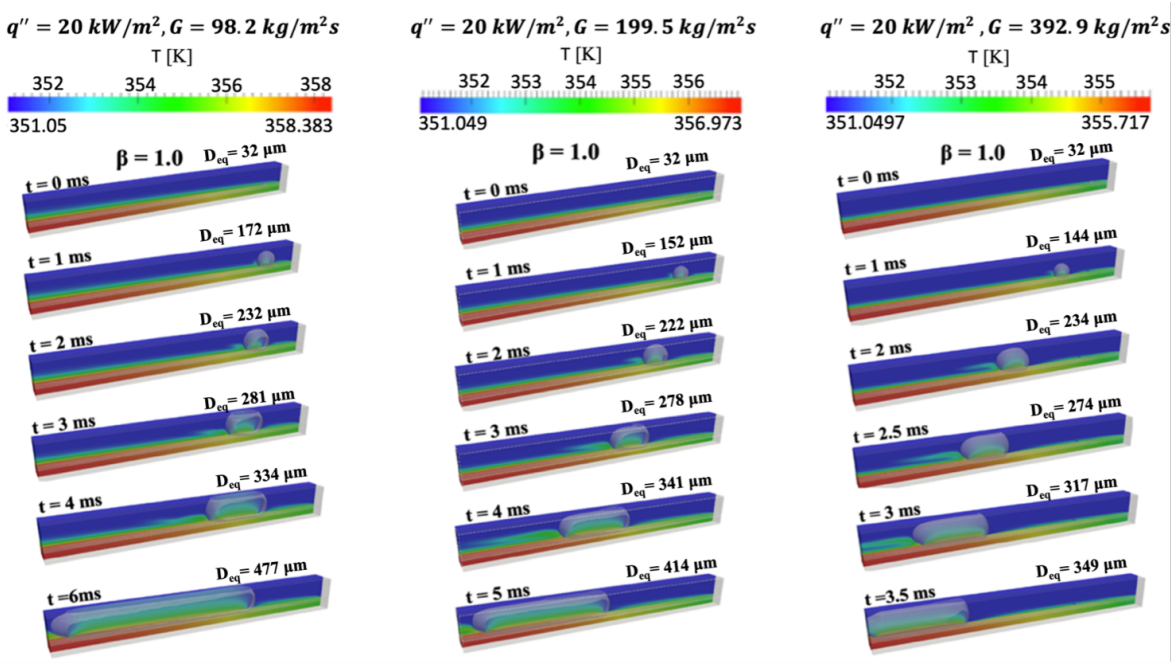

Figure 34: The spatial and temporal evolution of the generated vapour bubble ($q'' = 20\,\mathrm{kW\,m^{-2}}$, $\beta = 1.0$ and $G = 98.2, 199.5, 392.9\,\mathrm{kg\,m^{-2}\,s^{-1}}$).

For $\beta = 1.0$, the decrease of the applied mass flux leads to a considerable increase of the contact area of the vapour slug with the top wall of the channel, in comparison to what is observed for the medium mass flux value. The dry patch areas with the side walls are, however, similar for low and medium mass fluxes. On the other hand, the increase of the mass flux leads to a delay in the development of the dry patches with the top and the side walls of the channel. For all three of the considered mass fluxes contact line evaporation seems to be the prevailing heat transfer mechanism for $\beta = 1.0$. Finally, also for $\beta = 1.0$, the increase of the mass flux leads to a subsequent decrease in the vapour slug volume that reaches the outlet of the considered microchannel.

For $\beta = 2.5$, the decrease of the applied mass flux appears to have a negligible effect on the generated vapour slug dynamics. Both for low and medium mass fluxes, the bubble grows into an elongated vapour slug that maintains contact with the top and bottom walls of the channel throughout most of its length, without any dry patches developing at the side walls of the microchannel. However, for the higher mass flux value, the bubble appears to be in contact only with the bottom wall without any dry patches developing at the top and side walls. For all three of the considered mass fluxes, contact line evaporation is the prevailing heat transfer mechanism also for $\beta = 2.5$.

In order to identify and quantify the effects of channel aspect ratio on the local, instantaneous heat transfer, in Figure 36, the instantaneous local Nusselt number $Nu_{(x)}$ is plotted over the dimensionless length L^* of the considered microchannel, along the central longitudinal axis of the conjugate heat transfer boundary, for the three considered channel aspect ratios, for all values of the applied heat flux and for the medium of the examined mass fluxes, for three successive time instances in each case, respectively. In all cases, also the corresponding single-phase curve from the initial condition (Stage

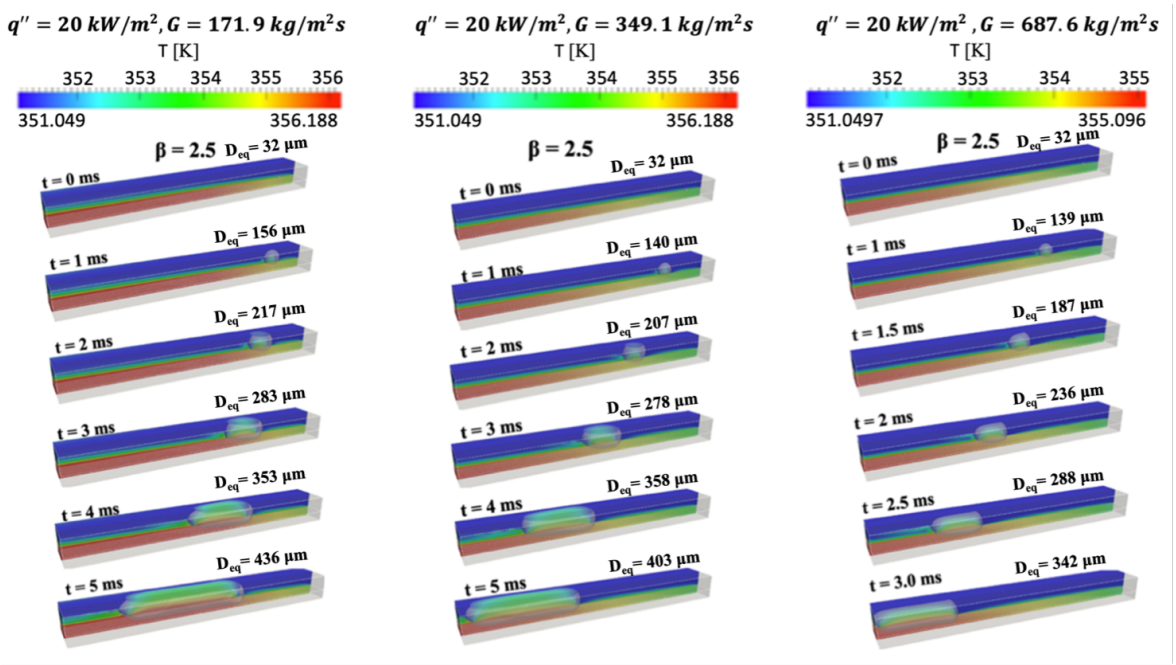

Figure 35: The spatial and temporal evolution of the generated vapour bubble ($q'' = 20\,kW\,m^{-2}$, $\beta = 2.5$ and $G = 171.9, 349.1, 687.6\,kg\,m^{-2}\,s^{-1}$).

1 simulations) of the corresponding two-phase simulation stages (Stage 2 simulations) is plotted as a reference. The local heat transfer coefficient is first calculated as the ratio of the applied heat flux over the temperature difference between the heated wall temperature and the saturation temperature, $h_{(x)}$, and then, the local Nusselt number is calculated as the ratio of the product of the heat transfer coefficient with the channel hydraulic diameter over the thermal conductivity of the liquid, $Nu_{(x)}$.

Focusing on the single-phase curves, it can be observed that the initial increase of β from 0.5 to 1.0, results in slightly lower values of $Nu_{(x)}$ along the heated wall. However, the further increase of β to 2.5 results in a significant increase in the values of $Nu_{(x)}$, indicating an enhancement in the local heat transfer coefficient, for all the examined heat fluxes. Examining now the resulting $Nu_{(x)}$ for the two-phase flow stages, it can be observed that, for all three values of the applied heat flux, at the early stages of the bubble growth (time $t = 1.0\,ms$ for $q'' = 20\,kW\,m^{-2}$, $t = 0.5\,ms$ for $q'' = 100\,kW\,m^{-2}$ and $t = 0.2\,ms$ for $q'' = 100\,kW\,m^{-2}$), two successive peaks in the Nu(x) values are encountered in comparison with the corresponding single-phase curves. These are due to the contact line evaporation at these points along the conjugate heat transfer boundary. As the bubble growth process continues (time $t = 2.0\,ms$ for $q'' = 20\,kW\,m^{-2}$, $t = 1.0\,ms$ for $q'' = 50\,kW\,m^{-2}$ and $t = 0.6\,ms$ for $q'' = 100\,kW\,m^{-2}$), for the narrow microchannel ($\beta = 0.5$), where the bubble maintains a minimal contact area with the heated wall, with a successively developing liquid film region, the local heat transfer is significantly enhanced due to liquid film evaporation, approaching local instantaneous Nu values similar to the wide microchannel ($\beta = 2.5$). In this case, it is characteristic that an enhanced local heat transfer zone is traced also upstream of the bubble position that gradually attenuates towards the inlet of the channel. As for

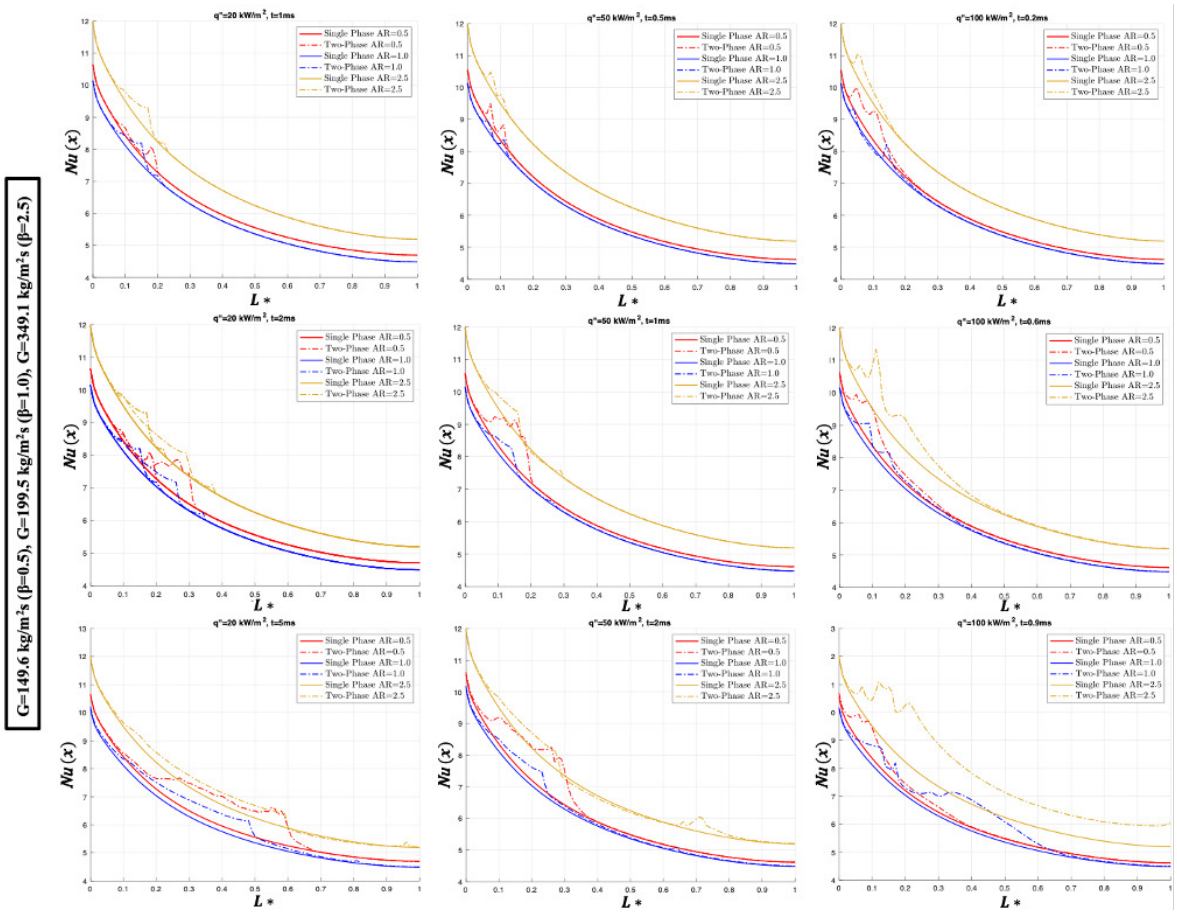

Figure 36: Effect of the aspect ratio (β) on the local instantaneous Nusselt number ($Nu_{(x)}$) along the conjugate heat transfer boundary as a function of dimensionless length (L^*), for different applied heat fluxes ($q'' = 20,\ 50,\ 100\,\mathrm{kW\,m^{-2}}$) and the medium in each case applied mass flux ($G = 149.6\,\mathrm{kg\,m^{-2}\,s^{-1}}$ for $\beta = 0.5$, $G = 199.5\,\mathrm{kg\,m^{-2}\,s^{-1}}$for $\beta = 1.0$, $G = 349.1\,\mathrm{kg\,m^{-2}\,s^{-1}}$ for $\beta = 2.5$).

the square ($\beta = 1.0$) and wide microchannels ($\beta = 2.5$), where the growing bubbles maintain a significant contact area with the conjugate heat transfer boundary, a local increase of the instantaneous Nu number (with respect to the single-phase curves) is observed, at the points where the central wall longitudinal axis (sampling line) meets the contact line between the bubble interface and the heated wall. Also, in these cases, upstream of the first peak point, an enhanced region of local heat transfer is traced that gradually attenuates to the single-phase values towards the inlet. This is due to the thermal inertia of the solid domain. In more detail, as the bubble grows and moves towards the microchannel outlet, due to either contact line evaporation or liquid film evaporation or due to a combination of these two mechanisms, the solid wall temperature is reduced significantly, increasing the local heat transfer coefficient, due to the resulting reduction in the temperature difference between the wall of the channel and the saturation temperature. However, due to the thermal inertia of the solid wall, it takes some time for the wall temperature to increase again. This has as a result the development of this region of enhanced local heat transfer, behind the moving bubbles.

The same behaviour is observed also for the later stages of the bubble growth process (time t = 5.0 ms for $q'' = 20\,kW\,m^{-2}$, t = 2.0 ms for $q'' = 50\,kW\,m^{-2}$ and t = 0.9 ms for $q'' = 100\,kW\,m^{-2}$). For $q'' = 100\,kW\,m^{-2}$, liquid films have been developed for all three of the considered aspect ratios, leading to a significant enhancement of the local heat transfer. From all these observations, it is evident that the variation of the aspect ratio of a microchannel has a significant effect on the local heat transfer coefficient, due to an enhancement in the single-phase heat transfer, combined with the alteration of the underpinned bubble growth dynamics (when boiling occurs and a two-phase flow is developed), that may result in different contributions of contact line versus liquid film evaporation. Furthermore, it is shown that the thickness and thermal properties of the channel walls have a major impact on the local instantaneous heat transfer, due to the associated thermal inertia of the solid domains. This last conclusion highlights the importance of considering Conjugate Heat Transfer simulations for flow boiling investigation within micro-passages and constitutes one of the main novelties of the present numerical investigation. For practical applications, since the time-averaged local heat transfer is more meaningful than the instantaneous one for microchannel heat sinks design, in Figure 37, the effect of the channel aspect ratio on the time-averaged local Nusselt number is plotted for all of the considered heat and mass flux levels. In each case, the corresponding initial condition curve (from the steady state, single-phase stage of the conducted simulations) is also plotted for reference.

As it can be observed, in general, for all combinations of applied heat flux and mass flux, the channel with $\beta = 2.5$ results in significantly higher Nusselt values in comparison to the other two values of aspect ratio ($\beta = 0.5$ and $\beta = 1.0$), which show comparable heat transfer performance for most of the heat flux and mass flux combinations. However, this can be mainly attributed to the significantly higher single-phase stage heat transfer for the channel with $\beta = 2.5$, with respect to the channels with $\beta = 0.5$ and $\beta = 1.0$ which both start from a similar initial condition. It is also obvious that for all the applied heat fluxes, and all the considered aspect ratios, the increase of the mass flux results in a subsequent decrease in the two-phase time-averaged local Nusselt number values. On the contrary, the increase of the applied heat flux does not seem to have a significant influence on the resulting two-phase Nusselt numbers, with respect to the single-phase stage curves. Just a local redistribution of the regions of higher Nusselt numbers, with respect to the corresponding single-phase curves, is observed with the increase of the applied heat flux, especially for the lower and medium mass fluxes. To further quantify the effect of the channel aspect ratio variation, Table 14 summarises the average and the maximum differences of the two-phase time-averaged Nusselt numbers, from the corresponding single-phase stage curves as well as the global Nusselt number, calculated as the area under the two-phase flow curves, for all the considered aspect ratios and applied heat flux and mass flux combinations. As it can be observed more clearly from the global Nusselt numbers, for all applied heat flux values and mass flux levels combinations, the channel with aspect ratio of $\beta = 2.5$ shows the highest heat transfer performance, while the other two channels with aspect ratios of $\beta = 0.5$ and $\beta = 1.0$ show a quite similar heat transfer performance

Table 14: Average and maximum differences of two-phase time-averaged Nusselt numbers from the corresponding single-phase stage curves, and global Nusselt number of two-phase simulation stages, for all the considered aspect ratio, applied heat flux and mass flux combination (single nucleation site cases).

Case	β (-)	q″ ($\frac{kW}{m^2}$)	G ($\frac{m}{m^2 s}$)	Average difference between single-phase and two-phase curves (%)	Maximum difference between single-phase and two-phase curves (%)	Nu_{glob} (-)
1	0.5	20	low	3.225	9.436	4.66
2	1	20	low	12.142	16.535	5.11
3	2.5	20	low	1.285	4.355	**5.35**
4	0.5	50	low	2.538	10.789	4.63
5	1	50	low	3.123	9.124	4.73
6	2.5	50	low	2.407	14.56	**5.42**
7	0.5	100	low	2.937	13.695	4.66
8	1	100	low	3.918	11.835	4.74
9	2.5	100	low	1.978	6.861	**6.86**
10	0.5	20	medium	2.768	6.65	6.04
11	1	20	medium	1.858	4.989	5.98
12	2.5	20	medium	1.493	3.76	**6.94**
13	0.5	50	medium	2.011	5.961	6.15
14	1	50	medium	4.026	6.25	6.09
15	2.5	50	medium	3.257	10.674	**7.03**
16	0.5	100	medium	2.071	12.201	6.17
17	1	100	medium	1.67	6.703	5.97
18	2.5	100	medium	1.55	8.115	**6.96**
19	0.5	20	high	2.237	4.91	7.87
20	1	20	high	1.747	4.251	7.86
21	2.5	20	high	1.587	3.956	**9.14**
22	0.5	50	high	1.782	5.46	7.97
23	1	50	high	1.091	3.96	7.79
24	2.5	50	high	2.561	6.409	**9.22**
25	0.5	100	high	1.401	5.723	7.86
26	1	100	high	0.841	4.269	7.8
27	2.5	100	high	0.621	4.195	**9.05**

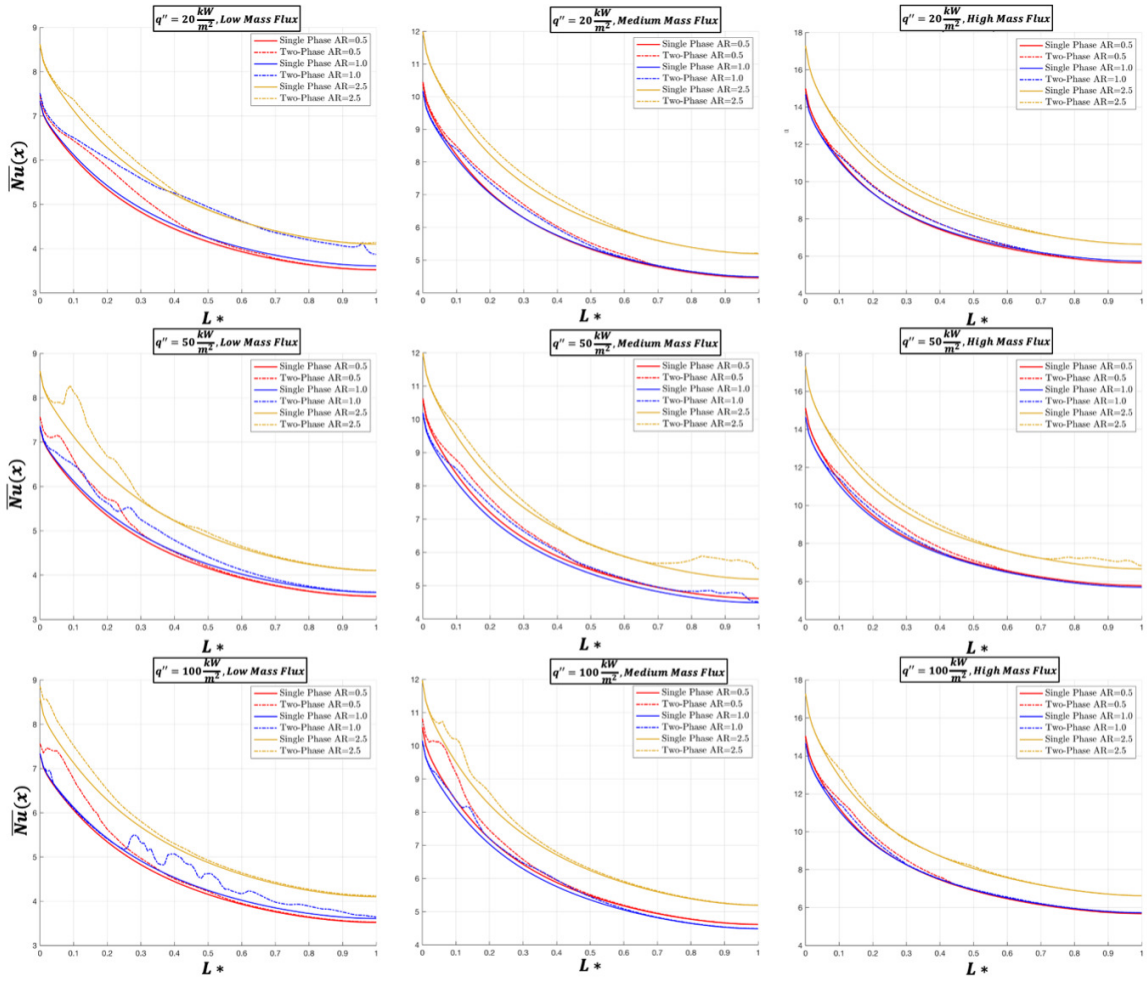

Figure 37: Effect of the aspect ratio (β) on the local time-averaged Nusselt number ($\overline{Nu}_{(x)}$) along the conjugate heat transfer boundary as a function of dimensionless length for different mass fluxes (low, medium, high) and heat fluxes (20 kW m^{-2}, 50 kW m^{-2} and 100 kW m^{-2}), using a single nucleation site.

4.2.4 Multiple Bubble Seeds Numerical Simulations

From the analysis and comparison of all considered cases so far, it is evident that the variation of the channel aspect ratio directly affects the resulting generated bubble dynamics that, in turn, has a noticeable effect on the resulting local and global heat transfer characteristics. However, since during flow boiling in micro-channels, usually multiple nucleation sites are activated simultaneously, and there could be bubble to bubble interactions that might additionally affect the developing two-phase flow regime and, therefore, the heat transfer characteristics, three additional cases are considered in the present investigation. In more detail, for the lowest of the examined heat fluxes and mass fluxes for each aspect ratio (worst case scenario from the heat transfer performance point of view), an additional simulation is performed, starting from the same initial single-phase flow stages as before, patching this time 30 arbitrary distributed bubble nuclei along the conjugate heat transfer boundary. The proposed simulations use the

same parameters as the corresponding ones previously presented, where the applied heat flux is $q'' = 20\,kW\,m^{-2}$ and the applied mass fluxes are G = 73.7, 98.2 and $171.9\,kg\,m^{-2}\,s^{-1}$, for the channels with aspect ratio $\beta = 0.5$, 1.0 and 2.5, respectively. The radius of the 30 initialised bubble nuclei is 20 µm, and their position remains the same with respect to the central longitudinal axis of the conjugate boundary in all three channels.

Figure 38 shows the spatial and temporal evolution of the 30 initiated bubble seeds for the first 1.3 ms from their initiation. As expected, the bubble seeds evaporate, grow, and coalesce. In all three cases, apart from an initial part in the vicinity of the channel inlet, from the early stages (t = 0.4 ms), the initial bubble seeds have grown significantly and merged into an elongated vapour slug that extends from the outlet of the channel up to a certain upstream point, a bit after the middle of the channel for the channels with aspect ratios $\beta = 0.5$ and 1.0, and a bit before the middle point of the channel for the channel with aspect ratio $\beta = 2.5$. From the inlet up to the proposed point, smaller bubbles, in a slug plug flow arrangement, are observed in all cases. The size of these upstream bubbles appears smaller in the case of $\beta = 2.5$ than in the cases of $\beta = 0.5$ and 1.0, where the proposed bubbles are of comparable size. However, it is evident that the aspect ratio has a considerable effect on the shape and form of the generated bubbles. In more detail, for $\beta = 0.5$, the generated bubbles maintain contact with the conjugate boundary (bottom heated wall) as well as with the side vertical channel walls, for the entire 1.2 ms that are considered here. With the increase of the aspect ratio to $\beta = 1.0$, not any contact with the side walls is observed and only a small contact area with the conjugate boundary is evident. Finally, in the case of the channel with aspect ratio $\beta = 2.5$, apart from the contact with the bottom heated wall, a significant contact area with the top channel wall is also evident.

To reach a more quantitative comparison, the time-averaged local Nusselt number along the dimensionless length of the channel is plotted for each channel aspect ratio (dashed lines), in Figure 39. The initial single-phase stage curves for each case are also plotted for reference (solid lines).

As it can be observed, in all three cases, the increase of the Nusselt number, in comparison to the single-phase stage curves, is significantly higher than in the corresponding single nucleation site cases (Figure 37). What is interesting is that, in the case of multiple nucleation sites, the two-phase flow curve of the channel with aspect ratio $\beta = 0.5$ shows comparable levels of local Nusselt number along the channel length, with respect to $\beta = 2.5$, even though the Nu at the initial single-phase stage of the simulations is significantly lower for $\beta = 0.5$. This was not evident in the single nucleation site runs Figure 37), where the $\beta = 2.5$ channel showed significantly higher local time-averaged Nusselt numbers than the other two channels with $\beta = 0.5$ and $\beta = 1.0$, which resulted in comparable to each other values. This is also evident comparing the Global Nusselt Numbers for each of the three cases which are summarised in Table 15. Table 15 also reports the average and maximum % difference between the single-phase flow initial stage and two-phase flow curves. It is evident that the channel with aspect ratio $\beta = 0.5$ show significantly higher both average and maximum % difference values, in comparison to the channels with aspect ratios $\beta = 1.5$ and $\beta = 2.5$, and, therefore, it results to a Global Nusselt number value that is quite close to the

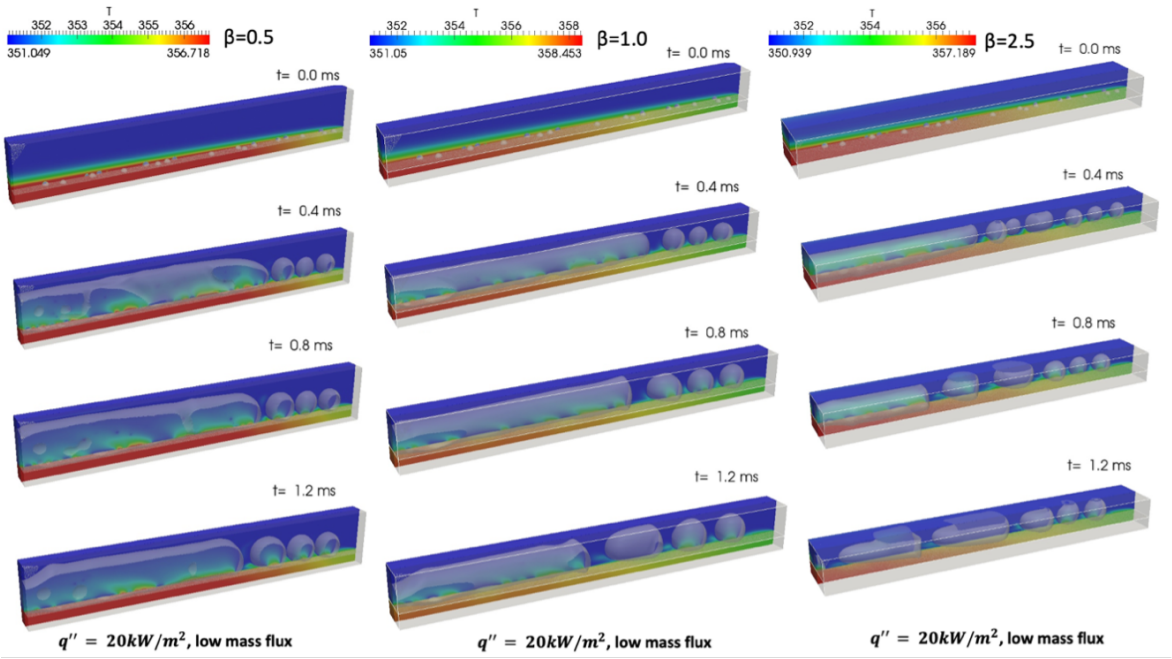

Figure 38: The spatial and temporal evolution of the generated vapour bubbles, $q'' = 20\,\mathrm{kW\,m^{-2}}$, and $G = 73.7$ ($\beta = 0.5$), 98.2 ($\beta = 1.0$) and 171.9 ($\beta = 2.5$) $\mathrm{kg\,m^{-2}\,s^{-1}}$.

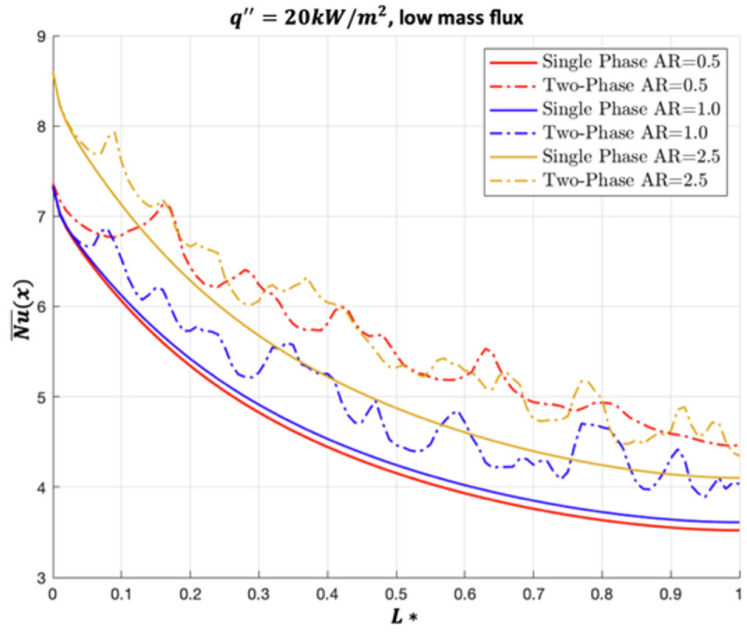

Figure 39: Effect of the aspect ratio (β) on the local time-averaged Nusselt number $\overline{Nu}_{(x)}$ along the conjugate heat transfer boundary as a function of dimensionless length for low mass fluxes and a heat fluxes of $20\,\mathrm{kW\,m^{-2}}$, using multiple simultaneous nucleation sites.

channel with aspect ratio $\beta = 2.5$.

At this point, it should also be mentioned that, as it was shown in the previous

Table 15: Average and maximum differences of two-phase time averaged Nusselt numbers from the corresponding single-phase stage curves, and global Nusselt number of two- phase simulation stages, for all the considered aspect ratios, applied heat flux $q'' = 20\,kW\,m^{-2}$ and low mass flux values G = 73.7 ($\beta = 0.5$) , 98.2 ($\beta = 1.0$) and $171.9\,kg\,m^{-2}\,s^{-1}$($\beta = 2.5$)

Case	β (-)	q'' ($kW\,m^{-2}$)	G ($kg\,m^{-2}\,s^{-1}$)	Average difference between single-phase and two-phase curves (%)	Maximum difference between single-phase and two-phase curves (%)	Nu_{glob} (-)
1	0.5	20	low	27.13	42.78	5.64
2	1	20	low	10.57	25.59	5.02
3	2.5	20	low	10.42	20.92	5.78

subsection 4.1, where the effect of wettability for a channel aspect ratio of $\beta = 0.5$ was investigated [197], the observed maximum and average percentage increase of the time-averaged local Nusselt number, in comparison to the initial single phase stage of the simulation as well as the global Nusselt number, can be further increased to even higher values, for the case of recurring nucleation events from multiple nucleation sites.

4.2.5 Conclusions

A fundamental analysis of the effect of the channel aspect ratio on the bubble dynamics and heat transfer characteristics at the early transient stages of the bubble growth within confined microchannels, under saturated flow boiling conditions, has been presented in the previous paragraphs. According to the Author's best knowledge, this is the first time that an investigation is focusing on the effect of the channel aspect ratio variation on the first transient stage of the bubble growth and heat transfer characteristics, illustrating the importance of this transient stage to the bubble growth dynamics as well as the underpinned heat transfer characteristics and mechanisms. A previously developed and validated, custom, enhanced, diabatic version of the VOF method in OpenFOAM, that accounts for spurious velocities dampening, accurate dynamic contact angle modelling, phase-change due to boiling and condensation, as well as conjugate heat transfer between solid and two-phase fluid domains, is utilised for this purpose. Different applied heat fluxes and mass fluxes were tested for each of the three considered channel aspect ratios. Ethanol was selected as the working fluid for all cases. Two different series of numerical simulations were conducted. In the first series, only a single nucleation event from a single nucleation site is considered to examine the effect of the channel aspect ratio on a single vapour slug development, trying to identify the prevailing heat transfer mechanism in each case, i.e., contact line versus liquid film evaporation. In the second series, multiple arbitrary located nucleation sites are used for the lower value of the applied heat fluxes from the first series of simulations as well

as for the lower level of applied mass fluxes in each case, to perform three more realistic scenarios with 30 arbitrary distributed simultaneous nucleation sites.

From the first series of numerical simulations, the following conclusions can be drawn:

- For low heat fluxes, the narrow microchannel ($\beta = 0.5$), liquid film evaporation is the dominant heat transfer mechanism, while for the square ($\beta = 1.0$) and wide ($\beta = 2.5$) microchannels, contact line evaporation dominates and contributes to the cooling of the heated solid domain. As the applied heat flux increases, liquid film evaporation progressively becomes dominant also in the case of the square and wide microchannels. The applied mass flux appears to have a considerable effect on the generated bubble growth dynamics for the case of the narrow channel, since either lowering or increasing the mass flux leads to a combination of contact line and liquid film evaporation, since the contact areas of the generated bubble with the walls of the channel increase significantly. For the case of the square and wide microchannels, the variation of the mass flux does not alter the dominant heat transfer mechanism, which for all the examined mass fluxes is contact line evaporation.

- The aspect ratio of a microchannel has a significant effect on the local heat transfer characteristics. This happens due to an enhancement in the single-phase heat transfer, prior to the onset of nucleate boiling, combined with the alteration of the underpinned bubble growth dynamics and the resulting differentiation in the contributions of contact line versus liquid film evaporation, when boiling occurs and a two-phase flow is developed.

- The thickness and thermal properties of the solid channel walls have a major impact on the local instantaneous heat transfer, due to the associated thermal inertia of the solid domains.

- Comparing the global Nusselt numbers, it is also concluded that the wide microchannel shows indeed the highest heat transfer performance, however, this is mainly due to the single-phase flow stage contribution.

From the second series of numerical simulations, the following conclusions can be drawn:

- In all three examined channel aspect ratio cases, the initially arbitrary distributed bubble nuclei on the heated wall grow rapidly and merge, forming an elongated vapour slug that extends from the channel inlet up to an upstream point, close to the middle of the channel. From that point and further upstream towards the outlet, smaller bubbles with the slug-plug flow arrangement are developed.

- The length of the elongated vapour slug decreases with the increase of the channel aspect ratio. Moreover, the shape and form of both the elongated vapour bubble as well as of the smaller bubbles upstream (i.e., contact areas with the channel walls) is also affected significantly by the increase of the aspect ratio, indicating an alteration in the contribution of the dominant heat transfer mechanisms.

- From the comparison of the time-averaged local Nusselt numbers along the channels, it can be concluded that, for all cases, the increase of the Nusselt numbers is much higher when more realistic cases, with multiple simultaneous nucleation sites, are simulated, especially for the narrow channel. This leads to a similar overall heat transfer performance with respect to the wide channel, which was superior in the case of the isolated single bubble. This is also evident by comparing the resulting global Nusselt numbers.

From the overall analysis and discussion of the numerical simulation predictions of the present study, the following more general conclusions can be drawn:

- The micro-passage aspect ratio has a significant effect on the generated bubble dynamics during the onset of the nucleate boiling regime, in the first transient period of the bubble growth and development within the confined liquid crossflow. This, in fact, regulates the size and position of the contact areas of the bubble with the microchannel walls, with a direct effect in the contribution and also the balance of the contact line versus liquid film evaporation.

- In general, the numerical simulations, which do not consider the conjugate heat transfer between solid and two-phase fluid domains, lead to poor results and should be avoided.

4.3 Effect of solid surface thermophysical properties on flow boiling in microchannels

Additional ways for increasing the heat transfer coefficient while keeping constant the surface area is by reducing the thermal resistance of the heat sink. This can be achieved by either changing the roughness Ra of the heated solid surface or using solid surfaces made of high thermal conductivity material. In the present subsection, the effect of solid surface thermophysical properties will be examined by performing an additional parametric analysis and isolating the effect of the thermophysical properties of the microchannel's solid material in the flow boiling.

4.3.1 Scope

Stainless steel, brass, copper and aluminium are materials that can be utilised for different reasons and under different conditions in the heat exchanger industry, therefore many investigations have been conducted in the past for flow boiling of tubes and minichannels in order to better understand how the thermophysical properties of these materials affect the heat dissipation and pressure drop. It is known that among the above-mentioned materials, copper has the highest thermal conductivity and in combination with its easy machinability has been selected in many cases to be used in different industrial applications. Aluminium alloys have less thermal conductivity than copper, however, are lightweight and cost less. Additionally, aluminium forms a very stable and tenacious oxide that is resistant to surface corrosion. Stainless steel has the lowest thermal conductivity among the above-mentioned materials and is preferred for applications such as regenerators within heat engines, where low thermal conductivity is desirable [198].

Bang and Choo [199] studied experimentally the effect of copper, aluminium and brass circular channels on flow boiling heat transfer coefficient using Freon 22 as coolant. The diameter of the channels was 1.67 mm. Tests were performed for a fixed mass flux of $600\,\mathrm{kg\,m^{-2}\,s^{-1}}$, and an applied heat flux between 5 and $30\,\mathrm{kW\,m^{-2}}$. The results showed that the flow boiling heat transfer coefficient in a minichannel varies only by heat flux, independent of mass flux and vapor quality. The effect of tube material was found to be small.

Recently, Al-Zaidi et al. [200] investigated experimentally the effect of surface material on flow boiling of HFE-7100 coolant in multi-microchannels, applied with heat flux up to $433.5\,\mathrm{kW\,m^{-2}}$ and mass flux values ranging between 50 and $250\,\mathrm{kg\,m^{-2}\,s^{-1}}$. It was concluded that at low heat flux ($<60\,\mathrm{kW/m^2}$) the effect of surface material on heat transfer coefficient was minor. On the other hand, for higher heat flux the difference was evident, with the aluminium surface having on average about 12% higher HTC compared to the copper surface. According to the authors, this is due to the higher amount of cavities found in the aluminium surface as well as the more significant peaks created by the machining process. However, the better performance of the aluminium surface came with higher flow boiling pressure drop penalty, compared to the copper, especially for moderate and high heat fluxes.

Different conclusions were reported by Hosseinni et al. [201], who also studied experimentally the surface material effect on nucleate pool boiling effects on horizontal

circular plates of copper, brass and aluminium for heat flux values between 8 to 200 $\mathrm{kW\,m^{-2}}$. Particularly it was found that the effect of surface material is more significant for high heat fluxes and that copper performed better among all tested surfaces, although it had the least Ra, whilst brass performed worse than copper but better than aluminium.

The effect of surface material (copper, brass, and stainless steel) and surface roughness (0.03 to 10.5 µm) on nucleate boiling heat transfer on conventional circular tubes of 19 mm was studied by Jabardo et al. [202]. It was reported that brass and copper surfaces presented close results regarding the heat transfer coefficient for both refrigerants tested, while significantly deviation of stainless steel compared to the other two surfaces resulting in consistently lower HTCs could be seen. Furthermore, the slope of the HTC versus the applied heat flux curve is strongly dependent on the solid surface material.

Lelea [175] studied the effect of the axial conduction in the solid when the microchannel is heated only at the first and last quarter of its total length. In more detail, a conjugate heat transfer solver was utilised in order to investigate numerically the effects of the losses of heat flux inside the solid when the microchannel is heated in the upstream part (near the inlet) and the downstream part (near the outlet). In total three different materials were investigated: steel, silicon and copper. The simulations were run in steady state condition with a single-phase flow and imposing a fixed value of heat power for every case. The results showed that the dispersion is different between the three materials only in the case of upstream heating of the channel and that the copper case has the biggest losses. This means that using the copper and heating just half of the channel, the heat released to the fluid flow is less compared to the steel. This is due to the bigger thermal conductivity of the copper as well as its capability to conduct better a fraction of heat inside the non-heated part of the solid.

Paz et al. [203] experimentally investigated the effect of solid surface material and surface roughness on low-pressure subcooled flow boiling of water on flat plates of seven heating surfaces made from copper, aluminium and stainless steel. From the results it was evident that a unique parameter of roughness measurement, Sa is not sufficient for the characterisation of a boiling model with regards to the surface morphology, however, it seemed to produce better characterisation compared to the commonly used roughness, whose directional nature is unsuitable for dealing with a multi-scale phenomenon such as boiling. It was concluded that to better understand the phenomena, further studies with the inclusion of other morphological parameters are required. A new correlation based on the experimental results was introduced and was found to fit well the experimental data for all of the examined surfaces and materials.

Heat exchanger materials that are frequently used in the industry such as Copper and Brass have very good thermal properties, but their corrosion and wear resistivity are considered rather poor. Therefore, it is very common that coatings to be applied to these solid surfaces. This process is considered essential for equipment that operates at corrosive or harsh environment [63, 204]. Additionally, coatings can also modify the thermal properties of the solid that is applied on, and in many cases can enhance heat transfer performance (however this needs to be further investigated, since it is not justified yet for micro-passages). Morshed et al. [205] experimentally investigated the

influence of Cu-Al_2O_3 nanocomposite coating on single-phase and two-phase flow boiling in a single rectangular microchannel of $D_h = 672\,\mu m$ ($0.36 \times 5 \times 26\,mm^3$). The coatings were applied at the bottom side while the channel was heated on one side only. The values of heat and mass flux varied between 4-60 $kW\,m^{-2}$ and 33-142 $kg\,m^{-2}\,s^{-1}$, respectively. De-ionized water was used as a working fluid. The Cu-Al_2O_3 nanocomposite coating, compared to the bare Cu has been found to enhance single-phase heat transfer rate marginally. For two-phase flow, the heat transfer is enhanced from 30% to 120% depending on the flow rate and surface temperature with an additional pressure drop penalty to be <15%. Furthermore, CHF is increased with the increase of the mass flux, whereas CHF was elevated by 35–55% for the modified surface. Finally, it was identified that Cu-Al_2O_3 nanocomposite coating is effective for decreasing the surface superheat temperature required for boiling inception, up to 8°C, compared to the bare surface.

Similar results were also provided by Phan et al. [206]. They conducted experiments of flow boiling in single rectangular channels of $D_h = 0.96\,mm$ and L=180 mm using four smooth and micro-structured titanium and hydrophilic polydimethylsiloxane coatings (Ti, μ-Ti, SiOχ and μ-SiOχ). Initially, it was found that the superheat for ONB is reduced from about 6°C to 2.5°C for SiOχ compared to μ-SiOχ. For the micro-structured surfaces, heat transfer enhancement up to 85% was obtained.

Heat transfer characteristics of FC-72 for saturated and subcooled flow boiling was experimentally studied by Lie et al. and Chang et al. [207, 208]. The test section used in these experiments included single rectangular microchannels that were heated from bottom structured surface with evenly distributed square pillars. It was reported that heat transfer performance was enhanced for the microstructured surfaces for both single-phase and two-phase flow. The greatest heat transfer enhancement could be seen for the pillars with the smallest cross-section.

From the above review it is clear that during the last years, the effect of thermophysical properties of the solid surface on boiling heat transfer within micro-passages and the associated bubble dynamics has received considerable attention from academic and industrial researchers worldwide. However, the majority of these works that are investigating the proposed phenomenon, in order to eliminate the effect of surface roughness that different materials have (otherwise this is also a parameter that needs to be taken into consideration), perform experiments on treated surfaces. This procedure minimises the roughness difference, but simultaneously results in the alteration of other material characteristics of the solid surface such as the surface wettability and boiling incipience characteristics, with each of these parameters playing an important role in boiling heat transfer and flow characteristics alone [2, 148], making the process of isolating the effect of solid surface thermophysical properties, a challenging task. On the other hand, the effect of solid surface properties can be easily isolated by conducting parametric numerical simulations on smooth surfaces, modifying only the characteristic(s) of interest, whereas all the other surface characteristics such as surface wettability, roughness, and fluid properties remain unchanged. Yet still, such numerical investigations are limited in the literature and have not been studied comprehensively. Additionally, the existing numerical and experimental works are mainly focusing on quasi-steady state conditions of the boiling and heat transfer process, ignoring the entrance length and the first stages of the underpinned bubble dynamics and the

two-phase flow regime development.

The primary objective and novelty of the present study is that the exact effect of having five different channel solid materials with different thermophysical properties (aluminium (Al), brass, copper (Cu), silver and stainless steel) is isolated, considering ideally smooth and wettable surfaces, and qualitatively and quantitatively compared, aiming to identify and quantify their effect on the bubble growth and heat transfer characteristics for the first stage of the boiling process, i.e. from bubble nucleation and growth up to the first stages of the two-phase flow pattern development. For this purpose, results that have been obtained after performing 3D conjugate heat transfer, transient simulations of saturated flow boiling within microchannels, are presented. Additionally, a new correlation for the prediction of the global Nusselt number, based on an existing correlation available in the literature, is proposed. The new correlation constitutes a modification of the existing one that was developed by Li and Wu [45], in order to take into account important solid surface thermophysical parameters such as density, heat capacity and thermal conductivity.

4.3.2 Numerical simulations set-up and process

In this subsection, numerical simulations of a single rectangular microchannel of two different heated solid surfaces will be conducted. The examined surfaces include: surfaces of stainless steel and copper. The same VOF-based enhanced conjugate heat transfer solver, numerical framework, boundary conditions and fluid properties as described in subsections 4.1.1 has been utilised. In order to isolate the actual effect of the thermophysical properties of the different surfaces, only the properties of the solid heated surfaces have been altered, whereas parameters such as aspect ratio, hydraulic diameter, heat ($q'' = 20\,kW\,m^{-2}$) and mass flux ($G = 150\,kg\,m^{-2}\,s^{-1}$) remain the same for the examined cases. The properties of the tested solid surfaces which the present investigation uses are summarised in Table 16. The working fluid is ethanol and its properties can be found in Table 3. For better observation of the effect and the flow boiling phenomena the length of the channel has been doubled from 2.4 mm that was used in the previous numerical investigations into 4.8 mm, while the grid cell size and aspect ratio remained unchanged at 2 µm and 0.5, respectively. The dimensions and total cells of the channel and solid heated plate are shown in Table 17, whereas the corresponding contact angle values can be seen in Table 18. As in the previous investigations presented in this thesis, the simulations were performed in two stages. In the first stage, the microchannel was filled with 100% liquid at saturation temperature and 1 bar pressure and was run up to a point where a fully developed thermal and velocity boundary layer is achieved. In the second stage, the time was initialised at 0 ms and 30 bubble seeds, of 40 µm diameter, are patched onto the conjugate heat transfer boundary interface in a position of 200 µm from the X-axis. Figure 40 depicts the mesh details, boundary conditions and position of the patched bubbles.

In order to create even more realistic investigation scenarios, after the initial patching of the 30 bubble seeds at $t = 0$ ms of the two-phase stage of the numerical simulations, multiple recurring nucleation events with a constant nucleation frequency of 2 kHz (or a period of 0.5 ms) at the same nucleation positions as shown in Figure 40c), are activated successively for all of the examined cases. Hence, each nucleation cycle lasts for 0.5 ms

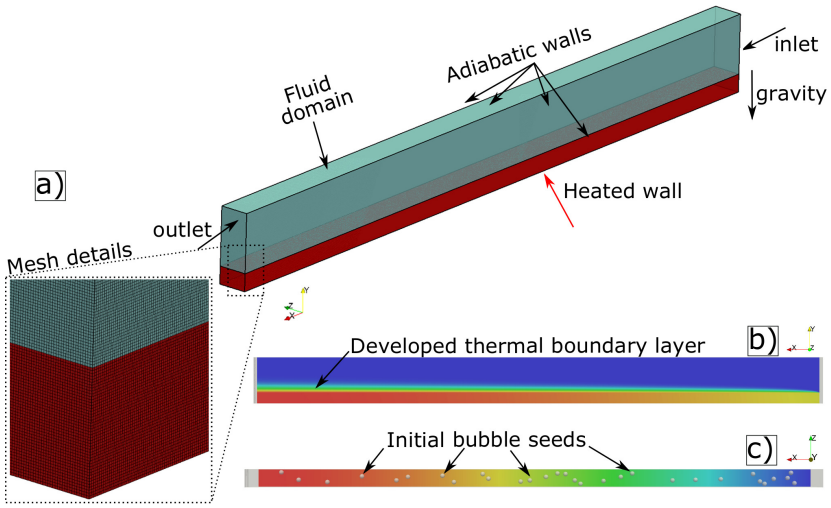

Figure 40: a) Computational domain, boundary conditions and mesh details, b) Developed initial thermal boundary layer at the end of the first stage of simulations (single-phase), c) Position of the 30 patched bubble seeds that have been used for all the numerical simulations, at the beginning of the second stage (referred as initial time t = 0 ms).

and a total of 8 nucleation cycles ($8 \times 0.5\,\text{ms} = 4.0\,\text{ms}$) are considered for all cases. For the conduction of the 3D, transient, numerical simulations, a High-Performance Computing (HPC) cluster has been utilised. For the single-phase stage of the simulations, each run required 200 computational cores. The duration of the computation for each of the five single-phase simulations (one for each material) was between 20 to 25 days. For the two-phase simulations, the duration of the computation was three to four days for each nucleation cycle since just a few milliseconds of real flow were required for the generated vapour bubble to reach the outlet of the channel in contrary to the single-phase stages that required hundreds of milliseconds. In total, more than 750,000 core-hours were utilised for the overall runs that are presented in the present paper. A variable calculation time step was utilised for the two-phase runs with the Courant number kept constant at 0.5. Hence the calculation time step was varied automatically ranging approximately from 10^{-8} up to 10^{-6} s.

Numerical results

In this section, the results of the main numerical investigation are reported. Initially, the effect of the thermophysical properties of the solid surface material on the resulted flow boiling regimes and the instantaneous local heat transfer coefficient $h_{(x)}$ is examined, quantitatively and qualitatively, focusing on various successive time instances of the two-phase simulation stages for each of the examined materials. Subsequently, the local time-averaged heat transfer coefficient enhancement of the two-phase simulation stages in comparison with the single-phase simulation stages are presented for each of the examined materials. Additionally, the effect of each material on the total generated vapour volume over time is also investigated. Finally, the two-phase simulation results

Table 16: Properties of the examined cases that were used for the simulations.

Solid surface	ρ_s ($\mathrm{kg\,m^{-3}}$)	$c_{p(s)}$ ($\mathrm{J\,kg^{-1}\,K^{-1}}$)	κ_s ($\mathrm{W\,m^{-1}\,K^{-1}}$)
Stainless Steel	7840	500.0	16.2
Brass	8800	380	119.0
Aluminium	2707	896	220.0
Copper	8933	392	396.8
Silver	10500	235	429.0

Table 17: Channel dimensions for the fluid and solid domain as well as total number of cells.

	Fluid (mm)	Solid (mm)
Length	4.80	4.80
Height	0.30	0.09
Width	0.15	0.15
Total cells	27.00 M	8.10 M

Table 18: Solid surface advancing and receding contact angles of ethanol with the solid surfaces examined.

	θ_α (°)	θ_r (°)
Stainless Steel	19	8
Brass	18	8
Aluminium	0	0
Copper	15	7
Silver	14	7

for the global Nusselt number are compared with an empirical correlation proposed by Li and Wu [45], and a new modified correlation based on [45] but taking into account important thermophysical properties of the utilised solid material (solid heat capacity, density and thermal conductivity) is proposed for the first time in the literature.

4.3.3 Numerical results: Effect of solid surface thermophysical properties on the instantaneous two-phase flow and heat transfer characteristics

In Figure 41, qualitative, flow visualisation results of the spatial and temporal evolution of the generated vapour bubbles for all the examined solid surfaces, are illustrated. For each metallic material case, the figure illustrates a top view and a 3D isometric view of five successive time instants. The coloured contours of the 3D view and top view indicate the instantaneous temperature distribution along the fluid and solid domains. The semi-transparent grey surface constitutes the liquid/vapour interface which is represented by the 0.5 volume fraction iso-surface. For each case, the solid material and the corresponding thermophysical properties are also indicated at the top. Overall, from the macroscopic observations, it can be inferred that the variation of the thermophysical properties of the solid surface has a substantial effect on the resulting flow boiling regimes and the corresponding heat transfer mechanisms. Initially, for all cases, the

generated bubbles grow due to contact line evaporation and also due to subsequent coalescence events, forming larger elongated Taylor bubbles (a bullet-shaped bubble, which flows and occupies almost the entire cross-section of the channel) which are carried away by the developed liquid cross-flow. When the elongated, bullet-shaped Taylor bubbles are formed after this initial stage, they fill up almost the entire cross-section of the micro-passage and they are separated from the solid boundaries through a thin liquid film of variable thickness. At this point, liquid film evaporation is the main heat transfer mechanism as the bottom side liquid film and parts of the side liquid films are within the thermal boundary layer. Some dry spots (i.e. Taylor bubble contact regions with the side walls) can also be observed in some time instants. In more detail, at the early stages of the boiling process from t = 0.5 ms up to t = 1.1 ms, a churn type of two-phase flow regime is observed for all of the examined cases, except the copper case. In the copper channel case, from the very early stages of the bubble growth and coalescence process, a big, elongated vapour slug that covers the entire length of the channel and maintains contact with the heated wall is formed, which is closer to an annular flow regime. For the other four channels, approximately for the first quarter of the microchannel close to the inlet, where the temperature of the solid wall is lower, the bubble growth and coalescence rate appear to be lower than in the case of the copper channel leading to the appearance of relatively small and spherical bubbles that they have either detached or they are still maintaining contact with the bottom wall boundary. For the remain three quarters, a formation of an elongated vapour slug that in some parts is still in contact with the heated wall and in some other parts it forms a liquid film, is observed. At the later stages of the boiling process for t = 2.2, 3.3 and 4.0 ms, as the temperature of the solid heated wall decreases with respect to time due to the prior contact line and in less extend liquid film evaporation events, the two-phase flow regime gradually transits to a slug-plug flow, with Taylor bubbles that are separated by liquid plugs. In most cases, a well-formed liquid film that separates the Taylor bubbles from the channel boundaries is evident while some minimal dry spots with the side and bottom walls can also be observed locally, at particular time instants. It is also evident that depending on the channel material the transition to the slug-plug flow regime occurs at different time instants. For the aluminium, brass and silver channels the proposed transition occurs around t = 2.2 ms, for the copper channel around t = 4.0 ms and for the stainless-steel channel somewhere between t = 1.1 and t = 2.2 ms. Finally, differences in the liquid film distribution in the longitudinal direction are also evident between the different solid cases.

In order to extract more information on localised and instantaneous two-phase flow regimes and to also investigate the effect of the microchannel solid material on the local heat transfer, the instantaneous local heat transfer coefficient $h_{(x)}$ is plotted over the dimensionless length L^* for three different time instants (t = 0.1, 2.2 and 4.0 ms), in Figure 42. At the top of each plot the corresponding side view snapshot of the boiling process, is placed, to indicate the instantaneous localised two-phase flow regime. Focusing on the first time instant at t = 0.1 ms, it can be seen that a bubbly flow regime is formed close to the inlet of the channel, for all channel material cases. This regime is evident for approximately the first 30% of the total length of the channel for all the cases except for the copper and the stainless-steel cases where the bubbly flow

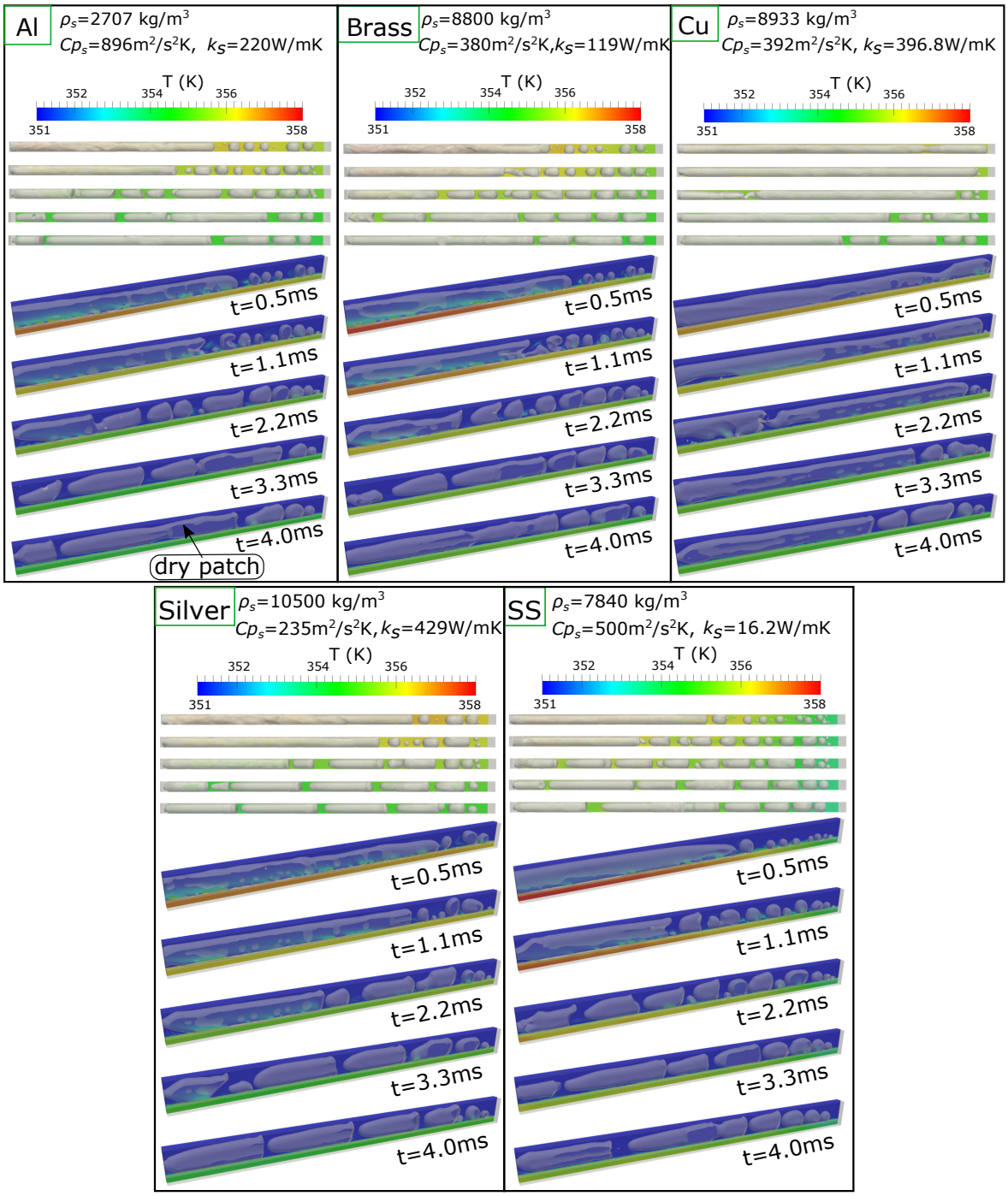

Figure 41: Flow visualization results of the five examined solid surfaces. Top and isometric views of five successive time instances. The density, heat capacity and thermal conductivity for each of the utilised solid materials are indicated at the top.

regime can be observed within the first 18% and 40% of the channel length, respectively. At the same time instant (t = 0.1 ms), for the cases of aluminium and brass, the bubbly flow regime region is followed by a quasi-slug flow region and then by a churn flow region that extends up to the outlet of the microchannel. For the copper, silver and stainless-steel cases, a churn flow regime region is evident right after the bubbly flow regime region. At t = 2.2 ms a slug-plug flow regime is evident for all materials for the entire length of the channels. The only exception is for the copper channel case where a bubbly flow regime region is evident close to the inlet and a semi-annular two-phase flow regime region is observed in the rest part of the channel. At t = 4.4 ms a slug-plug two-phase flow regime has been established in all solid channel cases, for the entire length of the channel. Bubble merging and bubble break-up events were also observed locally at particular time instants. The initiation of a bubble break-up event can be observed, and it is explicitly indicated in Figure 42(o). Now comparing the local instantaneous heat transfer coefficients along the channels in comparison to the corresponding local heat transfer coefficient of the single-phase stage in each simulation that constitutes the initial condition, and also comparing the different material cases to each other, it is evident that the channel material has a significant influence on the local heat transfer coefficient both in the single and two-phase flow stages. Initially, it can be observed that the trend of the single-phase simulations is similar regardless of the utilised solid material, however as it will be seen more clearly later, there is a substantial difference in the reduction rate of $h_{(x)}$ along the channel. Comparing the two-phase HTCs with the corresponding single-phase values along the channel for the three illustrated time instants it is evident that bubbly flow is the least effective boiling regime, whereas quasi-slug flow and churn flow appear to be more efficient (t = 0.1 ms). However, the slug-plug flow regime that is evident in the last two time instances (t = 2.2 ms and t = 4.0 ms) appears to be the most efficient flow regime, as it is evident from the significant enhancement of the HTC in comparison to the single-phase stage of the runs.

4.3.4 Effect of solid surface thermophysical properties on the time-averaged local heat transfer coefficient

In Figure 43 the effect of thermophysical properties of each material, on the time-averaged local heat transfer coefficient $\overline{h}(x)$ over the dimensionless length L^*, is depicted. It should be mentioned that each curve represents the time-averaged local HTC from t = 0 ms up to each nucleation event time instant. The steady-state local HTC from the single-phase stage of the simulations (initial condition) is also included for each channel material case. In all cases it can be observed that the curves representing the single-phase stage of the simulations begin at the highest value of HTC at the position $L^* = 0$ (i.e., the microchannel inlet position), following a gradually decreasing reduction rate until $L^* = 1$ (i.e., the microchannel outlet position). The reduction rate is much higher for the case of stainless-steel, which among the examined materials shows the highest HTC values near the inlet and the lowest values near the outlet. For the other four material cases, the difference in the HTC values between the inlet and the outlet is much lower, especially for the cases of aluminium, copper and silver which have comparatively higher values of thermal conductivity. The effect

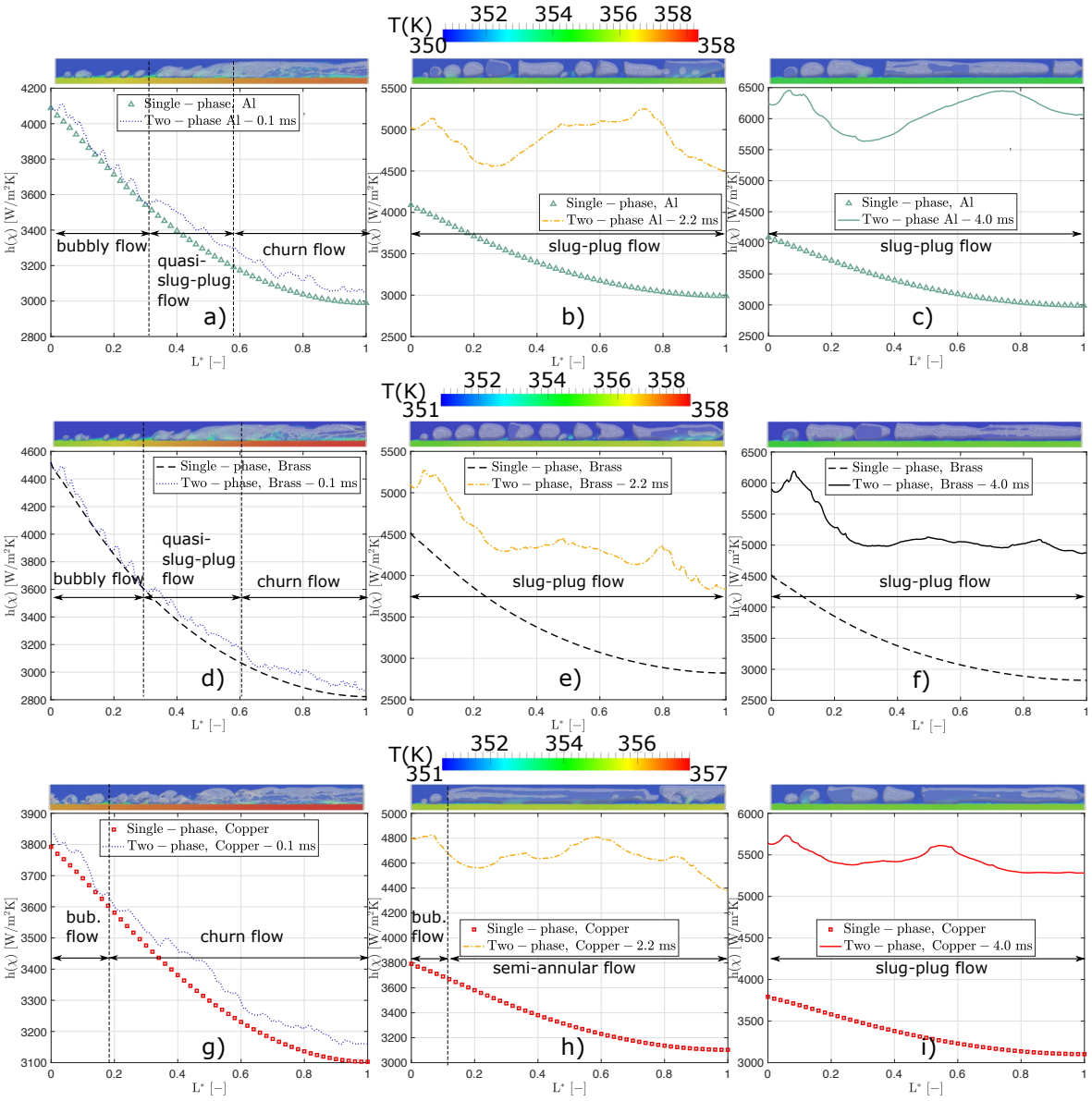

Figure 42: Comparison of the instantaneous local heat transfer coefficient h(x) of the single-phase and two-phase simulations over the dimensionless length L^* of the channel, for three different time instants (0.1, 2.2 and 4.0 ms), for Al, brass and Cu, silver and stainless-steel. Additionally, the corresponding instantaneous side view snapshot is placed on top of each plot showing the resulting flow boiling regime for each case.

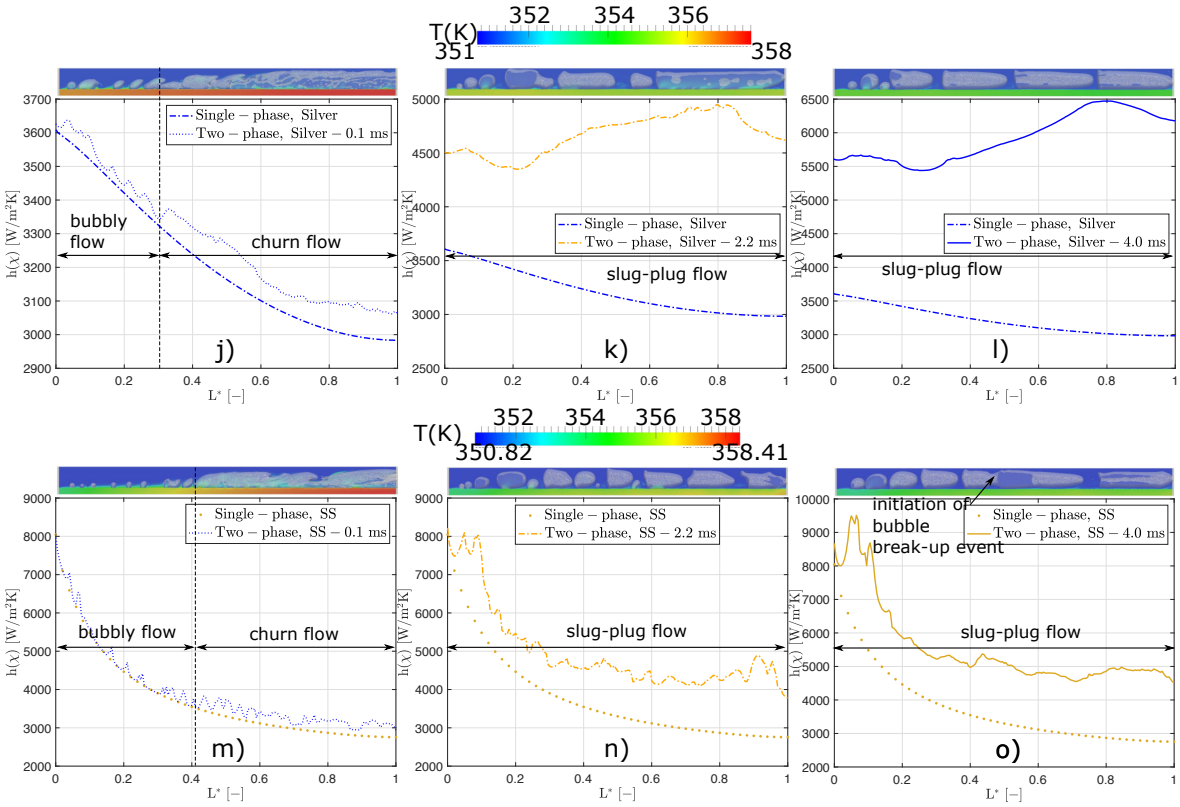

Figure 42: (continued).

of thermophysical properties of the utilised solid material is even more evident by observing the two-phase curves of each recurring nucleation cycle, as it is illustrated in the same figure. A gradual increase of the $\overline{h}_{(x)}$ after each nucleation cycle is evident in all cases. Furthermore, it is characteristic that for each nucleation cycle, a similar longitudinal distribution trend is observed with the local values increasing by similar percentages. As it is also evident from the time-averaged local heat transfer coefficient curves of Figure 43, apart from the stainless steel case, the longitudinal distribution of $\overline{h}(x)$ is more regular for the other four material cases. For the stainless steel case, an irregular distribution with a lot subsequent maxima and minima is observed. This might be attributed to the significantly lower thermal conductivity of stainless steel with respect to the other four materials. In order to do a direct comparison of the different cases to each other, the single-phase and the corresponding two-phase flow curves after the 10^{th} nucleation cycle are plotted together in Figure 44. It seen that, the ranges of the single-phase steady state HTC and the two-phase values of $\overline{h}(x)$ for the stainless steel surface are between 8100 to 3800 kW/m^2) and 8000 to 2800 kW/m^2), respectively, whereas for the other four cases the ranges are significantly smaller and particularly between 4500 to 2800 kW/m^2) for the single-phase and 5100 to 3800 kW/m^2) for the two-phase simulations. Again, this might be attributed to the orders of magnitude difference of the thermal conductivity value of the stainless steel surface in comparison to the other metallic surfaces simulated in this subsection (Table 16). The graphical representation of the timed-averaged local heat transfer coefficient enhancement $\Delta\overline{h} = [(\overline{h}(x)_{t-p} - \overline{h}(x)_{s-p})/\overline{h}(x)_{s-p}] \times 100\%$, comparing the

two-phase simulations after the 10^{th} nucleation cycle with their corresponding initial stage (single-phase simulations) in each case, is shown in Figure 45. It is clear from this diagram that the aluminium and silver channels show overall and locally the highest heat transfer enhancement compared to the corresponding single-phase simulations, while the case of brass shows the lowest enhancement. It is interesting to note also in this diagram that stainless steel shows once more an irregular distribution with high variations in the heat transfer enhancement along the channel, which may be attributed to the low thermal conductivity and thermal diffusivity compared to the other cases. These local heat transfer fluctuations are not desirable in flow boiling heat transfer within microchannels as they can generate local hot spots which is not optimum for electronic components.

Table 19 presents the two-phase global heat transfer coefficient h_{global} values, for each nucleation cycle. The table clearly shows quantitatively what has been depicted earlier in Figure 44. In more detail, the cases of silver and aluminium show the biggest increment compared to the single-phase simulations, of 41.66% ($h_{sp,glob,silver}$= 3.21 kW m^{-2} K^{-1} to $h_{tp,glob,silver}$= 4.55 kW m^{-2} K^{-1}) and 40.54% ($h_{sp,glob,al}$= 3.37 kW m^{-2} K^{-1} to $h_{tp,glob,al}$= 4.73 kW m^{-2} K^{-1}), respectively. Significant increase of 34.72% ($h_{sp,glob,cu}$= 3.52 kW m^{-2} K^{-1} to $h_{tp,glob,cu}$= 4.52 kW m^{-2} K^{-1}), can be seen also for the cases of copper surface. Finally, the cases of stainless steel and brass showed the lowest increase where the percentage difference values are 29.42%. ($h_{sp,glob,ss}$= 3.74 kW m^{-2} K^{-1} to $h_{tp,glob,ss}$= 4.84 kW m^{-2} K^{-1}), and 27.41% ($h_{sp,glob,brass}$= 3.36 kW m^{-2} K^{-1} to $h_{tp,glob,brass}$= 4.28 kW m^{-2} K^{-1}, respectively. The asymptotic value of the global HTC has also been estimated in each case using the predicted values from the first 10 nucleation events, utilising the resulting equations from best fit curves. These asymptotic values are indicated in the last row of Table 19. From these results, it can be inferred that the effect of surface thermophysical properties on the resulting bubble growth dynamics and heat transfer coefficient is significant from the very early stages of the boiling incipience and flow boiling process.

4.3.5 Effect of surface thermophysical properties on the volume of the vapour

The influence of the investigated effect in the volume of the vapour within the microchannel through the examined boiling process is shown in Figure 46. Overall, the case with the highest volume of vapour over time is the case of copper and the case with the least vapour volume is the case of stainless steel. In more detail, the vapour slugs formed in the cases of copper, silver and aluminium have the highest volume between the first 0.5 and 1.0 ms after the boiling incipience and also during the last available time instant of 4.0 ms, for the latter two cases. For the cases of stainless steel and brass, the highest volume of the resulted vapour slugs can be seen during the last available time instants (e.g. 4.0 ms). For the stainless steel cases, this is attributed to the high presence of bubbly flow and the comparatively smaller vapour slugs. Similar flow regimes could be also seen for the brass case. Conversely, the transition from the churn flow to elongated vapour slugs resulted in significantly higher volume vapour slugs for the case of copper.

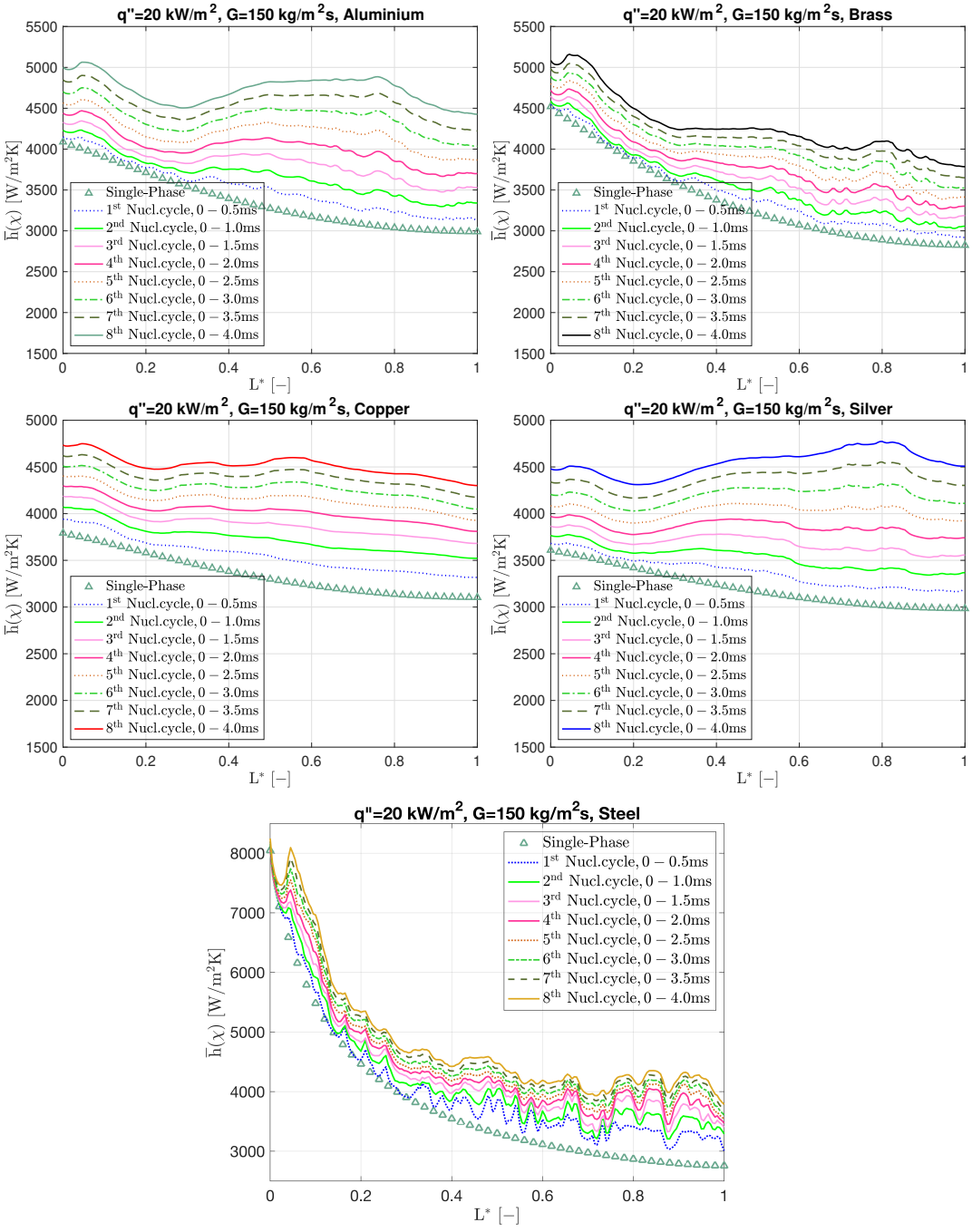

Figure 43: Time-averaged heat transfer coefficient over the dimensionless length of the channel for all the examined surfaces. Each subfigure contains the numerical predictions from the single-phase and the corresponding two-phase simulation stages for ten subsequent nucleation cycles.

Table 19: Cumulative two-phase global heat transfer coefficient for each nucleation cycle, for $q'' = 20\,kW\,m^{-2}$ and $G = 150\,kg\,m^{-2}\,s^{-1}$ for all the examined surfaces.

Bubble cycle	Material	h_{glob} ($kW\,m^{-2}$)	Material	h_{glob} ($kW\,m^{-2}$)	Material	h_{glob} ($kW\,m^{-2}$)
1^{st} nucl. cycle - (0-0.5ms)	Aluminium	3.52	Brass	3.48	Copper	3.56
2^{nd} nucl. cycle - (0-1.0ms)		3.68		3.58		3.73
3^{rd} nucl. cycle - (0-1.5ms)		3.84		3.69		3.89
4^{th} nucl. cycle - (0-2.0ms)		4.02		3.81		4.03
5^{th} nucl. cycle - (0-2.5ms)		4.20		3.93		4.16
6^{th} nucl. cycle - (0-3.0ms)		4.38		4.05		4.28
7^{th} nucl. cycle - (0-3.5ms)		4.56		4.17		4.40
8^{th} nucl. cycle - (0-4.0ms)		4.73		4.28		4.52
Asymptotic value		10.73 (after 6000 nucl. cycles)		7.00 (after 2500 nucl. cycles)		8.68 (after 4500 nucl. cycles)

Table 19: (continued).

Bubble cycle	Material	h_{glob} (kW m^{-2})	Material	h_{glob} (kW m^{-2})
1st nucl. cycle - (0-0.5ms)	Silver	3.37	Stainless Steel	4.05
2nd nucl. cycle - (0-1.0ms)		3.53		4.22
3rd nucl. cycle - (0-1.5ms)		3.69		4.35
4th nucl. cycle - (0-2.0ms)		3.86		4.47
5th nucl. cycle - (0-2.5ms)		4.03		4.57
6th nucl. cycle - (0-3.0ms)		4.20		4.66
7th nucl. cycle - (0-3.5ms)		4.38		4.75
8th nucl. cycle - (0-4.0ms)		4.55		4.84
Asymptotic value		10.30 (after 5500 nucl. cycles)		7.66 (after 2800 nucl. cycles)

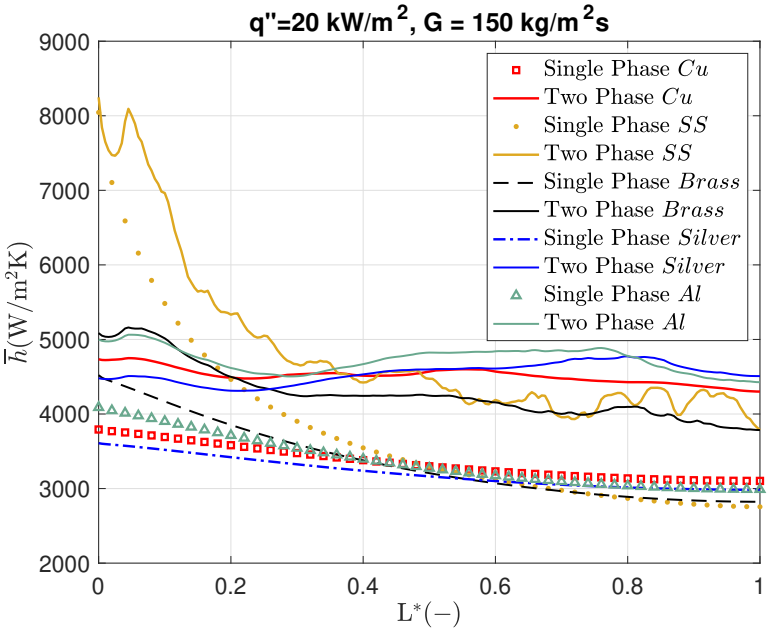

Figure 44: Comparison of the local time-averaged heat transfer between each of the examined materials for the single-phase and the two-phase simulations after ten in total nucleation cycles.

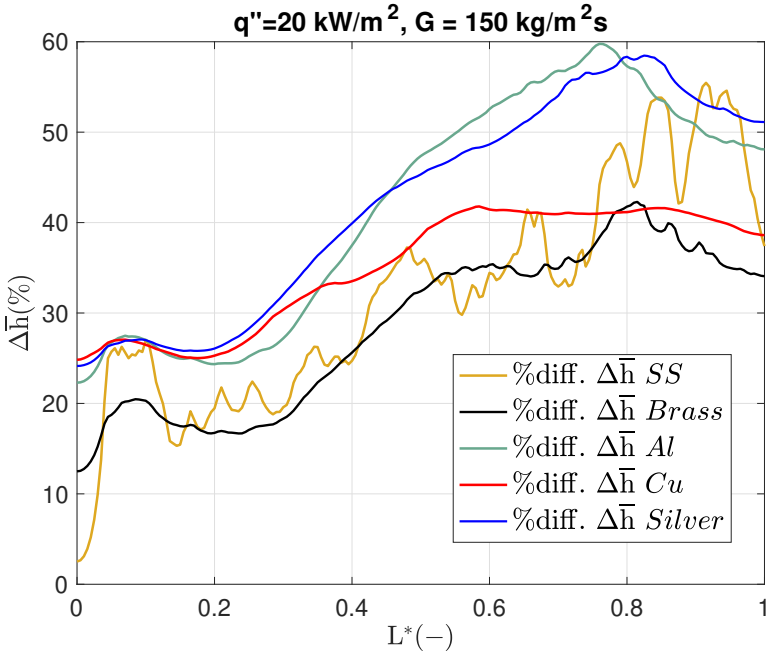

Figure 45: Percentage difference between two-phase and single-phase time averaged $\overline{h}_{(x)}$ over L*, for the five examined cases (the 10^{th} nucleation cycle is considered in all cases).

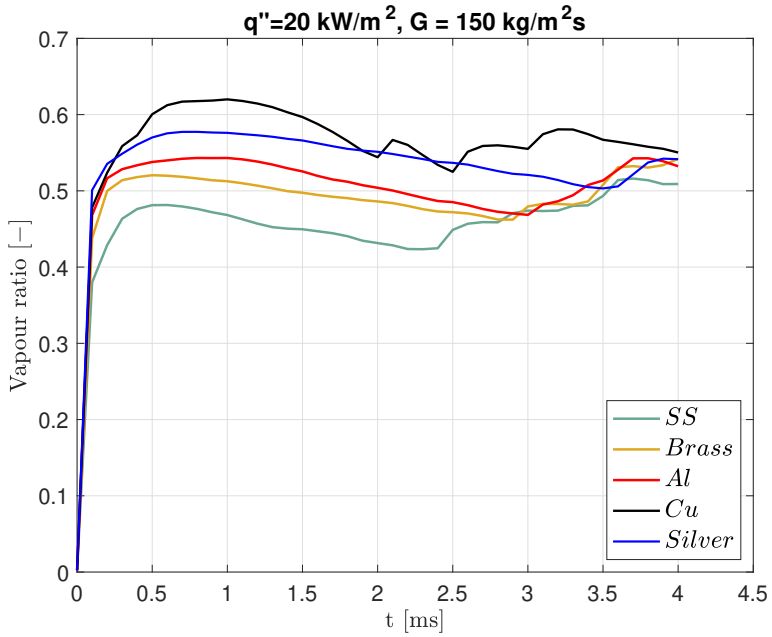

Figure 46: Comparison of the vapour volume ratio (vapour volume / total volume of channel) over time for each examined solid material.

4.3.6 Development of new analytical correlation

Many correlations have been developed in the past for the prediction of the heat transfer coefficient based on wide experimental data on flow boiling within microchannels and minichannels [46, 47, 209, 210], however, the majority of these works ignore the effect of the thermophysical properties of the solid surface, which as already shown in the present study, is substantial. Therefore, by taking into account the CFD results of this work, a new correlation based on an existing empirical correlation developed by Li and Wu [45] (eq. 70), is proposed. The original correlation [45] is based on 3700 data and 13 different working fluids on saturated flow boiling for circular and rectangular mini/microchannels with D_h varying between 0.2 to 3 mm. The correlation developed by [45], takes into account important nondimensional parameters such as the boiling number, ($Bl = qh_{lg}\dot{m}$), the Bond ($Bo = \Delta_\rho g D^2/\sigma$) number and the liquid phase Reynolds number ($Re_l = \rho U D/\mu_l$), for calculating the Nusselt number,

$$Nu_{t-p} = 334 Bl^{0.3} \left(Bo Re_l^{0.36}\right)^{0.4} \tag{70}$$

The nondimensional product $Bo \cdot Re_l^{0.36}$, shows the relative importance of surface tension, body forces, viscous forces and inertia forces in saturated flow boiling in mini/microchannels, whereas the Bl number may be interpreted as a measure of the nucleate boiling contribution. The newly proposed correlation of the present investigation is based on the idea of incorporating the solid material thermal diffusivity expression on eq. 70 and hence correcting the correlation originally suggested by Li and Wu [45] in order to explicitly account for the solid material properties of the smooth and wettable microchannels. For this purpose, the thermal diffusivity ratio is introduced. The proposed ratio is the ratio of the thermal diffusivity of the solid material in each

case to a reference thermal diffusivity. The proposed modified correlation is described by eq. 71,

$$Nu_{t-p} = 334Bl^{0.3}\left(BoRe_l^{0.36}\right)^{0.4}\left(\frac{\alpha}{\alpha_0}\right)^{\zeta} \tag{71}$$

where the term $\alpha = (k_s/\rho_s c_{p,s})$ is the thermal diffusivity of the solid material (in $\mathrm{m^2\,s^{-1}}$) and α_0 is the reference thermal diffusivity which for the present investigation it has been selected as that of the stainless steel channel (material with lowest α). In this way, the effect of the solid domain thermal inertia that is particularly important for flow boiling is taken into consideration.

The predictive accuracy of the above two correlations eq. 70 and 71 was measured utilising the Absolute Error (AE) relationship, i.e., comparing in global terms their predictions with the resulted global Nusselt numbers from the CFD simulations.

$$AE_{\text{old-cor.}} = \left[\frac{|Nu_{tp,global,\text{old-cor.}} - Nu_{tp,global,\text{CFD}}|}{Nu_{tp,global,\text{CFD}}} \times 100\right] \tag{72}$$

$$AE_{\text{new-cor.}}\left[\frac{|Nu_{tp,global,\text{new-cor.}} - Nu_{tp,global,\text{CFD}}|}{Nu_{tp,global,\text{CFD}}} \times 100\right] \tag{73}$$

Figure 47 shows the two-phase global Nusselt number values for the CFD measurements, the original correlation [45] and the new correlation proposed in this study, for all of the examined material cases, for $\zeta = 0.08$. Additionally, in Table 20 the AE values between the prediction from each correlation in comparison to the asymptotic values of the global Nusselt numbers estimated from the CFD predictions are shown. From the above quantitative comparison, it can be seen that the AE values of the global Nusselt number between the correlation of Li and Wu and the CFD data for the aluminium, brass, copper, silver and stainless steel are 35.54%, 1.15%, 20.25%, 32.82% and 9.65%, respectively.

The AE values are significantly reduced when the CFD data are compared with the new proposed correlation. In more detail the values for the aluminium, brass, copper, silver and stainless steel have differences of only 17.47%, 3.36%, 9.39%, 9.65% and 17.43%, respectively, improving considerably the predictive capability of the correlation, which reported a 26.1% average error.

The proposed correlation has been also validated against experimental data ([2, 210, 211]) of flow boiling within minichannels and microchannels. The correlation was tested against experiments of different channel metallic materials under different conditions. Details of the utilised experiments are summarised in Table 21. The validation results of the developed correlation can be seen in Figure 48. This Figure depicts the Nu_{glob} value for nine different experiments and each experimental case the measured Nu_{glob} value is compared with the Nu_{glob} value predicted by the Li and Wu [1] correlation as well as by using the correlation proposed in the present study, for ζ= -0.52. As can be seen for all the experimental cases, the new correlation shows better agreement with the experimental results, showing the importance of solid surface thermophysical properties for the prediction of heat transfer parameters such as the Nu_{glob}. The different ζ values for the comparison with the CFD predicted cases and experimental

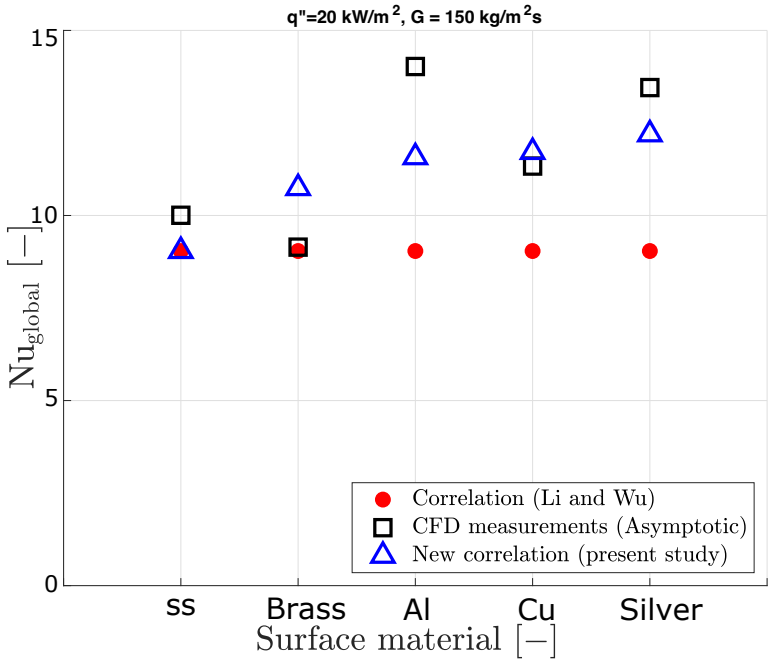

Figure 47: Comparison between the new correlation (proposed in this study) with the original one proposed by Li and Wu [45] and the measurements from the CFD simulations presented earlier, on the global Nusselt number for each examined material.

cases, respectively, can be attributed to the fact that the CFD cases do not represent actual flow boiling experiments (with full-length channels, quasi-steady state conditions and actual nucleation characteristics). Therefore, it is suggested that the corrected correlation that is proposed in the present investigation, should be used with ζ = -0.52. By observing Table 21, we can see that the new correlation is suitable for ranges of q″ between 20 and 400 kW m^{-2}, ranges of G between 150 to 600 kg m^{-2} s^{-1} and hydraulic diameters D_h between 200 to 600 mm.

4.3.7 Conclusions

A numerical investigation, on the effect of solid surface thermophysical properties on flow boiling heat transfer within a single rectangular microchannel has been conducted in the present study. The simulations have been conducted using a custom, enhanced VOF-based model that is also accounting for conjugate heat transfer effects, within the OpenFOAM CFD toolbox. The study is focusing on local instantaneous and time-averaged as well as global heat transfer characteristics, considering periods from the initial stages of the bubble nucleation and growth, up to the first stages of the two-phase flow pattern development. The hydraulic diameter of the considered microchannels is 200 μm, and a constant heat flux of 20 kW m^{-2} is applied at the bottom of the solid domain. The thermophysical properties of five different solid materials are considered, while only one single working fluid is considered flowing with a constant mass flux of 150 kg m^{-2} s^{-1}. The solid surface is ideal, without roughness (smooth) and wettable for all cases. For the first time in the literature the effect of the solid surface thermophysical properties on the two-phase flow and heat transfer characteristics is isolated, identified

Table 20: AE between the asymptotic value of the global Nusselt number estimated from the CFD results and the two correlations (the old correlation that is proposed by [45] and the newly developed correlation that is proposed in the current study).

Surface material	Nu_{glob}, Li and Wu [45], from eq. 70 (-)	Nu_{glob}, CFD measurements (asymptotic) (-)	Nu_{glob}, new proposed correlation from eq. 71	Percentage difference: CFD (asymptotic) vs Li and Wu correlation [45] (%)	Percentage difference: CFD (asymptotic) vs new-proposed correlation (%)
Al	9.04	14.03	11.57	35.54	17.47
Brass		9.15	10.74	1.15	3.36
Cu		11.34	11.72	20.25	9.39
Silver		13.46	12.19	32.82	9.65
SS		10.01	9.04	9.65	17.43

Table 21: Information about the experiments used for the validation of the correlation developed in the present study.

Exp. case	Authors	Microchannel material	q″ (kW m^{-2})	Nu_{glob} (-)	G (kg m^{-2} s^{-1})	D_h (mm)	β (-)
1	[210]	Copper	200	20.98	221	0.59	0.39
2			285	28.74	221	0.59	0.39
3			389	27.49	221	0.59	0.39
4	[2]	Copper	399	26.10	600	0.56	4.94
5			141	16.38	600	0.56	4.94
6			155	26.18	600	0.56	4.94
7	[211]	Brass	50	2.66	500	0.42	0.43
8			83	4.89	500	0.42	0.43
9			101	6.88	500	0.42	0.43

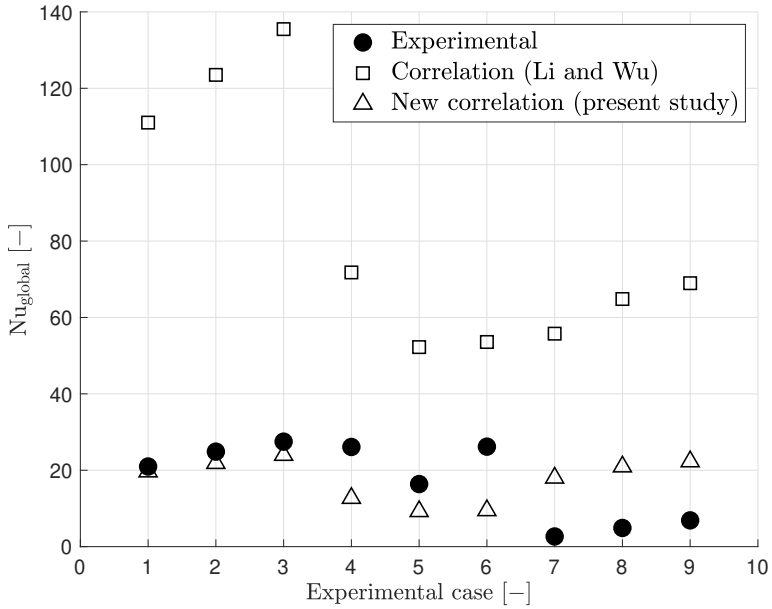

Figure 48: Experimental cases of Nu_{glob} available in literature ([2, 210, 211]), compared to Nu_{glob} calculated by the Li and Wu [1] correlation, and by the correlation proposed in the present study, under the same experimental conditions.

and quantified in detail. The qualitative and quantitative results showed that the variation of such properties substantially affects the resulting flow boiling regimes as well as the heat transfer characteristics and enhancement. A significant increase, compared to the initial single-phase stage simulations, in the time-averaged heat transfer coefficient of more than 40% has been observed for the cases of silver and aluminium, whereas the cases of stainless steel and brass demonstrated a lower heat transfer coefficient increase (e.g. $< 30\%$). The better performance of the aluminium, silver and copper surfaces are linked to the resulting flow boiling regimes, which are characterised by larger volume slugs, higher bubble coalescence rate, less presence of bubbly flow and thicker liquid films. It is important to note that for the case of the stainless steel microchannel, significant fluctuations of the heat transfer coefficient could be seen in the longitudinal direction. These fluctuations contribute to the development of local hot spots along the solid surface, a phenomenon that is non-desirable in microchannel heat sinks in cases where they are used for on-chip cooling. In addition to the above findings, the CFD results led to the development of a modified empirical correlation based on an existing correlation proposed by Li and Wu [45]. This new correlation takes into consideration, for the first time in the literature the thermal diffusivity of the solid material of the microchannels. The new correlation is found to predict the global Nusselt number for all the numerically examined surfaces with absolute error values up to 17.47% in comparison to the existing correlation that results in an absolute error of 35.54%. Finally, the new correlation is expected to contribute to the better design of microchannel heat sinks and their applications since it accounts for solid material characteristics, a parameter that has been shown to play an important role in the resulting fluid flow and heat transfer characteristics.

4.4 Effect of hydraulic diameter on flow boiling within microchannels

Ever since small-scale channels have been considered a promising solution for the efficient heat removal of devices with limited surface area, the classification between microchannels, minichannels, and conventional tubes has attracted the attention of several researchers. The hydraulic diameter D_h constitutes one of the various distinction criteria for this channel classification in the literature.

4.4.1 Scope

The literature reveals that previous experimental works that tried to identify and differentiate the transition limits between conventional tubes and micro-scale channels, in most cases, disagree in their findings. Some of these studies have concluded that the hydraulic diameter range for microchannels should be between 10 and 200 µm [156, 212] while some other studies state that this range should be between 1 and 1000 µm [13, 29, 213]. Such separation is therefore only conventional, and we will conservatively consider only small channels below 200 µm. In spite of the numerous studies on flow boiling experiments in micro-scale channels that have been conducted up to date, there are only a few works focusing on the influence of the hydraulic diameter D_h on important parameters such as the heat transfer coefficient, void fraction, as well as the developed two-phase flow regimes. This has resulted in a lack of accurate design correlations, making the effect of D_h one of the fundamental unresolved issues for comprehending and predicting the heat transfer and two-phase flow characteristics of flow boiling within microchannels. Even for macro-scale tubes, where more investigations have been conducted compared to microchannels, the widely used physical correlations for the prediction of phase-change heat transfer coefficient consider the effect of the hydraulic diameter not accurately enough [214, 215]. In the past years, the effect of D_h has been also included in correlations where minichannels are utilised [216–222]. In the following paragraphs, a review of published investigations is shown, aiming to determine the effect of hydraulic diameter on heat transfer and two-phase flow characteristics.

Lee and Mudawar [188] performed experiments on subcooled flow boiling of HFE 7100 on microchannels for studying the effects of various parameters, including the influence of hydraulic diameter, on heat transfer performance. The D_h of the tested channels varied between 175.7 and 415.9 µm at 1 cm length, and the aspect ratio (AR) was between 2.47 and 4.01. From the results, it is evident that the hydraulic diameter and width of the channel can play a complex role in cooling efficiency. Particularly, it has been observed that, under the same operating conditions, when D_h is decreased, the wetted area increases, leading to lower heat fluxes along the channel walls, causing a void fraction to decrease along the channels. However, decreasing the channel width continuously, results in bubbles spanning the entire width of the channel, promoting an early transition to slug flow.

A series of experimental studies on the effect of D_h were also performed by Harirchian and Garimella [73, 223, 224], using seven different units of parallel microchannels with widths varying between 100 and 5850 µm, all with a nominal length of 400 µm. The coolant FC-77 was used throughout the experiments at various mass flux values. In

their first work [223], the mass fluxes varied between 250 and 1600 $\mathrm{kg\,m^{-2}\,s^{-1}}$. It could be seen that, for a constant applied wall heat flux, the pressure drop was increased when the mass flux was increased, and the channel width was decreased. Additionally, for low mass flux, wall temperatures of the small channels were found to be lower, meaning that heat dissipation was increased when the width of the channel was decreased. Additionally, it was found that pressure drop depended strongly on channel size, as well as on mass flux. Finally, flow boiling was found to be governed primarily by nucleate boiling for a low mass flux of 250 $\mathrm{kg\,m^{-2}\,s^{-1}}$ and all channels $\leq 250\,\mu\mathrm{m}$, while convective boiling was dominant as the width of the channel and mass flux increased. The results have been compared against various correlations published in the literature for both pool boiling and flow boiling heat transfer. The correlation developed by Cooper [31] for nucleate pool boiling could predict the heat transfer coefficients of the performed experiments for the larger channels with an absolute percentage error of 9%. However, for lower mass fluxes and channels with smaller diameters (e.g., microchannels), this error increased. Subsequently, the same authors [73] conducted another study in order to investigate the channel size (100 to 500 µm) and mass flux effect (225 to 1420 $\mathrm{kg\,m^{-2}\,s^{-1}}$) on the transition of flow regimes. The results revealed that, in total, five two-phase flow patterns (bubbly, slug, churn, wispy-annular, and annular flow) have been observed in the experiments. For the 100 and 250 µm width microchannels, the flow regimes were similar to each other (slug flow) and different from those of higher widths. Particularly, when the width of the channel is increased, the bubbly slug flow is replaced by a bubbly flow, and an intermittent churn/annular flow pattern is replaced by an intermittent churn/wispy-annular flow. The reason for this transition was investigated in another work by Harirchian and Garimella [224], which indicated that in micro-scale channels, the cross-sectional area is the most influential parameter. Particularly, its modification resulted in a change of the governing flow boiling mechanism from the convective boiling heat transfer to nucleate boiling heat transfer for microchannels with an area larger than 0.089 $\mathrm{mm^2}$.

Wang and Sefiane [185] experimentally studied the effect of D_h (571, 762, and 1454 µm on 80 mm heated length) on flow boiling heat transfer within high aspect ratio (W/H) micro/mini-channels. Heat and mass flux values ranged between 0 and 18.6 $\mathrm{kW\,m^{-2}}$ and 11.2 to 44.8 $\mathrm{kg\,m^{-2}\,s^{-1}}$, respectively, and the coolant used was FC-72. The results showed that heat transfer is influenced negatively when D_h is increased and that the effect is more significant for higher mass flux values. Convective boiling was reported as the dominant boiling mechanism. The results also showed that, when D_h is increased, the critical heat flux is increased as well. Using the same channels and under the same experimental conditions as described above (heat and mass flux, FC-72), Wang et al. [225] performed an experimental study on flow boiling in channels of different hydraulic diameters in order to analyse two-phase pressure drop and flow fluctuations through thermographic measurements and visualisation results. From the experiments, fluctuations of low-frequency high-amplitude and high-frequency low-amplitude due to the reverse and re-wetting flow and the vapour slug cluster passage could be seen. As the heat flux value increases, the low-frequency high-amplitude fluctuation also increased, while the low-frequency oscillation is reduced by increasing mass flux. For a given mass flux in microchannels with smaller D_h, pressure drop fluctuation amplitudes of low

frequencies were influencing heat flux more. Additionally, when q/G was increasing, the average pressure drop increased as well.

An adiabatic two-phase flow experimental study was conducted by Chung and Kawaji [226] on flow characteristics of a nitrogen gas and water mixtures in round microchannels of 530, 250, 100, and 50 µm diameter with lengths of 277, 157, 64, and 46 mm, respectively. From the experiments, it was observed that microchannels of D_h = 250 and 530 µm had consistent flow regimes with the cases with a hydraulic diameter of 1000 µm (bubbly, slug, churn, slug–annular, and annular flow). For the cases of D_h = 50 and 100 µm, only slug flow could be seen for the investigated flow conditions, and this was related to the significant effects that surface tension and viscosity have on the liquid flow. Additionally, it was shown that when the channel diameter decreases, the multiphase flow frictional multiplier is no longer influenced by the mass flux. Finally, it was concluded that the cross-sectional size of the channel significantly affects the resulting flow regimes, with channel sizes of D_h = 250 and 100 µm showing the most significant changes on the two-phase flow characteristics, while when $D_h < 100$ µm, vividly different two-phase flow characteristics were observed, making the conventional correlations no longer suitable for such gas–liquid pairs. Kawahara et al. [227] further investigated the above research to study the effect of channel cross-sectional size and liquid properties on volume fraction again in isothermal two-phase flows (water/nitrogen gas and ethanol–water/nitrogen gas mixtures) within round channels of D_h = 50, 75, 100, and 251 µm. It has been concluded that the volume fraction changes significantly between channels of D_h = 251 and 100 µm. This is due to the surface tension effects, which play a substantial role as is reduced (e.g., < 251 µm).

Gunnasegaran et al. [228] performed numerical simulations on single-phase fluid flow characteristics and heat transfer, examining the effects of hydraulic diameter and microchannel shape. The simulations used three full-scale microchannel heat sinks, each with different geometrical shapes (rectangular, triangular, and trapezoidal). Each heat sink consisted of 25 parallel microchannels. Heat flux values varied from 100 to 1000 kW m^{-2} and were supplied to the solid (aluminium) through a top plate. For each geometrical shape, three cases were examined, each with a different hydraulic diameter, whereas the length was kept constant at L = 10 mm. The height/width ratio was 2.55, 1.53, and 1.03, and D_h varied between 148 and 385 µm. The working fluid was water, and the Reynolds number ranged between 100 and 1000. The simulation results indicated that for rectangular-shaped microchannel heat sinks, when D_h is decreased, the heat transfer is increased. When comparing the geometrical shapes, the rectangular shape microchannels showed the highest heat transfer rate and Poiseuille number, the trapezoidal case was in between, and the triangular shape had the lowest performance. Additionally, as expected, it was indicated that when the Re number is increased, the value of the heat transfer coefficient is increased as well.

Sahar et al. [229] also numerically studied the effect of D_h and aspect ratio on single-phase flow heat transfer in a single rectangular micro-passage using ANSYS Fluent 14.5. Two sets of simulations were performed. In the first case, hydraulic diameters ranged between 100–1000 µm, and the AR remained constant at 1. Subsequently, the AR ranged between 0.39 and 10, and the hydraulic diameter remained unchanged at 560 µm. The working fluid was water, and the Re numbers varied between 100 and 2000.

Constant heat-flux was applied at the bottom and the two side walls of the channel, whereas the top wall was considered adiabatic. Conjugate effects were ignored. The numerical results demonstrated that the average Nusselt number and friction factor increases when D_h is increased as well. Additionally, it was found that the effect of hydraulic diameter on heat transfer and friction factor is more influential than the effect of aspect ratio. Another numerical investigation on the channel confinement and hydraulic diameter effect on the single-phase fluid flow heat transfer on rectangular channels using ANSYS Fluent 15 was performed by Sathishkumar and Jayavel [230]. The hydraulic diameters ranged between 100 and 1000 µm (keeping constant AR = 1 and L = 62 mm) with Re numbers of 500 and 1500. The constant heat flux boundary condition was prescribed at the bottom and the two side walls, whereas the top wall was considered adiabatic, with a uniform inlet velocity condition being imposed at the inlet of the channel, and zero pressure was imposed at the exit of the channel. The channels consisted of a constant mesh size of 20 × 15 × 400 cells. Based on the simulation results, it is concluded that the heat transfer is significantly affected by the variation of D_h and channel confinement and that with the increase in D_h, the Nusselt number value increases for both Re cases.

Apart from studying the effect of channel diameter, more recent investigations have focused on the influence of the number of parallel microchannels, aiming to provide answers on whether the increase in the total number of microchannels could lead to a higher heat transfer performance [231, 232]. The influence of the number of parallel micro-passages on flow boiling heat transfer of water has been studied both experimentally and numerically in the past by Hedau et al. [233]. The applied heat flux values ranged between 230 and 2200 $\mathrm{kW\,m^{-2}}$ and mass flux between 250 and 500 $\mathrm{kg\,m^{-2}\,s^{-1}}$. For the numerical part, the VOF solver of ANSYS Fluent 16.0 has been employed, and the phase change model developed by Lee was utilised for the mass transfer process of evaporation [30]. The considered heat sinks included 6, 10, and 14 parallel microchannels for a D_h of 810, 590, and 384 µm, respectively. From the results, it was concluded that, for a high number of channels, a greater heat transfer coefficient is achieved. Specifically, the HTC for the 14 channels case and applied heat flux of 2200 $\mathrm{kW\,m^{-2}}$ was found to be increased by 240% compared to the case with the six channels for the same flow conditions. This was attributed to the low thickness of the film evaporation throughout the annular flow regime due to the increased available surface to volume ratio as compared to the case with six microchannels.

More recently, Dai et al. [234] conducted a numerical investigation on the effect of various parameters such as porosity, channel thickness, height, material, and channel number on flow boiling characteristics, using a microencapsulated phase change material slurry as the working fluid. A heat flux of 1000 $\mathrm{kW\,m^{-2}}$ was applied at the bottom side of the heat sink, whereas the inlet velocity was 2 $\mathrm{m\,s^{-1}}$. The commercial CFD software ANSYS Fluent 17.0 was utilised, with a grid size of approximately 800 K cells. The thermal resistance between multi-channel heat sinks, consisting of 30, 40, 50, 60, 70, and 80 channels, was measured, and it was found that, as the microchannel number increased, thermal resistance increased as well, attributing this to the reduction in copper vertical rib thickness, which was not kept constant for this investigation.

It is therefore evident that despite the fact that the effect of microchannel hydraulic

Table 22: Dimensions of the considered microchannels and total number of cells for the solid (s) and fluid (f) domains.

Case	D_h (mm)	H_f (mm)	W_f (mm)	H_s (mm)	W_s (mm)	No. of Cells ($\times 10^6$)	
						Solid	Fluid
I	50	75	37.5	90	37.5	1.0125	3.375
II	100	150	75	90	75	2.025	6.75
III	150	225	112.5	90	112.5	3.0375	13.125
IV	200	300	150	90	150	4.05	13.5

diameter has been widely studied, providing valuable information so far on the heat transfer and flow characteristics, the majority of these investigations also alter other important parameters, such as the aspect ratio and the geometrical shape of the cross-section, resulting in contradicting conclusions. Furthermore, the majority of these cases focus on results after a steady state condition has been achieved in the system, ignoring the early stages of the fluid flow characteristics and heat transfer. Finally, the majority of the numerical works are focusing either on single-phase flow phenomena or ignore the conjugate heat transfer effects. For this reason, the objective of the present work is to investigate the effect of channel hydraulic diameter on flow boiling heat transfer on the first transient stages of flow pattern development and heat transfer characteristics by performing numerical simulations where the channel hydraulic diameter will be varied and all other flow and channel design parameters will remain unchanged, thus isolating the investigated effect. This also constitutes the key novelty of the present work. As the exact isolation of the hydraulic diameter without affecting other important flow and heat transfer characteristics, also taking into account the conjugate heat transfer effects, is numerically examined for the first time in the literature. For a better understanding of the phenomena, different values of heat and mass flux have been considered, with a detailed qualitative and quantitative comparison of the numerical predictions. Additionally, in the present work, a comparison between a single microchannel and four parallel microchannels, of the same total hydraulic diameter, is also conducted. In this case, to isolate the investigated effect, the total volumetric flow rate for both cases remains constant, while the flow rate passing from each of the four parallel channels is reduced by a factor of four, accordingly.

4.4.2 Numerical set-up

The shape of the tested microchannels is rectangular, and the aspect ratio (AR = W/H) is set to 0.5 for all the cases. For the first set of simulations, the examined hydraulic diameters D_h are 50, 100, 150, and 2.4 µm, and the length of the channels is 2.4 mm. Information about the dimensions of the utilised microchannels is shown in Table 22.

As in the previously presented studies in this chapter a constant heat flux q″ boundary condition is applied at the bottom wall of the solid domain, whereas the other walls of the channels are considered adiabatic (more details about the boundary conditions

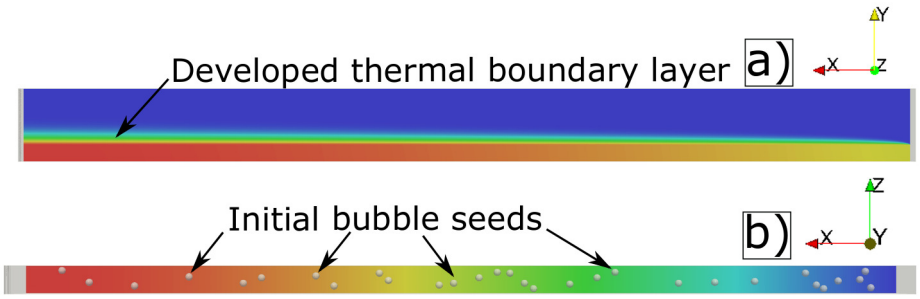

Figure 49: (a) Developed thermal boundary layer at the end of the first stage of simulations (single-phase). (b) Position of the 30 patched bubble seeds that has been used for all the numerical simulations at the beginning of the second stage (referred as initial time t = 0 ms).

can be found in subsection 4.1.2). Similarly, all the simulations were conducted in two phases (single-phase until fully developed hydrodynamic and thermal boundary layer is developed) and after that 30 bubbles (radius of 10 µm) along each channel, are positioned. The working fluid is ethanol (at 1 bar, Table 3) and the microchannel and heated plate material is considered stainless steel (Table 4). The mesh details and computational domain are shown in Figure 9. The developed thermal boundary layer (on side view) and the position of the thirty bubbles that have been patched at time 0 ms, on top view are shown in Figure 49.

For isolating the exact effect of the microchannel hydraulic diameter, all the fluid and solid properties, as well as the total applied heat transfer rate Q (in W), together with the volumetric flow rate $\dot{V}$ (in $m^3\,s^{-1}$), are kept constant. To keep Q and $\dot{V}$ values constant since the hydraulic diameter of each microchannel varies, the applied heat flux q″, velocity of the fluid flow U_l, and hence the mass flux G (see Eq. (16)) vary accordingly with respect to the hydraulic diameter variation. In order to be able to better understand the phenomena, under different conditions, each of the considered hydraulic diameters are tested for two different values of applied heat flux q″, keeping the heat transfer rate constant at values of Q = 7.20×10^{-3} W and 1.80×10^{-2} W, respectively. The above selected conditions for the simulations are selected to be similar to those reported in experimental investigations of saturated flow boiling within microchannels available in the literature, e.g., [2]. The overall operating conditions considered for the numerical experiments are summarised in Table 23.

In order to have a more realistic case scenario, after the initial nucleation of the thirty bubbles at t = 0 ms, multiple recurring nucleation events of thirty bubbles with constant nucleation frequency of every 0.4 ms and at the same nucleation position, as shown in Figure 49, have been chosen for the presented simulations. Hence, each nucleation cycle lasts for 0.4 ms, and a total of 10 nucleation cycles are considered (10×0.4 ms = 4.0 ms) for all of the considered D_h, heat, and mass fluxes. More than 800,000 core-hours were needed for the overall runs that are presented in this subsection.

Table 23: Operating conditions of the microchannels.

D_h (µm)	$\dot{V}$ ($m^3\,s^{-1}$)	U_l ($m\,s^{-1}$)	G ($kg\,m^{-2}\,s^{-1}$)	Re (-)	q″ ($kW\,m^{-2}$)	Heat Transfer rate Q (kW)	q″ ($kW\,m^{-2}$)	Heat Transfer rate Q (kW)
50	9.1611×10^{-9}	3.26	2400	271	q″ = 80	7.20×10^{-6}	q″ = 200	1.80×10^{-5}
100		0.81	600	135	q″ = 40		q″ = 100	
150		0.36	267	90	q″ = 26.67		q″ = 66.67	
200		0.2	150	67	q″ = 20		q″ = 50	

4.4.3 Numerical results: Effect of hydraulic diameter for a single microchannel

The results from the simulations examining the effect of hydraulic diameter considering a single rectangular microchannel are presented in the following paragraphs. Initially, the cases with constant Q = 7.20×10^{-3} W and varying heat fluxes (20, 26.7, 40, and 80 kW/m^2) and constant volumetric flow rate of $\dot{V} = 9.1611 \times 10^{-9}\,m^3\,s^{-1}$ with varying mass fluxes (150, 267, 600, 2400 kg/m^2), which correspond to hydraulic diameters of 200, 150, 100, and 50 µm, respectively, will be presented. In Figure 50, qualitative/macroscopic flow visualisation results of the spatial and temporal evolution of the generated vapour bubbles for all the examined hydraulic diameters are illustrated. A top view and a 3D isometric view are shown for four successive time instants in each case. Overall, from a first analysis of the qualitative data, it can be inferred that the effect of the D_h of the channel exerts a significant influence on the resulting two-phase flow regimes, with the diameter of a 100 µm to be considered as a flow regime transition threshold. For all cases, the initialised bubble seeds on the heated wall grow and merge, forming large, elongated bubbles, which are transferred downstream by the liquid cross-flow. For the cases of 50 µm and 100 µm, after each nucleation cycle, the detachment of the bubbles occurs rapidly, resulting in a churn flow for the former case and into an initially churn flow, during the early time instants (e.g., within the first millisecond), which is quickly transitioned into a slug flow for the 100 µm case. On the other hand, for the other two cases, bubble detachment lasts a few fractions of a millisecond more, leading to a direct slug flow regime. By observing both top and 3D views of the macroscopic results, it can be seen that, for all cases, there is no contact between the adiabatic top wall and the generated bubbles, whereas a contact between some of the bubbles with the two adiabatic sidewalls can be seen for all the cases, for at least one of the shown time instants. However, it is clear that the generated bubbles for the case of 100 µm have the least contact with the three adiabatic walls of the microchannel, meaning that no formation of dry patches is seen in these regions in this particular case. This may be attributed to the comparatively thicker liquid film surrounding the vapour slugs compared to the cases with higher hydraulic diameter. With regard to the shape of the vapour bubbles, after detaching from the surface and the leading edge approaches the outlet of the channel, a characteristic symmetric

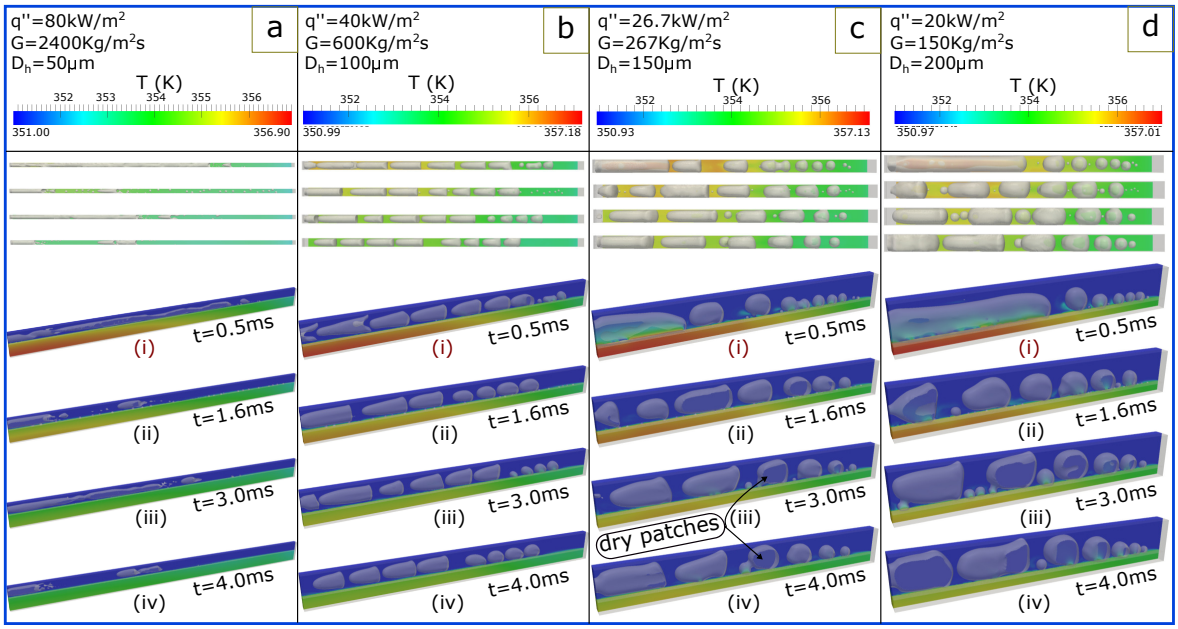

Figure 50: Numerical flow visualisation results for constant $Q = 7.20 \times 10^{-3}$ W and $\dot{V} = 9.1611 \times 10^{-9}\,m^3\,s^{-1}$. Four common time instants are shown for all cases, whereas at the top of each column, the heat flux, mass flux, and hydraulic diameter is shown..

bullet shape nose is observed for all cases. The curvature of the nose increases as the hydraulic diameter decreases, leading to an increment of the evaporation liquid film thickness. Overall, liquid film evaporation is the main heat transfer mechanism for all cases. For the cases of 150 µm and 200 µm, the primary heat transfer mechanism during the early stages of the vapour bubbles growth (e.g., 0.5 ms) is the contact line (meniscus) evaporation due to the delayed detachment of the bubbles from the heated surface. However, for the later time instants, the already generated elongated vapour slugs have detached from the heated surface, making liquid film evaporation the main heat transfer mechanism.

During the second set of simulations, the heat transfer rate for all the cases is increased to $Q = 1.80 \times 10^{-2}$ W by varying the corresponding applied heat fluxes to 50, 66.7, 100, and 200 $kW\,m^{-2}$ for each of the considered channel hydraulic diameters. The volumetric flow rate and mass flux have remained unchanged compared to the previous set of simulations, with the values being $\dot{V} = 9.1611 \times 10^{-9}\,m^3\,s^{-1}$ and G = 150, 267, 600 , and 2400 $kg\,m^{-2}\,s^{-1}$ for the cases of D_h = 200, 150, 100, and 50 µm, respectively. Figure 51 shows the qualitative numerical results for four common time instants. With regard to the flow characteristics, Figure 51 indicates that the increase in heat flux has resulted in an increased bubble growth rate; hence, more elongated bubbles for the cases of 100, 150, and 200 µm can be observed, whereas, for the 50 µm microchannel, no significant difference compared to the corresponding D_h case of Figure 50 can be observed. Churn flow appears to be the two-phase flow regime for the cases of 50 and 100 µm; however, a transition into slug flow is also observed for some cases. Similar to the previous set of simulations, the scaling down of D_h increases the curvature of the nose of the bubble(s) and hence the thickness of the liquid film. Finally, contact

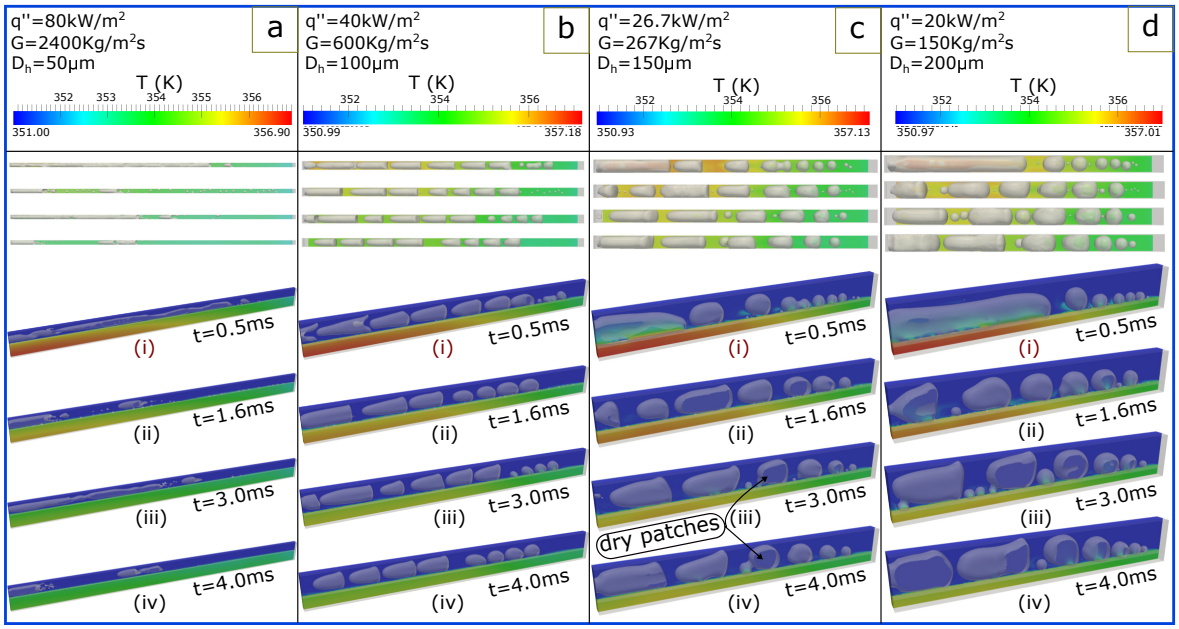

Figure 51: Numerical flow visualisation results of hydrophilic cases for constant Q=1.80×10^{-2} W and $\dot{V} = 9.1611 \times 10^{-9}\,\mathrm{m^3\,s^{-1}}$. Four common time instants are shown for all cases, whereas at the top of each column, the heat flux, mass flux, and hydraulic diameter is shown.

line evaporation can be considered as the main heat transfer mechanism during the very early stages of the evaporation process (e.g., 0.5 ms) for the cases of 200, 150, and 100 μm; however, for later time instants, the main heat transfer mechanism is liquid film evaporation. For the 50 μm case, the main heat transfer mechanism is liquid film evaporation.

A quantitative comparison of these cases is conducted in Figures 52 and 53. In Figure 52, the dimensionless time-averaged local Nusselt number $\overline{Nu}(x)$ over the dimensionless length of the channel L^* for all of the examined hydraulic diameter, heat, and mass flux combinations, together with their reference single-phase stage, is plotted. Subsequently, the percentage difference of the global Nusselt number (Nu_{glob}) between the two-phase simulations compared to the corresponding single-phase is shown in Table 24. At first glance, examining the resulting curves on Figure 52, it is clear that the increase in D_h implies a linear increase in the overall $\overline{Nu}(x)$ for both of the considered applied heat transfer rates for the single and two-phase simulations. Additionally, a negligible effect of the increase in the applied heat rate is observed in the single-phase curves for all cases as well as in the two-phase curves for some of the considered hydraulic diameters. In Figure 53, the percentage difference between the single-phase and the corresponding two-phase simulation of the local time-averaged heat transfer coefficient

$$\Delta\overline{h}(x) = \frac{\overline{h}(x)_{t-p} - \overline{h}(x)_{s-p}}{\overline{h}(x)_{s-p}} \times 100 \tag{74}$$

versus the L* is plotted for both examined heat transfer rates Q. It is clear from this

figure that the heat transfer coefficient variation is much smoother for the case of $D_h = 50\,\mu m$ compared to the case of 200 µm. Additionally, it is also clear that the case of 200 µm m shows the greatest increase in $\overline{h}(x)$, followed by the case of 100 µm and the cases of 200 µm and 150 µm, respectively. This is also evident by observing Table 24, where for $Q = 7.20 \times 10^{-3}$ W, the Nu_{glob} for the 50 µm two-phase case has been increased by 37.4%, compared to the corresponding single-phase simulation, and that for the 100 µm case has been increased 25.9%, whereas for the 150 and 200 µm cases, Nu_{glob} have both been increased by 22.2%. The increase in the heat transfer rate to Q= 1.80 $\times 10^{-2}$ W seems not to have positively or negatively affected the heat transfer performance of the 50 µm channel, while for the other cases, a further increase in the Nu_{glob} is observed.

Based upon the qualitative and quantitative results of the simulations presented so far, the following noteworthy conclusions can be drawn:

- The increase in heat transfer rate Q has resulted in an increase in bubble growth rate and bubble coalescence, resulting in more elongated vapour slugs.
- The bubbles grow to occupy the entire cross-section with elongated or intermittent vapour slugs within a few fractions of a millisecond.
- For the case of $Q = 7.20 \times 10^{-3}$ W, dry patches are formed only on the adiabatic side walls of the microchannel and mainly for the cases of hydraulic diameter $D_h = 200$ and 150 µm. For the case of Q = 1.80 $\times 10^{-2}$ W, dry patches are formed mainly on the two side walls of each channel, but also sometimes on the top adiabatic wall, close to the inlet of the channel.
- A characteristic bullet shape nose can be seen in all cases. The curvature of the nose is increased with the decrease in hydraulic diameter for both examined values of heat transfer rate. An increase in the curvature is also observed by increasing heat transfer rate
- For the simulations of low heat transfer rate, churn flow is the developed flow regime for the 50 µm channel, while churn flow is also seen in the first few milliseconds for the case of 100 µm, which then transitions into an intermittent vapour slug regime. For the cases of 150 µm and 200 µm, due to the comparatively delayed coalescence of the evaporating bubbles, a slug flow regime is developed.
- Liquid film evaporation is the main heat transfer mechanism for all cases. For the cases of 50 and 100 µm, this is evident throughout the numerical experiments, whereas for 150 and 200 µm, contact line evaporation is the main contributing heat transfer mechanism for the first two nucleation cycles and liquid film evaporation for the rest of the simulation.
- For the simulations of high heat transfer rate, churn flow is the flow regime for the 50 µm case, while an initial churn flow that transitions into a slug flow is evident for the other three cases. In other words, the increase in heat transfer rate did not affect qualitatively the flow characteristics of the 50 µm channel, whereas for

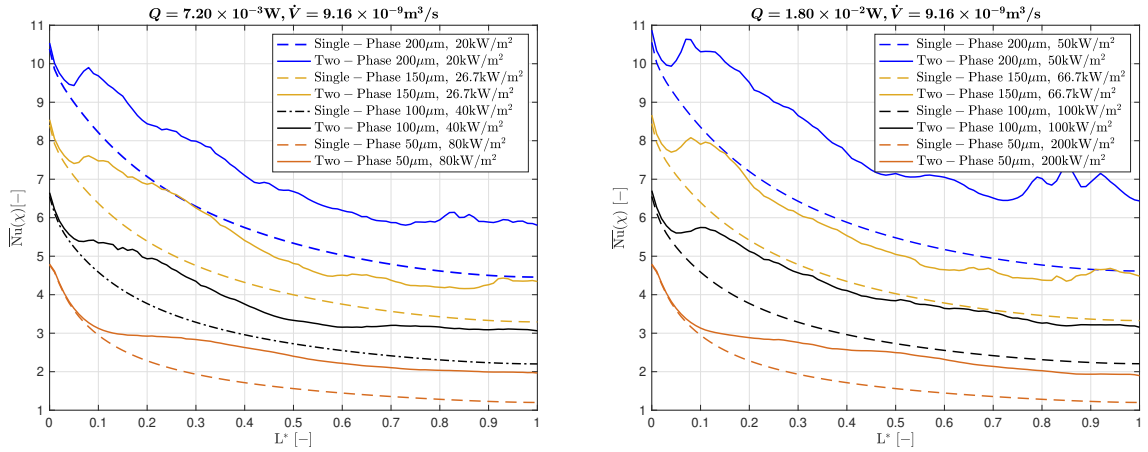

(a) **(b)**

Figure 52: Influence of hydraulic diameter on time-averaged local Nusselt number on both single and two-phase simulations on constant heat transfer and volumetric flow rates, and varying heat and mass fluxes.

the other three channels, higher bubble growth rates and comparatively more elongated slugs are observed.

- The difference in the two-phase flow regimes between the tested cases has also resulted in a different heat transfer performance.
- Heat transfer is deteriorated by increasing the hydraulic diameter of the channel when comparing the corresponding single and two-phase flow simulations, as shown by the time-averaged heat transfer coefficient difference $\Delta\overline{h}(x)$ comparison.
- The increase in the heat transfer rate indicated that the effect of channel diameter is more evident when the heat transfer rate is lower. Furthermore, when the heat transfer rate was increased a substantial enhancement of the heat transfer could be seen for the microchannels of 200, 150, and 100 µm, whereas no important difference could be seen for the microchannel with the smallest hydraulic diameter.
- The trend representing the global Nusselt number curve of the single-phase simulations is identical, regardless of the hydraulic diameter of the microchannel, and they all increase with the increase in hydraulic diameter. As expected, different trends could be seen when comparing the two-phase simulations.
- The variation of the time-averaged heat transfer coefficient difference $\Delta\overline{h}(x)$ versus the dimensionless length L^* is much smoother for the case of small hydraulic diameter compared to the case of 200 µm.

4.4.4 Numerical results: Effect of the number of parallel microchannels

As mentioned earlier, in addition to the effect of channel diameter, researchers have been also focused on the effect of the number of the microchannels in order to see whether the

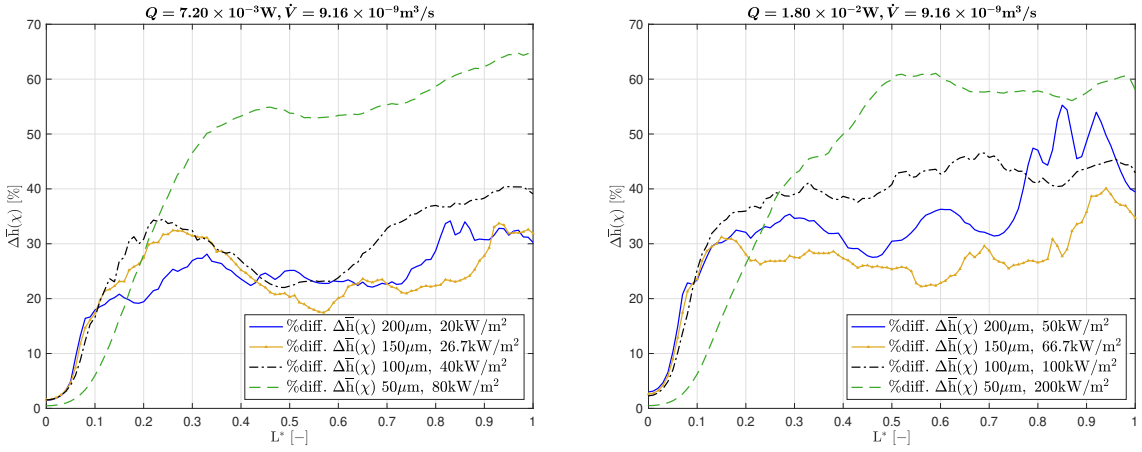

(a) **(b)**

Figure 53: Effect of hydraulic diameter on time-averaged heat transfer coefficient difference $\Delta\overline{h}(x)$ over the dimensionless length L^* between the corresponding single and two-phase simulations for the examined hydraulic diameters with constant heat transfer and volumetric flow rate and varying heat and mass fluxes.

Table 24: Comparison of the Nu_{glob} and percentage difference between single-phase and two-phase results for the examined Q and D_h.

	For Q $= 7.20 \times 10^{-3}$ W and $\dot{V} = 9.1611 \times 10^{-9}$ m^3 s^{-1}			Q $= 7.20 \times 10^{-2}$ W and $\dot{V} = 9.1611 \times 10^{-9}$ m^3 s^{-1}		
D_h (µm)	Single-Phase (–)	Two-Phase (–)	% Difference (%)	Single-Phase (–)	Two-Phase (–)	% Difference (%)
50	1.851	2.542	37.4	1.851	2.539	37.2
100	3.087	3.887	25.9	3.091	4.163	34.7
150	4.443	5.427	22.6	4.472	5.609	25.4
200	5.866	7.168	22.2	6.011	7.912	31.7

division of a single microchannel with specific D_h into a greater number of channels with smaller D_h, or vice versa, can enhance heat transfer and flow characteristics. In this subsection simulations of fully three-dimensional microchannel heat sinks accounting for conjugate effect are conducted, aiming to compare and propose an optimal geometric design where the minimum overall thermal resistance will be used as an objective function. This investigation considers the effect of a number of microchannels by performing numerical simulations of a single microchannel with $D_h = 200\,\mu m$ and four parallel microchannels, each having $D_h = 50\,\mu m$, totalling $D_h = 200\,\mu m$. In order to perform a more realistic investigation, both cases are surrounded by solid walls of stainless steel. As in the previous set of simulations, initially, single-phase simulations were run up to a point where the thermal and hydrodynamic profiles are fully developed. Consequently, the time was set to 0.4 ms, and thirty bubbles, each with a radius of 10 µm, were patched on the solid–liquid interface at the same position along the channels every 0.4 ms for seven nucleation cycles, up to 3.2 ms. Furthermore, in order to isolate the effect of channel number, all the other parameters, such as the total flow rate, heat flux, as well as the aspect ratio and wall thicknesses around the channels, were kept the same. An applied heat flux of $50\,kW\,m^{-2}$ was uniformly applied at the bottom wall, corresponding to a total heat transfer rate of $Q = 1.80 \times 10^{-2}$ W. The total volumetric flow for the two cases was selected to be $\dot{V} = 9.1611 \times 10^{-9}\,m^3\,s^{-1}$. Mesh details and boundary conditions for the numerical setups are shown in Figure 44a,b for the single and multiple microchannels cases, respectively. The corresponding geometrical characteristics of the tested microchannels and the fully developed thermal boundary layer at the beginning of the two-phase simulation (t = 0.4 ms) are shown in Figure 54c,d. Finally, a top view of the considered microchannels and the position of the patched bubbles at t = 0 ms (and at the beginning of every nucleation event) are shown in Figure 54e,f.

Flow visualisation results for both microchannels are shown in Figure 55. Initially, it can be observed that changing the design of the microchannel has resulted in a significant difference in the temperature gradient between the two cases. Specifically, for the case of a single microchannel, the spatial temperature difference ΔT between the hottest and the coolest spots is 6.7 K, whereas for the four parallel microchannel case, ΔT is 3.6 K. The different design also exhibited a difference in the generated two-phase flow regimes. For the case of the single channel heat sink, in the first half towards the inlet of the microchannel, the merging of the bubbles occur at such a rate where the detachment of the merged bubbles and their subsequent transformation into small vapour slugs requires approximately a complete nucleation cycle (0.4 ms). On the other hand, in the second half of the channel, churn flow is observed immediately after boiling incipience for the first four nucleation cycles (1.6 ms), which are characterised by a highly fluctuating, non-uniform interface between the liquid and the vapour phases. This can be attributed to the high coalescence rate, which is caused by the fast growth rate of each of the patched bubbles in this hotter region of the channel. However, as the temperature of the heated wall is decreased, a transition into slug flow is observed. For the case of the four parallel channels, churn flow is observed throughout the overall numerical experiment within all the parallel microchannels. It is worthwhile mentioning that, in all four microchannels, the developed two-phase flow regimes are quite similar at

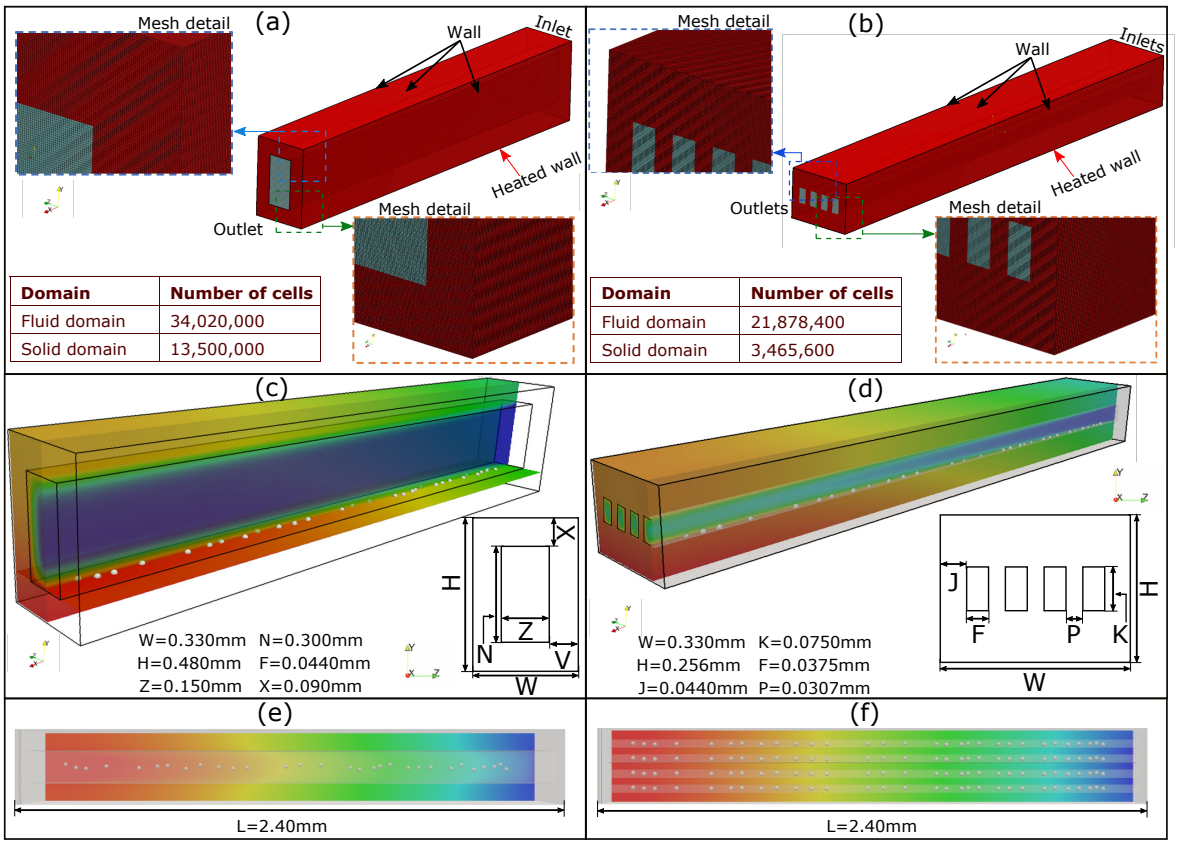

Figure 54: Left—case with single microchannel (D_h = 200 µm × 1 channel). Right—case with four parallel microchannels (D_h = 50 µm × 4 channels). (a,b) Computational domain and mesh details, (c,d) 3D angled view of the microchannel(s) and fully developed thermal boundary layer at t = 0 ms, (e,f) top view and patched bubbles position at t = 0 ms.

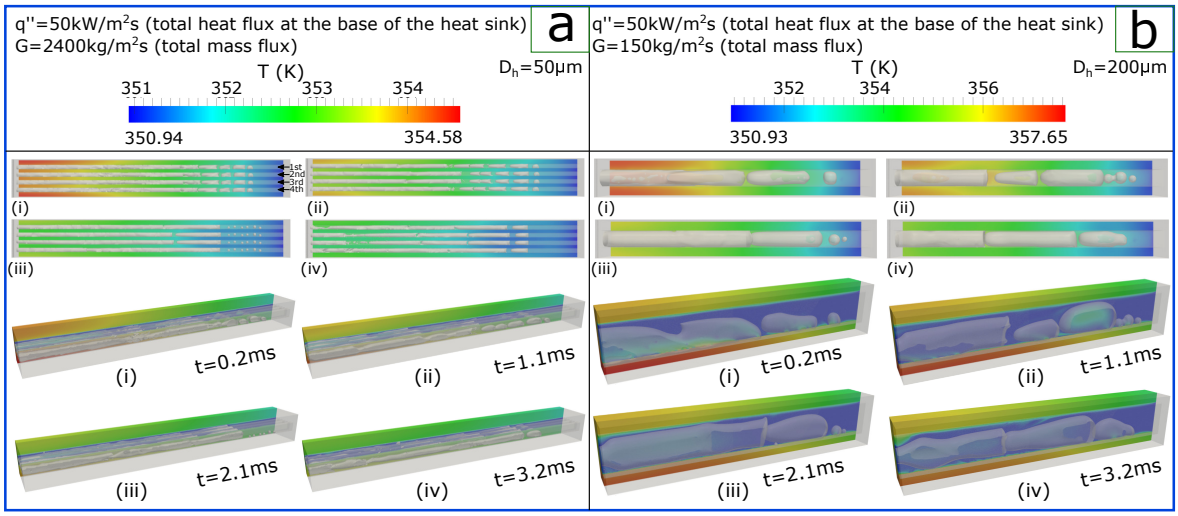

Figure 55: Top view and 3D side view comparison between the four parallel channels (a) and single case channel (b) for constant Q = 1.80 $\times 10^{-2}$ W and $\dot{V} = 9.1611 \times 10^{-9}\,\mathrm{m^3\,s^{-1}}$. Four common time instants are shown.

the earlier stages but have evident differentiation at later stages, especially between the end and middle channels. This is evidence of the effect of the solid domain inertia on the developed boundary conditions at the corresponding conjugate boundaries. Therefore, due to symmetry, the two middle channels and the two outer channels present similar two-phase flow patterns, but comparing the instantaneous two-phase flow pattern of an outer and an inner channel, noticeable differences exist. Additionally, by observing and comparing Figures 51a and 55a, it is evident that, for the latter case, where solid walls surround the microchannels, the developed flow boiling regime is not significantly affected. Dry patches are formed in the side walls of each channel, whereas the top wall has no contact with the bubbles. The main heat transfer mechanism for the bottom and top walls of the four-channel case is liquid film evaporation, with a very small contribution of contact line evaporation close to the inlet of each channel. Conversely, due to the significant presence of dry patches, contact line evaporation is the main heat transfer mechanism on the side walls of the same case. For the single channel case, contact line evaporation is the main heat transfer mechanism for the first millisecond of the boiling process. However, as the temperature gradient between the solid surface decreases and the flow regime is transitioned into slug flow, the main heat transfer mechanism is liquid film evaporation.

Figure 56 illustrates the local time-averaged thermal resistance, $\overline{R}_l$, of the two examined cases, measured in the solid–fluid interface along the channel for the single channel case and in the solid–fluid interface along each channel for the multiple parallel channel case. In order to evaluate the heat transfer performance of the multiple microchannel case and to compare it with the single channel case, both the global, R_{glob}, and local time-averaged thermal resistance, $\overline{R}_l$, are used:

$$R_{glob} = \sum_{i=j}^{n} R_{j,n}/L^* \tag{75}$$

where

$$\overline{R}_l = \left(\overline{T}_{\text{wall}} - T_{\text{sat}}\right) / A_{HA} q'' \tag{76}$$

From the results, it is evident that the different heat sink configuration has significantly affected the overall thermal resistance $\overline{R}_l$. Even though the trend lines between the single-phase results are similar, the case of the single microchannel has significantly higher $\overline{R}_l$ compared to the case of multiple channels. For both single-phase lines, the $\overline{R}_l$ starts at a minimum value in the inlet of the channel and increases linearly along the flow path, reaching a maximum value in the outlet of the microchannel(s). By comparing the dashed lines representing the single-phase simulations in Figure 56, it is clear that the multiple channel case has substantially less thermal resistance compared to the single channel case, meaning that the convection heat transfer is much more efficient in the multiple channel case. This is mainly due to the convective heat transfer coefficient being inversely proportional to the hydraulic diameter of the channels, which, in the single microchannel, is four times greater compared to the multiple channels case. Additionally, this may also be attributed to the fact that, for the four-channels case, the uniformity of the temperature distribution is significantly better compared to the single channel heat sink. As expected, when comparing the two-phase results, the contribution of the flow boiling has resulted in a lower temperature of the conjugate boundary, leading to lower thermal resistance compared to the corresponding single-phase simulations. These results reveal that there is a significant augmentation in flow boiling heat transfer performance in the case of four parallel channels, compared to the case of single channel. Initially, this can be attributed to different flow regimes and the thicker liquid film (either at the corners or walls) formed in the case of the single channel, which results in weaker liquid film evaporation and reduced heat transfer. Another reason for this difference is the fact that contact line evaporation, seen up to 1.0 ms in the single channel case, may have resulted in partial dry-out and further deterioration of the local heat transfer coefficient. In addition, as noted by Wang et al. [225], the complexity of the flow field is increased by the larger cross-sectional area, which has more space available for thicker liquid films.

4.4.5 Temperature and volume fraction comparison within each microchannel

As noted earlier, for the case of four parallel channels, the flow patterns were similar regardless of the position of each channel within the solid surface. Therefore, it is interesting to observe whether this behaviour is also observed quantitatively or not. Thus, the time - averaged temperature $\overline{T}$ at the fluid–solid interface of the bottom heated wall along the flow path, as well as the time averaged vapour volume within each microchannel, has been measured and presented in Figure 57. The $\overline{T}$ results L* shown in Figure 57 indicate that the $\overline{T}$ values through the flow boiling process remain almost unaffected for the end channels 1 and 4 as well as for the middle channels, channels 2 and 3 (the numbering of the channels can be seen in Figure 56). Furthermore, the trend of the four channels is also identical. As for the vapour volume, this has been plotted over time t and is shown in Figure 57b. From the results, it is noted that curves show similar trends; however, as in the cases of $\overline{T}$, the group of the end channels and

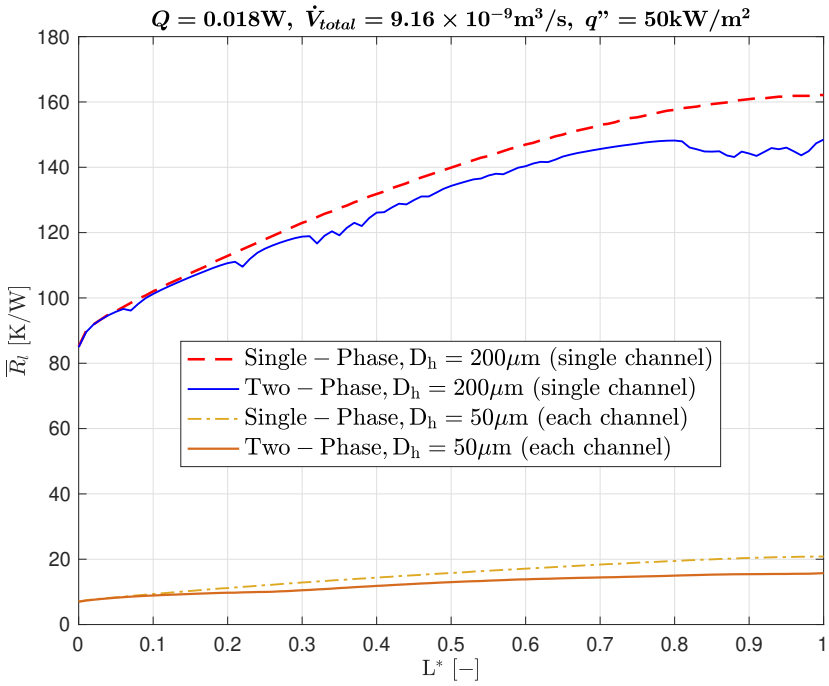

Figure 56: Time-averaged thermal resistance $\overline{R}_l$ comparison of single and two-phase simulations between single channel of $D_h = 200\,\mu\mathrm{m}$ and four parallels channels, each having $D_h = 50\,\mu\mathrm{m}$.

the middle channels show comparatively closer quantitative results. The 0.4 ms are attributed to the patched bubbles occurrence frequency. Overall, the difference in the vapour volume between the microchannels can be considered minor. Even though the above findings indicate that the effect of microchannel position on $\overline{T}$ and vapour volume is minor, it should be again pointed out that, in the present investigation, the first transient stages of the flow patterns development, is examined. This means that, for more macroscale applications, conjugate heat transfer effects are absolutely necessary to be taken into consideration when performing numerical simulations, as the solid inertia effects can be more significant (also during such early flow boiling stages) when other solid surfaces with different thermophysical properties are examined.

4.4.6 Conclusions

A detailed numerical investigation on the effect of microchannel hydraulic diameter as well as on the effect of the number of parallel microchannels within flow boiling microchannel heat sinks is performed. In total, two sets of simulations were performed and analysed separately. In the first set, the effect of microchannel hydraulic diameter on the global heat transfer characteristics is investigated within a single rectangular microchannel for four different hydraulic diameters of 200, 150, 100, and 50. It has been illustrated that the hydraulic diameter plays a significant role on both the resulting flow boiling regimes and heat transfer characteristics. Particularly, the values of the time-averaged heat transfer coefficient of the two-phase runs, compared to the corresponding single-phase cases is increased with the corresponding decrease in the

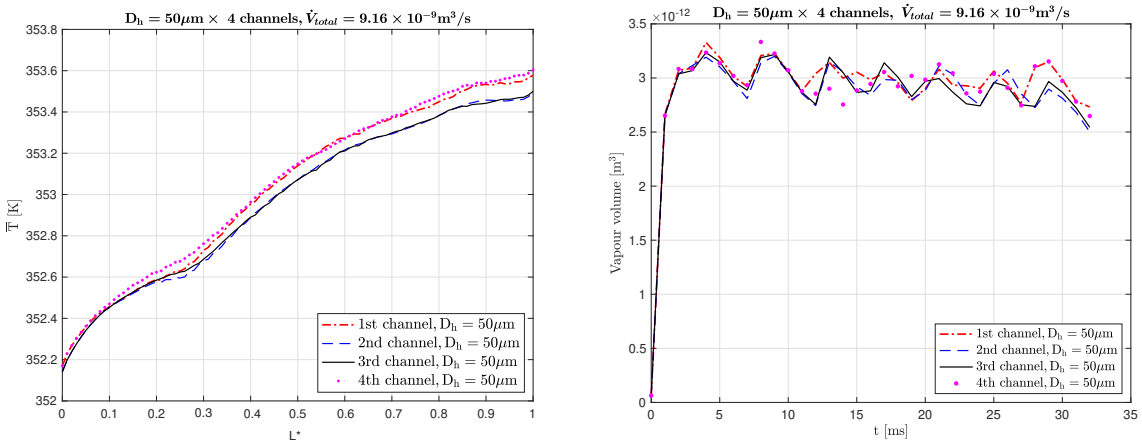

(a) **(b)**

Figure 57: For $q'' = 50\,kW\,m^{-2}$ and $G = 600\,kg\,m^{-2}\,s^{-1}$. (a) Comparison of time-averaged temperature $\overline{T}$ measured in the meniscus along each channel over L^*. (b) Comparison of the volume vapour of each channel over time t.

channel hydraulic diameter. Additionally, a fluctuating trend is exhibited for the case of higher hydraulic diameter (e.g., 200 µm), whereas the fluctuations are diminished as the hydraulic diameter decreases (e.g., 50 µm). For the case of the low applied heat transfer rate, an increase of 37.4%, 26.9%, 22.2%, and 22.2% of the global Nusselt number, compared to the corresponding single-phase stage of the simulations, could be seen for the microchannels with hydraulic diameter of 50, 100, 150, and 200 µm, respectively. Furthermore, for the case of high heat transfer rate, the global Nusselt number increased by 37.2%, 34.7%, 25.4%, and 31.7%, respectively. In the second set of simulations, a single microchannel with hydraulic diameter of 200 µm and four parallel microchannels, each with a hydraulic diameter of 50 µm, are performed. From this comparison, it could be seen that a difference in microchannel configuration results in the development of different flow regimes. The findings revealed that the local time-averaged thermal resistance $\overline{R}_l$ decreased with the decrease in the hydraulic diameter and the increase in the channel number n. For the single microchannel heat sink, the two-phase thermal resistance is decreased by 5.4% compared to its single-phase stage, whereas for the multiple channels case the thermal resistance is decreased by 23.3% compared to its single-phase stage. The difference in the thermal resistance can be attributed to the thicker liquid film that the case of 200 µm has compared to the 50 µm, leading to an increased convection and conduction resistance and hence a decrease in heat transfer performance. Additionally, the liquid film evaporation is higher in the case of thin films.

4.5 Summary / Conclusions

In the present chapter a detailed literature review on important aspects that have drawn attention and still remain open, on flow boiling within micro-passages has been presented. Additionally, by utilising an enhanced VOF-based method, a numerical investigation on the effect of various important parameters, including the effect of

surface wettability, solid surface thermophysical properties, channels' aspect ratio and channels' hydraulic diameter, on fluid flow characteristics and heat transfer coefficient has been presented. Each of these parameters has been extensively investigated both qualitatively and quantitatively and the investigation has been focused on flow boiling heat transfer on the first transient stages of flow pattern development and heat transfer characteristics by isolating the above-mentioned effects. This also constitutes the key novelty of the present work.

Some of the most important conclusions for each parameter include:

Effect of surface wettabilty:

- The effect of wettability on Nu_{glob} number for simulations with a single nucleation site and a single nucleation event is found to be minor.
- Liquid film evaporation is the dominant heat transfer mechanism for hydrophilic surfaces.
- By increasing the applied heat flux value and keeping the mass flux constant, a minor effect on the time-averaged Nu number is observed, however, when the mass flux is increased, the heat transfer coefficient is found to increase linearly.
- Liquid film evaporation is the dominant heat transfer mechanism in the hydrophilic surface case, with small contribution of contact line evaporation, mostly in the first half of the microchannel until fully departure of the bubble from the heated surface occurs. On the other hand, contact line evaporation is the dominant heat transfer mechanism in the hydrophobic surface case.

Effect of aspect ratio:

- The aspect ratio of a microchannel has a significant effect on the local heat transfer characteristics. This happens due to an enhancement in the single-phase heat transfer, prior to the onset of nucleate boiling, combined with the alteration of the underpinned bubble growth dynamics and the resulting differentiation in the contributions of contact line versus liquid film evaporation, when boiling occurs and a two-phase flow is developed.
- From the comparison of the time-averaged local Nusselt numbers along the channels, it can be concluded that, for all cases, the increase of the Nusselt numbers is much higher when more realistic cases, with multiple simultaneous nucleation sites, are simulated, especially for the narrow channel. This leads to a similar overall heat transfer performance with respect to the wide channel, which was superior in the case of the isolated single bubble. This is also evident by comparing the resulting global Nusselt numbers.

Effect of solid surface thermophysical properties:

- The qualitative and quantitative results showed that the variation of surface thermophysical properties, substantially affects the resulting flow boiling regimes as well as the heat transfer characteristics and enhancement.

- A significant increase, compared to the initial single-phase stage simulations, in the time-averaged heat transfer coefficient of more than 40% has been observed for the cases of silver and aluminium, whereas the cases of stainless steel and brass demonstrated a lower heat transfer coefficient increase (e.g. $< 30\%$). The better performance of the aluminium, silver and copper surfaces are linked to the resulting flow boiling regimes, which are characterised by larger in volume vapour slugs, higher bubble coalescence rate, less presence of bubbly flow and thicker liquid films.

- The empirical correlations that are available in the literature and are used for predicting analytically the heat transfer in such flows, do not take into account the solid surface thermophysical properties. Furthermore these correlations are based on data of flow boiling within conventional tubes and not specifically in microchannels.

- In this chapter, a new correlation based on the correlation by Li and Wu [45] has been developed. The developed correlation takes into consideration for the first time in the literature the thermal diffusivity of the solid material of the microchannels. The new correlation is found to predict the global heat transfer coefficient for all the numerically examined surfaces with absolute error values up to 17.47% in comparison to the existing correlation that results in an absolute error of 35.54%.

Effect of solid surface hydraulic diameter:

- Liquid film evaporation is the main heat transfer mechanism for all the examined cases. For the cases of 50 and 100 µm, this is evident throughout the numerical experiments, whereas for 150 and 200 µm, contact line evaporation is the main contributing heat transfer mechanism for the first two nucleation cycles and liquid film evaporation for the rest of the simulation.

- The increase in the heat transfer rate indicated that the effect of channel diameter is more evident when the heat transfer rate is lower. Furthermore, when the heat transfer rate was increased a substantial enhancement of the heat transfer could be seen for the microchannels of 200, 150, and 100 µm, whereas no important difference could be seen for the microchannel with the smallest hydraulic diameter. The trend representing the global Nusselt number curve of the single-phase simulations is identical, regardless the hydraulic diameter of the microchannel, and they all increase with the increase in hydraulic diameter. As expected, different trends could be seen when comparing the two-phase simulations.

- The variation of the time-averaged heat transfer coefficient difference Δh(x) versus the dimensionless length L^* is much smoother for the case of small hydraulic diameter compared to the case of 200 µm.

- For the case of multiple parallel channels, as expected, when comparing the two-phase results, the contribution of the flow boiling has resulted in a lower

temperature of the conjugate boundary, leading to lower thermal resistance compared to the corresponding single-phase simulations. These results reveal that there is a significant augmentation in flow boiling heat transfer performance in the case of four parallel channels, compared to the case of single channel.

- For the single microchannel heat sink, the two-phase thermal resistance is decreased by 5.4% compared to its single-phase stage, whereas for the multiple channels case the thermal resistance is decreased by 23.3% compared to its single-phase stage. The difference in the thermal resistance can be attributed to the thicker liquid film that the case of 200 µm has compared to the 50 µm, leading to an increased convection and conduction resistance and hence a decrease in heat transfer. performance.

5 Numerical investigation using the Eulerian-Eulerian two-fluid method

Generally, the VOF method is employed where the position of the interface is of great interest. Therefore, the simulations conducted and presented with the enhanced VOF-based solver of OpenFOAM are able to provide valuable information for some of the most important fluid flow and heat transfer characteristics for flow boiling within microchannels. However, such investigations require thousands of core hours and several weeks of finishing, making them too computationally expensive and time-consuming for utilising it directly in practical engineering calculations.

As previously presented, advances in numerical modelling techniques have given the opportunity of a wide selection of commercially available fluid flow models based on the Navier-Stokes equations for conducting numerical investigations. In our case, a model that can surpass the above-mentioned disadvantages of the VOF method and at the same time can reduce the computational cost and be used as a faster tool providing important information for macro-scale applications of flow boiling within micro-passages, is required to be employed. The Eulerian-Eulerian method has been successfully utilised in the past for the numerical study of such applications, providing accurate results compared to the experimental data.

Therefore, in this section a numerical investigation adopting the Eulerian-Eulerian (or two fluid) technique for reproducing experiments available in the literature for diabatic two-phase flow within long tubes ($D_h < 20$mm), will be performed. The results are obtained using standard inter-phase transfer modeling, including drag, lift, virtual mass and turbulent drag forces [[235]].

The scope of this investigation is to examine the validity of the Eulerian-Eulerian multiphase model implementation in v. 8.0 of the OpenFOAM CFD Toolbox in combination with the Rensselaer Polytechnic Institute (RPI) wall partitioning model, for the prediction of flow boiling within microchannels in comparison with appropriate literature available experimental results. The main aim is to identify problems and limitations in the existing closure sub-models particularly for the case of microchannels (e.g. $D_h < 1.5\,\text{mm}$) and to suggest ways that the overall data that were produced in Chapter 4 where the VOF methodology is applied could aid in the development of new closure relationships in the future, for improving the validity of the Eulerian-Eulerian RPI predictions.

5.1 Application of the numerical model

For the reproduction of the experiments, the Eulerian-Eulerian two-fluid model of OpenFOAM is utilised. This model is based on the equations presented in subsection 3.5. In OpenFOAM the Navier-Stokes equations are discretised using the Finite Volume Method (FVM). The selection of the proper discretisation schemes is important, as they can have a major impact on the final results [236]. The details of the selected schemes of the present study are shown in Table 25. For the calculation of the velocity and the pressure field which is found by solving the momentum and pressure equations, the PIMPLE algorithm is used in the present model. The PIMPLE algorithm is the

Table 25: Schemes used in the present study.

Modeling term	OF Scheme keywords	Description	Scheme
Convection term	divSchemes	Discretization of divergence terms ($\boldsymbol{\nabla}\cdot$)	Gauss linear Gauss linearUpwind limited Gauss vanLeer Gauss upwind
Gradient term	gradSchemes	Discretization of the gradient terms (∇)	Gauss linear
Diffusive term	laplacianSchemes	Discretization of laplacian terms (∇^2)	Gauss linear corrected
Time derivative	ddtSchemes	Discret. of first and second order time deriv.	Euler
Others	interpolationSchemes	Point to point interpolation of the value	Linear
	snGradSchemes	Component of gradient normal to a cell face	Corrected

Table 26: Experimental conditions of DEBORA 1-4.

Experiment	P [MPa]	G [$\mathrm{kg^2\,m^{-1}\,s}$]	q'' [$\mathrm{W^2\,m^{-1}\,K^{-1}}$]	T_{inlet} [K]	T_{sat} [K]
DEBORA 1	2.62	1996	73.89	341.67	359.98
DEBORA 2	2.62	1985	73.89	343.68	359.98
DEBORA 3	1.46	2028	76.20	301.67	331.25
DEBORA 4	1.46	2030	76.24	304.31	331.25

combination of PISO-SIMPLE predictor-corrector solver for large time step transient incompressible laminar or turbulent flows. It is based on an iterative procedure for solving equations for velocity and pressure. More details about the PIMPLE algorithm can be found here [237].

5.2 Experimental setup of DEBORA cases

The validation of the capabilities of the present numerical model is tested against the DEBORA experiments that were carried out at CEA in Grenoble by Manon [238] and Garnier et al. [239]. These experiments utilised subcooled flow boiling under high pressure conditions on a vertical tube, whereas the refrigerant R12 (Dichlorodifluoromethane) has been selected as the working fluid. The tube has an inner diameter of 19.2 mm and is divided into three parts; (i) an adiabatic inlet section of 1 m length, (ii) a heated section of 3.5 m and finally (iii) an adiabatic outlet section of 0.5 m, as shown in Figure 58a. The working fluid is injected from the bottom of the pipe, following a direction opposite with respect to the gravitational force, and then is heated up over the section where constant uniform heat flux is applied. The operating pressure of the experiments is ranging between 1.46 to 2.62 MPa, testing various inlet subcooling temperatures, heat fluxes and inlet velocities. In the present investigation, the utilised numerical model has been validated against the DEBORA experiments 1 to 4. The flow conditions of these experiments are summarised in Table 26.

The DEBORA experiments offer the possibility of comparing various two-phase flow and heat transfer parameters such as vapour fraction, liquid temperature, wall superheat etc., providing in this way the possibility of the validation of the numerical model at various important parameters and heat transfer characteristics. In more detail, the vapour volume fraction, the bubble detachment size, and vapour velocity profiles are measured on the radial axis at the end of the heated section using optical probes

Table 27: Liquid and vapour properties of the experiments/numerical investigation.

P (MPa)	T_{sat} (K)	σ ($\frac{N}{m}$)	ρ_l ($\frac{kg}{m^3}$)	ρ_v ($\frac{kg}{m^3}$)	ν_l ($\frac{m^2}{s}$)	ν_v ($\frac{m^2}{s}$)	Cp_l ($\frac{J}{kg\,K}$)	λ_l ($\frac{W}{m\,K}$)	Cp_v ($\frac{J}{kg\,K}$)	λ_v ($\frac{W}{m\,K}$)
2.62	359.98	0.00176	1016.4	172.51	8.76×10^{-8}	9.49×10^{-8}	1357.5	0.046	1200.7	0.018
1.46	331.25	0.00465	1177.0	84.97	1.11×10^{-7}	1.58×10^{-7}	1111.6	0.056	861.94	0.013

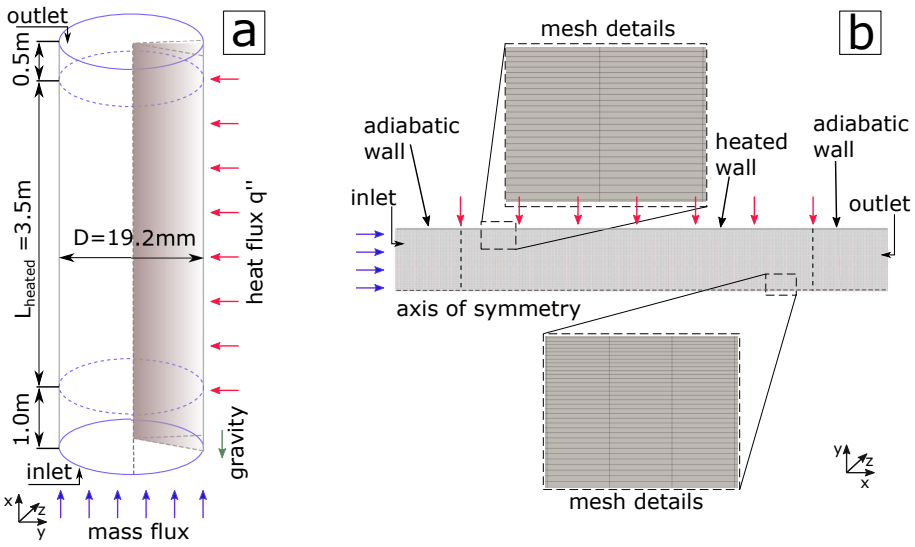

Figure 58: a) Experimental setup by Manon [238] and Garnier et al. [239] b) computational domain of the 2D axisymmetric simulations conducted in the present study.

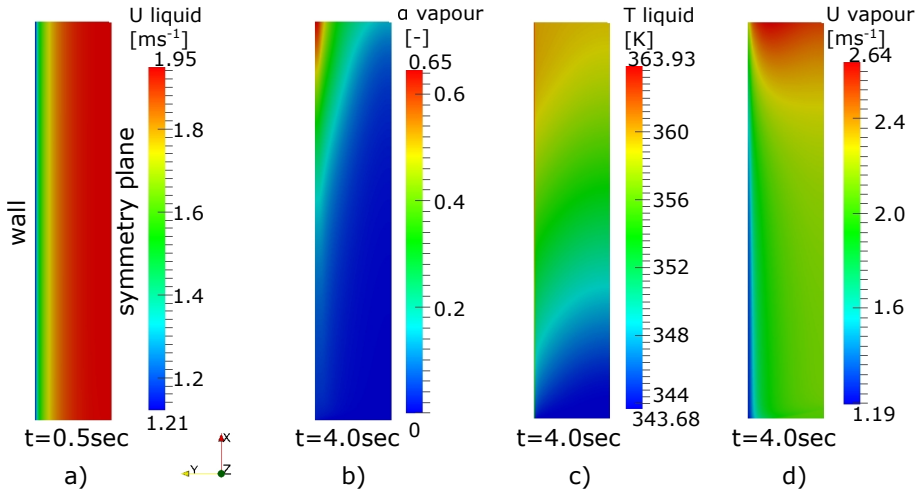

Figure 59: Countors of (a) velocity at 0.5 sec, b) vapour volume fraction at 4 sec, c) temperature of the liquid at 4 sec and velocity of the vapour at 4 sec for the DEBORA 2 case.

whereas the liquid temperature was measured at the same location using thermocouples. Additionally, parameters such as wall superheat and heat transfer coefficient are also measured along the heated length of the tube.

5.3 Computational geometry, boundary and initial conditions

As shown in Figure 58b the simulations were carried out for an axisymmetric geometry, using a computational domain that mimics the experimental setup described above. In more detail, a 5° wedge of the tube is used as the computational domain. OpenFOAM's meshing utilities *blockMesh* and *extrudeMesh* were used for the generation of the mesh. An inlet velocity boundary condition has been specified at the bottom and pressure boundary condition was imposed at the top outlet of the tube. The no-slip velocity boundary condition has been used at the wall for the liquid phase. For the vapour phase, the free slip condition has been specified as it has been found by some researchers that this boundary condition is better suited for such cases [240, 241]. A summary of the utilised boundary conditions of the present study is shown in Table 28.

All the simulations are conducted in two stages. In the first stage, in order to obtain a fully developed hydrodynamic boundary layer, an adiabatic single-phase simulation was performed for 0.5 sec of real flow, where the domain was filled up with the working liquid at the corresponding subcooled temperature with liquid entering the domain at a constant mass flux. The developed hydrodynamic boundary layer for the liquid phase at 0.5 sec can be seen in Figure 59a. In the second stage, a constant uniform heat flux was applied on the heated section of the domain. This stage was run for up to 4 sec in order to ensure that steady-state conditions have been reached. Subsequently, the measurements of the examined heat transfer and fluid flow characteristics could be made. Snapshots of the resulted vapour volume fraction, liquid temperature and vapour velocity at t=4 s for the DEB. 2 case, can be seen in Figure 59b, c, d, indicatively.

Table 28: Boundary condition and settings used in the present numerical study. More information about each of the below boundary conditions can be find in [242]

Field	Inlet	Outlet	Wall
alpha.gas	fixedValue	inletOutlet	zeroGradient
alphat.gas	calculated	calculated	compressible::alphatWallBoilingWallFunction
epsilon.gas	mapped	inletOutlet	epsilonWallFunction
k.gas	mapped	inletOutlet	kqRWallFunction
nut.gas	calculated	calculated	nutWallFunction
T.gas	fixedValue	inletOutlet	copiedFixedValue
U.gas	mapped	pressureInletOutletVelocity	slip
alpha.liquid	fixedValue	inletOutlet	zeroGradient
alphat.liquid	fixedValue	calculated	compressible::alphatWallBoilingWallFunction
epsilon.liquid	mapped	inletOutlet	epsilonWallFunction
k.liquid	mapped	inletOutlet	kqRWallFunction
nut.liquid	calculated	calculated	nutWallFunction
omega.liquid	mapped	inletOutlet	omegaWallFunction
T.liquid	fixedValue	inletOutlet	fixedMultiphaseHeatFlux
U.liquid	mapped	pressureInletOutletVelcity	noSlip
p	calculated	calculated	calculated
p_rgh	fixedFluxPressure	prghPressure	fixedfluxPressure

5.4 Mesh independency study

The selected mesh size of the present work has been chosen after the performance of a mesh independence study in order to ensure that the solution is not influenced by the size of the mesh. Five different meshes, consisting of hexahedral and prism cells, were constructed for this purpose. The mesh has a slight bias on the radial axis and towards the heated wall in order to capture in more detail the hydrodynamic and thermal boundary layers. The different cases consisted of cell sizes of 700 × 40, 1400 × 40, 2800 × 160, 5600 × 160, 11200 × 320 cells on the axial (x-axis) and radial axis (y-axis), respectively, of the 2D axisymmetric computational domain. The results indicated that the effect of the increasing mesh size on the distributions of the vapour fraction, liquid temperature and vapour velocity were minimal. Particularly, when the vapour fraction (Figure 60a) is compared the average percentage difference between the 1400 × 40 and the cases of 2800 × 80, 5600 × 160 and 11200 × 320, is 3.04%, 5.53% and 9.10%, respectively. For the case of liquid temperature (Figure 60b) the average percentage difference of temperature of the 1400 × 40 is 0.02%, 0.04% and 0.07% compared to the 2800 × 80, 5600 × 160 and 11200 × 320, respectively. Additionally, when comparing the average percentage difference of the vapour velocity (Figure 60e), the 1400 × 40 is less than 2% compared to the other mesh sizes (0.48, 0.95 and 1.47% for the 2800 × 80, 5600 × 160 and 11200 × 320 cases, respectively), similar results could be seen for the liquid velocity comparison but also for the bubble detachment diameter comparison. As for the comparison between the 1400 × 40 and the 700 × 40 case, the difference is below 1% for all the examined parameters. However, considering both the computational cost and the accuracy of the results, the case of 1400 × 40 cells in the axial and radial direction, respectively, has been finally selected for the modeling of the DEBORA experiments.

5.5 Numerical model validation results against DEBORA cases

In this section, the validation of the utilised model against the experiments of DEBORA 1-4 are presented in Figures 61 to 68. As previously mentioned, the experimental

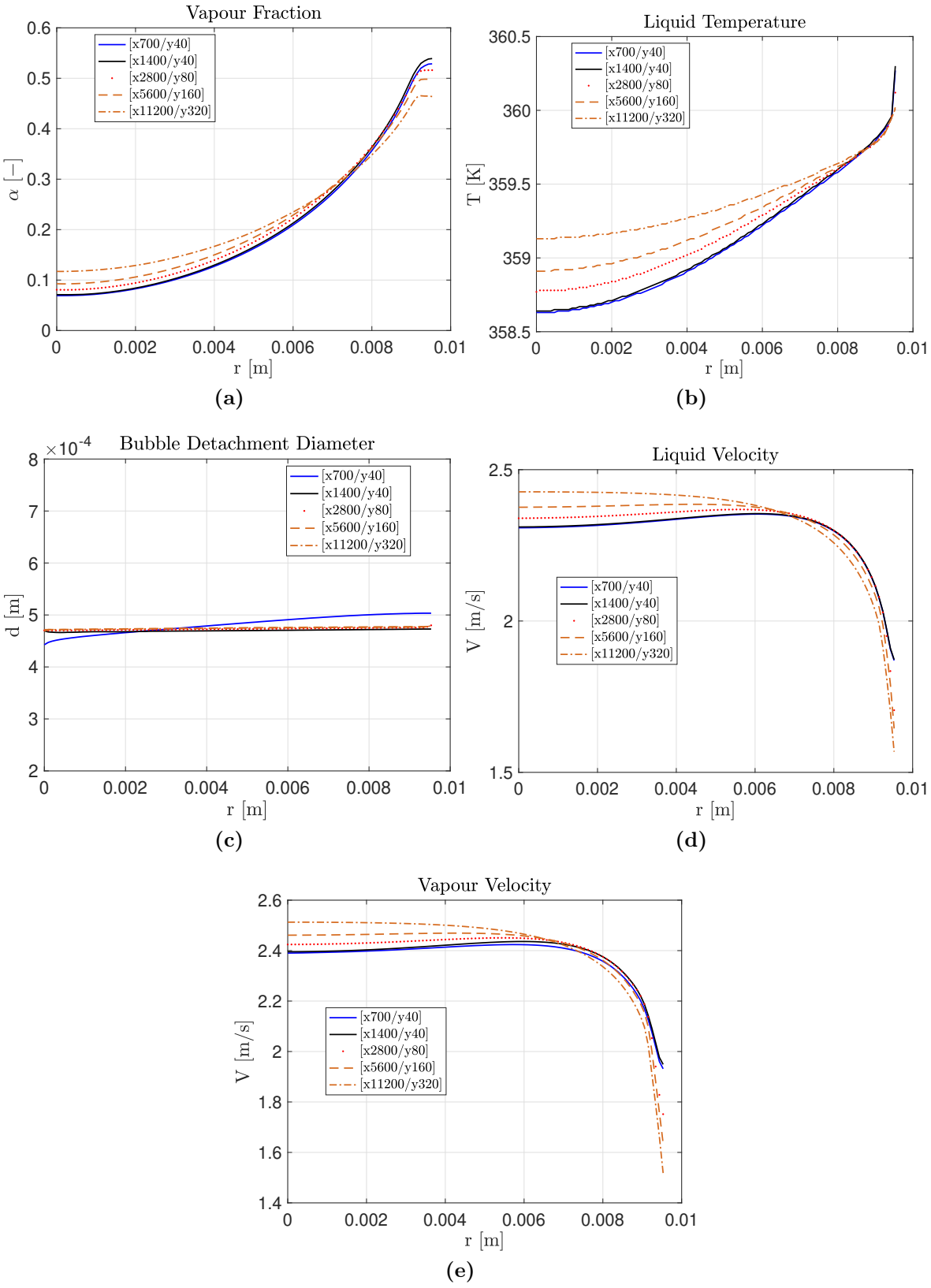

Figure 60: Mesh independency study comparison.

Table 29: Mesh details of the examined cases.

Tested cases (x/y axis) - No. of cells [-]	Total No. of cells [-]
700/40	28,000
1400/40	56,000
2800/80	224,000
5600/160	896,000
11200/320	3,584,000

Table 30: Values of the key parameters and empirical constants of the utilised sub-models of the two-fluid model for each DEBORA case.

	Nucl. site model -Lemm.-Chaw. [143] C_n [-]	Nucl. site model -Lemm.-Chaw. [143] N_{ref} [m^{-2}]$\times 10^6$	Nucl. site model -Lemm.-Chaw. [143] ΔT_{refN} [K]	Dep. diam. model -Tolubin.-Kost. [145] d_{ref} [mm]	Dep. freq. model- Kocam.-Ishii [144] C_f [-]
Present study- DEBORA 1	1.60	25	10	0.48	0.10
Present study- DEBORA 2	1.60	21	10	0.52	0.15
Present study- DEBORA 3	1.60	30	26	0.58	0.10
Present study- DEBORA 4	1.60	20	30	0.75	0.10

data (and hence also the numerical data of the present study) have been measured either along a radial profile at the outlet of the heated section and along the heated wall axis. The figures also include a curve of the corresponding numerical results by Krepper & Rzehak [235], for the same DEBORA cases, utilising ANSYS CFX, which constitutes an additional benchmark, confirming in this way the validity of the utilised model of OpenFOAM CFD Toolbox. For the accurate capturing of the experimental results, it was deemed necessary to tune some of the parameters and constants that the empirical correlations include in their relationships which are used as sub-models in the present numerical simulation framework. In more detail, the key parameters that were modified in order to obtain results that show good agreement with the corresponding experiments are the C_n, N_{ref} and the ΔT_{refN} values from the nucleation site density model of Lemmert and Chawla [143], the d_{ref} value of the departure diameter closure proposed by Tolubinski and Kostanchuk [145] and the C_f empirical constant proposed by Kocamustafaogullari and Ishii [144] for the bubble departure frequency model. The optimum values of the parameters for each DEBORA experiment are summarised in Table 30.

5.6 Numerical results of DEBORA 1 and DEBORA 2 experiments

The predictions and measurements for the radial profiles of the vapour fraction, bubble detachment diameter, vapour velocity, liquid velocity (experimental data not available) and liquid temperature, against the DEBORA 1 (DEB. 1) and DEBORA 2 (DEB. 2) experiments as well as the predictions and measurements for the axial profiles of the heat transfer coefficient and wall superheat measured at the heated wall, for the same

experiments, are illustrated in Figures 61 and 63, and Figures 62 and 64, respectively. The main difference between the two experiments is the inlet subcooling temperature of the coolant which is 341.67 K for DEB. 1 and 343.68 K for DEB. 2, while the operating pressure is 2.62 MPa, for both cases as shown in Table 26. The selected values for the DEB. 1 experiment for the C_n, N_{ref}, ΔT_{refN}, d_{ref} and C_f values are 1.60, 25 million (M), 10 K, 0.48 mm and 0.10, respectively. Whereas for the DEB. 2 experiment the values are C_n=1.60, N_{ref} = 21 M, ΔT_{refN}= 10 K, d_{ref}= 0.48 mm and C_f= 0.10. From the sensitivity analysis performed in the present study, it has been observed that the modification of the parameter d_{ref} of the departure diameter model had a major influence on all the examined fluid flow and heat transfer characteristics including the vapour fraction and the vapour velocity profile and of course on the bubble detachment diameter, whereas the N_{ref} value of the nucleation site density model had major impact on the resulting wall superheat but no significant influence on the radial temperature profile of the liquid phase. The empirical constants C_n and C_f of the nucleation site density and the bubble departure frequency model, respectively, had a major influence on the wall superheat and minimal influence on the liquid temperature measured on the radial axis, whereas had no influence on the volume fraction and velocity profiles. Finally, the variation of the ΔT_{refN} parameter had a significant impact on the wall superheat value. All these observations are summarised in Table 31.

Now, focusing on the radial axis results of DEB 1. and DEB. 2 cases shown in Figures 61 and 63, respectively, it is evident that the numerical model is able to accurately predict the vapour fraction and the liquid temperature profiles, showing consistency with the experimental data. On the other hand, it can be seen that the velocity profiles are underestimated by the numerical simulations for both cases. This may be attributed to the fact that since the experiments are conducted in vertical tubes when measuring at the end of the heated section, there are bigger bubbles coming at the center of the tube from lower positions which were formed due to coalescence of smaller bubbles that were detached from the heated wall, resulting in bubble acceleration in the center of the tube, due to buoyancy effects. This phenomenon cannot be captured in the numerical simulations of the present model since there is no bubble coalescence sub-model included. The lack of such sub-model in the present model is also evident when comparing the bubble detachment diameter shown in Figures 61b and 63b. Particularly, it can be seen that the simulation is unable to follow the trend of the experimental measurements, where as we approach the heated wall, the bubble detachment diameter is rapidly decreasing due to the coalescence with bigger bubbles, which are immediately dragging away the smaller bubbles from the wall. Conversely, when comparing the heat transfer coefficient and the wall superheat (Figures 62 and 64) which are measured on the heated wall, we can see that the numerical results show good agreement with the corresponding experimental data.

5.7 Numerical results of DEBORA 3 and DEBORA 4 experiments

The numerical results of the DEB. 3 and DEB. 4 experiments are shown in this subsection. In these experiments the operating pressure is 1.46 MPa for both cases

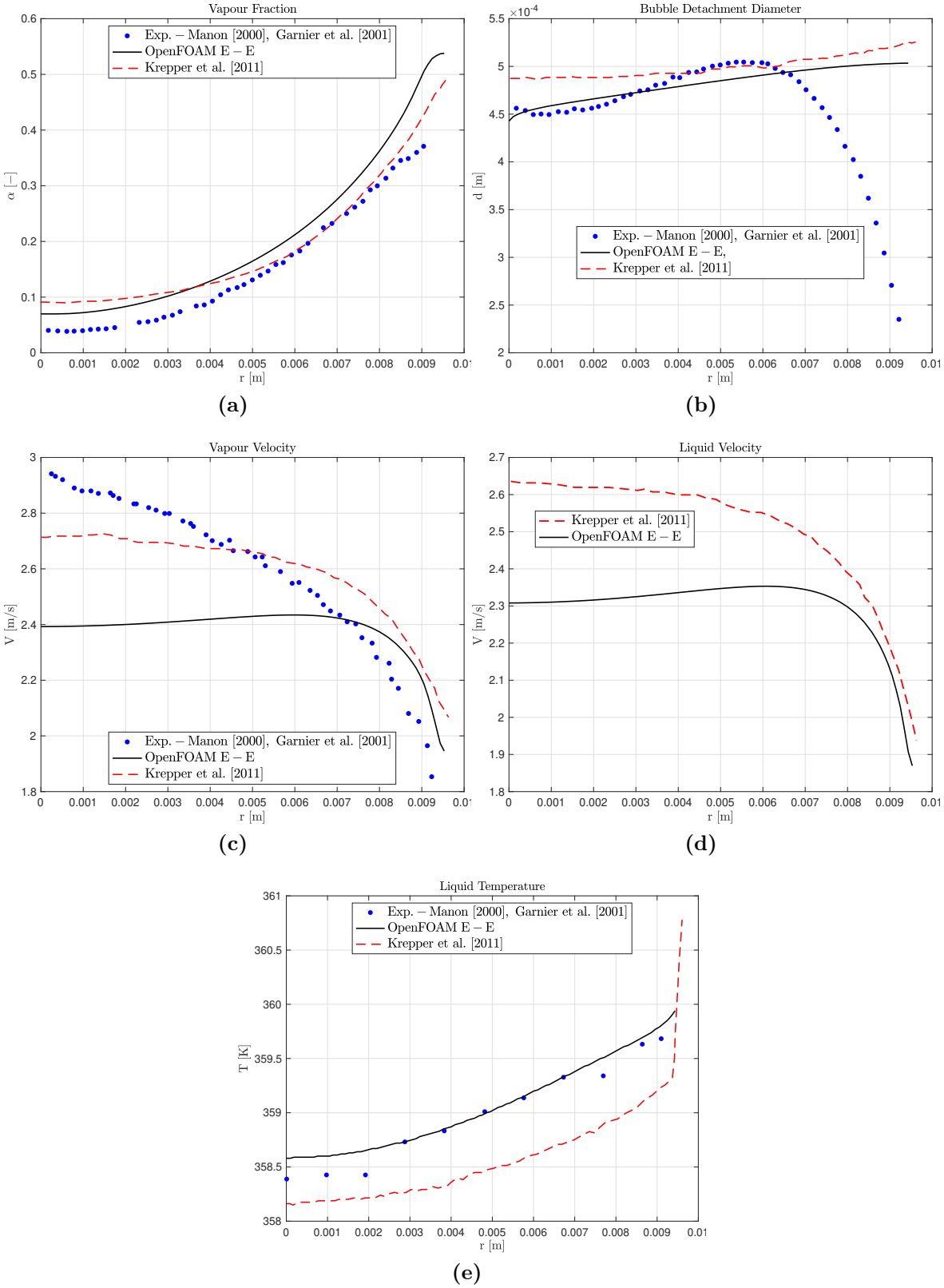

Figure 61: DEBORA 1 - Radial line captions: Numerical results and comparison between the present simulation, experiments of Manon [238] and Garnier et al. [239] and Krepper & Rzehak [235].

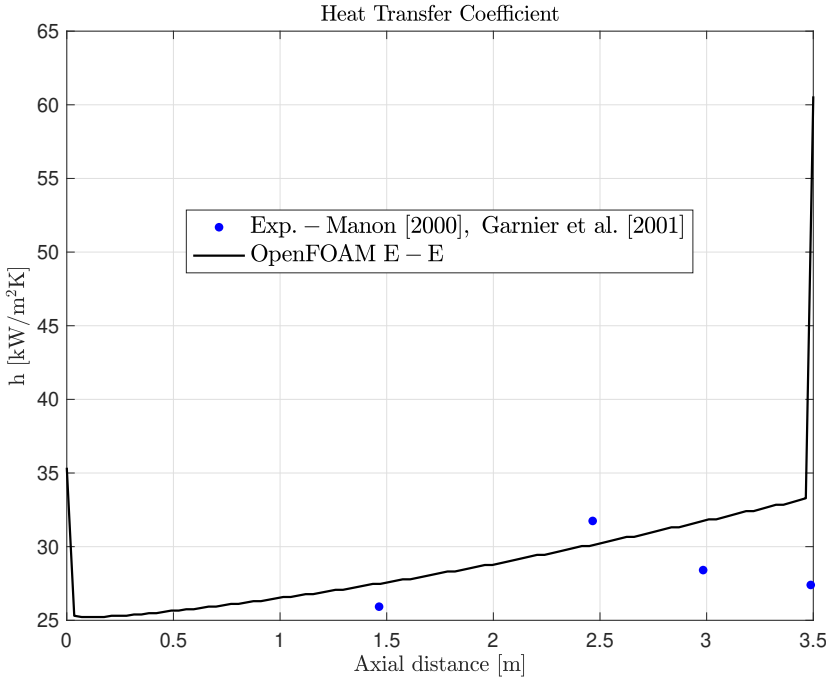

(a)

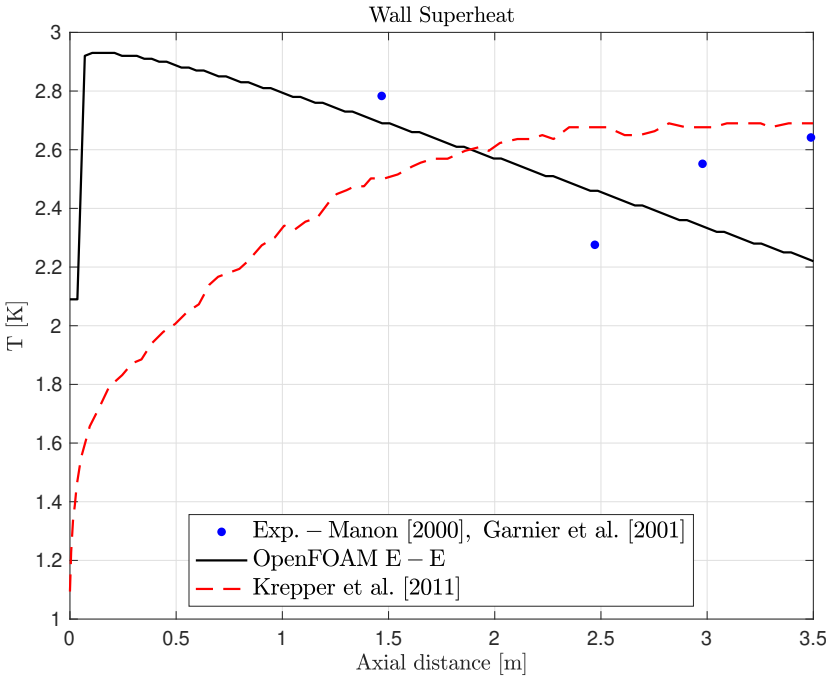

(b)

Figure 62: DEBORA 1 - Axial line captions: Numerical results and comparison between the present simulation, experiments of Manon [238] and Garnier et al. [239] and Krepper & Rzehak [235].

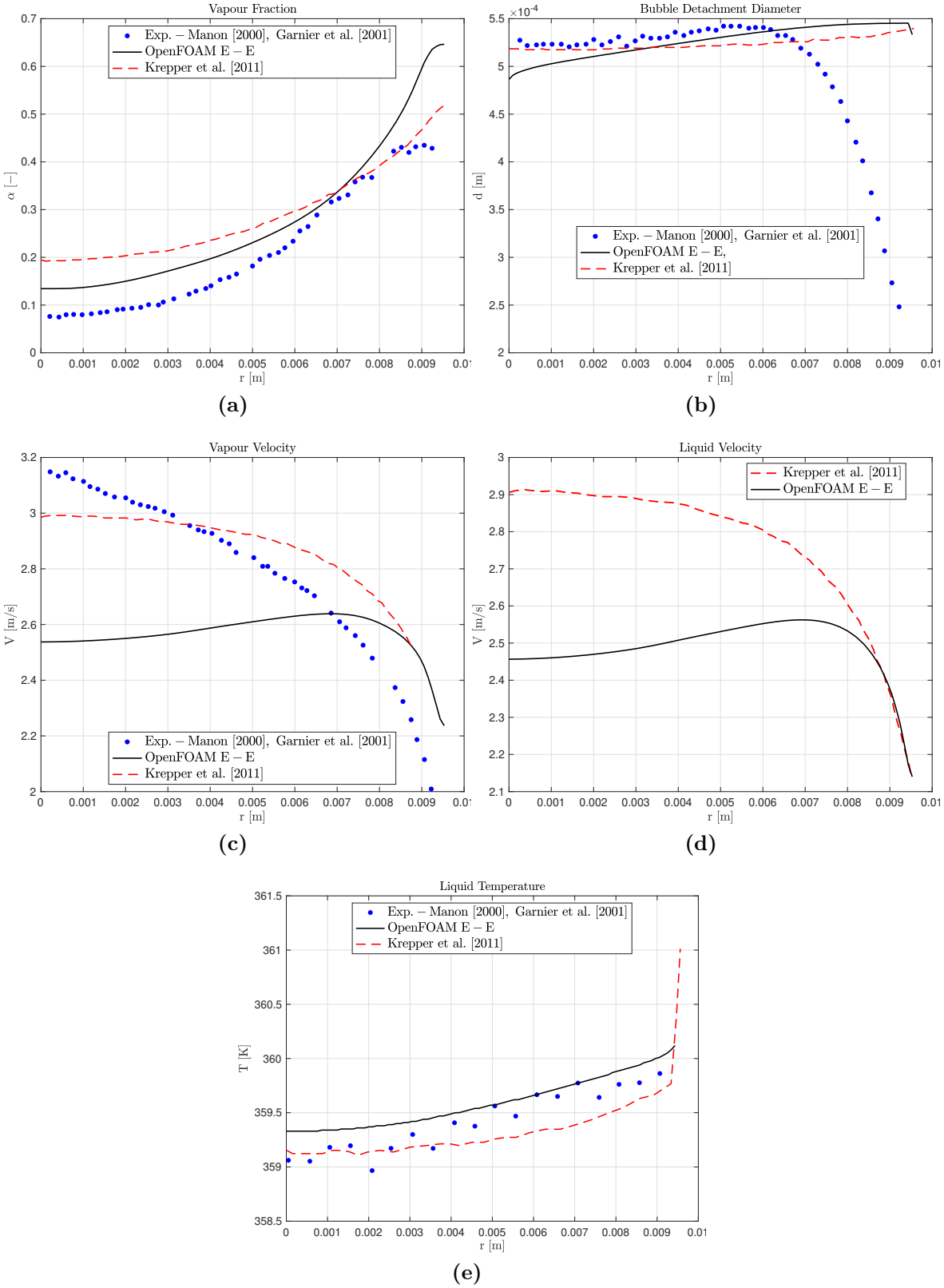

Figure 63: DEBORA 2 - Radial line captions: Numerical results and comparison between the present simulation, experiments of Manon [238] and Garnier et al. [239] and Krepper & Rzehak [235].

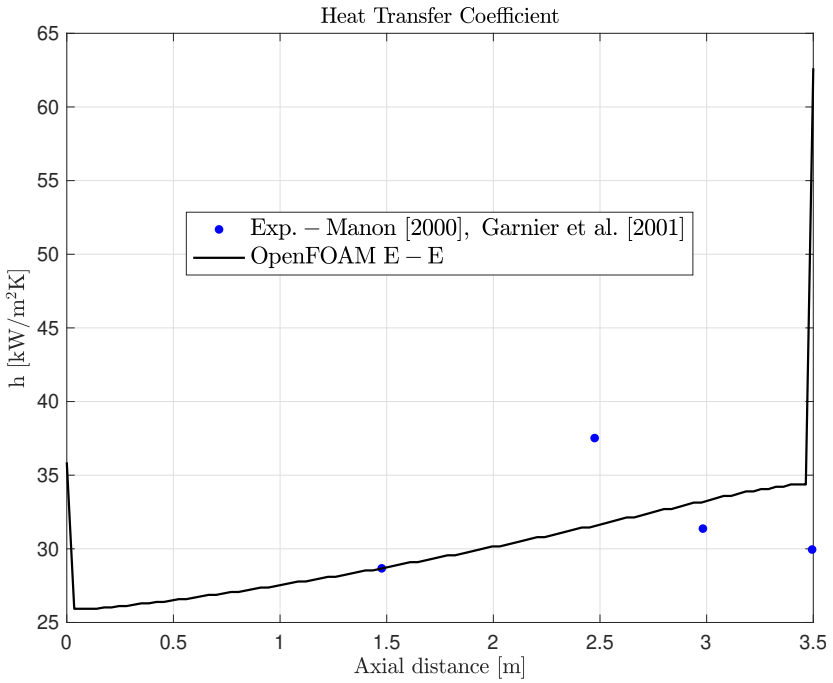

(a)

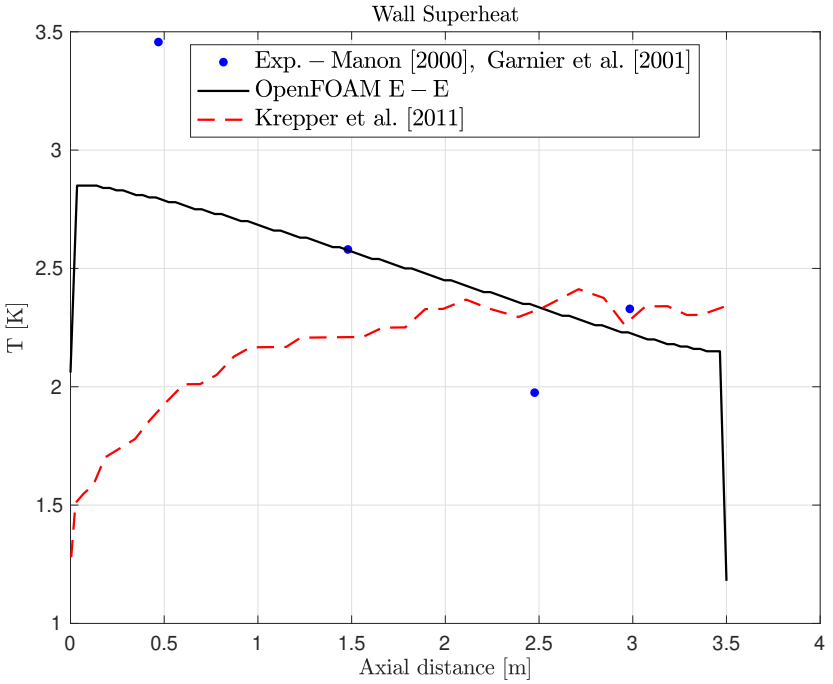

(b)

Figure 64: DEBORA 2 - Axial line captions: Numerical results and comparison between the present simulation, experiments of Manon [238] and Granier et al. [239] and Krepper & Rzehak [235].

Table 31: Influence of the modified parameters that are included in the selected models on the measured fluid and heat transfer characteristics.

	C_n	N_{ref}	ΔT_{refN}	d_{ref}	C_f
Volume fraction (radial)	minor	minor	minor	major	intermediate
Bubble detachment diameter (radial)	intermediate	minor	minor	major	intermediate
Velocity profile (radial)	minor	minor	minor	major	minor
Liquid temperature (radial)	intermediate	intermediate	intermediate	major	intermediate
Wall superheat /temperature (axial)	major	major	major	major	major

and the inlet subcooling temperature is 301.67 K for the DEB. 3 and 304.31 K for the DEB. 4 test. As it can be seen from Table 30, for the prediction of the corresponding experimental data, a further adjustment of the empirical correlations was necessary. In more detail, for the DEB. 3 case the values of C_n, N_{ref}, ΔT_{refN}, d_{ref} and C_f values were 1.60, 30 M, 26 K, 0.58 mm and 0.10, respectively. For the DEB. 4 case, the values for the C_n, N_{ref}, ΔT_{refN}, d_{ref} and C_f values are 1.60, 20 M, 30 K, 0.75 mm and 0.10, respectively.

Overall, it can be seen that as in the previous comparison, the numerical model can predict well the vapour fraction and the liquid temperature profiles measured on the radial axis for DEB. 3 and DEB. 4 shown in Figures 65a , 65d and 67a , 67d, respectively. The lack of bubble coalescence sub-model is evident also here since the velocity profiles are underpredicted and the bubble detachment diameter does not follow the trend of the experimental data as we approach the heated wall. Finally, it can be seen that the wall superheat measured on the axial axis along the heated wall, shows good agreement with the experimental results for both experiments.

From the above comparison it can be seen that with appropriate tuning, the present numerical model can predict well various important parameters of fluid flow and heat transfer characteristics and can be safely used in numerical investigations of flow boiling within conventional tubes. However, the introduction of a bubble coalescence model is necessary, for the better prediction of parameters such as the velocity profiles and bubble detachment diameter. Additionally, from the above results, it is evident that when the operating conditions change, even if not significantly (e.g. DEB. 3 VS DEB. 4), the tuning of some of the empirical constants and parameters of the empirical closures that are introduced as sub-model in the present numerical model, is required. This constitutes a significant constraint on industrial applications, as experimental data are required for the continuous validation of the model when the operating parameters are modified.

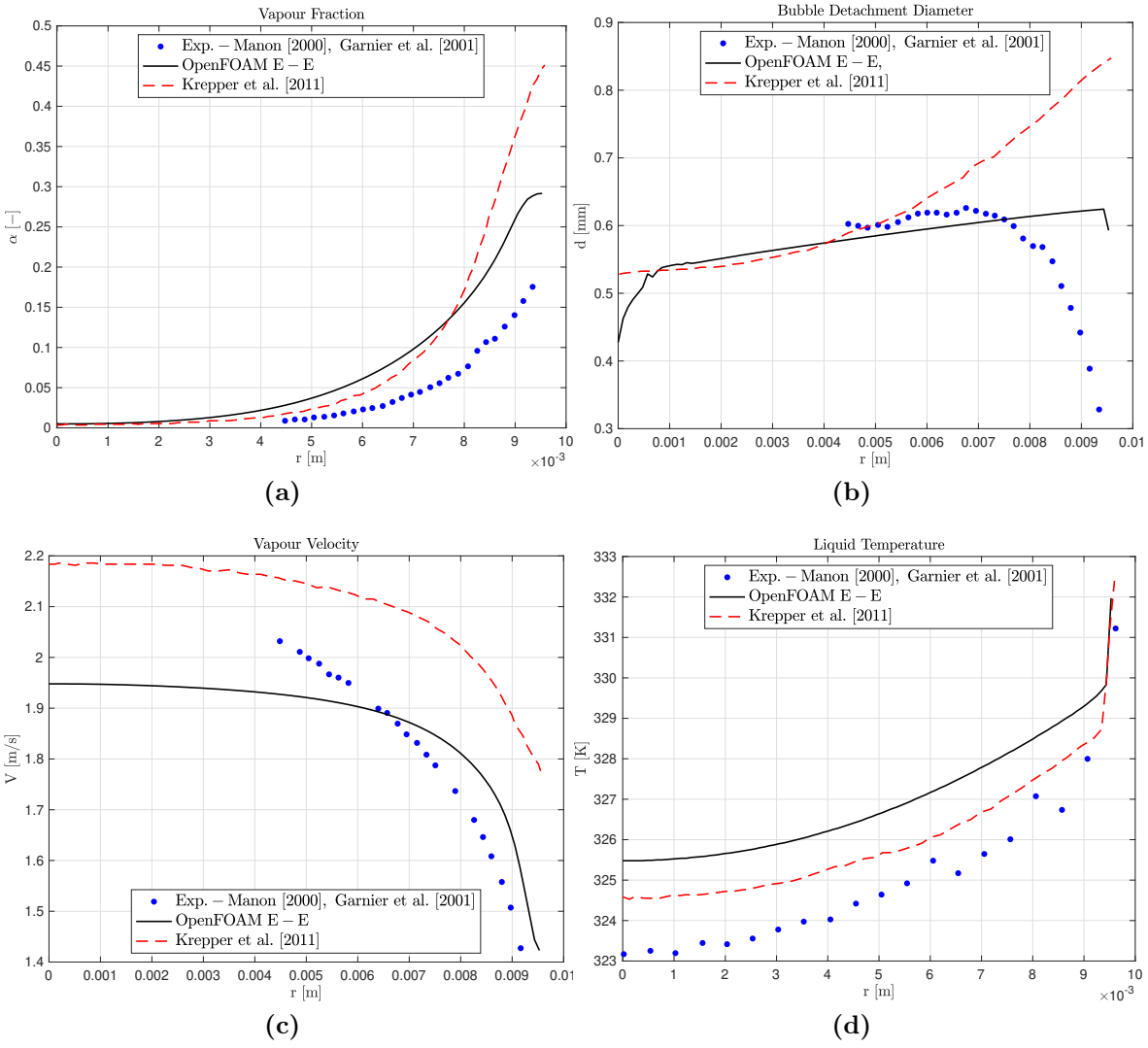

Figure 65: DEBORA 3 - Radial line captions: Numerical results and comparison between the present simulation, experiments of Manon [238] and Garnier et al. [239] and Krepper & Rzehak [235].

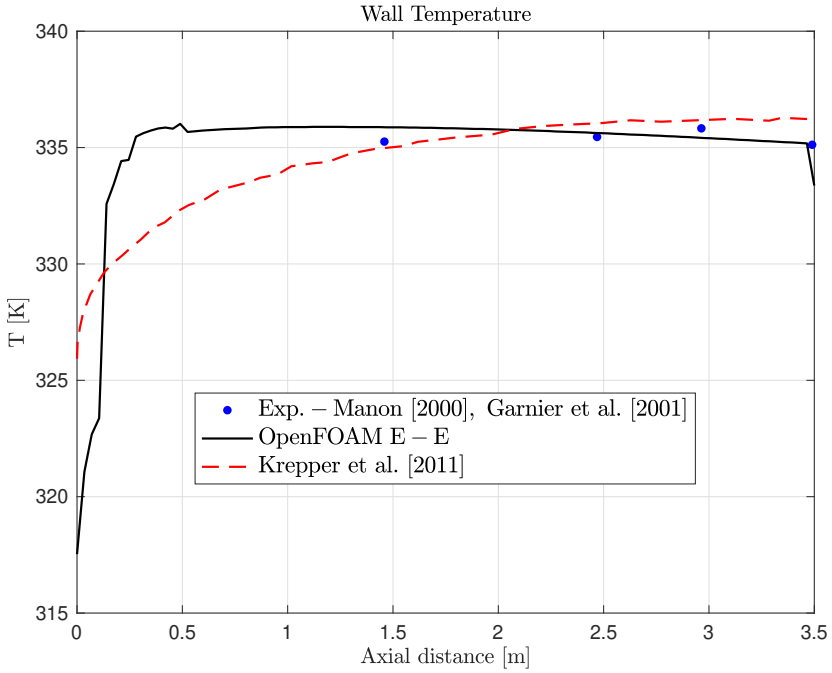

Figure 66: DEBORA 3 - Axial line captions: Numerical results and comparison between the present simulation, experiments of Manon [238] and Granier et al. [239] and Krepper & Rzehak [235].

5.8 Numerical model validation results which includes bubble coalescence model against DEBORA experiment

From the above results it is clear that good agreement compared to experimental data and other commercial CFD packages can be achieved by modifying the empirical constants that are included in the RPI wall partitioning model. However in order to capture parameters such as the vapour radial velocity the inclusion of an appropriate bubble coalescence model is necessary. OpenFOAM offers the possibility of including a bubble coalescence and breakup sub-model, therefore in this section additional results where such sub-model is added in the optimal case of E-E for DEB. 1 experiment that was presented in section 5.6 and Table 30, are presented. A widely used bubble coalescence and breakup sub-model is the interfacial area transport equation (IATE) method proposed by Wu et al. [146] and further developed by Ishii et al. [147]. As mentioned in section 3.10, the IATE sub-model includes three parameters that constitute important bubble interaction mechanisms. Namely, these are a) the bubble breakup rate caused by turbulent impact R_{TI}, b) the bubble coalescence rate caused by random collision R_{RC} and c) the bubble coalescence rate caused by wake entrainment R_{WE}. All three parameters include model coefficients in their expressions. Particularly, the expression of R_{TI} includes the experimental coefficients C_{TI} and We_{cr}. The R_{RC} expression includes the model coefficients C_{RC} and C and the maximum allowed vapour fraction value α_{max}. Finally the R_{WE} expression includes the model constant C_{WE}. The default coefficient values that the sub-model uses in OpenFOAM, are the same as the ones suggested by Ishii et al. [147]. However, after performing the first simulations

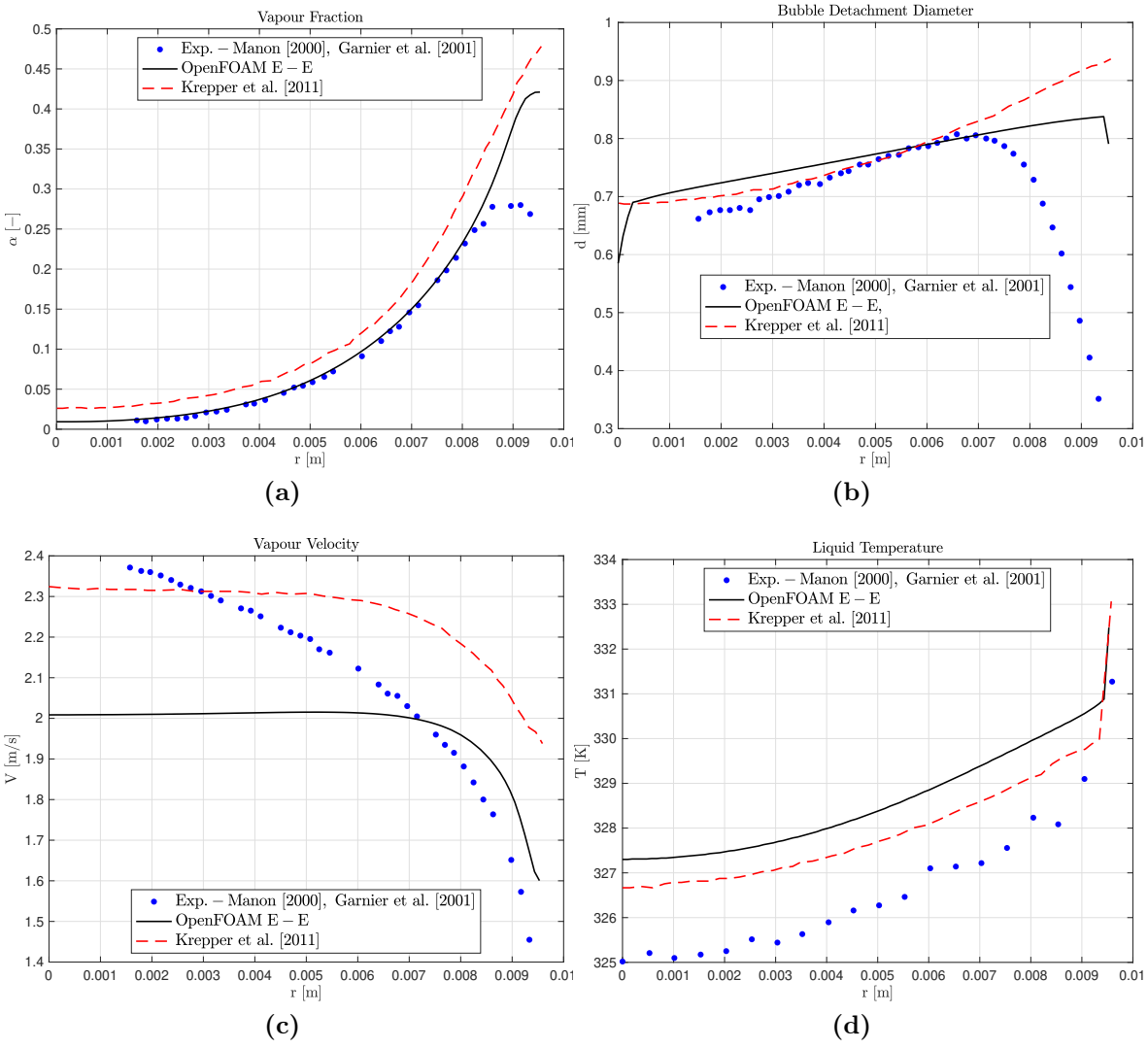

Figure 67: DEBORA 4 - Radial line captions: Numerical results and comparison between the present simulation, experiments of Manon [238] and Garnier et al. [239] and Krepper & Rzehak [235].

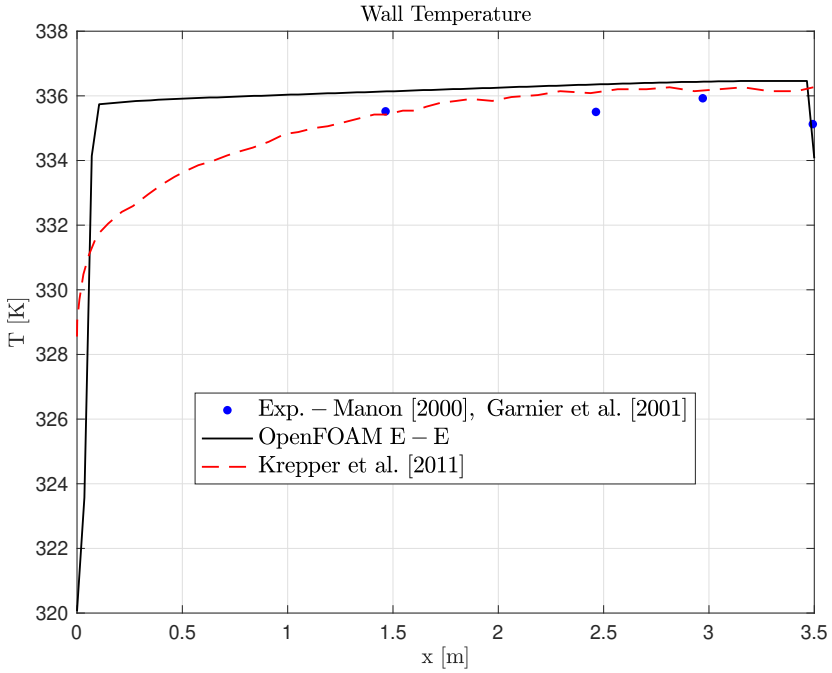

Figure 68: DEBORA 4 - Axial line captions: Numerical results and comparison between the present simulation, experiments of Manon [238] and Granier et al. [239] and Krepper & Rzehak [235].

it could be seen that by using these values in the optimal case of E-E of the DEB. 1 case, significantly changed and worsened the overall results compared to the corresponding experimental measurements. Therefore, it was deemed appropriate to conduct a further sensitivity analysis by keeping all the empirical constant values that are included in the interfacial momentum transfer models, the same as the optimal case for DEB. 1 presented earlier and at the same time modify accordingly the model coefficients of the IATE sub-model. Different values for each model coefficient have been tested. Initially, it should be mentioned that modifying the coefficient C_{WE} that is included in the wake entertainment expression, did not result in any significant changes on the examined radial profiles. Conversely, significant effects could be seen by modifying the model constants C_{TI} and C_{RC} of the turbulent impact and random collision models, respectively. Hence the focus of the sensitivity analysis has been on these two constants. In table 32 the default values of IATE mechanisms and model constants as proposed by [147] as well as two additional cases where only the constant C_{TI} and C_{RC} are modified are shown. In Figure 69 the corresponding results are plotted. These results indicate clearly that by decreasing the C_{TI} constant for about an order of magnitude, and keeping all the other parameters as the default values, then the vapour velocity value can be better captured with respect to the experimental value. However, this has resulted in a change (worsening) in the vapour fraction and a slight change in the radial liquid temperature. On the other hand, by increasing the C_{RC} constant, we can see that the vapour velocity profile shows the best agreement with the experimental results compared to other numerical cases. However, this has resulted in a significant change in the vapour fraction curve which exhibits an opposite trend compared to the other

Table 32: Values of model constants; as suggested by Ishii et al. [147] and the modified values of the present investigation.

Mechanisms	Default values of the original sub-model. Values taken by Ishii et al. [147] (except C_{RC} value where the proposed by [147] value is 0.004 but OpenFOAM uses default value of 0.04)**	Modifying model constant C_{TI}	Modifying model constant C_{RC}
R_{TI}	$C_{TI} = 0.085$ ($We_{cr} = 6.0$)	$C_{TI} = \mathbf{0.004}$ ($We_{cr} = 6.0$)	$C_{TI} = 0.085$ ($We_{cr} = 6.0$)
R_{RC}	$C_{RC} = 0.04$ (C = 3, $\alpha_{max} = 0.75$)	$C_{RC} = 0.04$ (C = 3, $\alpha_{max} = 0.75$)	$C_{RC} = \mathbf{0.12}$ (C = 3, $\alpha_{max} = 0.75$)
R_{WE}	$C_{WE} = 0.002$	$C_{WE} = 0.002$	$C_{WE} = 0.002$

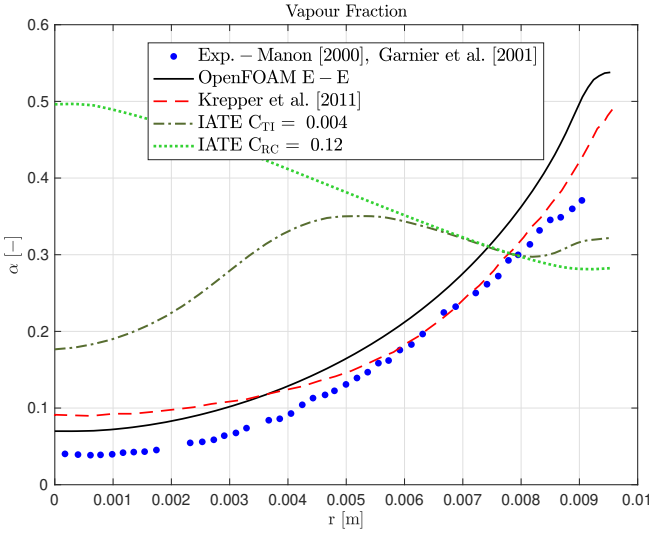

(a)

Figure 69: Radial line captions: Comparison between Numerical results of the IATE model, the optimal case of the E-E that was previously (without the IATE model) , experiments of Manon [238] and Garnier et al. [239] and Krepper & Rzehak [235].

cases. An increase in the difference between the numerical and the experimental results could be seen also for the liquid temperature measurements, however, the differences here are within the measurement error of the experiment. The above conclusions indicate how important a bubble coalescence and break-up sub-model is for better capturing parameters such as vapour velocity on two-phase flows within conventional tubes. However, it is also evident that the development of more accurate correlations is required that do not alter the remaining parameters prediction.

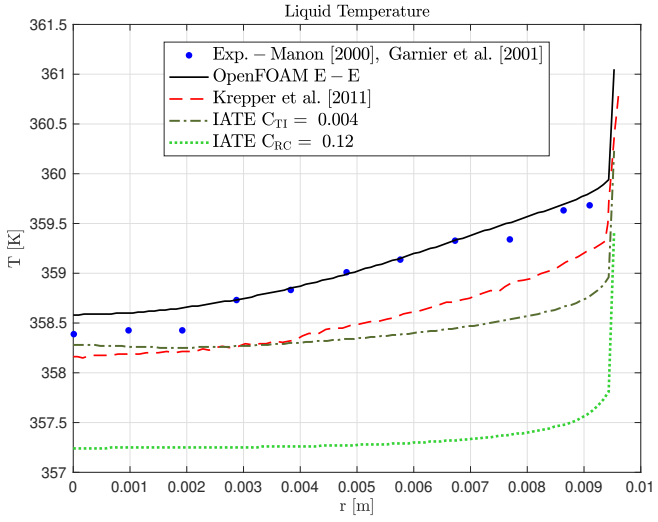

(a)

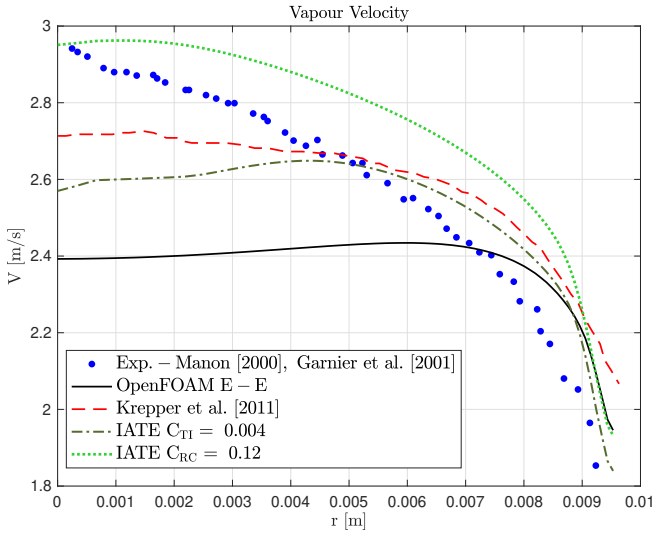

(b)

Figure 69 (continued): Radial line captions: Comparison between Numerical results of the IATE model, the optimal case of the E-E that was previously (without the IATE model) , experiments of Manon [238] and Garnier et al. [239] and Krepper & Rzehak [235].

5.9 Simulations on flow boiling in microchannels

As presented in the previous chapter, several numerical investigations have been performed, using a VOF-based solver, on some of the most important open aspects of flow boiling within rectangular microchannels, reporting important heat transfer and fluid flow characteristics [197, 243, 244], and developing new correlations based on data of flow boiling within microchannels. The new correlations are aimed to replace some of the existing empirical correlations of the Eulerian-Eulerian two-fluid model of OpenFOAM. However, before modifying the source-code of the original *multiphaseEulerFoam* solver of OpenFoam it is important to show that the tuning of the key parameters of the sub-models of the current code is not sufficient for mini/microchannels investigations, and the introduction of new closures based on data on microchannels and minichannels is necessary.

Below, the optimum model set-up for the DEBORA 1 case will be utilised for reproducing experiments on microchannels performed by Mahmoud et al [245]. These experiments were selected due to the fact that offer information (e.g. heat transfer coefficient) measured on the axial distance of the microchannel, whereas the vast majority of the experimental papers on flow boiling within microchannels provide information against the vapour quality.

5.10 Experimental and numerical setup on microchannel

In these experiments Mahmoud et al. [245] examined the effects of surface morphology on subcooled flow boiling of R134a within a single circular microchannel of two different cases with an inner diameter of 1.10 and 1.16 mm. Similar to the DEBORA experiments, the flow direction of Mahmoud et al. [245] investigation is vertically upwards whereas the microchannel consisted of an adiabatic calming section of 150 mm length, followed by a heated section of 150 mm length and a borosilicate visualisation section of 100 mm length with same inner diameter as the investigated tube. After the visualization section, another adiabatic calming section of 100 mm length was added. The experiments were conducted at constant pressure of 0.8 MPa for various heat fluxes from 12.6 to 95.5 $\mathrm{kW\,m^{-2}}$, for mass flux values ranging from 200 to 500 $\mathrm{kg\,m^{-2}\,s^{-1}}$. The same set-up as described by Mahmoud et al. [245] has been constructed for the performance of the 2D axisymmetric simulations of the present study, with the only exception being that the visualisation section that is included in the experimental setup, here has been neglected, meaning that after the heated section, a 100 mm adiabatic section is directly added instead. With regards to the computational domain, the same cell size as well as, the same boundary conditions as described in the previous section, have been used also here. The experimental set-up and numerical domain with the prescribed boundary conditions and domain dimensions can be seen in Figure 70.

5.11 Validation of the model in microchannels

For the validation of the model, the case of 41 $\mathrm{kW\,m^{-2}}$ for mass flux values of 200 $\mathrm{kg\,m^{-2}\,s^{-1}}$ and 300 $\mathrm{kg\,m^{-2}\,s^{-1}}$, with inner diameter of 1.16 mm, has been selected. The quantitative results, of the heat transfer coefficient against the axial distance of the

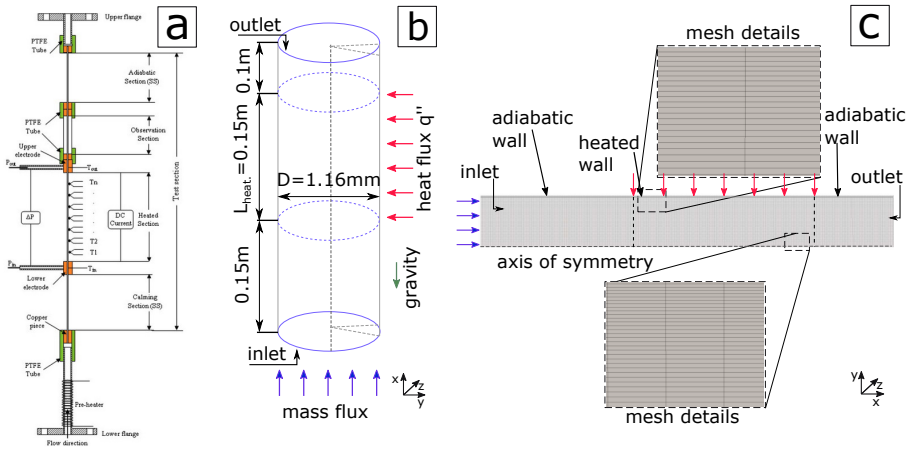

Figure 70: Experimental and numerical set-up. a) Experimental domain as provided by Mahmoud et al. [245] b) computational domain and dimensions, c) mesh details and boubndary conditions.

heated wall, are shown in Figure 71a and Figure 71b for the cases of $G = 200\,\mathrm{kg\,m^{-2}\,s^{-1}}$ and $G = 300\,\mathrm{kg\,m^{-2}\,s^{-1}}$, respectively. As it can be seen in addition to the DEBORA 1 setup where the value of d_{ref} is 0.48 mm, one more numerical case has been added where all the key parameters values are the same as DEBORA 1 set-up except the d_{ref} valued which has been modified to 0.70 mm. This way we can observe the sensitivity of the model when simulating flow boiling in microchannels, in a parameter that has been shown earlier that has major impact on all the examined fluid flow and heat transfer characteristics. From the quantitative results it is evident that the capability of predicting the heat transfer coefficient h is highly dependent on the value of the mass flux. Particularly, for higher mass flux (e.g. $300\,\mathrm{kg\,m^{-2}\,s^{-1}}$), overall the model is able to predict well the heat transfer coefficient along the axial distance of the channel. Conversely, this is not the case for lower mass flux (e.g. $200\,\mathrm{kg\,m^{-2}\,s^{-1}}$) where the model shows less accuracy compared to the experimental results. This can be attributed to the fact that for high mass fluxes the bubbles depart at a smaller diameter, which is closer to the sub-models for conventional tubes the model is currently using. On the other hand, for low mass fluxes in the case of microchannels, from the VOF results presented in the previous chapter, for similar ranges of heat and mass fluxes large elongated bubbles that fill the entire cross-section are observed. Additionally, as expected, the further tuning of the bubble detachment diameter model did not optimise the results. The above results indicate how numerical simulations from one completely different numerical model such as the VOF can contribute to a better understanding of the capabilities of another model such as the Eulerian-Eulerian two-fluid model and how these two can be "linked" in the future in order to improve the accuracy of the other and better understand the source of the problem. Finally, from the above example, it is clear that the closures that come with the original Eulerian-Eulerian solver of OpenFOAM and the majority of the commercial packages and are utilised in investigations of conventional tubes, are not suitable for investigating flow boiling phenomena in minichannels and microchannels.

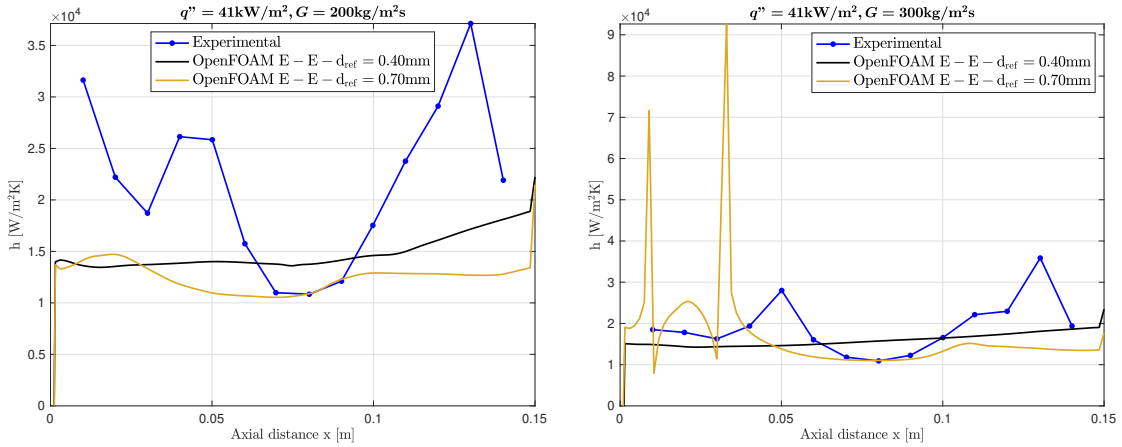

(a) **(b)**

Figure 71: Comparison between numerical simulation results for two different d_{ref} values and the experiment performed in [245].

5.12 Conclusions

The RPI wall boiling model using the OpenFOAM CFD package has been validated against experimental data available in literature. The validation has been conducted in two main stages; a) against experiments of subcooled flow boiling of R12 within a circular conventional tube and b) against experiments of subcooled flow boiling of R134a within circular microchannel. For the prediction of radial and axial profiles of the experimental data, the tuning of the empirical parameters that are included in the nucleation site density N_w, bubble detachment diameter D_w, and the bubble detachment frequency f sub-models, has been necessary. The remarks of the present investigation are summarised below:

a) from the investigation on flow boiling within a single conventional tube:

- The numerical model is able to predict the radial profiles of the vapour fraction and the liquid temperature, as well as the axial profiles of the heat transfer coefficient and wall superheat/temperature, after performing a recalibration of the constitutive correlations.

- The model cannot predict well the trend of the radial profiles for the velocity and the bubble detachment diameter. This is attributed to the fact that the present model does not account for bubble coalescence effects, meaning that the buoyancy effects resulting higher velocities than predicted towards the centre of the tube. Additionally, the attraction and coalescing of the small bubbles from the bigger bubbles that cause a significant reduction of the bubble detachment diameter towards the wall of the tube, can also not be captured here.

- The model shows high sensitivity when the operating conditions change (even not significantly such as DEBORA 3 VS DEBORA 4 case), and the tuning of the correlations is essential for the accurate prediction of the experimental data.

- From the sensitivity analysis of the parameters that comprise the empirical closures of the sub-models it has been shown that the reference diameter d_{ref} of the bubble detachment diameter closure, has a significant influence on all the examined fluid and heat transfer characteristics. Additionally, it can be seen that all the closures have a significant influence on the wall superheat/temperature profile, measured on the axial distance. Conversely the closure parameters C_n and N_{ref} and ΔT_{ref} of the nucleation site density sub-model, and the C_f constant, of the bubble detachment frequency sub-model, have either intermediate or minor influence on the radial profiles of the volume fraction, bubble detachment diameter, velocity and liquid temperature profiles.

- By adding a bubble coalescence and break-up model it could be seen that the velocity profile can be significantly improved after performing a sensitivity analysis, however other parameters such as the vapour fraction are significantly affected as well.

b) from the investigation on flow boiling within a single microchannel:

- The results showed good agreement compared to the experimental data for high mass flux values, however, poor agreement could be seen for lower mass flux values. This is attributed to different departure diameters of the nucleated bubbles, where for the case of higher mass flux the departure diameter is smaller agreeing to some extent with the current sub-models designed for conventional tubes. However, for lower mass fluxes where the bubble diameter is higher the existing correlations do not describe well the resulting phenomena.

- Even when the d_{ref} parameter of the bubble detachment diameter sub-model is modified, the present model is not able to better predict the heat transfer coefficient trend. This can be attributed to the different underlying physical phenomena of flow boiling within microchannels compared to conventional tubes, and by the fact that the included sub-models use empirical correlations based on experiments conducted in conventional tubes.

- The development of suitable closures that are based on data that have been obtained specifically from studies of flow boiling within microchannels at various operating conditions is necessary for being able to utilise the RPI model in such micro-scale investigations.

6 Conclusions and future work

6.1 Summary

Thermal management of new smart devices which follow the current trend of miniaturisation has become a critical problem for electronic devices of high heat flux and energy systems. In the past years, researchers have investigated various alternatives to the current conventional cooling solutions, e.g. air convection through fans or pumped liquid cooling since these cannot cope with such high rates of heat-dissipation. Flow boiling within microchannels is regarded as one of the most promising solutions that offer efficient thermal management of high-power density electronic components, dissipating high heat fluxes in the order of $\mathrm{MW\,m^{-2}}$. However, the lack of accurate design correlations in combination with the unclear understanding of fundamental underlying principles and mechanisms, have made a major challenge to the actual transition of this cooling method from the laboratory to commercial applications. The present PhD thesis initially investigates numerically various controlling parameters which play a significant role in better understanding of the underlying principles and mechanisms and for the prediction of heat transfer and fluid flow characteristics, under various conditions. This investigation is conducted by performing high-fidelity simulations, utilising an enhanced customised VOF-based solver of OpenFOAM CFD toolbox. Particularly, the utilised solver enhancements involve an appropriate treatment for spurious velocities dampening, an improved dynamic contact angle treatment, as well as the implementation of a phase-change model in the fluid domain also accounting for Conjugate Heat Transfer (CHT) with the solid domain.

Important design parameters of microhannels heat sinks including the surface wettability, aspect ratio, hydraulic diameter and solid surface thermophysical properties were isolated and extensively examined both qualitatively and quantitatively. The numerical simulations are focusing on the first transient stages of flow pattern development and heat transfer characteristics, stages that are often ignored in previous experimental and numerical studies. This constitutes the key novelty of the present PhD thesis as for the first time in the literature the effect of important controlling parameters is isolated, identified and quantified for the first transient stages of the two-phase flow development, correlating macroscopic flow visualisation results with quantitative heat transfer characteristics. Additionally, for the case of the thermophysical properties of the solid surface, a new correlation for the prediction of the global Nusselt number, based on an existing correlation available in the literature, is proposed.

As it has been illustrated by the wide series of parametric numerical experiments that were performed in this project, the VOF method is suitable for studies where the local phenomena are of great interest, however, it is computationally expensive and time-consuming for utilising it directly in practical engineering calculations at device scales. Conversely, a different numerical method such as the Eulerian-Eulerian two-fluid method is able to calculate complex phenomena including flow boiling within conventional tubes, at much lower computational cost and less computational time. In this method, the conservation equations are coupled with closures for the momentum and mass exchange between the liquid and vapour phases, as well as for the physical mechanisms such as the interfacial forces and the heat and mass forces across the

interface, determining in this way the degree of thermal and hydraulic non-equilibrium between the phases. The closures that relate to boiling heat transfer constitute part of the wall heat flux partitioning model, describing the partitioning of the wall heat flux into the physical mechanisms responsible for the heat transfer between the solid and fluid domain in cases of flow boiling. In the present PhD thesis, the RPI (Rensselaer Polytechnic Institute) wall partitioning model is utilised. This model has been validated in the past against experimental data of subcooled flow boiling within conventional tubes, however, the capabilities in more complex cases such as flow boiling within mini and micro-channels are still questioned since the correlations that are used in the submodels are based on data of flow boiling within conventional tubes. In the present PhD thesis, the Eulerian-Eulerian two-fluid model of OpenFOAM (v. 8.0) is used, in order to examine its capabilities on simulations of flow boiling in both conventional tubes and mini/micro-channels, aiming to show the need of developing new correlations based on data of flow boiling within microchannels, replacing the existing ones.

6.2 Conclusions

Initially, the effect of surface wettability on a single rectangular microchannel was studied on hydrophilic, hydrophobic and superhydrophobic surfaces. Different scenarios of artificially nucleation bubbles were examined (e.g. single nucleation site of single nucleation event, multiple nucleation sites of recurring events etc.), at various heat flux and mass flux values. The results indicated that surface wettability plays a significant role in the flow regime and the associated dominant heat transfer mechanism, for all the above described scenarios. Qualitatively it has been observed that liquid film evaporation is the dominant heat transfer mechanism for the hydrophilic cases while contact line evaporation is the dominant heat transfer mechanism for the hydrophobic cases. When the two-phase global Nusselt number was compared with the corresponding single-phase stage, for the hydrophilic surfaces an increase of 43.9% was observed within 8.4 ms, whereas for the hydrophobic surface an increase of just 17.8% could be seen. This difference has been attributed to the high efficiency of liquid film evaporation compared to contact line evaporation.

The aspect ratio of the microchannels has been also studied extensively in the present PhD thesis. Different aspect ratios at different heat and mass flux values were studied considering a single microchannel. The main findings were that for the more realistic case of multiple arbitrary distributed nucleation sites, the wide channel shows the highest values of both local and global time-averaged Nusselt numbers, which is however associated with its high single-phase stage values. However when the percentage difference between the single-phase stages and the corresponding two-phase stages was compared, then the case of the narrow channel showed the biggest increase with 27.13% compared to 10.57% and 10.42% for the squared and the wide channels, respectively. Differences between the cases were observed also on the resulting flow regimes. In more detail, after the merging of the nucleated bubbles, elongated vapour slugs could be seen for all three cases. However, it has been found that the length of the elongated vapour slug decreases with the increase of the channel aspect ratio. Moreover, the shape and form of both the elongated vapour bubbles as well as of the smaller bubbles upstream

(i.e., contact areas with the channel walls) is also affected significantly by the increase of the aspect ratio, indicating an alteration in the contribution of the dominant heat transfer mechanisms.

The thermophysical properties of the solid walls of the microchannel are considered vital for the design of microchannel heat sinks, therefore special attention should be given for the selection of the appropriate material in relation to each application. Isolating the properties of the solid surface thermophysical properties in order to examine its influence on flow and heat transfer characteristics, is a very challenging task to do experimentally, since other important parameters such as surface wettability and roughness, are also involved. In the present thesis, the thermophysical properties of five different surfaces have been isolated and studied numerically for realistic scenarios of multiple nucleation sites and recurring nucleation events, considering single microchannels. For the first time in the literature the proposed effect is isolated, identified and quantified focusing on the resulting interfacial dynamics and heat transfer characteristics during the first transient stage, from the bubble nucleation and growth up to the two-phase flow development. The results indicated that the variation of such properties, substantially affects the resulting flow boiling regimes as well as the heat transfer characteristics and enhancement. A significant increase, compared to the initial single-phase stage simulations, in the time-averaged heat transfer coefficient of more than 40% has been observed for the cases of silver and aluminium, whereas the cases of stainless steel and brass demonstrated a lower heat transfer coefficient increase (e.g. $< 30\%$). The better performance of the aluminium, silver and copper surfaces are associated with the resulting flow boiling regimes, which are characterised by larger in volume vapour slugs, higher bubble coalescence rates, less presence of bubbly flows and thicker liquid films. Additionally, a modified empirical correlation based on an existing correlation available in literature is proposed. This new correlation takes into consideration, for the first time in the literature the thermal diffusivity of the solid material of the microchannel. It is shown that the improved correlation can better predict the direct numerical simulation VOF results in comparison to the original one that does not consider the solid material properties.

Last but not least, the effect of microchannel hydraulic diameter has been also isolated and examined. During this study, four different hydraulic diameters were examined (keeping a constant heat transfer rate and a constant volumetric flow rate). The main findings were that smaller elongated bubbles/slugs are observed when the hydraulic diameter is increased, whereas the increase in the applied heat transfer rate has resulted in an increase in bubble growth rate and bubble coalescence events, resulting in more elongated vapour slugs. Additionally, the increase of the time-averaged heat transfer coefficient of the two-phase runs, compared to the corresponding single-phase cases, is progressively higher for lower values of channel hydraulic diameter. Additionally, a comparison of a single microchannel with a hydraulic diameter of 200 µm and four parallel microchannels, each with a hydraulic diameter of 50 µm, have been performed. The findings revealed that the local time-averaged thermal resistance decreased with the decrease in the hydraulic diameter and the increase in the channel number. For the single microchannel heat sink, the two-phase thermal resistance is decreased by 5.4% compared to its single-phase stage, whereas for the multiple channels case the thermal

resistance is decreased by 23.3% compared to its single-phase stage. The difference in the thermal resistance can be attributed to the thicker liquid film that the case of 200 µm has compared to the 50 µm, leading to an increased convection and conduction resistance and hence a decrease in heat transfer performance.

In the last part of the present thesis, the capabilities of the Eulerian-Eulerian two-fluid model of OpenFOAM are examined initially against experiments of flow boiling within conventional tubes and subsequently against experimental data of flow boiling within microchannels. The results showed that the Eulerian-Eulerian two-fluid model of OpenFOAM is able to adequately predict the radial profiles of the vapour fraction and the liquid temperature, as well as the axial profiles of the heat transfer coefficient and wall temperature, after performing a recalibration of the constitutive correlations tuning various empirical coefficients. However when the optimised/calibrated numerical simulation set-up was applied to numerically reproduce experiments of flow boiling in microchannels it has been found that the model is not able to predict the heat transfer coefficient trend for all the examined cases successfully, especially for the case of low to moderate mass fluxes. This is attributed to the different underlying physical phenomena of flow boiling within microchannels compared to conventional tubes, and by the fact that the included sub-models use empirical correlations based on experiments conducted in conventional tubes.

Finally, the above results indicate that the development of suitable closures that are based on data that have been obtained specifically from studies of flow boiling within microchannels at various operating conditions is necessary in order to be able to utilise the RPI model in such micro-scale investigations.

6.3 Future work

From the above findings, it is clear that future studies are expected to accomplish work on further developing correlations, for the prediction of the heat transfer coefficient/Nusselt number, which are based on data obtained from microchannel heat sink studies and will include important design parameters such as the ones examined in the present thesis. Furthermore, in order to be able to examine more global and macro-scale phenomena using the Eulerian-Eulerian two-fluid model and the RPI wall partitioning model, the replacement of the existing closure relationships with the new-developed sub-models is necessary. The huge database of the DNS results from the application of the VOF method that resulted from the investigation of the effect of important controlling parameters regarding flow boiling within micro-passages in combination with future high-resolution spatiotemporally resolved diagnostics could significantly aid in the development of such closure relationships in the future. Furthermore, the coupling of the VOF method with other meso-scale modelling approaches is also necessary in order to be able to account also for the onset of the boiling, i.e. the natural appearance of bubble embryos in the heated walls.

References

[1] D. Li, G. S. Wu, W. Wang, Y. D. Wang, D. Liu, D. C. Zhang, Y. F. Chen, G. P. Peterson, and R. Yang, *Enhancing flow boiling heat transfer in microchannels for thermal management with monolithically-integrated silicon nanowires*, Nano Letters **12**, 3385–3390 (2012).

[2] T. G. Karayiannis and M. M. Mahmoud, *Flow boiling in microchannels: Fundamentals and applications*, Applied Thermal Engineering **115**, 1372–1397 (2017).

[3] W. J. Minkowycz, E. Sparrow, and J. P. Abraham, *Nanoparticle Heat Transfer and Fluid Flow*, CRC Press, Boca Raton, 1st editio edition (2013).

[4] J. R. Thome and A. Cioncolini. *Chapter Four - Flow Boiling in Microchannels.* In E. M. Sparrow, J. P. Abraham, and J. M. Gorman, editors, *Advances in Heat Transfer.*, volume 49 of *Advances in Heat Transfer*, pages 157 – 224. Elsevier, (2017).

[5] B. Yang, P. Wang, and A. Bar-Cohen, *Mini-contact enhanced thermoelectric cooling of hot spots in high power devices*, IEEE Transactions on Components and Packaging Technologies **30**, 432–438 (2007).

[6] L. Jiang, J. Mikkelsen, J. M. Koo, D. Huber, S. Yao, L. Zhang, P. Zhou, J. G. Maveety, R. Prasher, J. G. Santiago, T. W. Kenny, and K. E. Goodson, *Closed-loop electroosmotic microchannel cooling system for VLSI circuits*, IEEE Transactions on Components and Packaging Technologies **25**, 347–355 (2002).

[7] D. S. Kercher, J. B. Lee, O. Brand, M. G. Allen, and A. Glezer, *Microjet cooling devices for thermal management of electronics*, IEEE Transactions on Components and Packaging Technologies **26**, 359–366 (2003).

[8] Y. Cai, Y. Wang, D. Liu, and F. Y. Zhao, *Thermoelectric cooling technology applied in the field of electronic devices: Updated review on the parametric investigations and model developments*, Applied Thermal Engineering **148**, 238–255 (2019).

[9] S. Trutassanawin and G. E. A. *Review of Refrigeration Technologies for High Heat Dissipation Electronics Cooling.* In *International Refrigeration and Air Conditioning Conference*, pages 1–10, Purdue, USA, (2004). International Refrigeration and Air Conditioning Conference.

[10] J. M. Koo, S. Im, L. Jiang, and K. E. Goodson, *Integrated microchannel cooling for three-dimensional electronic circuit architectures*, Journal of Heat Transfer **127**, 49–58 (2005).

[11] T. G. Karayiannis and M. M. Mahmoud. *Flow Boiling in Micro-Passages : Applications of Microchannel Heat Exchangers.* In *16th International Heat Transfer Conference, IHTC-16*, page 25, Beijing, (2018).

[12] D. B. Tuckerman and R. F. W. Pease, *High-Performance Heat Sinking for VLSI*, IEEE Electron Device Letters **EDL-2**, 126–129 (1981).

[13] W. Qu, S. M. Yoon, and I. Mudawar, *Two-phase flow and heat transfer in rectangular micro-channels*, Proceedings of the ASME Summer Heat Transfer Conference **2003**, 397–410 (2003).

[14] A. Koşar, C. J. Kuo, and Y. Peles, *Suppression of boiling flow oscillations in parallel microchannels by inlet restrictors*, Journal of Heat Transfer **128**, 251–260 (2006).

[15] T. M. Bandhauer, A. Agarwal, and S. Garimella, *Measurement and Modeling of Condensation Heat Transfer Coefficients in Circular Microchannels*, Journal of Heat Transfer **128**, 1050–1059 (2006).

[16] D. Attinger, C. Frankiewicz, A. R. Betz, T. M. Schutzius, R. Ganguly, A. Das, C.-J. Kim, and C. M. Megaridis, *Surface engineering for phase change heat transfer: A review*, MRS Energy and Sustainability **1**, 1–85 (2014).

[17] V. K. Dhir. *Phase change heat transfer – A perspective for the future.* In *Rohsenow Symposium on Future Trends in Heat Transfer*, pages 1–6, (2003).

[18] P. Cheng and H. Wu. *Mesoscale and Microscale Phase-Change Heat Transfer.* In G. A. Greene, J. P. Hartnett†, A. Bar-Cohen, and Y. I. Cho, editors, *Advances in Heat Transfer*, volume 39 of *Advances in Heat Transfer*, pages 461–563. Elsevier, (2006).

[19] H. J. Cho, D. J. Preston, Y. Zhu, and E. N. Wang, *Nanoengineered materials for liquid–vapour phase-change heat transfer*, Nature Reviews Materials **2**, 16092 (2016).

[20] D. Attinger, C. Frankiewicz, A. R. Betz, T. M. Schutzius, R. Ganguly, A. Das, C.-J. Kim, and C. M. Megaridis, *Surface engineering for phase change heat transfer: A review*, MRS Energy & Sustainability **1**, 1–40 (2014).

[21] Y. Liu, X. Han, C. Shen, F. Yao, and M. Zhang, *Experimental study on the evaporation and condensation heat transfer characteristics of a vapor chamber*, Energies **12** (2019).

[22] Y. Koizumi, M. Monde, and Y. Takata. *Outline of Boiling Phenomena and Heat Transfer Characteristics.* In *Boiling: Research and Advances*, chapter 1, pages 1–11. Elsevier Inc., (2017).

[23] C. E. Brennen, *Fundamentals of multiphase flow*, Fundamentals of Multiphase Flow **1**, 1–345 (2005).

[24] R. Rabiee, B. Rajabloo, M. Désilets, and P. Proulx, *Heat transfer analysis of boiling and condensation inside a horizontal heat pipe*, International Journal of Heat and Mass Transfer **139**, 526–536 (2019).

[25] H. Rusche. *Computational Dispersed Two-Phase Dynamics Flows of At Phase Fractions*. PhD thesis, Imperial College London, (2003).

[26] C. Kunkelmann. *Numerical Modeling and Investigation of Boiling Phenomena*. PhD thesis, Technical University Darmstadt, (2011).

[27] S. M. Ghiaasiaan, *Two-Phase Flow, Boiling, and Condensation: In Conventional and Miniature Systems*, Cambridge University Press, 2nd edition (2017).

[28] A. N. Guion. *Modeling and Simulation of Liquid Microlayer Formation and Evaporation in Nucleate Boiling using Computational Fluid Dynamics*. PhD thesis, Massachusetts Institute of Technology, (2017).

[29] D. P. D. Theodore L. Bergman, Adrienne S. Lavine, Frank P. Incropera, *Fundamentals of Heat and Mass Transfer*, Wiley, New York, 8th edition (2017).

[30] S. Nukiyama, *The maximum and minimum values of the heat Q transmitted from metal to boiling water under atmospheric pressure*, International Journal of Heat and Mass Transfer **9**, 1419–1433 (1966).

[31] M. G. Cooper. *Heat Flow Rates in Saturated Nucleate Pool Boiling-A Wide-Ranging Examination Using Reduced Properties*. In *Advances in Heat Transfer*, volume 16, chapter Heat Flow, pages 157–239. Elsevier, (1984).

[32] G. Ribatski and J. M. Jabardo, *Experimental study of nucleate boiling of halocarbon refrigerants on cylindrical surfaces*, International Journal of Heat and Mass Transfer **46**, 4439–4451 (2003).

[33] D. Jung, Y. Kim, Y. Ko, and K. Song, *Nucleate boiling heat transfer coefficients of pure halogenated refrigerants*, International Journal of Refrigeration **26**, 240–248 (2003).

[34] Y. A. Cengel, *Heat transfer: A Practical Approach*, McGraw-Hill, New York (2002).

[35] K. Stephan and M. Abdelsalam, *Heat-transfer correlations for natural convection boiling*, International Journal of Heat and Mass Transfer **23**, 73–87 (1980).

[36] T. Harirchian and S. V. Garimella, *A comprehensive flow regime map for microchannel flow boiling with quantitative transition criteria*, International Journal of Heat and Mass Transfer **53**, 2694–2702 (2010).

[37] M. K. Akbar, D. A. Plummer, and S. M. Ghiaasiaan, *On gas-liquid two-phase flow regimes in microchannels*, International Journal of Multiphase Flow **29**, 855–865 (2003).

[38] E. V. Rebrov, *Two-phase flow regimes in microchannels*, Theoretical Foundations of Chemical Engineering **44**, 355–367 (2010).

[39] S. G. Kandlikar and P. Balasubramanian, *An Extension of the Flow Boiling Correlation to Transition, Laminar, and Deep Laminar Flows and Microchannels*, Heat Transfer Engineering **25**, 86–93 (2004).

[40] G. Lazarek and S. Black, *Evaporative heat transfer, pressure drop and critical heat flux in a small vertical tube with R-113*, International Journal of Heat and Mass Transfer **25**, 945 – 960 (1982).

[41] P. A. Kew and K. Cornwell, *Correlations for the prediction of boiling heat transfer in small-diameter channels*, Applied Thermal Engineering **17**, 705–715 (1997).

[42] G. R. Warrier, V. K. Dhir, and L. A. Momoda, *Heat transfer and pressure drop in narrow rectangular channels*, Experimental Thermal and Fluid Science **26**, 53–64 (2002).

[43] W. Yu, D. M. France, M. W. Wambsganss, and J. R. Hull, *Two-phase pressure drop, boiling heat transfer, and critical heat flux to water in a small-diameter horizontal tube*, International Journal of Multiphase Flow **28**, 927–941 (2002).

[44] J. Lee and I. Mudawar, *Two-phase flow in high-heat-flux micro-channel heat sink for refrigeration cooling applications: Part II - Heat transfer characteristics*, International Journal of Heat and Mass Transfer **48**, 941–955 (2005).

[45] W. Li and Z. Wu, *A general correlation for evaporative heat transfer in micro/mini-channels*, International Journal of Heat and Mass Transfer **53**, 1778–1787 (2010).

[46] B. J. Jones and S. V. Garimella, *Surface roughness effects on flow boiling in microchannels*, Journal of Thermal Science and Engineering Applications **1**, 1–9 (2009).

[47] S. S. Bertsch, E. A. Groll, and S. V. Garimella, *Effects of heat flux, mass flux, vapor quality, and saturation temperature on flow boiling heat transfer in microchannels*, International Journal of Multiphase Flow **35**, 142–154 (2009).

[48] M. M. Mahmoud and T. G. Karayiannis, *Heat transfer correlation for flow boiling in small to micro tubes*, International Journal of Heat and Mass Transfer **66**, 553–574 (2013).

[49] L. Sun and K. Mishima, *An evaluation of prediction methods for saturated flow boiling heat transfer in mini-channels*, International Journal of Heat and Mass Transfer **52**, 5323–5329 (2009).

[50] H. Wang and X. Fang, *Evaluation Analysis of Correlations of Flow Boiling Heat Transfer Coefficients Applied to Ammonia*, Heat Transfer Engineering **37**, 32–44 (2016).

[51] M. Lee, Y. Y. Wong, M. Wong, and Y. Zohar, *Size and shape effects on two-phase flow patterns in microchannel forced convection boiling*, Journal of Micromechanics and Microengineering **13**, 155–164 (2003).

[52] K. K. Ferster, K. L. Kirsch, and K. A. Thole, *Effects of geometry, spacing, and number of pin fins in additively manufactured microchannel pin fin arrays*, Journal of Turbomachinery **140**, 1–10 (2018).

[53] X. Shi, S. Li, Y. Mu, and B. Yin, *Geometry parameters optimization for a microchannel heat sink with secondary flow channel*, International Communications in Heat and Mass Transfer **104**, 89–100 (2019).

[54] E. Bayrak, A. B. Olcay, and M. F. Serincan, *Numerical investigation of the effects of geometric structure of microchannel heat sink on flow characteristics and heat transfer performance*, International Journal of Thermal Sciences **135**, 589–600 (2019).

[55] S. Chamoli, R. Lu, H. Chen, Y. Cheng, and P. Yu, *Numerical optimization of design parameters for a modified double-layer microchannel heat sink*, International Journal of Heat and Mass Transfer **138**, 373–389 (2019).

[56] X. F. Peng, G. P. Peterson, and B. X. Wang, *Frictional flow characteristics of water flowing through rectangular microchannels*, Experimental Heat Transfer **7**, 249–264 (1994).

[57] K. A. Triplett, S. M. Ghiaasiaan, S. I. Abdel-Khalik, and D. L. Sadowski, *Gas-liquid two-phase flow in microchannels part I: Two-phase flow patterns*, International Journal of Multiphase Flow **25**, 377–394 (1999).

[58] K. A. Triplett, S. M. Ghiaasiaan, S. I. Abdel-Khalik, A. LeMouel, and B. N. McCord, *Gas-liquid two-phase flow in microchannels Part II: Void fraction and pressure drop*, International Journal of Multiphase Flow **25**, 395–410 (1999).

[59] J. P. Sharma, A. Sharma, R. D. Jilte, R. Kumar, and M. H. Ahmadi, *A study on thermohydraulic characteristics of fluid flow through microchannels*, Springer International Publishing (2020).

[60] C. Y. Zhao and T. J. Lu, *Analysis of microchannel heat sinks for electronics cooling*, International Journal of Heat and Mass Transfer **45**, 4857–4869 (2002).

[61] Y. H. Pan, R. Zhao, X. H. Fan, Y. L. Nian, and W. L. Cheng, *Study on the effect of varying channel aspect ratio on heat transfer performance of manifold microchannel heat sink*, International Journal of Heat and Mass Transfer **163**, 120461 (2020).

[62] W. T. Yan, W. B. Ye, and C. Li, *Effect of aspect ratio on saturated boiling flow in microchannels with nonuniform heat flux*, Heat Transfer - Asian Research **48**, 3312–3327 (2019).

[63] Y. K. Prajapati and P. Bhandari, *Flow boiling instabilities in microchannels and their promising solutions – A review*, Experimental Thermal and Fluid Science **88**, 576–593 (2017).

[64] T. G. Karayiannis, M. M. Mahmoud, and D. B. Kenning, *A study of discrepancies in flow boiling results in small to micro diameter metallic tubes*, ASME 2011 9th International Conference on Nanochannels, Microchannels, and Minichannels, ICNMM 2011 **2**, 543–563 (2011).

[65] P. Hrnjak and X. Tu, *Single phase pressure drop in microchannels*, International Journal of Heat and Fluid Flow **28**, 2–14 (2007).

[66] Y. Li, G. Xia, Y. Jia, D. Ma, B. Cai, and J. Wang, *Effect of geometric configuration on the laminar flow and heat transfer in microchannel heat sinks with cavities and fins*, Numerical Heat Transfer; Part A: Applications **71**, 528–546 (2017).

[67] Z. Dai, D. F. Fletcher, and B. S. Haynes, *Impact of tortuous geometry on laminar flow heat transfer in microchannels*, International Journal of Heat and Mass Transfer **83**, 382–398 (2015).

[68] M. Sattari-Najafabadi, M. Nasr Esfahany, Z. Wu, and B. Sundén, *The effect of the size of square microchannels on hydrodynamics and mass transfer during liquid-liquid slug flow*, AIChE Journal **63**, 5019–5028 (2017).

[69] T. Cubaud and T. G. Mason, *Capillary threads and viscous droplets in square microchannels*, Physics of Fluids **20** (2008).

[70] O. Abouali and N. Baghernezhad, *Numerical investigation of heat transfer enhancement in a microchannel with grooved surfaces*, Journal of Heat Transfer **132**, 1–8 (2010).

[71] P. M. Chung, M. Kawaji, A. Kawahara, and Y. Shibata, *Two-phase flow through square and circular microchannels - Effects of channel geometry*, Journal of Fluids Engineering, Transactions of the ASME **126**, 546–552 (2004).

[72] D. F. Sempértegui-Tapia and G. Ribatski, *The effect of the cross-sectional geometry on saturated flow boiling heat transfer in horizontal micro-scale channels*, Experimental Thermal and Fluid Science **89**, 98–109 (2017).

[73] T. Harirchian and S. V. Garimella, *Effects of channel dimension, heat flux, and mass flux on flow boiling regimes in microchannels*, International Journal of Multiphase Flow **35**, 349–362 (2009).

[74] J. F. Tullius, R. Vajtai, and Y. Bayazitoglu, *A review of cooling in microchannels*, Heat Transfer Engineering **32**, 527–541 (2011).

[75] J. Dix and A. Jokar. *A microchannel heat exchanger for electronics cooling application.* In *Sixth International ASME Conference on Nanochannels, Microchannels and Minichannels ICNMM2008*, page 2, Darmstadt, Germany, (2018).

[76] L. ming Pan, R. gang Yan, H. jie Huang, H. He, and P. fei Li, *Experimental study on the flow boiling pressure drop characteristics in parallel multiple microchannels*, International Journal of Heat and Mass Transfer **116**, 642–654 (2018).

[77] D. F. Sempértegui-Tapia and G. Ribatski, *Chute de pression frictionnelle diphasique dans les canaux horizontaux à micro-échelle: Analyse des données expérimentales et développement d'une méthode prédictive*, International Journal of Refrigeration **79**, 143–163 (2017).

[78] K. Balasubramanian, P. Lee, C. Teo, and S. Chou, *Flow boiling heat transfer and pressure drop in stepped fin microchannels*, International Journal of Heat and Mass Transfer **67**, 234–252 (2013).

[79] P. C. Lee and C. Pan, *Boiling heat transfer and two-phase flow of water in a single shallow microchannel with a uniform or diverging cross section*, Journal of Micromechanics and Microengineering **18**, 025005 (2008).

[80] G. Tryggvason, R. Scardovelli, and S. Zaleski, *Direct Numerical Simulations of Gas–Liquid Multiphase Flows*, Cambridge University Press (2011).

[81] J. Donea, A. Huerta, and J. Ponthot, *Chapter 14: Arbitrary Lagrangian–Eulerian Methods*, Encyclopedia of Computational **1**, 1–25 (2004).

[82] H. Versteeg and W. Malalasekera, *An Introduction to Computational Fluid Dynamics*, Pearson Education Limited (2007).

[83] J. M. Hyman, *Numerical Methods for Tracking Interfaces*, Interface **12**, 396–407 (1984).

[84] A. Q. Raeini, M. J. Blunt, and B. Bijeljic, *Modelling two-phase flow in porous media at the pore scale using the volume-of-fluid method*, Journal of Computational Physics **231**, 5653–5668 (2012).

[85] S. Quan and D. P. Schmidt, *A moving mesh interface tracking method for 3D incompressible two-phase flows*, Journal of Computational Physics **221**, 761–780 (2007).

[86] S. Popinet and S. Zaleski, *A front-tracking algorithm for accurate representation of surface tension*, International Journal for Numerical Methods in Fluids **30**, 775–793 (1999).

[87] L. Chen, Z. Xiao, P. C. Chan, Y. K. Lee, and Z. Li, *A comparative study of droplet impact dynamics on a dual-scaled superhydrophobic surface and lotus leaf*, Applied Surface Science **257**, 8857–8863 (2011).

[88] F. Denner. *Balanced-Force Two-Phase Flow Modelling on Unstructured and Adaptive Meshes.* PhD thesis, Imperial College London, (2013).

[89] B. S. Mirjalili, S. S. Jain, and M. S. Dodd. *Interface-capturing methods for two-phase flows : An overview and recent developments.* Technical Report 1, Stanford University, (2017).

[90] C. W. Hirt and B. D. Nichols, *Volume of fluid (VOF) method for the dynamics of free boundaries*, Journal of Computational Physics **39**, 201–225 (1981).

[91] Osher, S. Sethian J. A., *Level Set Methods and Dynamic Implicit Surfaces*, Applied Mechanics Reviews (1980).

[92] F. Chen and H. Hagen. *A Survey of Interface Tracking Methods in Multi-phase Fluid Visualization.* In *Conference Series*, pages 11–199, (2010).

[93] A. Georgoulas, P. Koukouvinis, M. Gavaises, and M. Marengo, *Numerical investigation of quasi-static bubble growth and detachment from submerged orifices in isothermal liquid pools: The effect of varying fluid properties and gravity levels*, International Journal of Multiphase Flow **74**, 59–78 (2015).

[94] A. Georgoulas, M. Andredaki, and M. Marengo, *An enhanced VOF method coupled with heat transfer and phase change to characterise bubble detachment in saturated pool boiling*, Energies **10**, 1–35 (2017).

[95] E. Teodori, P. Pontes, A. Moita, A. Georgoulas, M. Marengo, and A. Moreira, *Sensible heat transfer during droplet cooling: Experimental and numerical analysis*, Energies **10**, 1–27 (2017).

[96] K. Vontas, M. Andredaki, A. Georgoulas, K. S. Nikas, and M. Marengo. *Numerical Investigation of Droplet Impact on Smooth Surfaces with Different Wettability Characteristics: Implementation of a dynamic contact angle treatment in OpenFOAM.* In *Proceedings ILASS–Europe 2017. 28th Conference on Liquid Atomization and Spray Systems*, number September in ILASS Europe, pages 1–8, Valencia, Spain, (2017).

[97] K. Vontas, C. Boscariol, M. Andredaki, A. Georgoulas, C. Crua, J. H. Walther, and M. Marengo, *Droplet Impact on Suspended Metallic Meshes: Effects of Wettability, Reynolds and Weber Numbers*, Fluids **5**, 1–28 (2020).

[98] P. Pontes, R. Cautela, E. Teodori, A. S. Moita, A. Georgoulas, and A. L. N. M. Moreira, *Bubble Dynamics and Heat Transfer on Biphilic Surfaces: Experiments and Numerical Simulation*, Journal of Bionic Engineering **17**, 1–13 (2020).

[99] M. Andredaki, A. Georgoulas, and M. Marengo, *Numerical investigation of quasi-sessile droplet absorption into wound dressing capillaries*, Physics of Fluids **32**, 092112 (2020).

[100] A. Georgoulas and M. Marengo. *Numerical simulation of flow boiling in microchannels: bubble growth, detachment and coalescence.* In *UK Heat Transfer Conference 2015, Edinburgh, 7-8 September*, (2015).

[101] M. Andredaki, A. Georgoulas, N. Miché, and M. Marengo, *Break-up Mechanisms and Conditions for Vapour Slugs Within Mini-Channels*, 15th UK Heat Transfer Conference, UKHTC2017, Brunel University London, 4-5 September 2017 **44**, 4–5 (2017).

[102] M. Andredaki, A. Georgoulas, N. Miche, and M. Marengo, *Numerical investigation of liquid film instabilities and evaporation in confined oscillating slug-plug flows*,

WIT Transactions on Engineering Sciences, Computational and Experimental Methods in Multiphase and Complex Flow X **123**, 127–138 (2019).

[103] B. J. Cantwell. *Chapter 6: The Conservation Equations.* In *Applied Aerodynamics*, chapter 6, pages 1–38. Stanford University, Stanford, CA (USA), (2012).

[104] J. U. Brackbill, D. B. Kothe, and C. Zemach, *A continuum method for modeling surface tension*, Journal of Computational Physics **100**, 335–354 (1992).

[105] A. E. M. Mora, A. L. F. de Lima e Silva, and S. M. M. de Lima e Silva, *Numerical study of the dynamics of a droplet in a T-junction microchannel using OpenFOAM*, Chemical Engineering Science **196**, 514–526 (2019).

[106] D. A. Hoang, V. V. Steijn, L. M. Portela, M. T. Kreutzer, and C. R. Kleijn, *Computers and Fluids Benchmark numerical simulations of segmented two-phase flows in microchannels using the Volume of Fluid method*, Computers and Fluids **86**, 28–36 (2013).

[107] S. S. Deshpande, L. Anumolu, and M. F. Trujillo, *Evaluating the performance of the two-phase flow solver interFoam*, Computational Science and Discovery **5** (2012).

[108] *OpenFOAM - The OpenFOAM User Guide*, (2013).

[109] R. Scardovelli and S. Zaleski, *Direct Numerical Simulation of Free-Surface and Interfacial Flow*, Annual Review of Fluid Mechanics **31**, 567–603 (1999).

[110] R. W. Schrage. *A theoretical study of interphase mass transfer.* PhD thesis, University of Michigan, New York, (1953).

[111] S. Hardt and F. Wondra, *Evaporation Model for Interfacial Flows Based on a Continuum-field Representation of the Source Terms*, J. Comput. Phys. **227**, 5871–5895 (2008).

[112] C. Kunkelmann, K. Ibrahem, N. Schweizer, S. Herbert, P. Stephan, and T. Gambaryan-Roisman, *The effect of three-phase contact line speed on local evaporative heat transfer: Experimental and numerical investigations*, International Journal of Heat and Mass Transfer **55**, 1896–1904 (2012).

[113] C. Kunkelmann and P. Stephan, *CFD simulation of boiling flows using the volume-of-fluid method within OpenFOAM*, Numerical Heat Transfer; Part A: Applications **56**, 631–646 (2009).

[114] C. Kunkelmann and P. Stephan, *Numerical simulation of the transient heat transfer during nucleate boiling of refrigerant HFE-7100*, International Journal of Refrigeration **33**, 1221–1228 (2010).

[115] M. Magnini. *CFD Modeling of Two-Phase Boiling Flows in the Slug Flow Regime with an Interface Capturing Technique.* PhD thesis, EPFL, (2012).

[116] S. F. Kistler, *Hydrodynamics of wetting*, Wettability **6**, 311–430 (1993).

[117] A. Alali. *Development and Validation of a New Solver Based on the Interfacial Area Transport Equation for the Numerical Simulation of Sub-cooled Boiling with.* PhD thesis, Technical Univeristy Munich, (2014).

[118] N. Kurul and M. Podowski. *Multidimensional effects in forced convection subcooled boiling.* In *Proceedings of the 9th International Heat Transfer Conference*, Jerusalem, Israel, (1990).

[119] H. Steiner, A. Kobor, and L. Gebhard, *A wall heat transfer model for subcooled boiling flow*, International Journal of Heat and Mass Transfer **48**, 4161–4173 (2005).

[120] E. Koncar, Bostjan; Krepper. *CFD Simulation of forced convective boiling in heated channels.* In *Workshop on Benchmarking of CFD Codes for Application to Nuclear Reactor Safety (CFD4NRS)*, pages 673–684, (2006).

[121] M. L. de Bertodano and D. Prabhudharwadkar. *CFD Two Fluid Model for Adiabatic and Boiling Bubbly Flows in Ducts.* In H. W. Oh, editor, *Computational Fluid Dynamics*, chapter 2. IntechOpen, Rijeka, (2010).

[122] B. J. Yun, A. Splawski, S. Lo, and C. H. Song, *Prediction of a subcooled boiling flow with advanced two-phase flow models*, Nuclear Engineering and Design **253**, 351–359 (2012).

[123] E. Krepper, R. Rzehak, C. Lifante, and T. Frank, *CFD for subcooled flow boiling: Coupling wall boiling and population balance models*, Nuclear Engineering and Design **255**, 330–346 (2013).

[124] D. Prabhudharwadkar, M. A. Lopez-de Bertodano, T. Hibiki, and J. R. Buchanan, *Assessment of subcooled boiling wall boundary correlations for two-fluid model CFD*, International Journal of Heat and Mass Transfer **79**, 602–617 (2014).

[125] S. Cheung, S. Vahaji, G. Yeoh, and J. Tu, *Modeling subcooled flow boiling in vertical channels at low pressures – Part 1: Assessment of empirical correlations*, International Journal of Heat and Mass Transfer **75**, 736–753 (2014).

[126] H. Enwald, E. Peirano, and A. E. Almstedt, *Eulerian two-phase flow theory applied to fluidization*, International Journal of Multiphase Flow **22**, 21–66 (1996).

[127] C. Crowe, J. Schwarzkopf, M. Sommerfeld, and Y. Tsuji, *Multiphase Flows with Droplets and Particles*, Taylor & Francis (1997).

[128] J. Hinze, *Turbulence*, McGraw-Hill (1975).

[129] Y. Sato, M. Sadatomi, and K. Sekoguchi, *Momentum and Heat Transfer in Two-Phase Bubble Flow - I Theory*, International Journal of Multiphase Flow **7**, 167 : 177 (1981).

[130] F. R. Menter and T. Esch, *16th Brazilian Congress of Mechanical Engineering Elements of Industrial Heat Trasfer Predictions*, 16th Brazilian Congress of Mechanical Engineering **28** (2001).

[131] Q. Wang and W. Yao, *Computation and validation of the interphase force models for bubbly flow*, International Journal of Heat and Mass Transfer **98**, 799–813 (2016).

[132] G. H. Yeoh, C. P. Cheung, and J. Tu, *Multiphase Flow Analysis Using Population Balance Modeling. Bubbles, Drops and Particles*, Elsevier, Oxford, United Kingdom, 1st edition (2014).

[133] I. M. and Z. N., *Drag Coefficient and Relative Velocity in Bubbly, Droplet or Particulate Flows*, AlChE Journal **25**, 843–854 (1979).

[134] D. Drew and R. Lahey, *The virtual mass and lift force on a sphere in rotating and straining inviscid flow*, International Journal of Multiphase Flow **13**, 113–121 (1987).

[135] A. Tomiyama, *Struggle with computational bubble dynamics*, Multiphase Science and Technology **10**, 369–405 (1998).

[136] D. Legendre and J. Magnaudet, *The lift force on a spherical bubble in a viscous linear shear flow*, Journal of Fluid Mechanics **368**, 81–126 (1998).

[137] S. P. Antal, R. T. Lahey, and J. E. Flaherty, *Analysis of phase distribution in fully developed laminar bubbly two-phase flow*, International Journal of Multiphase Flow **17**, 635–652 (1991).

[138] M. Lopez de Bertodano, R. T. Lahey, and O. C. Jones, *Turbulent bubbly two-phase flow data in a triangular duct*, Nuclear Engineering and Design **146**, 43–52 (1994).

[139] W. E. Ranz and J. W. R. Marshall, *Vaporation from Drops, Part I*, Chem. Eng. Prog **48**, 141–146 (1952).

[140] L. A. Gilman. *Development of a General Purpose Subgrid Wall Boiling Model from Improved Physical Understanding for Use in Computational Fluid Dynamics*. PhD thesis, MIT, (2014).

[141] V. H. Del Valle and D. B. Kenning, *Subcooled flow boiling at high heat flux*, International Journal of Heat and Mass Transfer **28**, 1907–1920 (1985).

[142] J. S. Murallidharan, B. V. Prasad, B. S. Patnaik, G. F. Hewitt, and V. Badalassi, *CFD investigation and assessment of wall heat flux partitioning model for the prediction of high pressure subcooled flow boiling*, International Journal of Heat and Mass Transfer **103**, 211–230 (2016).

[143] M. Lemmert and J. Chawla, *Influence of flow velocity on surface boiling heat transfer coefficient*, Heat Transfer in Boiling **237** (1977).

[144] G. Kocamustafaogullari and M. Ishii, *Foundation of the interfacial area transport equation and its closure relations*, International Journal of Heat and Mass Transfer **38**, 481–493 (1995).

[145] V. Tolubinsky and D. Kostanchuk. *Vapour bubbles growth rate and heat transfer intensity at subcooled water boiling.* In *International Heat Transfer Conference 4*, volume 23. Begel House Inc., (1970).

[146] Q. Wu, S. Kim, M. Ishii, and S. G. Beus, *One-group interfacial area transport in vertical bubbly flow*, International Journal of Heat and Mass Transfer **41**, 1103–1112 (1998).

[147] M. ISHII, S. KIM, and J. KELLY, *Development of Interfacial Area Transport Equation*, Nuclear Engineering and Technology **37**, 11 (2005).

[148] K. Zhou, C. Coyle, J. Li, J. Buongiorno, and W. Li, *Flow boiling in vertical narrow microchannels of different surface wettability characteristics*, International Journal of Heat and Mass Transfer **109**, 103–114 (2017).

[149] A. M. Barajas and R. L. Panton, *The effects of contact angle on two-phase flow in capillary tubes*, International Journal of Multiphase Flow **19**, 337–346 (1993).

[150] A. Serizawa, Z. Feng, and Z. Kawara, *Two-phase flow in microchannels*, American Society of Mechanical Engineers, Heat Transfer Division, (Publication) HTD **26**, 703–714 (2002).

[151] P. Rapolu and S. Y. Son, *Characterization of wettability effects on pressure drop of two-phase flow in microchannel*, Experiments in Fluids **51**, 1101–1108 (2011).

[152] T. Cubaud and C. M. Ho, *Transport of bubbles in square microchannels*, Physics of Fluids **16**, 4575–4585 (2004).

[153] T. Cubaud, U. Ulmanella, and C. M. Ho, *Two-phase flow in microchannels with surface modifications*, Fluid Dynamics Research **38**, 772–786 (2006).

[154] S. C. Cho and Y. Wang, *Two-phase flow dynamics in a micro channel with heterogeneous surfaces*, International Journal of Heat and Mass Transfer **71**, 349–360 (2014).

[155] S. G. Kandlikar, *Scale effects on flow boiling heat transfer in microchannels: A fundamental perspective*, International Journal of Thermal Sciences **49**, 1073–1085 (2010).

[156] S. G. Kandlikar and W. J. Grande, *Evolution of microchannel flow passages-thermohydraulic performance and fabrication technology*, Heat Transfer Engineering **24**, 3–17 (2003).

[157] R. Rioboo, M. Marengo, S. Dall'Olio, M. Voue, and J. De Coninck, *An innovative method to control the incipient flow boiling through grafted surfaces with chemical patterns*, Langmuir **25**, 6005–6009 (2009).

[158] H. T. Phan, N. Caney, P. Marty, S. Colasson, and J. Gavillet, *Flow boiling of water on nanocoated surfaces in a microchannel*, Journal of Heat Transfer **134**, 1–6 (2012).

[159] T. Y. Liu, P. Li, C. Liu, and C. Gau, *Boiling flow characteristics in microchannels with very hydrophobic surface to super-hydrophilic surface*, International Journal of Heat and Mass Transfer **54**, 126–134 (2011).

[160] W. Li, K. Zhou, J. Li, Z. Feng, and H. Zhu, *Effects of heat flux, mass flux and two-phase inlet quality on flow boiling in a vertical superhydrophilic microchannel*, International Journal of Heat and Mass Transfer **119**, 601–613 (2018).

[161] W. Li, Z. Chen, J. Li, K. Sheng, and J. Zhu, *Subcooled flow boiling on hydrophilic and super-hydrophilic surfaces in microchannel under different orientations*, International Journal of Heat and Mass Transfer **129**, 635–649 (2019).

[162] C. Choi, J. S. Shin, D. I. Yu, and M. H. Kim, *Flow boiling behaviors in hydrophilic and hydrophobic microchannels*, Experimental Thermal and Fluid Science **35**, 816–824 (2011).

[163] H. Wang, Y. Yang, M. He, and H. Qiu, *Subcooled flow boiling heat transfer in a microchannel with chemically patterned surfaces*, International Journal of Heat and Mass Transfer **140**, 587–597 (2019).

[164] J. M. Kim, T. Kim, D. In, H. Noh, M. Hwan, K. Moriyama, and H. Sun, *Effect of heterogeneous wetting surface characteristics on fl ow boiling performance*, International Journal of Heat and Fluid Flow **70**, 141–151 (2018).

[165] J. Kim, J. Y. Cho, and J. S. Lee, *Flow boiling enhancement by bubble mobility on heterogeneous wetting surface in microchannel*, International Journal of Heat and Mass Transfer **153**, 1–13 (2020).

[166] S. Gong and P. Cheng, *Numerical investigation of saturated flow boiling in microchannels by the lattice boltzmann method*, Numerical Heat Transfer; Part A: Applications **65**, 644–661 (2014).

[167] S. Gong and P. Cheng, *Lattice Boltzmann simulation of periodic bubble nucleation, growth and departure from a heated surface in pool boiling*, International Journal of Heat and Mass Transfer **64**, 122–132 (2013).

[168] J. Kim and J. S. Lee, *Numerical study on the effects of inertia and wettability on subcooled flow boiling in microchannels*, Applied Thermal Engineering **152**, 175–183 (2019).

[169] U. K. Alugoju, S. K. Dubey, and A. Javed, *3D Transient heat transfer analysis and flow visualization study in diverging microchannel for instability mitigated two-phase flow : A numerical study*, International Journal of Heat and Mass Transfer **160**, 120212 (2020).

[170] F. Yang, W. Li, X. Dai, and C. Li, *Flow boiling heat transfer of HFE-7000 in nanowire-coated microchannels*, Applied Thermal Engineering **93**, 260–268 (2016).

[171] K. Vontas. *Numerical Investigation of Droplet Impact on Metallic Meshes*. PhD thesis, Technical University of Denmark, (2018).

[172] X. Peng and G. Peterson, *Convective heat transfer and flow friction for water flow in microchannel structures*, International Journal of Heat and Mass Transfer **39**, 2599–2608 (1996).

[173] E. A. Chinnov, F. V. Ron'shin, V. V. Guzanov, D. M. Markovich, and O. A. Kabov, *Two-phase flow in a horizontal rectangular microchannel*, High Temperature **52**, 681–687 (2014).

[174] E. W. Lemmon, M. L. Huber, and M. O. McLinden. *REFPROP V 7.0, NIST*, (2002).

[175] D. Lelea, *The conjugate heat transfer of the partially heated microchannels*, Heat and Mass Transfer/Waerme- und Stoffuebertragung **44**, 33–41 (2007).

[176] M. Andredaki, A. Georgoulas, and M. Marengo, *Numerical investigation of quasi-sessile droplet absorption into wound dressing capillaries*, Physics of Fluids **32**, 092112 (2020).

[177] A. Mukherjee, S. G. Kandlikar, and Z. J. Edel, *Numerical study of bubble growth and wall heat transfer during flow boiling in a microchannel*, International Journal of Heat and Mass Transfer **54**, 3702–3718 (2011).

[178] K. Ling, G. Son, D. L. Sun, and W. Q. Tao, *Three dimensional numerical simulation on bubble growth and merger in microchannel boiling flow*, International Journal of Thermal Sciences **98**, 135–147 (2015).

[179] P. Zhang and H. W. Jia, *Evolution of flow patterns and the associated heat and mass transfer characteristics during flow boiling in mini-/micro-channels*, Chemical Engineering Journal **306**, 978–991 (2016).

[180] B. Markal, O. Aydin, and M. Avci, *Effect of aspect ratio on saturated flow boiling in microchannels*, International Journal of Heat and Mass Transfer **93**, 130–143 (2016).

[181] B. Markal, O. Aydin, and M. Avci, *Prediction of Heat Transfer Coefficient in Saturated Flow Boiling Heat Transfer in Parallel Rectangular Microchannel Heat Sinks: An Experimental Study*, Heat Transfer Engineering **38**, 1415–1428 (2017).

[182] U. Soupremanien, S. L. Person, M. Favre-Marinet, and Y. Bultel, *Influence of the aspect ratio on boiling flows in rectangular mini-channels*, Experimental Thermal and Fluid Science **35**, 797–809 (2011).

[183] B. R. Fu, C. Y. Lee, and C. Pan, *The effect of aspect ratio on flow boiling heat transfer of HFE-7100 in a microchannel heat sink*, International Journal of Heat and Mass Transfer **58**, 53–61 (2013).

[184] S. Singh, A. Kulkarni, S. Duttagupta, B. Puranik, and A. Agrawal, *Impact of aspect ratio on flow boiling of water in rectangular microchannels*, Experimental Thermal and Fluid Science **33**, 153–160 (2008).

[185] Y. Wang and K. Sefiane, *Effects of heat flux, vapour quality, channel hydraulic diameter on flow boiling heat transfer in variable aspect ratio micro-channels using transparent heating*, International Journal of Heat and Mass Transfer **55**, 2235–2243 (2012).

[186] A. Al-Zaidi, M. Mahmoud, and T. Karayiannis. *Flow boiling of HFE-7100 in Multi-Microchannels: Aspect Ratio Effect.* In *6th Micro and Nano Flows Conference Atlanta,USA, 9-12 September 2018*, volume 44, page 2, (2018).

[187] A. Candan, B. Markal, O. Aydin, and M. Avci, *Saturated flow boiling characteristics in single rectangular minichannels: effect of aspect ratio*, Experimental Heat Transfer **31**, 531–551 (2018).

[188] J. Lee and I. Mudawar, *Fluid flow and heat transfer characteristics of low temperature two-phase micro-channel heat sinks. Part 1 : Experimental methods and flow visualization results*, International Journal of Heat and Mass Transfer **51**, 4315 : 4326 (2008).

[189] J. Lee and I. Mudawar, *Fluid flow and heat transfer characteristics of low temperature two-phase micro-channel heat sinks – Part 2. Subcooled boiling pressure drop and heat transfer*, International Journal of Heat and Mass Transfer **51**, 4327–4341 (2008).

[190] M. R. Ozdemir, M. M. Mahmoud, and T. G. Karayiannis. *Flow boiling heat transfer in a rectangular copper microchannel.* In *Int. conf. on advances in mechanical engineering, 13-15 may 2015, Yildiz Technical University,*, Istanbul, (2015).

[191] A. H. Al-Zaidi, M. M. Mahmoud, and T. G. Karayiannis, *Effect of aspect ratio on flow boiling characteristics in microchannels*, International Journal of Heat and Mass Transfer **164**, 120587 (2020).

[192] P. S. Lee and S. V. Garimella, *Thermally developing flow and heat transfer in rectangular microchannels of different aspect ratios*, International Journal of Heat and Mass Transfer **49**, 3060–3067 (2006).

[193] P.-S. Lee and S. V. Garimella, *Saturated flow boiling heat transfer and pressure drop in silicon microchannel arrays*, International Journal of Heat and Mass Transfer **51**, 789–806 (2008).

[194] D. R. S. Raghuraman, R. Thundil Karuppa Raj, P. K. Nagarajan, and B. V. A. Rao, *Influence of aspect ratio on the thermal performance of rectangular shaped micro channel heat sink using CFD code*, Alexandria Engineering Journal **56**, 43–54 (2017).

[195] M. Magnini and O. K. Matar, *Numerical study of the impact of the channel shape on microchannel boiling heat transfer*, International Journal of Heat and Mass Transfer **150**, 119322 (2020).

[196] M. Andredaki, K. Vontas, A. Georgoulas, N. Miché, and M. Marengo, *The effect of channel aspect ratio on flow boiling characteristics within rectangular micro-passages*, International Journal of Heat and Mass Transfer **183** (2022).

[197] K. Vontas, M. Andredaki, A. Georgoulas, N. Miché, and M. Marengo, *The effect of surface wettability on flow boiling characteristics within microchannels*, International Journal of Heat and Mass Transfer **172** (2021).

[198] R. B. Peterson, *Numerical modeling of conduction effects in microscale counterflow heat exchangers*, Microscale Thermophysical Engineering **3**, 17–30 (1999).

[199] K. H. Bang and W. H. Choo. *Flow boiling in minichannels of copper, brassm and aluminium round tubes.* In *ICMM2004 The 2nd International Conference on Microchannels and Minichannels*, number 1 in International Conference on Microchannels and Minichannel, pages 1–6, Rochester, NY, (2004).

[200] A. H. Al-Zaidi, M. M. Mahmoud, and T. G. Karayiannis. *Flow Boiling of HFE-7100 in Multi-Microchannels: Effect of Surface Material.* In *Proceedings of the 5th World Congress on Momentum, Heat and Mass Transfer*, number October in World Congress on Momentum, Heat and Mass Transfer, pages 1–5, Lisbon, (2020).

[201] R. Hosseini, A. Gholaminejad, M. Nabil, and M. H. Samadinia. *Concerning the effect of surface material on nucleate boiling heat transfer of R-113.* In *ASME/JSME 2011 8th Thermal Engineering Joint Conference, AJTEC 2011*, pages 1–6, Hawai, USA, (2011).

[202] J. M. Jabardo, G. Ribatski, and E. Stelute, *Roughness and surface material effects on nucleate boiling heat transfer from cylindrical surfaces to refrigerants R-134a and R-123*, Experimental Thermal and Fluid Science **33**, 579–590 (2009).

[203] M. C. Paz, M. Conde, E. Suárez, and M. Concheiro, *On the effect of surface roughness and material on the subcooled flow boiling of water: Experimental study and global correlation*, Experimental Thermal and Fluid Science **64**, 114–124 (2015).

[204] X. Dai, F. Yang, R. Fang, T. Yemame, J. A. Khan, and C. Li, *Enhanced single- and two-phase transport phenomena using flow separation in a microgap with copper woven mesh coatings*, Applied Thermal Engineering **54**, 281–288 (2013).

[205] A. K. Morshed, T. C. Paul, and J. Khan, *Effect of Cu-Al2O3 nanocomposite coating on flow boiling performance of a microchannel*, Applied Thermal Engineering **51**, 1135–1143 (2013).

[206] H. T. Phan, N. Caney, P. Marty, S. Colasson, and J. Gavillet, *Enhancement of flow boiling heat transfer in microchannels by nano- and micro-surface treatments*, Mecanique et Industries **12**, 151–155 (2011).

[207] Y. M. Lie, J. H. Ke, W. R. Chang, T. C. Cheng, and T. F. Lin, *Saturated flow boiling heat transfer and associated bubble characteristics of FC-72 on a heated micro-pin-finned silicon chip*, International Journal of Heat and Mass Transfer **50**, 3862–3876 (2007).

[208] W. R. Chang, C. A. Chen, J. H. Ke, and T. F. Lin, *Subcooled flow boiling heat transfer and associated bubble characteristics of FC-72 on a heated micro-pin-finned silicon chip*, International Journal of Heat and Mass Transfer **53**, 5605–5621 (2010).

[209] S. M. Kim and I. Mudawar, *Universal approach to predicting saturated flow boiling heat transfer in mini/micro-channels – Part II. Two-phase heat transfer coefficient*, International Journal of Heat and Mass Transfer **64**, 1239–1256 (2013).

[210] D. Liu and S. V. Garimella, *Flow boiling heat transfer in microchannels*, Journal of Heat Transfer **129**, 1321–1332 (2007).

[211] Q. A. Al-Nakeeb, E. M. Fayyadh, and M. R. Hasan, *Experimental Investigation of Sub-Cooled Flow Boiling Heat Transfer in Single Rectangular Metallic Micro-Channel*, IOP Conference Series: Materials Science and Engineering **1094**, 012056 (2021).

[212] S. G. Kandlikar, *Fundamental issues related to flow boiling in minichannels and microchannels*, Experimental Thermal and Fluid Science **26**, 389–407 (2002).

[213] S. S. Mehendale, A. M. Jacobi, and R. K. Shah, *Fluid flow and heat transfer at micro- and meso-scales with application to heat exchanger design*, Applied Mechanics Reviews **53**, 175–193 (2000).

[214] B. Agostini, B. Watel, A. Bontemps, and B. Thonon. *Boiling heat transfer in mini-channels : influence of the hydraulic diameter To cite this version :.* In *Conference: International Congress of Refrigeration - At: Washington*, page 8, Washington, (2003).

[215] M. M. Shah, *Applicability of Correlations for Boiling/Condensing in Macrochannels to Minichannels*, Heat and Mass Transfer Research Journal **2** (2018).

[216] D. Steiner and J. Taborek, *Flow boiling heat transfer in vertical tubes correlated by an asymptotic model*, Heat Transfer Engineering **13**, 43–69 (1992).

[217] E. Ishibashi and K. Nishikawa, *Saturated boiling heat transfer in narrow spaces*, International Journal of Heat and Mass Transfer **12**, 863–894 (1969).

[218] M. Horiguchi and A. Sudi, *Thermo-hydraulics of boiling two-phase flow in high (thermo-hydraulics at low velocities)*, International Journal of Multiphase Flow **19**, 51–63 (1993).

[219] T. N. Tran, M. W. Wambsganss, M. Chyu, and D. France. *A Correlation for Nucleate flow boiling in small channels.* In *Compact Heat Exchangers for the Process Industries*, pages 1–30, Utah, (1997).

[220] S. G. Kandlikar and M. E. Steinke. *Predicting Heat Transfer During Flow Boiling in Minichannels and Microchannels.* In *ASHRAE Transactions*, pages 667–676. ASHRAE Transactions, (2003).

[221] Y. Xu, X. Fang, G. Li, D. Li, and Y. Yuan, *An experimental study of flow boiling heat transfer of R134a and evaluation of existing correlations*, International Journal of Heat and Mass Transfer **92**, 1143–1157 (2016).

[222] X. Fang, F. Zhuang, C. Chen, Q. Wu, Y. Chen, Y. Chen, and Y. He, *Saturated flow boiling heat transfer: review and assessment of prediction methods*, Heat and Mass Transfer/Waerme- und Stoffuebertragung **55**, 197–222 (2019).

[223] T. Harirchian and S. V. Garimella, *Microchannel size effects on local flow boiling heat transfer to a dielectric fluid*, International Journal of Heat and Mass Transfer **51**, 3724–3735 (2008).

[224] T. Harirchian and S. V. Garimella, *International Journal of Multiphase Flow The critical role of channel cross-sectional area in microchannel flow boiling heat transfer q*, International Journal of Multiphase Flow **35**, 904–913 (2009).

[225] Y. Wang, K. Sefiane, Z. G. Wang, and S. Harmand, *Analysis of two-phase pressure drop fluctuations during micro-channel flow boiling*, International Journal of Heat and Mass Transfer **70**, 353–362 (2014).

[226] P. M. Chung and M. Kawaji, *The effect of channel diameter on adiabatic two-phase flow characteristics in microchannels*, International Journal of Multiphase Flow **30**, 735–761 (2004).

[227] A. Kawahara, M. Sadatomi, K. Okayama, M. Kawaji, and P. M.-Y. Chung, *Effects of Channel Diameter and Liquid Properties on Void Fraction in Adiabatic Two-Phase Flow Through Microchannels*, Heat Transfer Engineering **26**, 13–19 (2005).

[228] P. Gunnasegaran, H. A. Mohammed, N. H. Shuaib, and R. Saidur, *The effect of geometrical parameters on heat transfer characteristics of microchannels heat sink with different shapes*, International Communications in Heat and Mass Transfer **37**, 1078–1086 (2010).

[229] A. M. Sahar, J. Wissink, M. M. Mahmoud, T. G. Karayiannis, and M. S. Ashrul Ishak, *Effect of hydraulic diameter and aspect ratio on single phase flow and heat transfer in a rectangular microchannel*, Applied Thermal Engineering **115**, 793–814 (2017).

[230] D. Sathishkumar and S. Jayavel, *Effect of channel confinement and hydraulic diameter on heat transfer in a micro-channel*, Springer Singapore (2019).

[231] C. Leng, X. D. Wang, T. H. Wang, and W. M. Yan, *Optimization of thermal resistance and bottom wall temperature uniformity for double-layered microchannel heat sink*, Energy Conversion and Management **93**, 141–150 (2015).

[232] Z. H. Wang, X. D. Wang, W. M. Yan, Y. Y. Duan, D. J. Lee, and J. L. Xu, *Multi-parameters optimization for microchannel heat sink using inverse problem method*, International Journal of Heat and Mass Transfer **54**, 2811–2819 (2011).

[233] G. Hedau, P. Dey, R. Raj, and S. K. Saha, *Experimental and numerical investigation of the effect of number of parallel microchannels on flow boiling heat transfer*, International Journal of Heat and Mass Transfer **158**, 119973 (2020).

[234] H. Dai, W. Chen, Q. Cheng, Y. Liu, and X. Dong, *Analysis of thermo-hydraulic characteristics in the porous-wall microchannel with microencapsulated phase change slurry*, International Journal of Heat and Mass Transfer **165**, 120634 (2021).

[235] E. Krepper and R. Rzehak, *CFD for subcooled flow boiling: Simulation of DEBORA experiments*, Nuclear Engineering and Design **241**, 3851–3866 (2011).

[236] B. E. Larsen, D. R. Fuhrman, and J. Roenby, *Performance of interFoam on the simulation of progressive waves*, Coastal Engineering Journal **61:3**, 18 (2018).

[237] T. Holzmann. *Mathematics, Numerics, Derivations and OpenFOAM - The basics for numerical simulations.* Technical Report 7, University of Leoben, Austria, (2017).

[238] E. Manon. *Contribution à l analyse et à la moé lisation locale des é coulements boillants sous-saturé s dans les conditions des Ré acteurs à Eau sous Pression.* Phd thesis, Ecole Centrale Paris, (2000).

[239] J. Garnier, E. Manon, and G. Cubizolles, *Local measurements on flow boiling of refrigerant 12 in a vertical tube*, Multiphase Science and Technology **13**, 1–111 (2001).

[240] E. Krepper and R. Rzehak, *CFD for subcooled flow boiling: Analysis of DEBORA tests*, Journal of Computational Multiphase Flows **6**, 329–359 (2014).

[241] G. Nagayama, T. Matsumoto, K. Fukushima, and T. Tsuruta, *Scale effect of slip boundary condition at solid-liquid interface*, Scientific Reports **7**, 1–8 (2017).

[242] O. Foundation. *OpenFOAM Guide*, (2012).

[243] K. Vontas, F. Latella, A. Georgoulas, N. Miché, and M. Marengo. *A numerical study on flow boiling within micro-passages: The effect of solid surface thermophysical properties.* In *15th International Conference on Heat Transfer, Fluid Mechanics and Thermodynamics*, page 6, Amsterdam, (2021).

[244] K. Vontas, M. Andredaki, A. Georgoulas, N. Mich, and M. Marengo, *The Effect of Hydraulic Diameter on Flow Boiling within Single Rectangular Microchannels and Comparison of Heat Sink Configuration of a Single and Multiple Microchannels*, Energies **5** (2021).

[245] M. M. Mahmoud, T. G. Karayiannis, and D. B. Kenning, *Surface effects in flow boiling of R134a in microtubes*, International Journal of Heat and Mass Transfer **54**, 3334–3346 (2011).

Resulted List of Scientific Publications

Vontas, K., Georgoulas, A., Miché, N., Marengo, M. A numerical investigation of the solid surface material influence on flow boiling within microchannel, **2022**, *Applied Thermal Engineering, Special Issue: 2022 HEFAT*, pages 18.

Vontas, K., Andredaki M., Georgoulas, A., Miché, N., Marengo, M. The effect of surface wettability on flow boiling characteristics within microchannels, **2021**, *International Journal of Heat and Mass Transfer*, *172*, pages 18.

M. Andredaki, K. Vontas, A. Georgoulas, N. Miché, M. Marengo, The effect of channel aspect ratio on flow boiling characteristics within rectangular micro-passages, **2021**, *International Journal of Heat and Mass Transfer*, *183*.

Vontas K., Andredaki M., Georgoulas A., Miche N., Marengo M. The Effect of Hydraulic Diameter on Flow Boiling within Single Rectangular Microchannels and Comparison of Heat Sink Configuration of a Single and Multiple Microchannels, *Energies*, **2021**.

Vontas K., Pavarani M., Georgoulas A., Miche N., Marengo M. Validation of the Eulerian-Eulerian two-fluid methodand RPI wall partitioning model of OpenFOAM against experiments in conventional tubes and microchannels, **2022**, (Under Review).

K. Vontas, F. Latella, A. Georgoulas, N. Miche, M Marengo. A Numerical Study on Flow Boiling Within Micro-Passages: The Effect of Solid Surface Thermophysical Properties, 15th International Conference on Heat Transfer, Fluid Mechanics and Thermodynamics, *Amsterdam - Netherlands*, **2021**

M. Andredaki, K. Vontas, A. Georgoulas, N. Miché, M. Marengo, Effect of Channel Aspect Ratio on Flow Boiling Characteristics within Rectangular Micro-passages, *Proc. 5th World Congr. Momentum, Heat Mass Transf.*, Lisbon, **2020**: pp. 1–8.

K. Vontas, M. Andredaki, A. Georgoulas, N. Miché, M. Marengo, Wettability effect on flow boiling characteristics within micro-passages, *Proc. 5th World Congr. Momentum, Heat Mass Transf.*, Lisbon **(2020)** 1–9.